ERRATA

| Page | Paragraph | Correction |
|---|---|---|
| 32 | 3 | Read "wind components (u,v) along north and east axes (x,y)" as "wind components (u,v) along east and north axes (x,y)". |
| 38,39 | | Read "surface layers" as "surface layer" throughout. |
| 53 | Table (2.3) | Read "140" as "180" for values of the constant of proportionality, M. |
| 55 | 1 | Read "day of year and latitude. (Equation (A.4b, Appendix A)." as "day of year and latitude (Equation (A.4b), Appendix A)." |
| 55 | 2 | Read "($h_m \approx 1400$ m for $u_{10} = 10$ m.s$^{-1}$)" as "(eg, $h_m = 1800$ for $u_{10} = 10$ m.s$^{-1}$)" |
| 64 | 2 | Read "u" as "$\bar{u}$" in Equation (2.26). |
| 64 | 3 | Read "are based on the trajectory" as "is based on the trajectory". |
| 69 | 1 | Read "15,000 Curies of 1131" as "16,000 Curies of I131". |
| 96 | 2 | Read "cloud cover 0-9 oktas" as "cloud cover 0-8 oktas". |
| 101 | 1 | Read "the interpolations was found" as "the interpolations were found". |
| 105 | Fig. (4.6) | Read "intermittment rainfall" as "intermittent rainfall". |
| 106 | Fig. (4.5) | Read notation "$J_c$" as "J". |
| 128 | 2 | Read "exposure generally decreases with increasing distance from source" as "exposure generally decreases with increasing distance from source (Figure (5.4a))." |
| 158 | Table (5.5) | Read the probability (%) of exposure at receptor 5700 from 3 hr releases as "9" instead of "19". |

ERRATA (continued)

| Page | Paragraph | Correction |
|---|---|---|
| 162 | 2 | Read "average levels of exposure have been considered" as "average levels of exposure, when receptors are exposed, have been considered". |
| 179 | 5 | Read "The frequency of different levels of I131(P)" as "The frequencies of different levels of I131(P)". |
| 217 | 3 | Read "140" in Equation (A6) as "180". |
| 219 | 2 | Read "absorbed into the mixing layer" as "absorbed into the mechanical layer". |

# LONG-RANGE ATMOSPHERIC DISPERSION OF RADIOISOTOPES

John Wrigley, MSc, A.R.C.S.

A thesis submitted for the degrees of
Ph.D, London University and D.I.C., Imperial College

Environmental Safety Group,
Nuclear Power Section,
Department of Mechanical Engineering,
Imperial College,
London, S.W.7.

February, 1982

## ABSTRACT

A computer model has been developed to predict the long-range dispersion of pollutant releases in the lower atmosphere. The model simulates the advection, dilution and removal of pollutant species over distances of about one thousand kilometres from the site of the release. The dispersion is modelled in a time dependent manner by allowing for the changing meteorological conditions along the path of the release.

Methods have been developed to process routine meteorological data, reported from the European network of weather stations and ships, into a form which is suitable for use in the dispersion model. The methods are generally applicable, and meteorological databases have been established to give meteorological conditions over Europe at three-hourly intervals for the years 1973 and 1976.

The model and meteorological databases have been applied to studies of the atmospheric dispersion of notional radioactive releases from nuclear installations. Patterns of air contamination and ground deposition resulting from long-term continuous releases of a selection of nuclides at different sites have been considered. The dispersion calculations have also been used to generate statistical information on the likelihood of different levels of exposure from short-term releases. The application of the model and databases is shown to be a suitable methodology for assessing the possible consequences of planned and unplanned releases from nuclear installations.

ACKNOWLEDGEMENTS

I would like to thank my supervisors, Dr. A. J. H. Goddard and Dr. H. M. ApSimon for their useful discussions and friendly guidance during this work. The project was jointly supported by CEA/EURATOM and I acknowledge the resources which have been made available.

Help from Helen ApSimon, Stuart Strachan and Roger Wootton in preparing this thesis is warmly appreciated. Sarah Gravestock also deserves credit for her speedy and efficient typing.

Most of all, special thanks (and apologies) to my wife for her long-suffering, but always loving, support.

To Irene

CONTENTS


| | | Page |
|---|---|---|
| | Abstract | 2 |
| | Acknowledgements | 3 |
| | Contents | 4 |
| | List of Figures | 9 |
| | List of Tables | 13 |
| | Notation | 15 |
| CHAPTER 1 | INTRODUCTION | |
| 1.1 | Environmental Safety and the Nuclear Industry | 19 |
| | 1.1.1 The Role of Atmospheric Dispersion Modelling | 20 |
| 1.2 | Behaviour of Pollutants in the Atmosphere | 20 |
| | 1.2.1 Dispersion of Pollutants | 22 |
| | 1.2.2 Removal of Pollutants | 23 |
| 1.3 | Methods of Modelling Atmospheric Dispersion | 23 |
| 1.4 | Aims of the Present Work | 25 |
| | 1.4.1 Motivation and Objectives | 25 |
| | 1.4.2 Description of the Work | 26 |
| CHAPTER 2 | THE MESOS MODEL FOR LONG-RANGE DISPERSION | |
| 2.1 | Introduction | 28 |
| 2.2 | Model Description | 28 |
| | 2.2.1 Puff Development | 29 |
| | 2.2.2 Exposures from a Continuous Release | 30 |
| 2.3 | Puff Trajectories | 32 |
| | 2.3.1 Boundary Layer Winds | 32 |
| | 2.3.2 The Advecting Wind | 33 |
| | 2.3.3 Derivation of Trajectories | 35 |
| | 2.3.4 Accuracy of Trajectories | 35 |


/Continued ...

Contents (continued)


| | | Page |
|---|---|---|
| 2.4 | Development of Individual Puffs | 37 |
| | 2.4.1 Dry Deposition | 37 |
| | 2.4.2 Wet Deposition | 42 |
| | 2.4.3 Lateral Dispersion | 43 |
| | 2.4.4 Vertical Dispersion | 45 |
| | 2.4.5 Pollutant Fluxes | 47 |
| 2.5 | Specification of Boundary Layer Parameters | 51 |
| | 2.5.1 The Geostrophic and 10m Winds | 54 |
| | 2.5.2 Daytime Boundary Layers over Land | 54 |
| | 2.5.3 Night-time Boundary Layers over Land | 55 |
| | 2.5.4 Boundary Layers over Sea | 56 |
| 2.6 | Example Puff History Calculations | 57 |
| 2.7 | Simulation of a Continuous Release using Puff Histories | 61 |
| | 2.7.1 Trajectory Model of a Plume | 61 |
| | 2.7.2 Exposures within a Plume | 62 |
| | 2.7.3 The Method of Calculation | 64 |
| 2.8 | Summary | 66 |
| CHAPTER 3 | STUDY OF THE 1957 WINDSCALE ACCIDENT USING THE MESOS MODEL | |
| 3.1 | Introduction | 68 |
| 3.2 | The Source Term | 68 |
| 3.3 | Meteorological Conditions | 69 |
| 3.4 | Measurements of 1131 after the Release | 70 |
| 3.5 | Dispersion Calculations | 75 |
| | 3.5.1 Trajectory Analysis | 75 |
| | 3.5.2 Regional Dispersion | 82 |
| | 3.5.3 Long-Range Dispersion | 87 |
| | 3.5.4 Accuracy of the MESOS Calculations | 87 |
| 3.6 | Summary | 88 |


/Continued ...

Contents (continued)


| | | Page |
|---|---|---|
| CHAPTER 4 | DEVELOPMENT OF THE METEOROLOGICAL DATABASE | |
| 4.1 | Introduction | 91 |
| 4.2 | Data Sources | 91 |
| 4.3 | Pressure Data | 92 |
| 4.4 | Synoptic Data | 95 |
| | 4.4.1 Interpolation Procedure for Synoptic Data | 98 |
| | 4.4.2 Estimation of Rainfall from the Present Weather Code | 101 |
| 4.5 | Database Production | 107 |
| 4.6 | Quality of the Database Information | 107 |
| 4.7 | Summary | 112 |
| CHAPTER 5 | ASSESSMENT OF THE DISPERSION CHARACTERISTICS OF PLANNED AND UNPLANNED NOTIONAL RELEASES FROM MOL DURING 1973 | |
| 5.1 | Introduction | 113 |
| 5.2 | Operational Methods | 113 |
| | 5.2.1 Derivation of Puff Histories | 114 |
| | 5.2.2 Treatment of Exposures | 118 |
| 5.3 | Long-Range Transport | 120 |
| | 5.3.1 Trajectory Analysis | 121 |
| | 5.3.2 Probability of Exposure | 124 |
| 5.4 | Exposure from Unplanned Releases | 129 |
| | 5.4.1 Exposure Frequency Distributions for Three-Hourly Releases | 130 |
| | 5.4.2 Consideration of the Exposure Frequency Distributions | 131 |
| | 5.4.3 Representation of the Exposure Frequency Distributions | 141 |


/Continued ...

Contents (continued)


| | | Page |
|---|---|---|
| 5.4.4 | Episodes Leading to Relatively High Exposures | 145 |
| 5.4.5 | Consideration of Release Duration | 154 |
| 5.5 | Annual Average Exposures | 161 |
| 5.5.1 | Time Integrated Air Concentrations | 162 |
| 5.5.2 | Dry and Wet Deposition | 163 |
| 5.6 | Summary | 167 |
| CHAPTER 6 | COMPARISON OF THE DISPERSION OF PLANNED AND UNPLANNED NOTIONAL RELEASES FROM SELECTED SITES DURING 1973 AND 1976 | |
| 6.1 | Introduction | 169 |
| 6.2 | The 1973 Studies for Karlsruhe and Heysham | 170 |
| 6.2.1 | Trajectory Analysis | 170 |
| 6.2.2 | Annual Average Patterns of Exposure | 175 |
| 6.2.3 | Exposure from Notional Unplanned Releases | 179 |
| 6.3 | Comparison between the 1973 and 1976 Studies for Mol | 184 |
| 6.3.1 | Trajectory Analysis | 187 |
| 6.3.2 | Long-Term Patterns of Exposure | 189 |
| 6.3.3 | Exposure from Notional Unplanned Releases | 195 |
| 6.4 | Summary | 198 |
| CHAPTER 7 | CONCLUSIONS | |
| 7.1 | Contributions of the Work | 199 |
| 7.2 | Future Work | 200 |
| REFERENCES | | 202 |
| APPENDIX A | THE DEPTH OF THE DAYTIME MIXING LAYER | |
| A.1 | Introduction | 212 |
| A.2 | Model for the Convective Growth of the Mixing Layer | 212 |


/Continued ...

Contents (continued)


| | | Page |
|---|---|---|
| A.3 | Specification of the Surface Heat Flux | 215 |
| A.4 | Solution Method | 216 |
| | A.4.1 Convective Mixing | 216 |
| | A.4.2 Wind Induced Mixing | 217 |
| A.5 | Validation of the Model | 219 |
| | A.5.1 Comparison with Measurements | 220 |
| | A.5.2 Comparison with Smith's Nomogram | 220 |
| A.6 | Sensitivity of Mixing Layer Development to Temperature Stratification in the Boundary Layer | 224 |

## LIST OF FIGURES

Figure

(2.1) Features of Long-Range Dispersion Modelled in MESOS.

(2.2) The Effect of Changes in Mixing Depth on the Vertical Development of Puffs.

(2.3) Sensitivity of Airborne Pollutant Fluxes to Atmospheric Conditions during Transport.

(2.4) Derivation of Exposures at a Receptor using the Puff Method.

(3.1) Sequence of Events and Postulated Release Patterns of I131 during the Accident.

(3.2) Synoptic Pressure Fields during the Accident.

(3.3a) Measurements of I131 Air Concentrations over Northern Europe.

(3.3b) Measurements on the Variation of Air Activity at Different Locations.

(3.4) Measurements of I131 Deposition over North-West England.

(3.5) Sensitivity of Trajectories to Backing Angle and Mean Wind-speed.

(3.6) Trajectories for Puffs Released at 0600, 0900, 1200 hours on the 10th October 1957.

(3.7) Trajectories for Puffs Released at 2100 and 2400 hours on the 10th October 1957.

(3.8) Trajectories of Puffs Released at 0600, 0900, 1200 hours on the 11th October 1957.

(3.9a) Predicted and Measured Levels of I131 Time Integrated Air Concentrations over North-West England (Release Pattern (a)).

(3.9b) Predicted and Measured Levels of I131 Time Integrated Air Concentrations over North-West England (Release Pattern (b)).

(3.10a) Predicted and Measured Levels of I131 Time Integrated Air Concentrations over North-West Europe (Release Pattern (a)).

(3.10b) Predicted and Measured Levels of I131 Time Integrated Air Concentrations over North-West Europe (Release Pattern (b)).

(3.11) Comparison of MESOS Calculations with Measurements.

/Continued...

Figures (continued)

(4.1) Distribution of Reporting Weather Stations.

(4.2) Contents of Land Station Reports.

(4.3) Flowchart for Synoptic Data Processing.

(4.4) Interpolation Scheme for Synoptic Data.

(4.5) Typical Structure of a Rainstorm.

(4.6) Comparison between Intermittent and Continuous Rainfall Rates.

(4.7) Comparison of Rainfall Episodes from the 1973 Database with Measurements at OECD Sites in Norway.

(4.8) Comparison of Total Rainfall from the 1973 Database with Corresponding Totals Measured at European Weather Stations.

(5.1) Comparison of Observed Wind Direction Frequencies at Mol (1973) with Winds Derived from the MESOS Database.

(5.2) Radial Grid System for Mol.

(5.3) Trajectory Rose for Mol (1973).

(5.4) Probability of Air Contamination and Wet Deposition due to Daily Releases from Mol during 1973.

(5.5) Trajectory Characteristics at the Time of Receptor Exposure.

(5.6) Histograms for Time Integrated Air Concentrations due to Three-Hourly Releases of I131(P) from Mol during 1973.

(5.7) Histograms for Time Integrated Air Concentrations due to Three-Hourly Releases of Kr85 from Mol during 1973.

(5.8) Histograms for Time Integrated Air Concentrations due to Three-Hourly Releases of Xe135 from Mol during 1973.

(5.9) Histograms for Wet Depositions due to Three-Hourly Releases of I131(P) from Mol during 1973.

(5.10) Scatter Diagrams for Nuclide Exposures at 100 km Receptors.

(5.11) Scatter Diagrams for Nuclide Exposures at 800 km Receptors.

(5.12) Cumulative Frequency Distributions of Nuclide Exposures at the 100 km North Receptor due to Three-Hourly Releases.

(5.13) Cumulative Frequency Distributions of Nuclide Exposures at the 800 km North Receptor due to Three-Hourly Releases.

/Continued ...

Figures (continued)

(5.14) Development of the Synoptic Pressure Field during 4th-11th September 1973.

(5.15) Development of the Synoptic Pressure Field during 26th-29th October 1973.

(5.16) Cumulative Frequency Distributions of Kr85 Time Integrated Air Concentrations at the 800 km East Receptor for Different Release Durations.

(5.17) Variation of Time Integrated Air Concentrations and Probability of Exposure with Release Duration.

(5.18) Annual Average I131(P) Exposures from Mol Releases during 1973.

(5.19) Annual Average Cs137 Exposures from Mol Releases during 1973.

(5.20) Annual Average Kr85, Xe133 and Xe135 Exposures from Mol Releases during 1973.

(6.1) Location of Receptors for Karlsruhe, Heysham and Mol.

(6.2) Trajectory Rose for Karlsruhe (1973).

(6.3) Trajectory Rose for Heysham (1973).

(6.4) Annual Average I131(P) and Kr85 Exposures from Karlsruhe Releases during 1973.

(6.5) Annual Average I131(P) and Kr85 Exposure from Heysham Releases during 1973.

(6.6) Histograms for Time Integrated Air Concentrations due to Unit Releases of I131(P) over 24 Hours from Mol during 1973.

(6.7) Histograms for Time Integrated Air Concentrations due to Unit Releases of I131(P) over 24 Hours from Karlsruhe during 1973.

(6.8) Histograms for Time Integrated Air Concentrations due to Unit Releases of I131(P) over 24 Hours from Heysham during 1973.

(6.9) Trajectory Rose for Mol (1976).

(6.10a) Seasonal Average I131(P) Exposures from Mol Releases during 1976.

(6.10b) Seasonal Average Kr85 and Xe135 Time Integrated Air Concentrations from Mol Releases during 1976.

(6.11a) Comparison of Annual Average I131(P) Exposures from Mol Releases during 1973 and 1976.

/Continued ...

Figures (continued)

(6.11b) Comparison of Annual Average Kr85 and Xe135 Time Integrated Air Concentrationsfrom Mol Releases during 1973 and 1976.

(6.12) Comparison of Receptor Exposure Characteristics for Three-Hourly Releases from Mol during 1973 and 1976.

(A.1) Model of the Convective Mixing Layer.

(A.2a) Mixing Layer Development over a Timestep.

(A.2b) Adaption for Mechanical Mixing.

(A.3) Measurements and Model Calculations on Day 33 of the Wangara Study.

(A.4) Comparison of Model Calculations.

(A.5) Temperature Profiles at Dawn.

# LIST OF TABLES

Table

(1.1) Critical Routes to Exposure for Some Important Nuclides.

(2.1) Reduction in Typical Nuclide Deposition Velocities due to the Resistance to Downward Diffusion in Stable Conditions.

(2.2) Boundary Layer Parameterization Schemes Incorporating Reported Meteorological Data.

(2.3) Wind Profile Parameters used in MESOS.

(2.4) Sensitivity of Airborne Pollutant Fluxes to Release Conditions.

(4.1) The Present Weather Code and Database Indices.

(4.2) Rainfall Rates for Common Precipitation Types.

(4.3) Availability of Synoptic and Pressure Data in the 1973 Database.

(5.1) Organisation of the MESOS Dispersion Calculations.

(5.2) Depletion Rates for Nuclides.

(5.3) Episodes Leading to Relatively High Nuclide Exposures at the 100 km Receptors.

(5.4) Episodes Leading to Relatively High Nuclide Exposures at the 800 km Receptors.

(5.5) Probability of Air Contamination and Wet Deposition for Different Release Durations.

(5.6) Maximum and Average Time Integrated I131(P) Air Concentrations from Mol Releases during 1973.

(5.7) Maximum and Average I131(P) Wet Depositions from Mol Releases during 1973.

(6.1) Maximum and Average Time Integrated I131(P) Air Concentrations from Karlsruhe Releases during 1973.

(6.2) Maximum and Average Time Integrated I131(P) Air Concentrations from Heysham Releases during 1973.

/Continued ...

List of Tables (continued)

Table

(A.1) Reduction Factors for Cloud Cover.

(A.2) Comparison of Mixing Layer Maximum Depths Predicted by HTBL2 and Carson and Smith's Nomogram.

(A.3) Effect of Stability on Maximum Mixing Layer Depths.

## NOTATION

| | | Units |
|---|---|---|
| $A$ | Entrainment parameter. | |
| $A_{ij}, R_{ij}$ | Averaged and reported meteorological data. | [$^oK$, mm.hr$^{-1}$, etc.] |
| $a_1, a_2, a_3$ | Parameters defining receptor position relative to a plume. | [$m^2$] |
| $B$ | Puff breath. | [m] |
| $C$ | Pollutant concentration. | [Kg.m$^{-3}$ or Ci.m$^{-3}$] |
| $c$ | Cloud cover. | [oktas] |
| $c_p$ | Specific heat of air at constant pressure. | [J.Kg$^{-1}$.$^oK^{-1}$] |
| $D$ | Random variable. | |
| $d$ | Day of year. | |
| $d_o$ | Location parameter in Weibull distribution. | |
| $E$ | Heat content of air column in mixing layer. | [J.m$^{-2}$] |
| $\delta E$ | Change in heat content over time step $\delta t$ | [J.m$^{-2}$] |
| $E_N(\underline{x}, \Delta T)$ | Exposure at receptor $\underline{x}$ from a release of duration $\Delta T$. | [Ci.s.m$^{-3}$ or Ci.m$^{-2}$] |
| $F$ | Downward flux of material. | [Kg.s$^{-1}$.m$^{-2}$ or Ci.s$^{-1}$.m$^{-2}$] |
| $f$ | Coriolis parameter. | [s$^{-1}$] |
| $f_e(m)$ | Fraction of material entrained into mixing layer from $m^{th}$ stable layer. | |
| $f_I(m)$ | Fraction of material isolated from mixing layer into $m^{th}$ stable layer. | |
| $G$ | Geostrophic windspeed | [m.s$^{-1}$] |
| $H$ | Sensible heat flux | [W.m$^{-2}$] |
| $h$ | Depth of mixing layer | [m] |
| $\delta h$ | Change in mixing depth over time step $\delta t$ | [m] |
| $h_{max}$ | Maximum depth of mixing layer during travel | [m] |
| $I$ | Database rainfall index | |
| $J$ | Rainfall rate | [mm.hr$^{-1}$] |
| $k$ | Diffusivity | [m$^2$.s$^{-1}$] |
| $k_1$ | Average diffusivity above surface layers | [m$^2$.s$^{-1}$] |
| $L$ | Longitudinal dispersion of puff | [m] |
| $\ell$ | Trajectory length | [m] |

/Continued ...

Notation (continued)

| | | Units |
|---|---|---|
| $M(P)$ | Constant of proportionality for mechanical mixing depth. | [s] |
| $m$ | Number of releases giving non-zero exposure; stable layer index. | |
| $n$ | Number of releases in a given period. | |
| $P$ | Pasquill category; intermediate puff | |
| $P_1, P_2$ | Puffs released at times $T_1$ and $T_2$ respectively | |
| $Pr$ | Probability of exposure | |
| $pr$ | Probability | |
| $p$ | Atmospheric pressure | $[N.m^{-2}]$ |
| $Q_N$ | Quantity of material in mixing layer | [Kg or Ci] |
| $Q^N$ | Quantity of material in stable layers | [Kg or Ci] |
| $R$ | Incoming solar radiation | $[W.m^{-2}]$ |
| $Res$ | Resistance term in deposition velocity | $[s.m^{-1}]$ |
| $r$ | Distance between source and receptor | [m] |
| $r(c)$ | Reduction factor for cloud cover c | |
| $S$ | Separation between successive trajectories | [m] |
| $s_t, s_b$ | Release height range | [m] |
| $T$ | Time of puff release | [s] |
| $\Delta T$ | Release duration | [s] |
| $t$ | Time; travel time along trajectory | [s] |
| $\delta t$ | Time step | [s] |
| $t_{dep}$ | Depletion time-scale | [s] |
| $t_{dif}$ | Diffusion time-scale | [s] |
| $t_n$ | Time of local noon | [hr.] |
| $U(z)$ | Windspeed profile in boundary layer | $[m.s^{-1}]$ |
| $u, v$ | Boundary layer wind components | $[m.s^{-1}]$ |
| $u_G, v_G$ | Geostrophic wind components | $[m.s^{-1}]$ |
| $u_{10}$ | Windspeed at 10m above ground | $[m.s^{-1}]$ |
| $\bar{u}$ | Mean windspeed advecting puff | $[m.s^{-1}]$ |
| $\underline{\bar{u}}$ | Mean wind vector advecting puff | $[m.s^{-1}]$ |
| $V_N$ | Measured deposition velocity | $[m.s^{-1}]$ |
| $V_{N,e}$ | Effective deposition velocity | $[m.s^{-1}]$ |
| $x, y, z$ | Coordinates | [m] |
| $\underline{x}$ | Position vector of puff centre or receptor | [m] |
| $\Delta z$ | Stable layer thickness | [m] |
| $z_o$ | Surface roughness height | [m] |

/Continued ...

Notation (continued)

| | | Units |
|---|---|---|
| $z_1$ | Depth of surface layers | [m] |
| $z_d$ | Height of deposition velocity measurement | [m] |
| $z_t, z_b$ | Height of puff top and bottom above ground | [m] |

Greek Symbols

| | | |
|---|---|---|
| $\alpha$ | Backing angle of wind | [degrees] |
| $\alpha_{10}$ | Backing angle of 10m wind | [degrees] |
| $\overline{\alpha}$ | Mean backing angle over puff depth | [degrees] |
| $\beta$ | Exponents in power law relationships | |
| $\nu, \mu$ | Projective coordinates defining puff arrival time at a receptor | |
| $\zeta, \eta$ | Terms in Equation [A4.b] for insolation | |
| $\kappa$ | Trajectory "tortuosity" factor | |
| $\phi$ | Latitude | [degrees] |
| $\lambda_N$ | Radioactive decay constant | $[s^{-1}]$ |
| $\lambda^*_N$ | Total depletion rate in mixing layer | $[s^{-1}]$ |
| $\lambda^*_s$ | Total depletion rate in stable layers | $[s^{-1}]$ |
| $\Lambda_N$ | Washout coefficient | $[s^{-1}]$ |
| $\Lambda^*_N$ | Washout coefficient for rainfall rate of $1mm.hr^{-1}$ | $[s^{-1}]$ |
| $\Omega$ | Angular velocity of Earth's rotation | $[s^{-1}]$ |
| $\rho$ | Density of air | $[kg.m^{-3}]$ |
| $\sigma_y, \sigma_z$ | Lateral and vertical standard deviations | [m] |
| $\tau_{zx}, \tau_{zy}$ | Horizontal shear stresses | $[N.m^{-2}]$ |
| $\psi_R$ | Fraction of release contributing to exposure | |
| $\theta$ | Potential temperature | [°K] |
| $\delta\theta$ | Change in potential temperature over time step $\delta t$ | [°K] |
| $\Delta\theta$ | Change in potential temperature across entrainment layer | [°K] |
| $\theta_i, \gamma_i$ | Constants defining stable temperature profile above mixing layer | $[°K, °K.m^{-1}]$ |
| $\theta_{sea}$ | Sea temperature | [°K] |
| $\theta_{s1}$ | Air temperature just above sea | [°K] |
| $\theta_o$ | Surface air temperature | [°K] |
| $\theta_{300}$ | Air temperature 300 m above surface | [°K] |

/Continued ...

Notation (continued)

Subscripts

| | |
|---|---|
| A to F | Location of points A to F |
| G | Geostrophic |
| N | Nuclide |
| c | Convective mixing |
| m | Mechanical mixing |
| s | Stable layers |
| t | Time of peak exposure |

Superscripts

| | |
|---|---|
| N | Nuclide |
| - | Average; annual average |
| ^ | Average when exposed |

# CHAPTER 1 INTRODUCTION

## 1.1 Environmental Safety and the Nuclear Industry

The safety aspects of nuclear reactors and reprocessing facilities have recently caused growing concern amongst the general public, particularly in relation to the commitment of many industrialised countries to increase progressively their nuclear power programmes. Recent examples of public concern and debate can be found in the Windscale Inquiry (Parker (1978)) and the choice of future reactor types within the United Kingdom. The efforts of the nuclear industry to convince the public of the safety of its activities has involved demonstrating that adequate safety standards can be achieved in an economic manner.

The siting, design and operation of nuclear facilities is strictly controlled by limits on the potential exposure to plant personnel and the general public. Legislative control is generally based on such factors as compliance with dose limits and the demonstration of best practicable means to reduce exposure levels. Recent emphasis has also been placed on the justification of all radioactive releases, however small (ICRP-26 (1977)), the underlying concept being that there is no proven threshold below which exposure is absolutely safe. Although the discharge of activity during planned emissions are relatively small, they must be carefully controlled in order to avoid any possible cumulative effects on the surrounding population. In particular, considerable effort and resources are also employed to minimise the probability of accidental releases which may possibly lead to casualties and contamination of the environment over a large area.

The consequences of possible accidental releases may be analysed using probabilistic methods. Notable examples are the reactor safety studies undertaken in the United States (Rasmussen (1975)) and West Germany (1979). Reliability and risk analysis techniques may be used to derive the frequencies of radioactive releases for different reactor types. Atmospheric dispersion models can then be

used to estimate the probabilities of different levels of exposure and deleterious effects occurring within the population. These methods have allowed the estimated risks to be compared to other non-nuclear risks which are tolerated by society. A probabilistic representation of the consequences of accidental releases is therefore of considerable interest, since this information can be used as an aid to decision-making both within and outside the nuclear industry.

### 1.1.1 The Role of Atmospheric Dispersion Modelling

The need to understand and quantify the atmospheric dispersion of radioactivity arises when estimating the potential population exposures resulting from planned and unplanned releases. A wide range of nuclides could be released to the atmosphere, particularly in uncontrolled conditions, but the main interest is in doses from the most radiologically significant nuclides. Exposure to the population may arise in the following ways:

- external irradiation from airborne and deposited activity
- inhalation of airborne activity
- ingestion of contaminated foodstuffs

Critical routes to exposure are shown in Table (1.1) for a selection of important nuclides. In order to estimate the doses resulting from these exposures, information on the spatial variations of time integrated air concentrations and ground depositions are required for each nuclide. Atmospheric dispersion therefore provides the important link between the source of nuclide emission and the population groups potentially at risk to exposure.

## 1.2 Behaviour of Pollutants in the Atmosphere

The behaviour of a pollutant released into the atmosphere is determined by the prevailing weather conditions and the physical properties of the pollutant. The density of the pollutant material is particularly important in the initial stages of dispersion. For example, buoyancy

| Nuclide | Form | Critical Exposure Route | | | Critical Organ |
|---|---|---|---|---|---|
| I131 | (i) Absorbed onto particulates<br>(ii) Methyl iodide vapour | Airborne activity | → Inhalation | | Thyroid |
| | | Ground deposited activity | → Ingestion | | |
| Cs137 | Absorbed onto particulates | Airborne activity | → Inhalation | | Whole body |
| | | Ground deposited activity | → Ingestion | | |
| Kr85 | Inert gas | → Airborne activity | → External irradiation | → | Skin |
| Xe133<br>Xe135 | Inert gas | → Airborne activity | → External irradiation | → | Whole body |

Table (1.1) Critical Routes to Exposure for Some Important Nuclides

effects may cause relatively hot gases to rise a considerable height above the point of release, whereas gases or particulate material denser than air will settle to ground level. Although large particle sizes may deposit within a few kilometres of the source, any density differences between gaseous effluent and the air will gradually disappear due to entrainment of surrounding air into the plume. In this case, the pollutant will adjust to the behaviour of a passive tracer, following the flow patterns within the atmosphere.

### 1.2.1 Dispersion of Pollutants

Pollutant material will be transported away from the source by the winds in the atmosphere. The speed and direction of these winds generally varies with height above ground level. The upper airflow is primarily driven by large-scale pressure features such as anticyclones and depressions. At lower levels within the atmospheric boundary layer, the influence of the ground produces winds which decrease in strength and back in direction relative to the upper winds.

Turbulence within the atmospheric boundary layer causes pollutant spreading and dilution during transport. Turbulent motions arise from the drag of the airflow over the ground and are also associated with convective thermals set up due to the heating of the ground by the sun. Stability conditions have an important influence on the scale of these eddy motions and the rate at which a pollutant disperses. Unstable conditions, which may occur during the day when convective processes dominate, lead to relatively rapid pollutant dispersion. However, the rate of dispersion may be considerably less at night if turbulence is suppressed by a stable temperature stratification.

The region of the lower atmosphere in which turbulent motions are significant is called the mixing layer. The depth of the mixing layer can vary considerably (≈100m - 2000m) according to windspeed and ground heating conditions. Pollutant emitted within the mixing layer will spread vertically until reaching ground level and the top

of the mixing layer. The pollutant is then likely to remain trapped within the mixing layer until future mixing layer development occurs.

### 1.2.2 Removal of Pollutants

A pollutant will generally have a characteristic residence time within the atmosphere which is determined by its physical properties and atmospheric conditions during transport. For example, radioactive decay or chemical conversion to other substances will reduce the amount of material which remains airborne.

The ultimate fate of many pollutants is deposition onto the ground. In addition to gravitational settling, ground deposition may occur due to a variety of other mechanisms such as absorption or impaction on vegetation. These removal processes, which are only operative after material has reached the surface, are collectively referred to as dry deposition. Wet deposition will also occur when the pollutant is scavenged from the atmosphere by precipitation. Consequently, the occurrence and intensity of rainfall events during atmospheric transport is an important factor for many pollutants which are susceptible to removal by precipitation.

## 1.3 Methods of Modelling Atmospheric Dispersion

In general, the objective of an atmospheric dispersion model is to estimate pollutant concentrations and depositions in different atmospheric conditions. Meteorological conditions may vary over relatively short timescales during atmospheric dispersion. This complicates the simulation of pollutant behaviour and approximate methods are generally employed. A wide range of dispersion models have been developed in recent years with different levels of sophistication and emphasis. Three basic approaches are briefly described below, which provide the main ingredients of most dispersion models.

(i) The Gaussian plume model is probably the most widely used dispersion model, due to its simplicity and ability to produce useful results in many practical applications. In the model, the crosswind pollutant concentrations are taken to be Gaussian in form. The lateral and vertical dimensions of the plume are then characterised by the standard deviations $\sigma_y$ and $\sigma_z$, which are chosen according to the prevailing stability conditions. Various schemes have been proposed which allow $\sigma_y$ and $\sigma_z$ values to be selected for use in the Gaussian model (e.g. Pasquill (1961), Turner (1970), Gifford (1976)). These schemes normally introduce a simple classification of stability conditions; for example, the Pasquill categories A to F, according to windspeed and insolation conditions. The downwind variation of $\sigma_y$ and $\sigma_z$ is then specified for each stability condition.

Although the basic Gaussian model can be adapted to approximate such effects as dry deposition and pollutant trapping within the mixing layer, the model is only strictly valid in unchanging boundary layer conditions. Another limitation is that vertical variations in windspeed and stability conditions, which may substantially affect the vertical concentration profile, are neglected in the model. Conservative choices for parameters are often used to overcome these uncertainties in estimating downwind concentrations.

(ii) A more fundamental approach is to derive pollutant concentrations from the diffusion equation. Variations in the turbulent mixing processes are represented in terms of horizontal and vertical diffusivities, which may be deduced from experimental measurements. A more realistic wind profile may also be considered.

Attempts to solve the three-dimensional diffusion equation usually involve numerical techniques, although the main features of the concentration profile may be derived using the method of moments (Aris (1956), Saffman (1962)). Solutions

of the two-dimensional diffusion equation may be obtained using Fourier transform techniques (Prahm and Cristensen (1977)) or by employing Green's functions (Maul (1977)). The Gaussian plume model can be derived from the simple diffusion equation in which windspeeds and diffusivities are taken as constants. The diffusion equation therefore gives scope for a more realistic description of pollutant dispersion at the cost of extra computational effort.

(iii) Puff trajectory models are often used in regional or long-range dispersion studies where the time dependent features of atmospheric transport are important. Pollutant advection is described by the trajectories of individual puffs which are sequentially released from source. These puff trajectories are derived from the boundary layer windfields which may be allowed to vary both in space and in time.

The vertical and lateral development of each puff along its trajectory can then be specified from a solution of the diffusion equation (Maul (1980)) or by using a conventional Gaussian model (Le Grand et al (1980)). Atmospheric conditions which influence the puff development may be assessed from appropriate boundary layer models. Pollutant depletion by precipitation scavenging, dry deposition and radioactive decay may also be included by applying a pollutant mass balance for each puff.

## 1.4 Aims of the Present Work

### 1.4.1 Motivation and Objectives

The important role of atmospheric dispersion modelling in safety assessments within the nuclear industry has been briefly discussed in Section (1.1.1). In general, relatively simple dispersion models have been used in the calculation of exposures from routine and accidental releases. Gaussian plume models are usually employed and weather conditions are often assumed to remain constant during atmospheric trans-

port (e.g. Fryer and Kaiser (1978), Strachan (1979)). Although this assumption is reasonable for relatively short-range dispersion, say at distances less than 10 km, extrapolations of site wind directions and weather conditions over longer distances often introduce considerable uncertainties in the dispersion estimates. The limitations of these methods, particularly in long-range accidental studies, are widely recognised; this is shown by the following comments taken from the U.S. Reactor Safety Study (Rasmussen (1975), p.17):

> "A much more difficult problem is presented by the weather which can change in a large variety of ways during the dispersion of radioactivity. No completely realistic method now exists (1975) for treating the dispersion of pollutants and existing models are felt to be particularly uncertain at long distances from the point of release".

These comments express the main motivation for the work described in this thesis. A primary aim is to establish a method which can allow for the effects of changing weather conditions during long-range transport. The method involves the use of an appropriate dispersion model which incorporates real meteorological data into the calculation scheme. It is hoped that a better description of long-range transport will result from this approach.

### 1.4.2 Description of the Work

A puff trajectory model, MESOS, has been developed in order to simulate the long-range transport of pollutants released into the atmosphere (Chapter 2). The influence of variable atmospheric conditions on the long-range dispersion is represented in a relatively simple and economical manner. Pollutant puffs, released at regular three-hourly intervals, are tracked through the evolving wind fields. The dispersion and depletion of puffs along each trajectory are derived according to the state of the boundary layer which is assessed from local meteorological conditions.

Meteorological data has been organised into a suitable form for use in the MESOS dispersion model. This meteorological data originates from weather observations which are reported at regular three-hourly

intervals by the European network of land stations and ships. The methods used to process the relevant meteorological data are described in Chapter 4. Particular consideration is given to the treatment of important variables such as rainfall and pressure observations. These methods have been used to generate European meteorological databases for the periods 1973-74, and, more recently, 1976.

The MESOS program and databases have been extensively applied in order to study the long-range dispersion of hypothetical radioactive releases from sites within the European Community. The aim of these studies is to give an assessment of possible levels of exposure from planned and unplanned releases at nuclear installations. Dispersion calculations for 1973 and 1976 have been used to derive frequency distributions showing the chances of different levels and types of contamination occuring in regions following notional unplanned releases at a remote site. This application is particularly appropriate for investigating the possible trans-frontier effects of accidental releases, as specified by Article 37 of the Euratom Treaty. Contamination due to notional planned releases has also been considered in the dispersion studies. Results from these applications of the MESOS program and meteorological databases are described in Chapters 5 and 6.

In addition, the MESOS model has been used to study the regional and long-range dispersion of I131 emissions during the 1957 Windscale accident. Contamination was recorded over a large area following this accident. These measurements are compared with the MESOS calculations in Chapter 3.

# CHAPTER 2 THE MESOS MODEL FOR LONG-RANGE DISPERSION

## 2.1 Introduction

This Chapter describes the MESOS model which has been used for all the dispersion studies presented in this thesis. The model has been developed to predict the time integrated concentrations and ground depositions resulting from a continuous release over a few hours or more from a chosen site. Although the passive dispersion of any non-reactive pollutant can be treated by MESOS, the model has been mainly applied to the dispersion of radionuclides.

The model is specifically designed to incorporate the time dependent features of the boundary layer which can have a significant influence on the behaviour of pollutants during long-range transport. Although the nearfield dispersion is represented in the model, the simplifying assumptions which are used become more appropriate as material disperses further away from the source of the release. Consequently, the model is most suitable for describing the dispersion of material beyond the first few tens of kilometres and up to distances of several hundred kilometres or more from source.

A general description of the model is given in the next section. The rest of the Chapter is concerned with the relevant aspects of the model and the methods used in the calculation procedure.

## 2.2 Model Description

The main features of the MESOS model are illustrated in Figure (2.1). A continuous release of material is simulated using a puff method in which the dispersion of discrete parts of the release (puffs) are considered in detail. The derived puff histories are then used to give a representation of the plume and allow the resulting exposures to be calculated. The model consists of two parts which are described separately.

### 2.2.1 Puff Development

The MESOS program calculates the trajectories and development of individual puffs which are initiated at regular three-hourly intervals from a chosen site. Each puff is treated simply as a vertical column of material which diffuses laterally and evolves vertically according to conditions within the atmospheric boundary layer.

The puff trajectories in the boundary layer are derived from the vertical wind profile which is assessed from the nature of the underlying terrain, the boundary layer stability and the free-stream geostrophic wind (Section (2.3)). These boundary layer winds, averaged vertically over the depth of the puff, are used to advect the puff and define the trajectories. The tracking of puffs can therefore be described as quasi-geostrophic where the development of the synoptic pressure field, during and after the release period, essentially determines the puff trajectories and the lateral spread of the plume.

The initial vertical dispersion of a puff is calculated using a well-established $\sigma_z$ scheme (Smith (1972)), and stability conditions are allowed to vary during the vertical development. This scheme is used until material reaches ground level and the top of the mixing layer. Both the ground and the typical inversion above the mixing layer are treated as effective barriers to the vertical spread of material. The subsequent vertical development of puffs is then controlled by the variations in mixing layer depth along the puff trajectories (Section (2.4.4)). Material may be carried upwards within a growing mixing layer, isolated aloft above an inversion as mixing subsides, and then possibly re-entrained by later mixing layer growth. Material isolated above the mixing layer does not experience depletion by dry deposition at ground level, and this can lead to relatively high concentrations above the mixing layer, say during the night. The depth of the mixing layer is therefore an important parameter, and a numerical scheme has been included in the MESOS code to predict the variations in mixing depth (typically 100m - 2000m) which are caused by the diurnal convective cycle, changes in wind strength and nature of the underlying terrain.

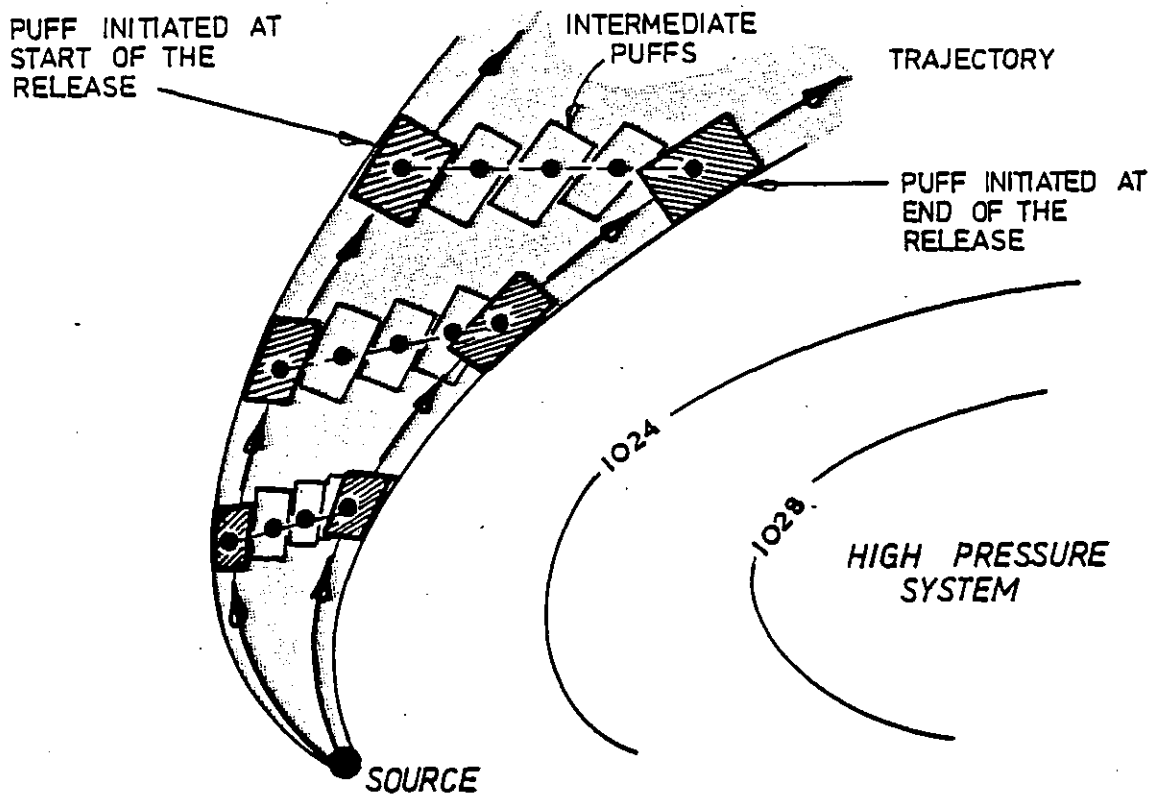
The lateral and vertical spread of a puff will lead to the dilution of material within the puff, and additional dilution may occur due to the loss of material from a puff. Radioactive decay, dry and wet deposition are represented in the model. As concentration profiles within the mixing layer are assumed to be uniform at a given time, an effective deposition velocity is used to allow for the resistance to downward diffusion within the mixing layer (Section (2.4.1)). Wet deposition can be an important removal mechanism, and is estimated from the rainfall rate which may vary along a puff trajectory (Section (2.4.2)).

The parameters necessary for the puff development calculations include the puff velocity, the depth of mixing and degree of turbulence within the mixing layer. Information on the location and intensity of precipitation is also required. These parameters are specified in terms of the local meteorological conditions along a puff trajectory (Section (2.5)). The model is therefore normally used with a meteorological database which has been developed from the routine reports of European weather stations (Chapter 4).

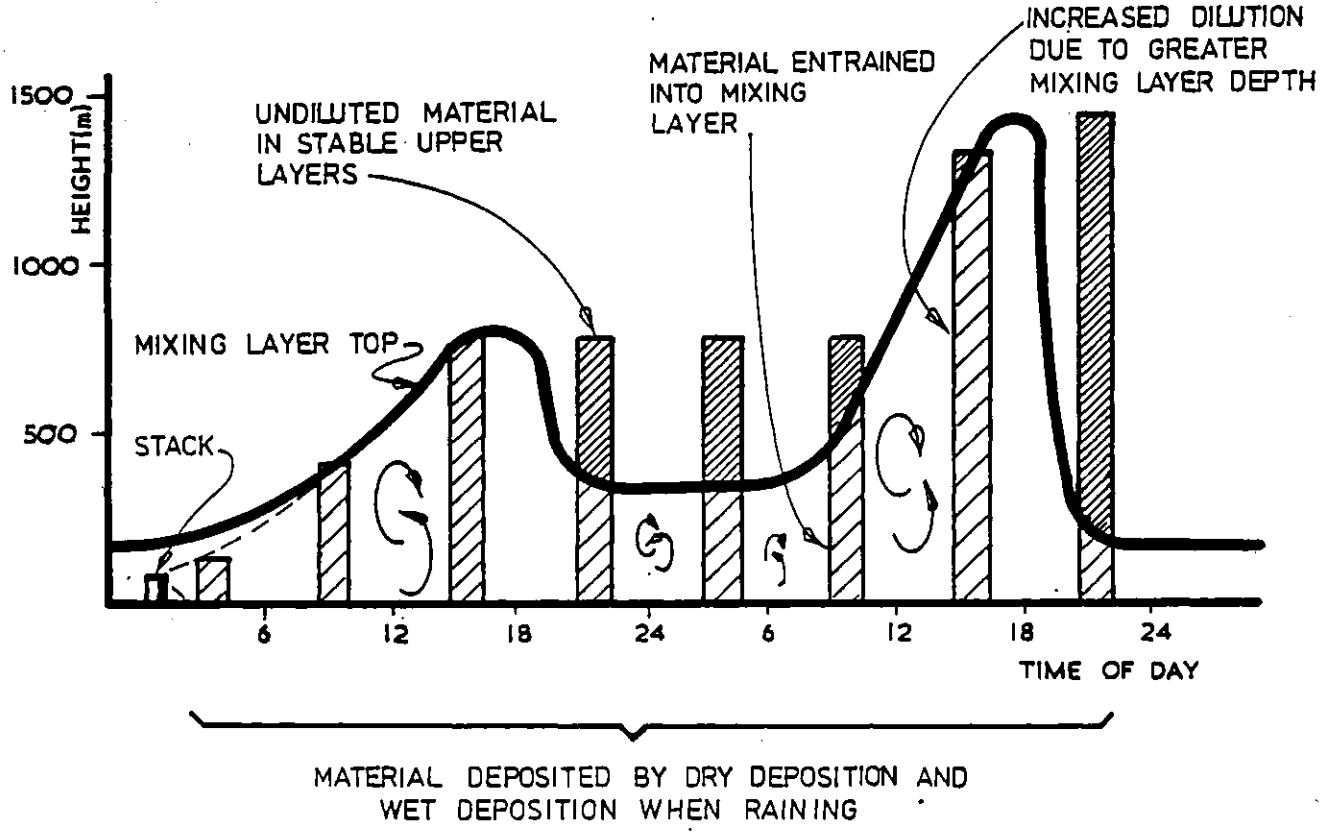
### 2.2.2 Exposures from a Continuous Release

A continuous release over a three hour period is simulated by considering the dispersion of an assembly of intermediate puffs fanning out between the calculated trajectories of the two puffs which span the release. The area between the calculated trajectories will be completely exposed and the synoptic lateral dispersion of the plume is modelled explicitly by the divergence of the puff trajectories. Small-scale lateral dispersion of individual puffs will also lead to some fringe exposure outside the bounding trajectories (Figure (2.1)).

The calculations of puff development along the bounding trajectories are used to estimate time integrated air concentrations, dry and wet depositions within the plume. These exposures are calculated at fixed points within a grid system which may be specified by the user. The method of calculation is independent of the choice of the grid system and is described in Section (2.7). Exposures from long-term releases




(a) Lateral Dispersion




(b) Vertical Dispersion

Figure (2.1) Features of Long-Range Dispersion Modelled in MESOS

are simulated from the cumulative exposures of consecutive three-hourly releases. A time varying release rate can therefore be easily incorporated into the calculations by applying appropriate weightings to each three-hourly exposure.

## 2.3 Puff Trajectories

The long-range transport of material is represented by a sequence of specimen puff trajectories initiated at regular three-hourly intervals from the site of the release. The puff trajectories are derived from the vertically averaged boundary layer winds over the depth of a puff and are two-dimensional in a horizontal plane. A quasi-geostrophic tracking procedure is used in order to allow for the influence of the large-scale pressure systems on the long-range transport.

### 2.3.1 Boundary Layer Winds

The horizontal wind components (u,v) along north and east axes (x,y), fixed on the earth's surface, depend on the horizontal pressure gradient and the shear stresses within the boundary layer:

$$\rho \frac{du}{dt} - \rho f v = \frac{-\partial p}{\partial x} + \frac{\partial}{\partial z}(\tau_{zx})$$

$$\rho \frac{dv}{dt} + \rho f u = \frac{-\partial p}{\partial y} + \frac{\partial}{\partial z}(\tau_{zy}) \qquad \ldots (2.1)$$

The Coriolis force, involving the parameter $f = 2\Omega \sin \phi$, represents the apparent deflecting force on the air flow due to the rotation of the earth.

The horizontal shear stresses ($\tau_{zx}$, $\tau_{zy}$) decrease with height above the ground as the influence of surface drag on the air flow diminishes. At the top of the boundary layer, the effect of surface drag is negligible, and, if acceleration is small, the air flow adjusts to a geostrophic balance between the Coriolis force and the synoptic pressure gradient:

$$u_G = -\frac{1}{\rho f}\frac{\partial p}{\partial y}$$

$$v_G = \frac{1}{\rho f}\frac{\partial p}{\partial x}$$

$$G = (u_G^2 + v_G^2)^{\frac{1}{2}} \qquad \ldots (2.2)$$

The geostrophic wind ($u_G$, $v_G$) is determined by the synoptic pressure field and represents flow along the pressure isobars. The geostrophic windspeed G may be as low as 3 $m.s^{-1}$ in very slack pressure gradients (e.g. anticyclones), but can exceed 30 $m.s^{-1}$ when the isobars are closely spaced (e.g. deep depressions). Although the geostrophic approximation is only strictly valid for steady flow with straight isobars, it usually gives an adequate representation of the winds above the mixing layer.

At lower levels within the boundary layer, the frictional forces give rise to boundary layer winds which decrease in strength and back in direction relative to the geostrophic wind. This wind profile depends on the stability conditions within the boundary layer and the nature of the underlying terrain. In practice, the winds near the surface are usually variable due to the turbulent motions within the boundary layer and the details of the wind profile can be difficult to specify. However, in general, the mean windspeed profile can be approximated by a simple power law (Pasquill (1974)):

$$U(z) = \begin{cases} G(\frac{z}{h})^{\beta} & \text{for } z < h \\ G & \text{for } z \geqslant h \end{cases} \qquad \ldots (2.3)$$

The turning of the wind with height may be represented by the backing angle $\alpha(z)$ from the geostrophic wind direction. The power $\beta$ and backing angle $\alpha$ are usually found to increase with increasing stability and surface roughness (Section (2.5.1)).

### 2.3.2 The Advecting Wind

The geostrophic approximation and the power law representation of the

wind profile are used to calculate the advecting wind at each time step along a puff trajectory in the MESOS calculations.

A vertically averaged windspeed over the depth of the puff is used to define the advecting windspeed:

$$\bar{u} = (z_t - z_b)^{-1} \int_{z_b}^{z_t} U(z)\, dz \qquad \ldots (2.4)$$

where $(z_t - z_b)$ is the depth of the puff column which will increase with time as the puff diffuses in the vertical. In practice, a discrete puff or cloud will be subject to along-wind distortion due to the differential windspeeds across the depth of the puff. However, the longitudinal dispersion of a puff does not have to be specified in the MESOS model since the calculations relate to time integrated concentrations, rather than absolute concentrations (Section (2.7.2)).

To allow for the backing of winds in the boundary layer, the direction of the advecting wind $\bar{\alpha}$, relative to the geostrophic wind direction, is taken as:

$$\bar{\alpha} = \frac{G - \bar{u}}{(G - u_{10})}\, \alpha_{10} \qquad \ldots (2.5a)$$

Thus:

$$\bar{\alpha} \to 0 \quad \text{as } \bar{u} \to G$$

$$\bar{\alpha} \to \alpha_{10} \quad \text{as } \bar{u} \to u_{10} \qquad \ldots (2.5b)$$

where $\alpha_{10}$ is the backing of the 10m wind relative to the geostrophic wind direction. The differential wind directions over the depth of a puff will tend to increase the lateral dispersion of material, and this effect is discussed in Section (2.4.3).

The specification of boundary layer wind parameters is described in Section (2.5.1). The advecting wind vector $\underline{\bar{u}}$ can then be determined from Equations (2.2) to (2.5) once the vertical extent of a puff is

known. Puff development and trajectories are calculated simultaneously using a time step procedure.

### 2.3.3 Derivation of Trajectories

The trajectory position $\underline{x}(T,t)$ of a puff centre, after travel time t, is determined from the advection equation:

$$\frac{d}{dt}\underline{x} = \underline{\bar{u}} \qquad \ldots (2.6)$$

A simple first order integration scheme is used to calculate the trajectory segment over the time interval $(t_1, t_2)$:

$$\underline{x}(T,t_2) - \underline{x}(T,t_1) = \underline{\bar{u}}.(t_2-t_1) \qquad \ldots (2.7)$$

Puff development and trajectory positions are calculated using a ten minute time step during the first three hours of travel when the puff is likely to be diffusing at a relatively rapid rate within the mixing layer. Hourly time steps are then used and puffs are tracked for four days or until they leave the European map area.

### 2.3.4 Accuracy of Trajectories

The accuracy of the quasi-geostrophic tracking procedure used in MESOS has been critically reviewed by ApSimon et al (1978). There are two main sources of error involved in the trajectory calculations:

(i) The use of the geostrophic approximation to represent the windfield above the mixing layer.

(ii) Inaccuracies in the synoptic pressure data which is used to derive the geostrophic wind and errors in the numerical integration of the windfield to define the trajectories.

The synoptic pressure fields in the meteorological database are gener-

ated by fitting interpolation polynomials to the scatter of surface pressure observations (Section (4.3)). Sykes and Hatton (1976) show that the estimation of geostrophic winds from such pressure data usually involves random errors of about 1 to 2 $m.s^{-1}$ in the windspeed. These random errors are likely to occur at each time step in the integration of the wind field to define the trajectories (Equation (2.7)). Sykes and Hatton also show that this source of error is generally more important than the numerical errors associated with the chosen integration scheme. Although the random errors in the estimated windspeed are relatively small, they can lead to significant trajectory errors, particularly when the synoptic wind direction changes systematically over relatively short distances. This occurs, for example, in frontal regions or near the centre of depressions. The sensitivity of trajectories in such synoptic conditions is considered further in Chapter 3.

The geostrophic approximation is only strictly valid for steady equilibrium flow between straight pressure isobars. The geostrophic departure (ageostrophic components) in the wind field is most significant when either the synoptic pressure field is developing rapidly in time or when the air flow is associated with large pressure gradients across highly curved isobars. Consequently, the geostrophic approximation is least likely to be appropriate in frontal systems and deep centres of low pressure. Large-scale vertical motions may also occur when the airflow is not in geostrophic balance, due to the convergence or divergence of air masses within the atmosphere. These vertical motions are generally associated with anticyclones, depressions and frontal systems, but the vertical velocities are usually small ($\sim$ few $cm.s^{-1}$).

Although it is possible to model the ageostrophic and vertical components using the available synoptic pressure data (ApSimon et al (1978), Maul (1980)), these effects are not included in the present statistical application of the MESOS model because of the limited computer resources. The objective of the present work is to study the long-term dispersion characteristics and patterns of exposure rather than accurately forecast a few individual trajectories. Similarly, the influence of

topography and thermal effects (e.g. land-sea breezes) on trajectories are not presently modelled in MESOS. All of these effects may be important in given situations, but it is believed that they are unlikely to influence systematically the distribution of trajectories which are sequentially initiated over long time periods.

## 2.4 The Development of Individual Puffs

This section describes the methods used to determine the development of individual puffs during long-range transport. The MESOS model simulates puff development in a Lagrangian manner with puff spreading, dilution and depletion calculated in a series of time steps along the puff trajectories. This approach allows the time dependent depletion processes (dry and wet deposition) and the variable state of the boundary layer to be more easily included in the model.

### 2.4.1 Dry Deposition

Dry deposition of pollutant at ground level can occur from several physical processes including absorption by vegetation and trapping by the ground roughness elements (Slinn (1978), Sehmel (1980)). It is conventional to represent the deposition processes in terms of a deposition velocity $V_N$ so that the deposition flux[1] at a level $z_d$, just above the roughness elements, is given by:

$$F(z_d) = V_N C(x,y,z_d) = \left(K(z) \frac{\partial C}{\partial z}\right)_{z_d} \quad \ldots (2.8)$$

The dry deposition of pollutant at ground level will lead to a depletion of material within the mixing layer and this depletion can be represented by using the source depletion concept (Van der Hoven, (1968)).

---

[1] Dry deposition measurements to determine $V_N$ are normally taken at a convenient reference height ($z_d \simeq 1$m) above ground level.

Source depletion models assume that dry deposition has no effect on the shape of the vertical concentration profile, and can be treated as an immediate and equal removal of material throughout the mixing layer. However, when vertical diffusion is inhibited, material near ground level may be depleted faster than it can be replenished from above, and a vertical concentration gradient will develop. In these circumstances, the assumption of an unaffected concentration profile in a source depletion model may lead to a considerable overestimation of dry deposition during transport (Scriven and Fisher (1975), Horst (1977), Prahm and Berkowicz (1978)).

In order to avoid this possible error, yet retain the convenient source depletion concept, an effective deposition velocity, $V_{N,e}$ is used in the MESOS calculations. The specification of the effective deposition velocity therefore attempts to allow for the effect of finite diffusivity and resistance to downward diffusion within the mixing layer.

### 2.4.1.1 The Effective Deposition Velocity

#### (i) Resistance within the surface layers

The main variation in the diffusivity and concentration profiles usually occurs within the surface layers near the ground. The downward flux F(z) within the surface layers can be reasonably assumed to be almost constant with height:

$$F(z) = F = K(z) \frac{\partial C}{\partial z} \qquad \ldots (2.9)$$

Integration of this equation over the vertical depth ($z_d$, $z_1$), therefore gives:

$$C(x,y,z_1) = C(x,y,z_d) + F \int_{z_d}^{z_1} \frac{d\zeta}{K(\zeta)} \qquad \ldots (2.10)$$

Consequently, if an effective deposition velocity, $V_{N,e}$ is defined

at a height $z_1$ ($\simeq$ 10-20m) above the main variation in the concentration profile, such that:

$$V_{N,e}\, C(x,y,z_1) = F = V_N\, C(x,y,z_d) \qquad \ldots (2.11)$$

Then:

$$\frac{1}{V_{N,e}} = \frac{1}{V_N} + \int_{z_d}^{z_1} \frac{d\zeta}{K(\zeta)} \qquad \ldots (2.12)$$

The term: $\int_{z_d}^{z_1} \frac{d\zeta}{K(\zeta)}$ represents a resistance to transfer of material through the surface layers. Scriven and Fisher (1975) obtained the equivalent form:

$$\frac{1}{V_{N,e}} = \frac{1}{V_N} + \frac{z_1}{K(z_1)} \log_e \left(\frac{z_1}{z_o}\right) \qquad \ldots (2.13)$$

by considering a linear diffusivity profile K(z) in the surface layers above the roughness height $z_o$.

(ii) Resistance above the surface layers

Allowance must also be made for the possible resistance to downward diffusion throughout the depth of the mixing layer. Although the assumption of constant flux is not valid above the surface layers, an indication of the effect of finite diffusivity within the mixing layer can be obtained from a comparison of the diffusion and depletion timescales. Maul (1977) has shown that the details of the diffusivity profile within the mixing layer are not very important during long-range transport, provided that a representative diffusivity $K_1$ is taken above the surface layers. In this case, the timescale for diffusion through the mixing layer $\left(t_{dif} \simeq \frac{h^2}{2K_1}\right)$ can be compared to the timescale for depletion

of material within the mixing layer ($t_{dep} \simeq \frac{h}{V_N}$). If the diffusion timescale is much shorter than the depletion timescale, i.e.:

$$V_N << \frac{2K_1}{h} \qquad \ldots (2.14)$$

then the finite rate of diffusion is expected to be relatively unimportant. Since deposition velocities $V_N$ for the range of nuclides considered in the MESOS calculations are no greater than $3.10^{-3}ms^{-1}$, the finite diffusivity will not greatly affect the dry deposition, apart from deposition in stable conditions ($K_1 \simeq 1\ m^2s^{-1}$, $h \simeq 200m$). This conclusion is also suggested by the work of Draxler and Elliot (1977).

Scriven and Fisher (1975) give a solution of the diffusion equation based on a model of constant diffusivity throughout the mixing layer with dry deposition on a flat surface. When steady conditions persist for a period longer than the diffusion timescale, Scriven and Fisher show that the asymptotic rate of depletion can be represented by introducing a resistance term into the deposition velocity:

$$\frac{1}{V_{N,e}} = \frac{1}{V_N} + \frac{4}{\pi^2}\left(\frac{h}{K_1}\right) \qquad \ldots (2.15)$$

This expression is similar to the criterion (2.14) and also indicates that only small modifications to the deposition velocity are appropriate in most stability conditions when the deposition velocity $V_N$ is relatively low.

Consequently, the approach used in MESOS is to allow for the resistance to downward diffusion in stable conditions by incorporating a resistance term into the deposition velocity:

$$\frac{1}{V_{N,e}} = \frac{1}{V_N} + Res \qquad \ldots (2.16)$$

A resistance term is chosen for given stability conditions during transport over land and sea (Table (2.1)). The resistance terms are necessarily tentative due to the limited applicability of the above

| Underlying Surface | Stability Conditions (Pasquill Category) | Resistance Term Res ($s.m^{-1}$) | Deposition Velocity $V_N$ ($m.s^{-1}$) | Effective Deposition Velocity $V_{N,e} = (1/VN + Res)^{-1}$ ($m.s^{-1}$) |
|---|---|---|---|---|
| LAND | E | 20 | $1.0\ 10^{-3}$<br>$3.0\ 10^{-3}$ | $9.8\ 10^{-4}$<br>$2.8\ 10^{-3}$ |
| | F | 40 | $1.0\ 10^{-3}$<br>$3.0\ 10^{-3}$ | $9.6\ 10^{-4}$<br>$2.7\ 10^{-3}$ |
| SEA | E | 300 | $1.0\ 10^{-3}$<br>$3.0\ 10^{-3}$ | $7.7\ 10^{-4}$<br>$1.6\ 10^{-3}$ |
| | F | 800 | $1.0\ 10^{-3}$<br>$3.0\ 10^{-3}$ | $5.5\ 10^{-4}$<br>$8.8\ 10^{-4}$ |

Table (2.1) Reduction in Typical Nuclide Deposition Velocities due to the Resistance to Downward Diffusion in Stable Conditions

considerations. For example, the adjustment to the deposition velocity represented in Equation (2.15) is only strictly valid for sufficiently long travel times and also relates to deposition on a perfectly flat surface. In stable conditions over land the airflow will tend to divide around small hills and obstacles, bringing pollution at higher levels into contact with the surface topography. Thus, the reduction in deposition may be less than that suggested by the flat surface model.

However, the values of the effective deposition velocities given in Table (2.1) show that the reduction in deposition is relatively insensitive to the choice of the resistance term in the MESOS calculations. This is due to the low nuclide deposition velocities, and the adjustments are usually small for transport over land. The largest reduction in dry deposition (50-70%) will occur for prolonged transport in stable conditions over the sea due to the smooth surface ($z_o \approx .1$mm). The choice of relatively large resistance terms over the sea may overestimate airborne nuclide fluxes and is therefore conservative in the context of long-range transport.

### 2.4.2 Wet Deposition

Pollutants may be scavenged from a puff and deposited onto the underlying ground when precipitation occurs along a puff trajectory. There are two separate processes which can contribute to precipitation scavenging:

(i) Rainout (in-cloud scavenging) occurs when pollutant particles act as possible condensation nuclei for the formation of water droplets in the rain cloud.

(ii) Washout (below-cloud scavenging) occurs when pollutant is collected by water droplets as they fall from the rain cloud to ground level.

Precipitation scavenging is therefore likely to remove pollutant from the entire vertical depth of a puff and can be an important depletion process for some nuclides (Section (2.6)).

Rainout is not currently modelled in MESOS, due to the complicated physical processes which are involved and the limited availability of the meteorological data needed to quantify these processes. Although a large number of different physical processes contribute to below-cloud scavenging, it is conventional to represent the total removal effect simply in terms of a washout coefficient (Pasquill (1974)). This washout coefficient can be defined as the fraction of pollutant removed per unit time during the precipitation event:

$$\Lambda_N = -\frac{1}{Q_N}\frac{dQ_N}{dt} \qquad \ldots (2.17)$$

The scavenging rate is known to depend on the rainfall rate (e.g. Engelmann (1965,1971)) and in MESOS the washout coefficient is taken as:

$$\Lambda_N = \Lambda^*_N \, J^{0\cdot8}(t) \qquad \ldots (2.18)$$

where $\Lambda^*_N$ is a constant which characterises the washout coefficient of a particular pollutant, and J(t) is the time dependent rainfall rate ($mm.hr^{-1}$) along a puff trajectory.

Precipitation may have considerable variability in space and time (e.g. showers) and so differential rainfall and removal rates may occur throughout a plume which has dispersed over a wide area (Ritchie et al (1976)). An averaged rainfall rate is therefore used in the MESOS calculations in an attempt to allow for such factors as the timescale and spread of precipitation. The methods used to derive an appropriate rainfall rate from fixed observations at weather stations are described in Section (4.4.2). Precipitation fields are available in the meteorological database at regular three-hourly intervals, and this gives a good representation of the location and intensity of precipitation.

### 2.4.3 Lateral Dispersion

The lateral dispersion of a cloud of pollutant can be attributed to

the mixing action of eddies and the horizontal windshear across the cloud. In general, the size of the eddies most effective in dispersing the cloud, at any given time, will be comparable to the lateral dimensions of the cloud. Initially, the small-scale turbulent eddies ($\sim 10^{-3}$m) will dominate the dispersion, but for long-range transport over several hundred kilometres, the large-scale synoptic circulations (depressions, anticyclones $\sim 10^{3}$ km) will become progressively more important. Although the lateral dispersion due to the large-scale synoptic features is explicitly modelled in MESOS by the divergence between successive puff trajectories, the lateral dispersion of individual puffs, due to small-scale dispersion, is also represented.

The lateral spread of individual puffs due to small-scale eddies and windshear can be complicated in nature. In particular, lateral dispersion can be enhanced by the vertical movement of pollutant particles between different levels at which the wind varies in direction and strength. Although these effects can be modelled (e.g. Csanady (1973), Saffman (1962)), the resulting expressions for lateral dispersion are only valid for a limited range of travel times and usually involve quantities (e.g. horizontal diffusivities) which are difficult to assess from readily available meteorological data.

Fortunately, the MESOS calculations of time integrated air concentrations and ground depositions due to a continuous release are relatively insensitive to the lateral spread of individual puffs (Section (2.7)). For example, if the lateral spread of individual puffs is overestimated, this will lead to an underestimation of puff concentrations, but this will be effectively compensated by the larger number of puffs contributing to exposure at a point. Moreover, the lateral spread of individual puffs is usually dominated by the divergence of successive trajectories in the synoptic pressure field. For these reasons, a relatively simple representation of lateral spread has been adopted in the MESOS model. The lateral spread of an individual puff is taken to be:

$$B(t) = \sqrt{2\pi}\ 0.5t \qquad \ldots (2.19)$$

where B(t) is the puff breath in metres after a travel time of t seconds. This rate of puff growth is equivalent to about 4.5 $km.hr^{-1}$ and is based on Heffter's (1964) review of experimental data, from several authors, on lateral spread during long-range transport. This value therefore represents an average lateral spread over different meteorological conditions and, as such, may be inappropriate for particular situations. However, the Heffter approximation is generally adequate for long-range dispersion calculations in MESOS.

### 2.4.4 Vertical Dispersion

Vertical dispersion is modelled by treating the atmosphere as a well-mixed turbulent boundary layer of variable depth (the mixing layer), surmounted by a series of stably stratified layers with negligible turbulence. The vertical development of a puff can then be considered in two separate stages:

(i) The initial vertical diffusion from source until material is dispersed throughout the mixing layer. This will occur at relatively short downwind distances ($\sim$ few km).

(ii) The subsequent vertical development due to variations in the depth of the mixing layer during long-range transport ($\sim$ few hundred km).

#### (i) Initial vertical dispersion

A release of material at source is taken to be uniformly dispersed over the height range ($s_b$, $s_t$). An appropriate height range may be chosen in MESOS to allow for the local dilution of material due to differential release heights, plume rise and entrainment in the wake of nearby buildings. A height range of 50-100m has been chosen in all the nuclide dispersion calculations described in this thesis, since this is fairly representative of stack heights at nuclear installations.

Provided that the release occurs in the mixing layer, the puff will spread vertically until it reaches ground level and the top of the mixing layer. Material is assumed to be uniformly spread over the increasing vertical depth of the puff, which, at any time, is represented in terms of the vertical dispersion parameter $\sigma_z$:

$$\text{Puff top:} \quad z_t = \min.\ (s_t + \sigma_z\sqrt{\tfrac{\pi}{2}}, h)$$

$$\text{Puff bottom:} \quad z_b = \max.\ (s_b - \sigma_z\sqrt{\tfrac{\pi}{2}}, 0) \qquad \ldots (2.20)$$

The constant factor $\sqrt{\frac{\pi}{2}}$ is included so that for a fairly low level source, the concentrations near the ground are the same as for a Gaussian plume with vertical dispersion parameter $\sigma_z$.

The value of $\sigma_z$ is estimated using the extension of the Pasquill scheme (1961) proposed by Smith (1972). Beyond distances of about 20 km from source there are relatively few reliable data on the values of $\sigma_z$. Smith therefore derived numerical solutions of the diffusion equation to give $\sigma_z$ curves for distances of up to 100 km from source. The scheme requires the Pasquill category to be specified, and this is assessed on the basis of windspeed, cloud cover and sensible heat flux, at each time step in the MESOS calculations (Section (2.5)). At the beginning of a time step, the current Pasquill category and $\sigma_z$ value are used to increment $\sigma_z$ over the following time interval according to the relevant $\sigma_z$ curve. If the Pasquill category changes between successive time steps, the model uses the value of $\sigma_z$ before the transition to determine the rate of change of $\sigma_z$ in the new Pasquill category, rather than distance from source. This method therefore allows time dependent stability conditions to be represented in MESOS and avoids the extrapolation of source meteorology as in conventional models.

(ii) Long-range vertical dispersion

A puff will eventually spread vertically to fill the complete depth of the mixing layer. Once this stage is reached, the Pasquill-Smith $\sigma_z$

curves are no longer used since vertical dispersion will be limited by the effective barriers at ground level and at the upper inversion which typically occurs above the mixing layer. Consequently, the subsequent vertical development is essentially determined by changes in the mixing depth along the puff trajectory. Typical changes in mixing depth and the resulting effect on the vertical development are illustrated in Figure (2.2).

If the mixing depth decreases, material already at levels near the top of the old mixing layer will become isolated in the stable layers above the new mixing layer. Material trapped in these stable layers is assumed to travel in almost laminar flow, with negligible vertical dispersion and so cannot be depleted by dry deposition at ground level. These conditions are most likely to occur during the night after the daytime convective mixing has subsided.

When the mixing depth increases, material will be spread over the increased depth. However, this does not necessarily imply that ground level concentrations will immediately decrease, since it is possible that any material at higher levels will also be re-entrained into the growing mixing layer. This fumigation event is most likely to occur during the morning, due to the relatively rapid convective growth of the mixing layer. If material is initially released above the mixing layer, then subsequent entrainment into a growing mixing layer is the only process by which material can subsequently reach ground level.

### 2.4.5 Pollutant Fluxes

The influence of variable mixing depth on the vertical development of puffs is particularly relevant to the derivation of pollutant fluxes along puff trajectories in the MESOS model.

Suppose that the mixing depth changes from $h(t_1)$ to $h(t_2)$ over the time step $(t_1,t_2)$ along the trajectory of a puff which is released from source at time T and has subsequently filled the mixing layer. It is then required to determine the quantity of material within the mixing layer, $Q_N(T,t)$, and the distribution of material in the stable

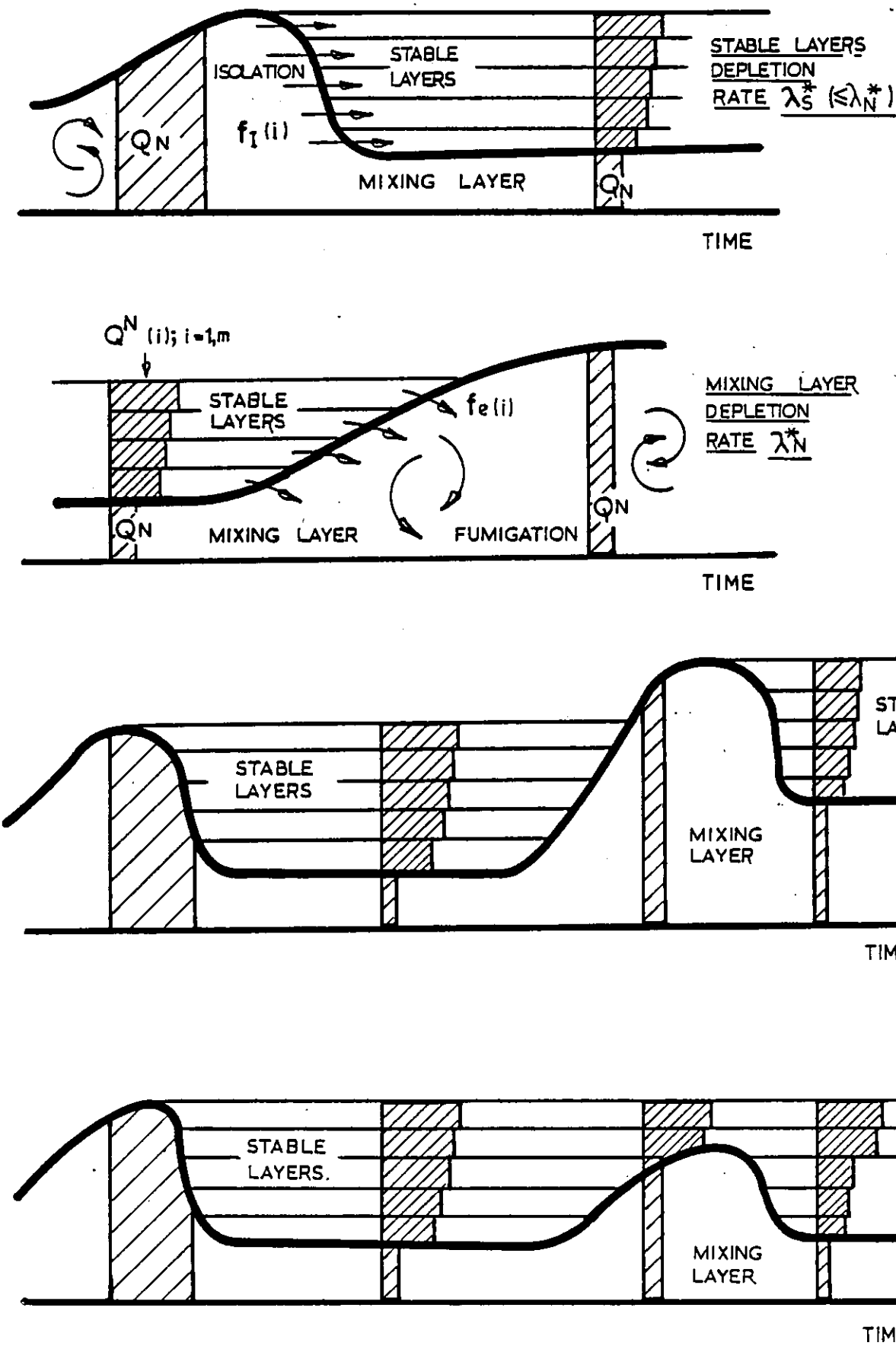



Figure (2.2) The Effect of Changes in Mixing Depth on the Vertical Development of Puffs

layers above the mixing layer after travel time t. Let $Q^N(T,t,m)$ represent the quantity of material residing in the $m^{th}$ stable layer between the levels $(m-1).\Delta z \leqslant z < m.\Delta z$. All the puff material may be subject to washout and natural decay, but only material within the mixing layer can be depleted by dry deposition at ground level. Consequently, two different depletion rates may be operative:

$$\text{Depletion in mixing layer} \qquad \lambda^*_N = \Lambda^*_N J^{0.8}(t) + \frac{V_{N,e}}{h(t)} + \lambda_N$$

$$\text{Depletion in stable layers} \qquad \lambda^*_s = \Lambda^*_N J^{0.8}(t) + \lambda_N \qquad \ldots (2.21)$$

If the mixing depth remains constant ($h(t_1) = h(t_2)$) then the depletion of airborne material is determined by:

$$\frac{dQ_N}{dt} = -\lambda^*_N Q_N$$

$$\frac{dQ^N}{dt} = -\lambda^*_s Q^N$$

$$Q_N(T,t_2) = Q_N(T,t_1) \exp - \lambda^*_N (t_2 - t_1)$$

$$Q^N(T,t_2,m) = Q^N(T,t_1,m) \exp - \lambda^*_s (t_2 - t_1) \qquad \ldots (2.22a)$$

However, in addition to depletion, any change in the mixing depth may also cause material to be redistributed between the mixing layer and the upper stable layers. The behaviour will be different for growing and subsiding mixing layers, and can be approximated in the following manner:

(i) Increase in mixing depth ($h(t_2) > h(t_1)$)

Material may be entrained into the mixing layer from the upper stable layers:

$$Q_N(T,t_2) = [Q_N(T,t_1) + \sum_m Q^N(T,t_1,m)\, f_e(m)] \exp - \lambda^*_N (t_2 - t_1)$$

$$Q^N(T,t_2,m) = Q^N(T,t_1,m)(1 - f_e(m)) \exp - \lambda^*_s (t_2 - t_1) \qquad \ldots (2.22b)$$

where $f_e(m)$ is the fraction of material, originally in the $m^{th}$ stable layer, which is entrained into the growing mixing layer. Entrainment will occur over the depth $h(t_1) \leqslant z \leqslant h(t_2)$ provided that there is already material above the mixing layer.

(ii) Decrease in mixing depth ($h(t_2) < h(t_1)$)

Conversely, material will be lost from the mixing layer and isolated in the stable layers, if the mixing depth decreases. Thus:

$$Q_N(T,t_2) = Q_N(T,t_2) \cdot \frac{h(t_2)}{h(t_1)} \cdot \exp - \lambda^*_N(t_2 - t_1)$$

$$Q^N(T,t_2,m) = [Q^N(T,t_1,m) + Q_N(T,t_1).f_I(m)] \exp - \lambda^*_s(t_2 - t_1) \quad \ldots (2.22c)$$

where $f_I(m)$ represents the fraction of material originally within the mixing layer which is left in the $m^{th}$ stable layer. Material will be isolated from the mixing layer over the depth $h(t_2) \leqslant z \leqslant h(t_1)$ and an amount of material,

$$Q_N[1 - \frac{h(t_2)}{h(t_1)}],$$

will be lost from the mixing layer, so that:

$$\sum_m Q_N(T,t_1).f_I(m) = Q_N(T,t_1)[1 - \frac{h(t_2)}{h(t_1)}]$$

The vertical distribution of material within a puff can be found from Equations (2.21) and (2.22), allowing for variations in mixing depth, dry deposition and precipitation scavenging along a puff trajectory.

(iii) Calculation scheme

The numerical scheme employed in MESOS derives, at each time step along a trajectory, the quantity of material within a puff which is above and below the top of the mixing layer. Above the mixing layer

material may reside in a series of stable layers, each of depth $\Delta z$ = 100m, up to a ceiling of 3000m; mixing layer depths and vertical development are very unlikely to exceed this height. The exchange of material between the mixing layer and stable layers is calculated at each time step to give the airborne fluxes and ground depositions for a set of pollutants. Three depositing pollutants and one non-depositing pollutant may be treated simultaneously in the MESOS puff history calculations. Additional pollutants could be included, with only a relatively small increase in computer time, provided that sufficient core space were available.

## 2.5 Specification of Boundary Layer Parameters

Complex parameterizations and numerical schemes describing the detailed structure of the boundary layer (e.g. Deardorff (1972)) are not really suitable for extensive use in long-range dispersion models such as MESOS. Simple methods of describing the most important features of the boundary layer are required in order to make repeated dispersion computations feasible. It would seem reasonable to expect the general character of the boundary layer to be largely determined by external influences such as solar insolation, the geostrophic wind and the nature of the underlying terrain. Relatively simple schemes for describing the internal structure of the boundary layer in terms of external influences are available (e.g. Smith (1975), Carson and Smith (1977)), and the parameterizations in MESOS are based on these schemes.

The most important boundary layer parameters required in the MESOS model are the puff velocity, the Pasquill category, the mixing layer depth and the occurrence and intensity of rainfall. These parameters are estimated at each time step along a puff trajectory using relevant meteorological data. The schemes used in MESOS are such that each parameter can be estimated from pressure data, cloud cover, surface temperature and rainfall reports from the network of European weather stations (Chapter 4). The derivation of the boundary layer parameters from these meteorological data is summarised in Table (2.2).

| Parameter | Source Data (items from database underlined) | Derivation Scheme |
|---|---|---|
| Puff velocity $\underline{\bar{u}}$ | Geostrophic wind $(u_G, v_G)$ from synoptic pressure field, $u_{10}$, $\alpha_{10}$, h, $z_t$, $z_b$ | Windspeed profile U(z) fitted to $u_{10}$ and G at top of mixing layer h. Advecting windspeed $\bar{u}$ and backing angle $\bar{\alpha}$ averaged over depth of puff ($z_t$ - $z_b$) |
| Pasquill category P | | |
| (i) Over land | Cloud cover c, sensible heat flux H, and $u_{10}$ | Pasquill-Smith scheme (1975) |
| (ii) Over sea | Surface temp. $\theta_o$, Sea temp. $\theta_{sea}$, temp. at 300m $\theta_{300}$, geostrophic windspeed G | (a) For G > 12 $m.s^{-1}$, neutral stability<br>(b) For G < 12 $m.s^{-1}$, stability is assessed by comparing $\theta_{300}$ with $\theta_{s1}$ the air temp. just above sea |
| Mixing depth h | | |
| (i) Over land during day | Initial mixing depth h(0) and temp. profile $\theta(z)$, sensible heat flux H and $u_{10}$. | Mixing layer development derived using routine HTBL2, allowing for convective and mechanical mixing (Appendix A) |
| (ii) Over land during night and over sea | Pasquill category P, and $u_{10}$. | Mechanical mixing depth proportional to $u_{10}$: $h_M = M(P)u_{10}$ |
| Rainfall rate J | Rainfall index I | Rainfall index assigned to reports on the "Present Weather" which describe precipitation type, duration and intensity (Section (4.4.2)) |

Table (2.2) Boundary Layer Parameterization Schemes Incorporating Reported Meteorological Data

| Underlying Surface | Stability Conditions (Pasquill Category) | Windspeed Ratio $u_{10}/G$ | Backing Angle $\alpha_{10}$ (degrees) | Constant of Proportionality for Mechanical Mixing M (s) |
|---|---|---|---|---|
| Land | A | 0.5 | 25° | 140 |
| | B | 0.5 | 25° | 140 |
| | C | 0.5 | 25° | 140 |
| | D | 0.5 | 25° | 140 |
| | E | 0.5 | 30° | 100 |
| | F | 0.5 | 45° | 50 |
| Sea | D | 0.85 | 10° | 50 |
| | E | 0.85 | 10° | 50 |
| | F | 0.85 | 10° | 50 |

Table (2.3) Wind Profile Parameters used in MESOS

### 2.5.1 The Geostrophic and 10m Winds

The method of deriving boundary layer winds and puff trajectories requires the geostrophic wind, the 10m windspeed $u_{10}$ and the backing angle $\alpha_{10}$ to be specified (Section (2.3)). Stability conditions and the depth of mechanical mixing also depend on $u_{10}$, as discussed below.

The geostrophic wind is derived from the gradient pressure field (Equation (2.2)). Synoptic pressure fields are available at three-hourly intervals in the meteorological database. The pressure data are given at all grid points within a rectangular grid system (grid mesh of 0.5° latitude by 1° longitude) which covers the data-base map area. This pressure data is accessed during the MESOS calculations, and the geostrophic wind is calculated using a simple finite differencing scheme to determine the pressure gradient.

The value of $u_{10}$ is derived from the geostrophic windspeed using appropriate scalings for average rural terrain and typical conditions over the sea (Smith (1975)). The backing angle $\alpha_{10}$ is chosen according to the stability conditions (Pasquill category). Typical values of $u_{10}$ and $\alpha_{10}$ for different stability conditions and underlying surface are given in Table (2.3) and these values are used in the MESOS calculations.

The underlying surface along a puff trajectory is identified as either land or sea by accessing a coded map of Europe stored in the computer. This method allows a separate treatment of boundary layer conditions over land and sea.

### 2.5.2 Daytime Boundary Layers over Land

An important feature of the daytime boundary layer over land is the upward sensible heat flux due to the incoming solar insolation. This heat flux can have considerable influence on stability conditions and the depth of the convective mixing layer.

Stability conditions are assessed in terms of the Pasquill category using the scheme of Smith (1975). This scheme requires the 10m windspeed and sensible heat flux to be specified during the day. The sensible heat flux is determined from the incoming solar insolation with an appropriate reduction factor according to the amount of cloud cover (Section (A.3)). The incoming solar insolation is estimated on the basis of the elevation of the sun and depends on time of day, day of year and latitude. (Equation (A.4b), Appendix A).

The evolution of the daytime mixing layer is predicted from a numerical model which is described in detail in Appendix A. The model is based on the representation of the mixing layer proposed by Carson and Smith (1974) and includes both convective and mechanically induced mixing processes. The convective growth of the mixing layer is largely dependent on the time integrated sensible heat flux during the day, and in light wind conditions the mixing depth will usually increase to a maximum in the late afternoon. The depth of the fully developed convective mixing layer typically varies between 200m for low insolation conditions in Winter, to about 2000m with clear skies and strong insolation during Summer. Mechanically induced turbulence can also produce deep mixing layers in strong wind conditions ($h_m \simeq 1400$ m for $u_{10} = 10 m.s^{-1}$). Usually either convective or mechanical mixing will dominate in a given situation but the numerical model used in MESOS can predict mixing depths for quite general windspeed and insolation conditions. Although the model is only strictly valid for an idealised situation in which the terrain is uniform and the atmosphere is dry, it is believed that reasonable estimates of mixing layer depth can be obtained from the rapid computational procedure in the MESOS code.

### 2.5.3 Night-time Boundary Layers over Land

Convective mixing will subside after dusk and in calm conditions any turbulent mixing will tend to be rather spasmodic. Radiative cooling of the surface air layers frequently produces a stable temperature stratification, particularly in calm and clear sky conditions. However, in strong wind conditions, there will be some degree of mechanical mixing and neutral stability conditions are then more likely to occur.

The Pasquill category is again assessed using the scheme of Smith (1975), but the windspeed and amount of cloud cover are the parameters which determine the stability during the night. The depth of mixing within the nocturnal boundary layer is taken to be proportional to $u_{10}$ with the constant of proportionality M(P) decreasing with increasing stability:

$$h_m = M(P).u_{10} \qquad \ldots (2.23)$$

The values of M(P) used in this calculation are given in Table (2.3), and are based on the suggestions of Smith (1975). Minimum values of the mixing depth are imposed for stable conditions during the night so that dry deposition at the surface can always be represented in the computational procedure ($h \geq 100$m in category F conditions, and $h \geq 200$m in category D and E conditions).

## 2.5.4 Boundary Layers over the Sea

Boundary layers over the sea tend to be less variable than over the land, since the sensible heat flux and roughness heights are relatively small. However, the transition in the boundary layer structure as air moves from land to sea can be an important consideration. For example, advective changes in stability are likely to occur when the air temperature over land is different from the sea temperature. When warm air passes over a relatively cold sea, the air stream just above the sea will be cooled more rapidly than the air aloft, and this is likely to lead to the formation of a stable layer in all but very strong wind conditions. Conversely, when cold air passes over a relatively warm sea, the air will tend to become less stable.

The MESOS model attempts to predict the likely changes in stability conditions for puffs which are advected from land over the sea using a very simple and approximate scheme. The change in surface air temperature after a sufficiently long fetch ($\sim$ 100 km) is estimated using prescriptions from the Forecaster's Reference Manual (Met. Office (1975)), whereas the potential temperature at

300m above the sea is assumed to remain unchanged. The difference between the air temperature at the surface and at 300m is then used to assess the new stability conditions over the sea. The exact criteria used in this scheme are summarised by ApSimon et al (1978) and are based on the dependence of temperature profiles on stability conditions. The Dutton temperature profiles (Dutton (1977)) are used in the assessment, and these are discussed in Section (A.6).

Convective mixing is generally limited over the sea and the diurnal cycle of solar insolation does not greatly affect the mixing layer depth (Carson and Smith (1977)). It is therefore assumed that the mixing depth is determined only by mechanical mixing processes. This depth of mechanical mixing is taken to be proportional to the wind speed at 10m, as in the scheme for over land. However, typical roughness heights over the sea (≃ .1mm) are considerably less than roughness heights associated with average rural terrain (≃ 30cm). Consequently, the depth of mechanical mixing is substantially reduced over the sea and will typically lie in the range 100m to 500m (Table (2.3)).

## 2.6. Example Puff History Calculations.

The previous sections have described the methods used to characterise the development of puffs in terms of the vertical structure of the boundary layer and the meteorological conditions experienced along the puff trajectories. The importance of modelling the state of the boundary layer and allowing for time dependent meteorology is considered in this section. Example MESOS calculations are given to illustrate the sensitivity of pollutant fluxes to these factors.

The sensitivity of pollutant fluxes surviving at 100 km from source has been considered by ApSimon et al (1978a). Example calculations were presented for a dry depositing pollutant ($V_N$ = 1 cm.s$^{-1}$) released at different times over the height ranges 0-30m and 100-130m. Two windspeed conditions were considered to show the influence of mixing layer development. The results of this simple sensitivity study are

shown in Table (2.4). The flux surviving at 100 km varies by almost two orders of magnitude, according to the conditions during transport. Material emitted during the day in unstable light wind conditions spreads rapidly through the convective mixing layer and dry deposition losses are relatively small, particularly when a substantial fraction of material subsequently becomes isolated above a night-time inversion. In contrast, the vertical development of a low-level release at night in light winds is limited, and this leads to relatively high ground level concentrations and dry deposition losses before material reaches 100 km. The circumstances of a release and the prevailing conditions during the first few hours of transport can therefore be very important in determining pollutant fluxes during the subsequent long-range transport.

Wrigley et al (1979) have presented example MESOS calculations which show the importance of allowing for the changing meteorological conditions along puff trajectories. The development of three separate puffs released at consecutive three-hourly intervals were derived using the 1973 meteorological database. The airborne fluxes of I131 ($V_N$ = 0.3 $cm.s^{-1}$, $\Lambda^*_N$=1.6 $10^{-4}$, half-life eight days) were calculated along each puff trajectory (Figure (2.3)). Although the trajectories follow similar paths, the calculations indicate different puff development in the vertical. The mixing depths experienced by puffs show the typical daytime convective cycle, but strengthening winds lead to the development of a deep mechanically mixed layer as puffs leave the map. However, the most interesting feature of this example is the different periods of precipitation along the puff trajectories. The first puff is released in a rainy period, but the rain dies out at source before the last puff is released six hours later. Consequently, the different patterns of wet deposition along puff trajectories produce significant differences in airborne fluxes. For example, the airborne flux which remains after six hours of travel is about 90% for the last puff, but less than 30% for the first puff. The calculations also show the efficiency of precipitation scavenging with airborne fluxes decreasing rapidly during the rainy periods.

These simple examples illustrate the wide range of dispersion conditions which are likely to occur in the atmosphere. Dilution within a mixing

Case 1: Light winds G = 2 $m.s^{-1}$ for 24 hours, increasing to 10 $m.s^{-1}$ over 8 hours and then staying constant.

| Height Range of Release | Time of Release | | | |
|---|---|---|---|---|
| | 0600 hrs | 1200 hrs | 1800 hrs | 2400 hrs |
| 0 - 30m | 30% | 71% | 1.3% | 5.6% |
| 100 - 130m | 52% | 76% | 67% | 58% |

Case 2: Steady winds G = 10 $m.s^{-1}$ throughout.

| Height Range of Release | Time of Release | | | |
|---|---|---|---|---|
| | 0600 hrs | 1200 hrs | 1800 hrs | 2400 hrs |
| 0 - 30m | 72% | 87% | 66% | 66% |
| 100 - 130m | 91% | 90% | 77% | 77% |

All cases apply to clear skies in Spring. Airborne fluxes relate to a pollutant with deposition velocity of $10^{-2}$ $m.s^{-1}$ (no radioactive decay or washout).

Table (2.4) Sensitivity of Airborne Pollutant Fluxes to Release Conditions (taken from ApSimon et al (1978a))

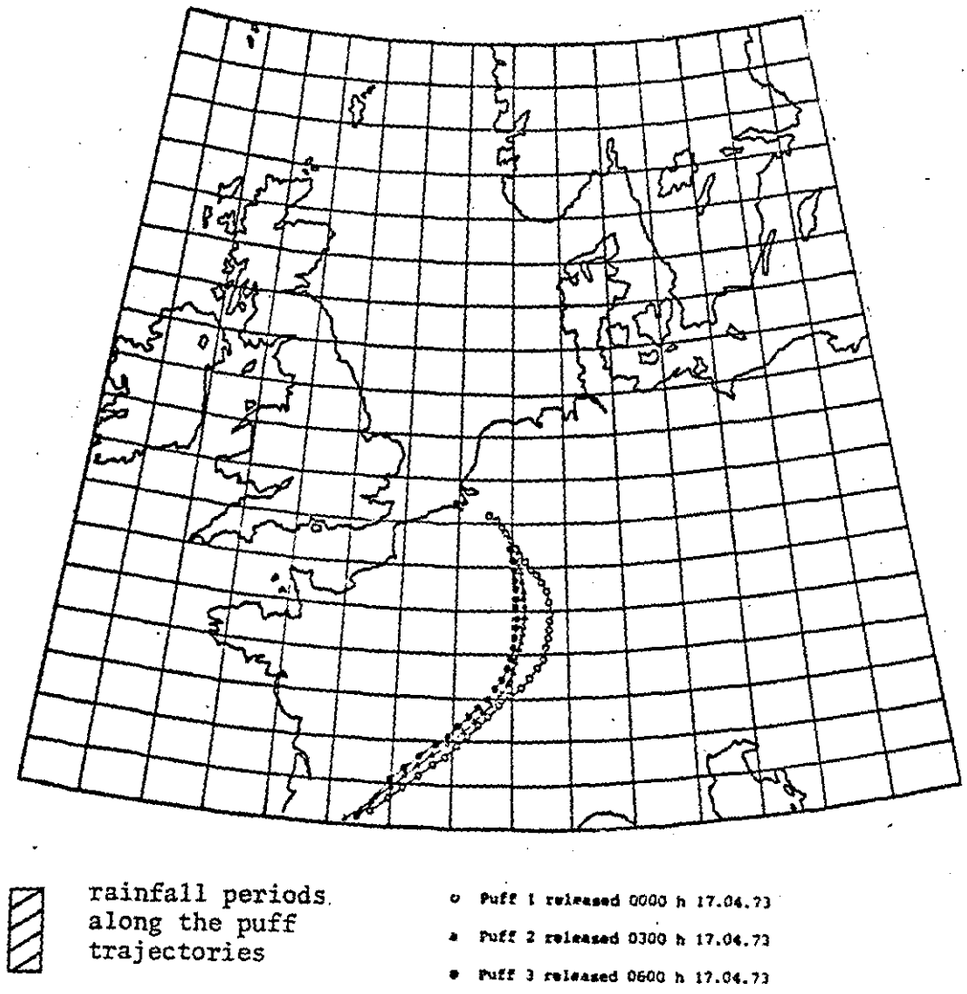



Fig. (2.3) Sensitivity of Airborne Pollutant Fluxes to Atmospheric Conditions during Transport (taken from Wrigley et al (1979))

layer of variable height, isolation of material above an inversion with possible fumigation effects, variable dry and wet deposition losses can all combine to produce fluctuating ground level concentrations and ground depositions.

## 2.7 Simulation of a Continuous Release using Puff Histories

This section describes the methods used to simulate the dispersion of a continuous release and to calculate exposures at an arbitrary point within the plume using the previously derived puff histories.

### 2.7.1 Trajectory Model of a Plume

The trajectories and widths of the two puffs which span the release are used to define the plume boundaries. If it could be assumed that the puff widths are always large in comparison to the trajectory separation, then concentrations inside the plume could be adequately represented by superposing Gaussian distributions along each trajectory with $\sigma_y$ matched to the puff widths. However, if the boundary trajectories diverge faster than the rate of puff lateral spread, this approach would lead to an overestimation of concentrations near each trajectory and an underestimation at the centre of the plume. Trajectory separation is often much larger than puff lateral spread during long-range transport. Consequently, in MESOS, a plume is represented as an infinite sequence of puffs fanning out between the trajectories of the two puffs spanning the release.

The puff method used in MESOS is shown schematically in Figure (2.4). A three-hourly continuous release over the period $(T_1,T_2)$ is simulated by using the calculated trajectories and dispersion of the two puffs $P_1,P_2$ which are initiated from source at times $T_1,T_2$. Suppose that the trajectories of these puff centres are described by the position vectors $\underline{x}(T_1,t)$ and $\underline{x}(T_2,t)$ respectively, where t is the travel time from source. During a travel time interval $(t_1,t_2)$, suppose that $P_1$ moves from $A \equiv \underline{x}(T_1,t_1)$ to $B \equiv \underline{x}(T_1,t_2)$ and $P_2$ moves from $C \equiv \underline{x}(T_2,t_1)$ to $D \equiv \underline{x}(T_2,t_2)$. It is assumed that any puff initiated at an intermediate time $T(T_1 \leqslant T \leqslant T_2)$, during the release, will follow a path EF lying between AB and CD during the travel time interval $(t_1,t_2)$, such that if:

$$T = T_1 + \mu(T_2 - T_1) , \qquad (0 \leqslant \mu \leqslant 1)$$

then:

$$\underline{x}(T,t_1) = \underline{x}(T_1,t_1) + \mu[\underline{x}(T_2,t_1) - \underline{x}(T_1,t_1)]$$

$$\underline{x}(T,t_2) = \underline{x}(T_1,t_2) + \mu[\underline{x}(T_2,t_2) - \underline{x}(T_1,t_2)] \qquad \ldots (2.24a)$$

The centre of puff P will thus arrive at E after travel time $t_1$ and at F after travel time $t_2$. The centre of puff P will reach a point $R \equiv \underline{x}(T,t)$, along EF, after travel time t, such that if:

$$t = t_1 + \nu(t_2 - t_1) , \qquad (0 \leqslant \nu \leqslant 1)$$

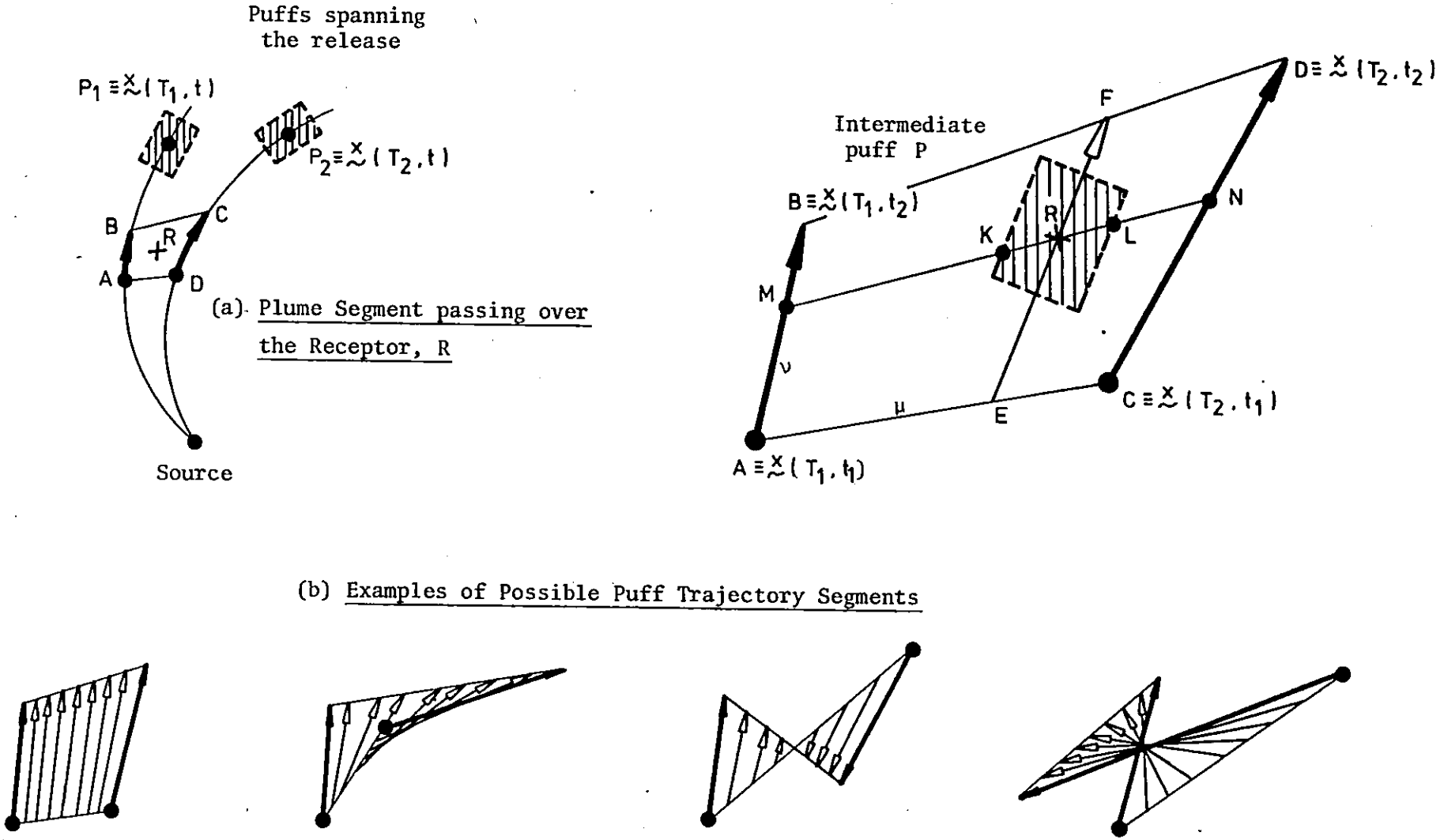
then:

$$\underline{x}(T,t) = \underline{x}(T,t_1) + \nu[\underline{x}(T,t_1) - \underline{x}(T,t_2)] \qquad \ldots (2.24b)$$

The above specifications define intermediate puff trajectories which swing at a uniform rate from that of $P_1$ to that of $P_2$ during the release period. The position of any intermediate puff centre is uniquely defined within the envelope of trajectories spanning the release and the plume will cover an area up to half a puff width outside the envelope of trajectories.

### 2.7.2 Exposures within a Plume

This representation of a plume allows exposures to be derived at a given point R from the calculated historic development of the boundary puffs $P_1$ and $P_2$. Suppose the puff P has a quantity $Q_N(T,t)$ of nuclide N remaining airborne in the mixing layer as its centre passes over R. The exposure time at R will depend on the longitudinal dispersion L and the windspeed $\bar{u}$ at the time of overhead passage of the puff. Since the puff will take a time $(L/\bar{u})$ to pass completely over the point, the time integrated air concentration from the single puff will be:




(a) Plume Segment passing over the Receptor, R

(b) Examples of Possible Puff Trajectory Segments

Fig. (2.4) Derivation of Exposures at a Receptor using the Puff Method

$$\frac{Q_N(T,t)}{B\,L\,h} \cdot \left(\frac{L}{\bar{u}}\right) = \frac{Q_N(T,t)}{B\,\bar{u}h} \qquad \ldots (2.25)$$

Time integrated concentrations are therefore independent of the longitudinal dimensions of a puff and it is not necessary to represent explicitly longitudinal dispersion in the MESOS model.

Significant contributions to exposure at R will come from all intermediate puffs with tracks that pass within half a puff width of R. Consequently, the accumulated time integrated concentrations and ground depositions from the complete release over $(T_1,T_2)$ can be represented as:

$$\begin{aligned}
&\text{Time integrated air conc. } (Ci.m^{-3}.s) = \psi_R\left[\frac{Q_N}{Buh}\right]_R \\
&\text{Dry deposition } (Ci.m^{-2}) = \psi_R\left[\frac{V_N.eQ_N}{Buh}\right]_R \\
&\text{Wet deposition } (Ci.m^{-2}) = \psi_R\left[\frac{\Lambda_N Q_N}{Bu}\right]_R \qquad \ldots (2.26)
\end{aligned}$$

where $\psi_R$ is the fraction of the release contributing to exposure at R, or equivalently, the proportion of puffs with trajectories that pass within half a puff width of R. The suffix R denotes interpolation of puff characteristics at the point R. The method of calculation is described below.

### 2.7.3 The Method of Calculation

The method used to identify the puffs which contribute to exposure are based on the trajectory envelope model of a plume (Equation (2.24)). The numerical method is complicated by the fact that the geometry of the plume can take any form. For example, the trajectory segments of the puffs $P_1$ and $P_2$ may be found to lie in opposite directions, or may even intersect (Figure (2.4)). Although there are obvious uncertainties in defining a plume in such circumstances, the trajectory representation gives a plausible and consistent method of analysis.

The time of initiation T and travel time t of a puff which passes over the point R can be found by resolving Equation (2.24) into x,y (latitude and longitude) component form and solving for the projective coordinates $\mu$ and $\nu$.

$$a_1\nu^2 + a_2\nu + a_3 = 0$$

$$\mu = \frac{(x_R - x_A) - \nu(x_B - x_A)}{(x_C - x_A) + \nu[(x_D - x_B) - (x_C - x_A)]}$$

where:

$$a_1 = (y_B - y_A)(x_D - x_C) - (x_B - x_A)(y_D - y_C)$$

$$a_2 = (x_R - x_A)(y_D - y_C) + (y_B - y_A)(x_C - x_R) - (y_R - y_A)(x_D - x_C) - (x_B - x_A)(y_C - y_R)$$

and:

$$a_3 = (x_R - x_A)(y_C - y_A) - (y_R - y_A)(x_C - x_A) \qquad \ldots (2.27)$$

For certain geometries of the trajectory quadrilateral ABCD, two intermediate puffs may pass directly over R, each with different values of $\mu$ and $\nu$. However, in practice, puff trajectories usually move in similar directions, and if ABCD is a parallelogram, the coefficient of $\nu^2$ vanishes, and only one intermediate puff centre will pass directly over R. For a point lying within the envelope of puff trajectories, $\mu$ and $\nu$ will lie in the limits $0 \leqslant \mu,\nu \leqslant 1$ and the characteristics of a puff passing directly over an interior point may be interpolated from the characteristics of the specimen puffs $P_1$,$P_2$ which have been calculated at the points A,B,C and D (Figure (2.4)).

Once the projective coordinates $(\mu,\nu)$ have been determined at R, it is possible to define the locus MN of puff centres after travel time $t = t_1 + \nu(t_2 - t_1)$. The length of MN is therefore representative of the separation between the trajectories of $P_1$ and $P_2$ when R is exposed. A puff centred on R leads to the exposure of all points, between K and L, which lie within half a puff width of R. Conversely, it is assumed that all puffs with centres which pass between K and L will contribute

to exposure at the point R. Consequently the proportion of puffs contributing to exposure is given by the overlap of KL on MN:

$$\psi_R = \frac{KL \cap MN}{MN}$$

$$= (\mu_L - \mu_K)_n (0 \leq \mu_K \leq 1)_n (0 \leq \mu_L \leq 1) \qquad \ldots (2.28)$$

where $\mu_L$ and $\mu_K$ are the values of $\mu$ associated with trajectories which pass through K and L respectively. This geometric interpretation therefore identifies the portion of the release which will contribute to exposure at the arbitrary point R within the plume.

## 2.8 Summary

The MESOS model has been developed to allow time dependent meteorology to be incorporated into the description of long-range transport and dispersion. The model is applicable to releases of three hours duration or longer, and takes account of the spatial and temporal changes in the boundary layer along the path of a release.

The trajectories of a sequence of puffs are computed from the surface pressure field, so that the synoptic scale lateral spread is allowed for explicitly. Each of these tracked puffs is treated as a column of material spreading vertically and laterally, according to the local conditions along a trajectory. The vertical development of puffs during long-range transport is strongly influenced by variations in the depth of the mixing layer. These variations in mixing depth are represented in MESOS using a fast computational routine which includes the effects of mechanical and convective mixing processes. In addition to dilution by puff spreading, depletion by natural decay, dry deposition and wet deposition are also included in the MESOS model. The MESOS code has been adapted to allow for these effects on a more realistic basis.

A continuous release over a three hour period is represented by a series of discrete puffs following intermediate trajectories and dis-

persion. The area between the calculated trajectories of the two puffs spanning the release will be exposed and the dispersion histories of these puffs are used to calculate the resulting time integrated concentrations, dry and wet depositions at fixed points within the plume.

The puff trajectory method used in MESOS allows the advection, dilution and removal of material to be readily assessed from the prevailing meteorological conditions. The model parameters are derived from appropriate meteorological data and the MESOS dispersion calculations are generated by accessing a meteorological database which contains the relevant data in a suitable form. The use of real meteorological data, reported at three-hourly intervals from the European network of weather stations and ships, should therefore give an improved representation of the long-range dispersion of pollutant releases.

# CHAPTER 3 STUDY OF THE 1957 WINDSCALE ACCIDENT USING THE MESOS MODEL

## 3.1 Introduction

The Windscale accident over the 10th and 11th October 1957 produced significant releases of radioactivity to the atmosphere during a period of changing meteorological conditions. Measurements of I131 showed that the emissions were subsequently dispersed over a large area of Northern Europe. The Windscale accident is therefore one of the few occasions for which long-range dispersion calculations, relating to releases of radioactivity into the boundary layer, can be compared with detailed measurements.

A study of the dispersion of I131 from Windscale, using the MESOS model, is described in this Chapter, and the results are discussed in relation to I131 measurements. This allows for an assessment of the quality of model calculations and the sources of uncertainty in simulating the dispersion of unplanned releases.

## 3.2 The Source Term

The control of the incident in the No. 1 Pile at Windscale on the 10th and 11th October 1957 has been described in the report of the Committee of Enquiry (Atomic Energy Office, 1957). A brief summary of the time-scale of events during the incident is shown in Figure (3.1). An increase in the level of activity was first registered by the stack meter at 8.10 am on the 10th October. Although the time history of releases from the 120m stack is not known quantitatively, reports suggest that peak emissions occurred late on the 10th October and again after 9 am on the 11th October, when water was used to extinguish the fire.

Stack measurements at Windscale gave little indication of the amount of fission products released during the incident. Most estimates are therefore based on subsequent air concentration and grass deposition measurements some distance away from Windscale (Section (3.4)). Various

estimates indicate that between 20,000 and 30,000 Curies of I131 were released to the atmosphere. Crabtree (1959) deduces that an airborne flux of about 22,000 Curies passed over a line from Liverpool, across Northern England, to Flamborough Head. This value can be added to the 5,000 Curies deposited on ground over Northern England (Chamberlain, 1959), to give an approximate total for the I131 release at Windscale. However, there are considerable uncertainties in using such estimates, since they do not account for the possible transport of material over the sea. Clarke (1974) uses a different approach by deriving the fission product inventory at the time of the accident and obtains good agreement with ground deposition measurements near Windscale by assuming 15,000 Curies of I131 to be released in the final phase of the accident.

Two postulated release patterns have been considered separately in the MESOS calculations, in order to test the sensitivity of the model predictions to these uncertainties in the I131 source term. These release patterns are shown in Figure (3.1). Release pattern (a) is a simple two peaked distribution with a total I131 release of 25,000 Curies. Release pattern (b) allows for a more gradual release through the accident and includes a small quantity of early emissions. Both postulated source terms are in qualitative agreement with the description of the accident and, in particular, represent a release of 15,000 Curies during the final phase of the accident, as suggested by Clarke (1974).

## 3.3 Meteorological Conditions

The development of the synoptic pressure field over Northern Europe, during and after the release period, is shown in Figure (3.2). At noon on the 10th October, a cold front lay across Central Scotland, with low pressure to the north, giving light south-westerly winds over Windscale. During the afternoon the synoptic pressure field remained fairly constant, but during the evening the front slowly moved south-east and passed over Windscale shortly after midnight. The geostrophic winds ahead of the front were light and south-westerly, but northerly winds followed behind the front as it passed over Windscale. A surface

inversion had formed during the evening at Windscale and the surface winds differed from winds at higher levels due to a local land breeze (Crabtree, 1959).

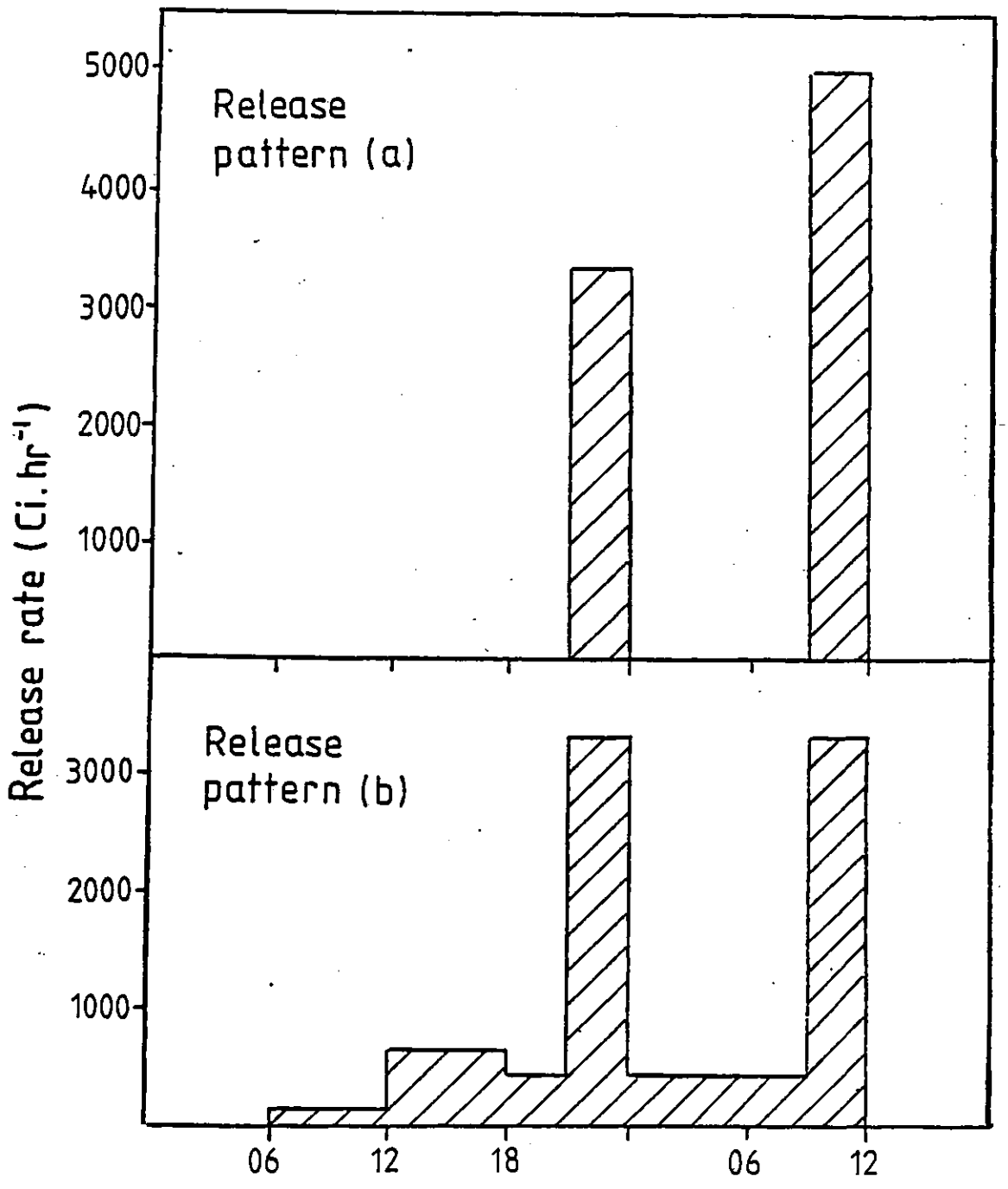
Cloud and scattered light showers were also associated with the front, but these showers were mainly confined to the Lake District. Records at Barrow show that most of the rainfall occurred between 1700 and 1900 hrs. on the 10th October before the first peak in the release from Windscale. Since conditions were otherwise dry, it was decided that this period of limited rainfall was unlikely to be important in the MESOS calculations.

The front continued to move south across England on the 11th October, and gradually weakened as it approached the Continent. A centre of high pressure became established behind the front and slowly moved east, bringing variable light winds over Central and Southern England, and strengthening Westerlies over the North of England and the North Sea.

## 3.4 Measurements of I131 after the Release

The range of dispersion after the release can be appreciated from Stewart and Crooks' (1958) summary of I131 air concentration measurements, shown in Figure (3.3a). Activity was recorded over most of England, with smaller amounts reaching Europe and Scandinavia. The measurements came from the analysis of dust collected on filters which were used for the routine monitoring of industrial pollution. Most filters were only changed daily during the course of the accident, but at a few sites, moving strip filters were exposed. Crabtree (1959) gives examples of continuous monitoring at Harrow and other stations in Europe. These traces are reproduced in Figure (3.3b) to indicate the arrival time of activity at different locations.

Extensive measurements of I131 ground deposition over North West England are reported by Chamberlain (1959). These deposition measurements (Figure (3.4)) give a fairly complete idea of the regional dispersion and, in particular, illustrate the two peak representation of the




0810 increased stack activity

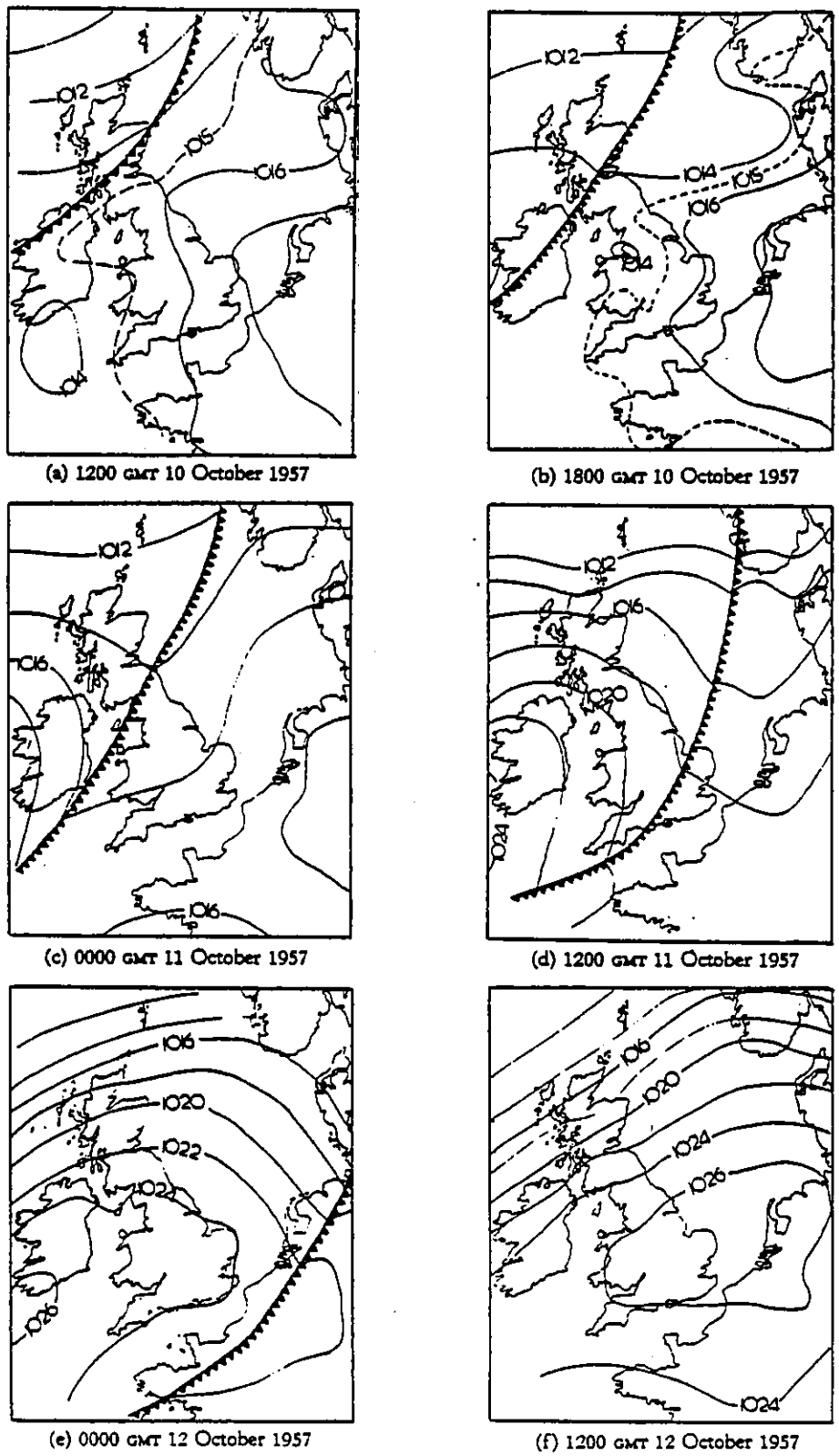
1200 fan damper opened (15 min)

1340 fan damper opened (5 min) (stack meters showed increase)

2300 approx. 150 channels of fuel involved (likely peak in the release)

0855 water switched on (likely peak in the release)

Figure (3.1) Sequence of Events and Postulated Release Patterns of I131 During the Accident




(a) 1200 GMT 10 October 1957

(b) 1800 GMT 10 October 1957

(c) 0000 GMT 11 October 1957

(d) 1200 GMT 11 October 1957

(e) 0000 GMT 12 October 1957

(f) 1200 GMT 12 October 1957

Figure (3.2) Synoptic Pressure Fields During the Accident

[taken from Crabtree (1959)]

Figure (3.3a)
Measurements of I131 Air Concentrations over Northern Europe
[taken from Stewart and Crooks (1958)]

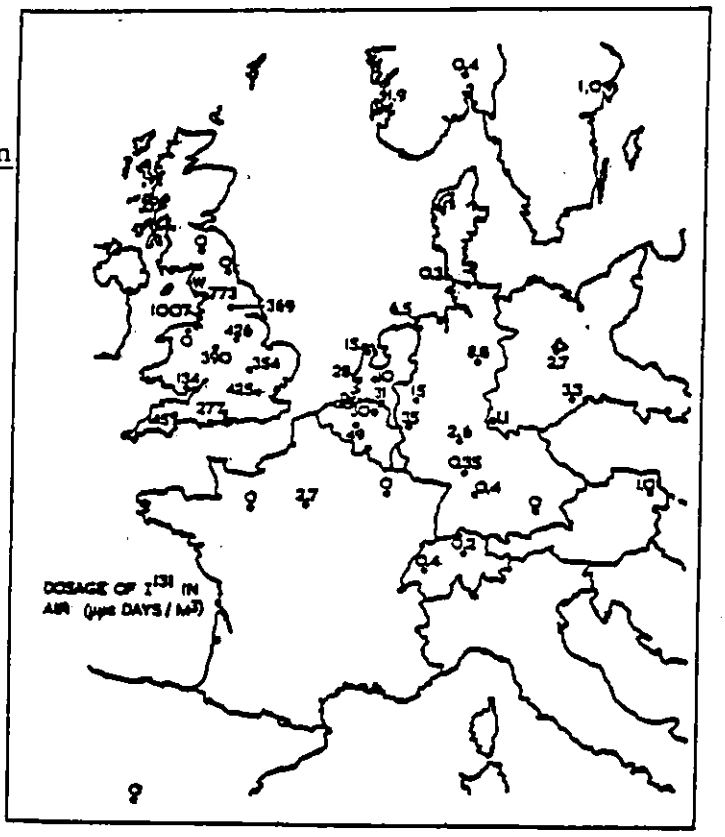
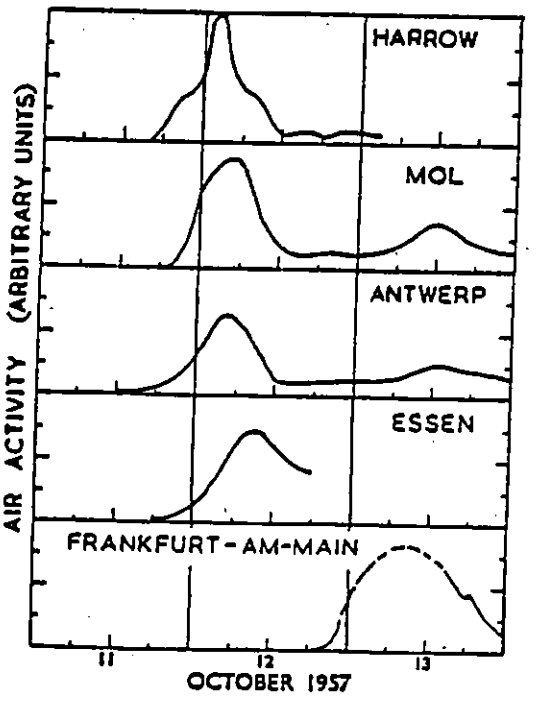
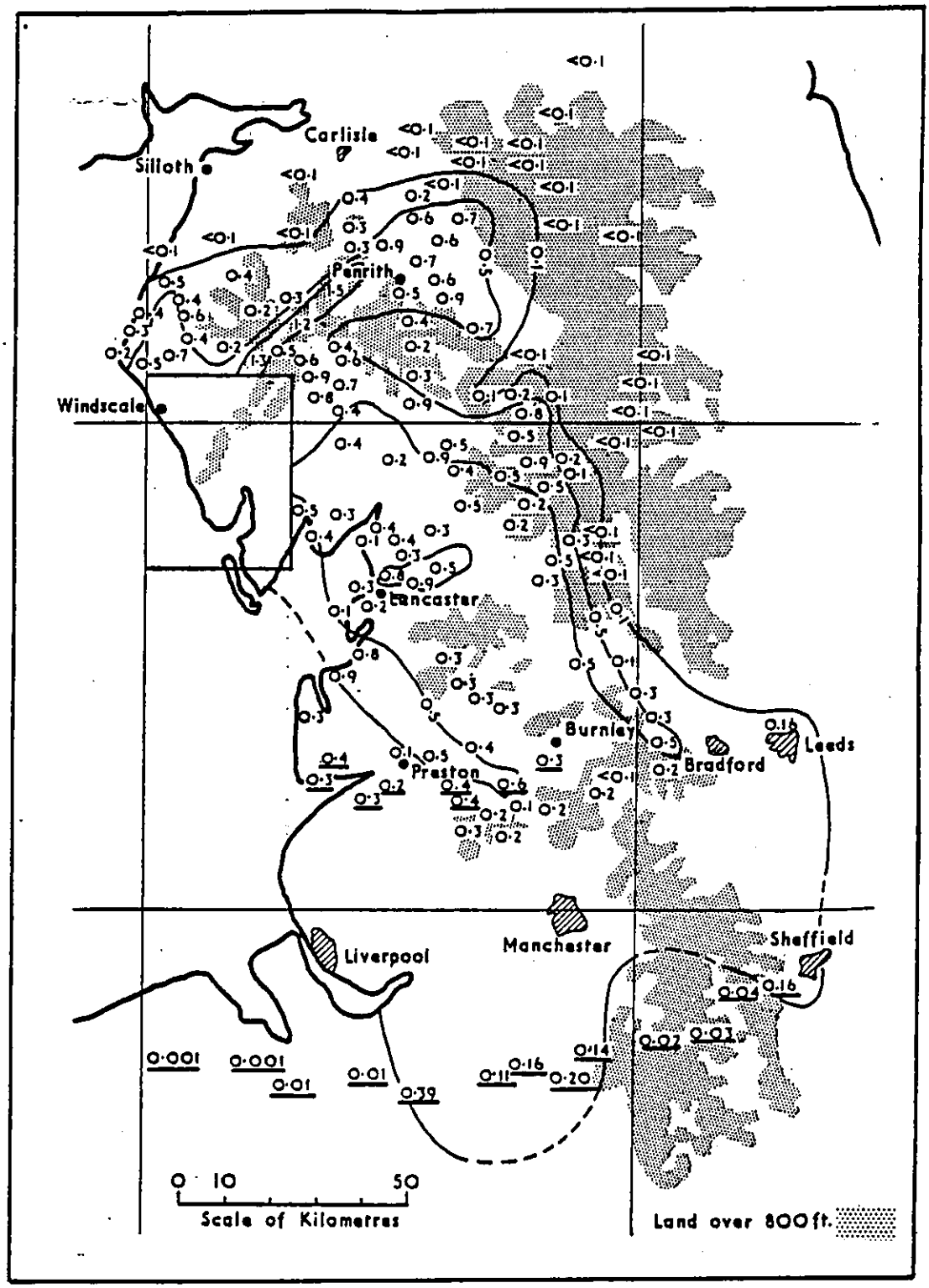



Figure (3.3b)
Measurements on the Variation of Air Activity at Different Locations
[taken from Crabtree (1959)]






Types of measurement are denoted: 0.2 Grass samples

I131 deposition in $\mu Ci.m^{-2}$ units. 0.2 Gamma survey

Figure (3.4) Measurements of I131 Deposition over North-West England [taken from Chamberlain (1959)]

release and the barrier effect of the Pennines.

## 3.5 Dispersion Calculations

The results of the MESOS dispersion calculations are discussed in the following sections. Trajectories representing different parts of the release are first considered to give a qualitative account of the advection of activity away from Windscale. The trajectory analysis also indicates possible sources of error in the dispersion calculations. The trajectories were incorporated into the MESOS model to trace the development of specimen puffs initiated at three-hourly intervals throughout the release period. The puff histories were then used to give time integrated I131 air concentrations for each proposed release pattern (Section (3.2)) and these results were compared with the measurements taken after the accident.

### 3.5.1 Trajectory Analysis

Trajectories, based on the geostrophic wind, have been plotted by hand from the synoptic pressure charts, because pressure data in the form normally used by MESOS was unavailable for 1957. The accuracy of hand plotted trajectories is limited by uncertainties in estimating the advecting boundary layer winds. For example, it is often difficult to determine, with confidence, wind direction and speed in areas of slack pressure gradient and in frontal regions. Both these situations arose in tracking releases from Windscale. The backing and reduction in strength of the advecting boundary layer wind, relative to the geostrophic wind, depends on the stability conditions and vertical development of the material being tracked. These aspects are normally allowed for in the MESOS calculations, but could not be adequately represented in the manual tracking procedure. In practice, it was necessary to simplify the tracking procedure by using a constant backing angle $\overline{\alpha}$ and a constant ratio $\overline{u}/G$ of the advecting windspeed to the geostrophic windspeed.

The sensitivity of trajectories to the representation of the advecting

wind has been considered by plotting separate trajectories using different values of $\overline{\alpha}$ and $\overline{u}/G$. Typical errors which can occur in the trajectories, initiated during the Windscale release, are illustrated in Figure (3.5). Relatively small changes in $\overline{\alpha}$ and $\overline{u}/G$ can lead to significant differences in trajectories, particularly when trajectories move into regions where the wind direction changes systematically over relatively small distances. Trajectories deviate at the frontal region and, at a later stage, within the high pressure system. Trajectory analysis is probably the major limitation in attempts to simulate the Windscale release. The stability of trajectories in the synoptic pressure fields prevailing during the Windscale release is discussed, in more detail, by ApSimon et al (1978).

Hand plotted trajectories spanning the period of the accident are shown in Figures (3.6) to (3.8). These trajectories were derived using a constant backing angle $\overline{\alpha} = 10°$ and the geostrophic windspeed was taken as representative of the advecting windspeed. Trajectories are discussed separately for releases occurring before and after the front passed over Windscale.

(i) Trajectories for releases before the front passed over Windscale

Trajectories associated with early releases of activity on the morning of the 10th October, are shown in Figure (3.6). These trajectories move slowly to the north-east in the light winds ahead of the front, and reach out over the North Sea until being swept south towards the Continent in the northerly winds behind the front. Trajectories initiated early in the morning reach further east over the North Sea because they can travel greater distances before being influenced by the frontal system.

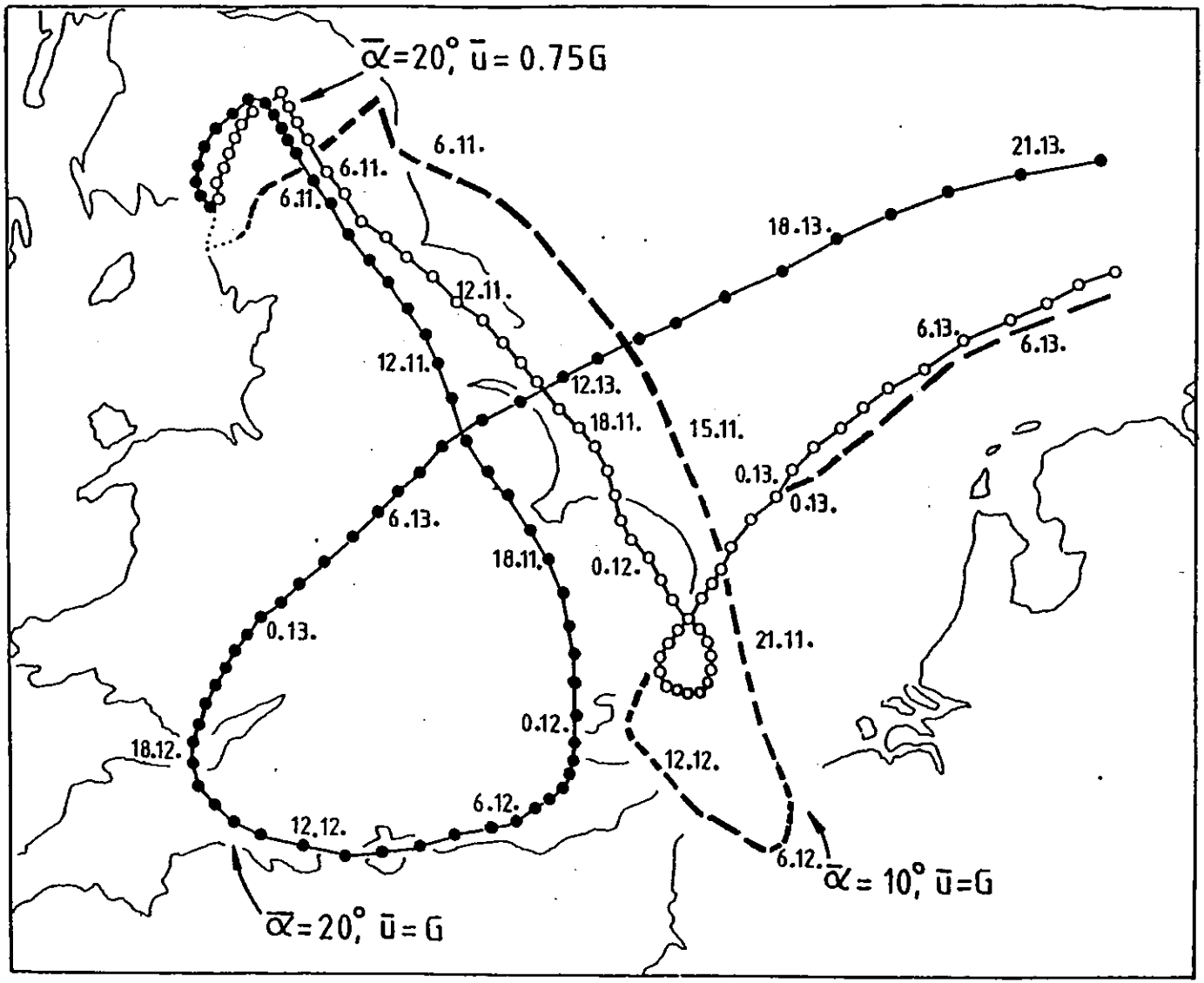
Stack activity at Windscale was first noticed at 8.10 am, and the trajectories show how material released at this time could have reached the Continent. The plotted trajectories subsequently reached the Continent early on the 12th October, and this is in reasonable agreement with the observed arrival of activity at Mol, Antwerp and Essen, shown in Figure (3.3b).

Trajectories representing the first probable peak in emissions at Windscale which occurred between 2100 and 2400 hrs. on the 10th October, are shown in Figure (3.7). Trajectories initiated before midnight are again carried to the north-east before the front passed over Northern England. Conditions were stable at this time, and the I131 deposition measurements in Figure (3.4) suggest that material was trapped in the Pennine valleys before moving south under the influence of the winds behind the front. The simple trajectory analysis does not allow for the blocking effect of the Pennines, and this will be seen to cause the most serious errors in the regional dispersion calculations. The geostrophic trajectories therefore probably reach too far to the east in the initial stages. However, this error is gradually cancelled by the further neglect of an eastward isallobaric component in the wind as trajectories move south into the developing anticyclone over Central England. The trajectories subsequently pass to the west of London and are in good agreement with the observed time of arrival of activity at Harrow. The trajectories do not reach the Continent, but slowly move along the South Coast and circle back over Central England under the geostrophic control of the anticyclone. The trajectories then pass over the North Sea and reach Denmark early on the 14th October. Activity was first recorded in Norway on the 15th October and this suggests that windspeeds may have been overestimated in the trajectory analysis.

(ii) Trajectories released after the front passed over Windscale

Trajectories associated with the second peak in emissions during the morning of the 11th October are shown in Figure (3.8). The front had passed over Windscale by this time, and the trajectories initially move south over Lancashire and lead to the highest levels of contamination south of Windscale. The trajectories move around the anticyclone passing over North Wales and back over Northern England. No activity was recorded in North Wales, and it seems likely that the geostrophic tracking produced trajectories which circle back too far to the north. Manual tracking was particularly difficult for these trajectories because of the very light winds associated with the anticyclone. Crabtree (1959) has attempted to use geostrophic tracking

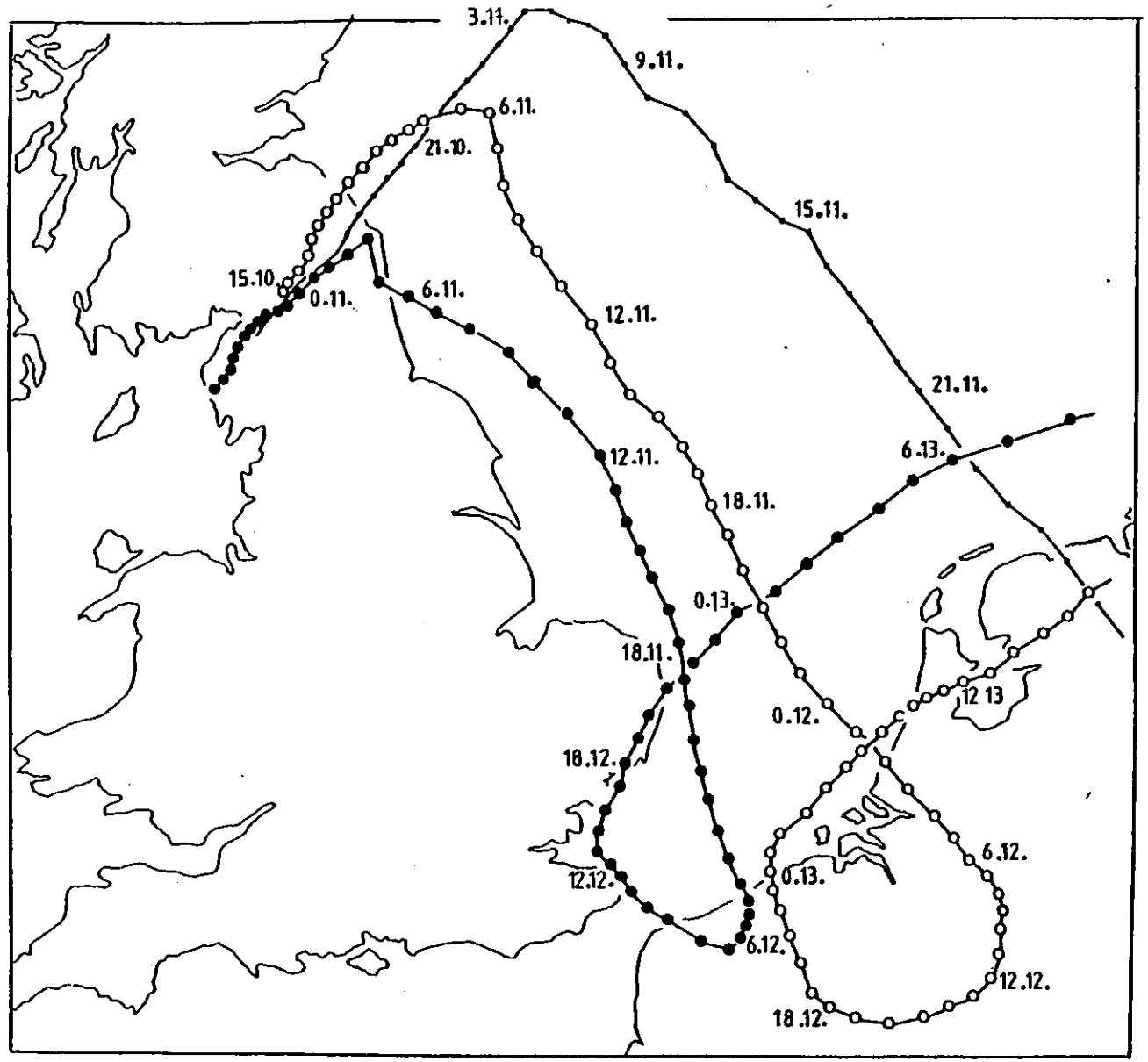
Figure (3.5)
Sensitivity of Trajectories to Backing Angle and Mean Wind Speed




All trajectories initiated from Windscale at 1200 hours, 10th October.

Figure (3.6)

Trajectories for Puffs Released at 0600, 0900, 1200 Hours on the 10th October, 1957



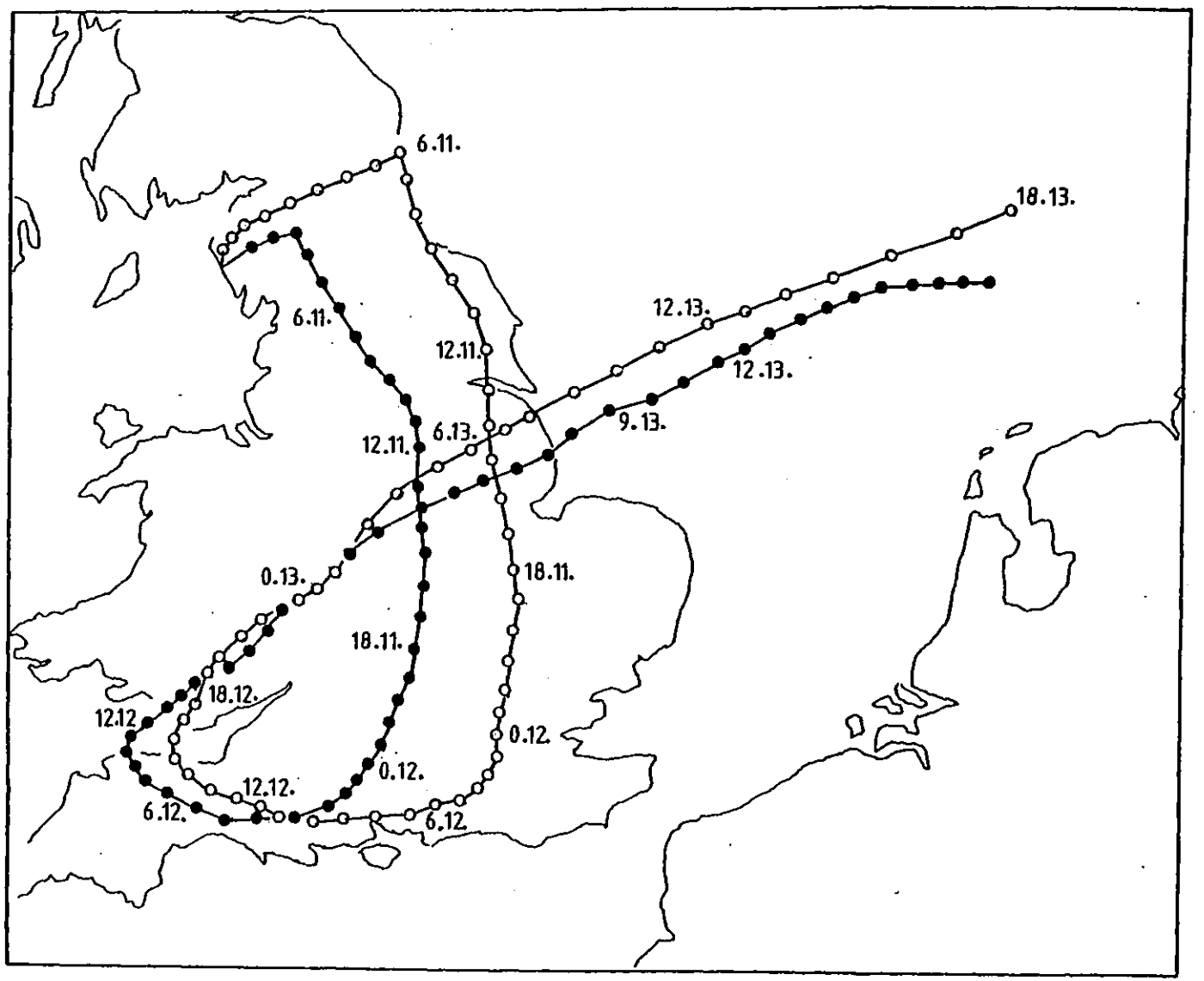

0600 hours

0900 hours

1200 hours

Figure (3.7)

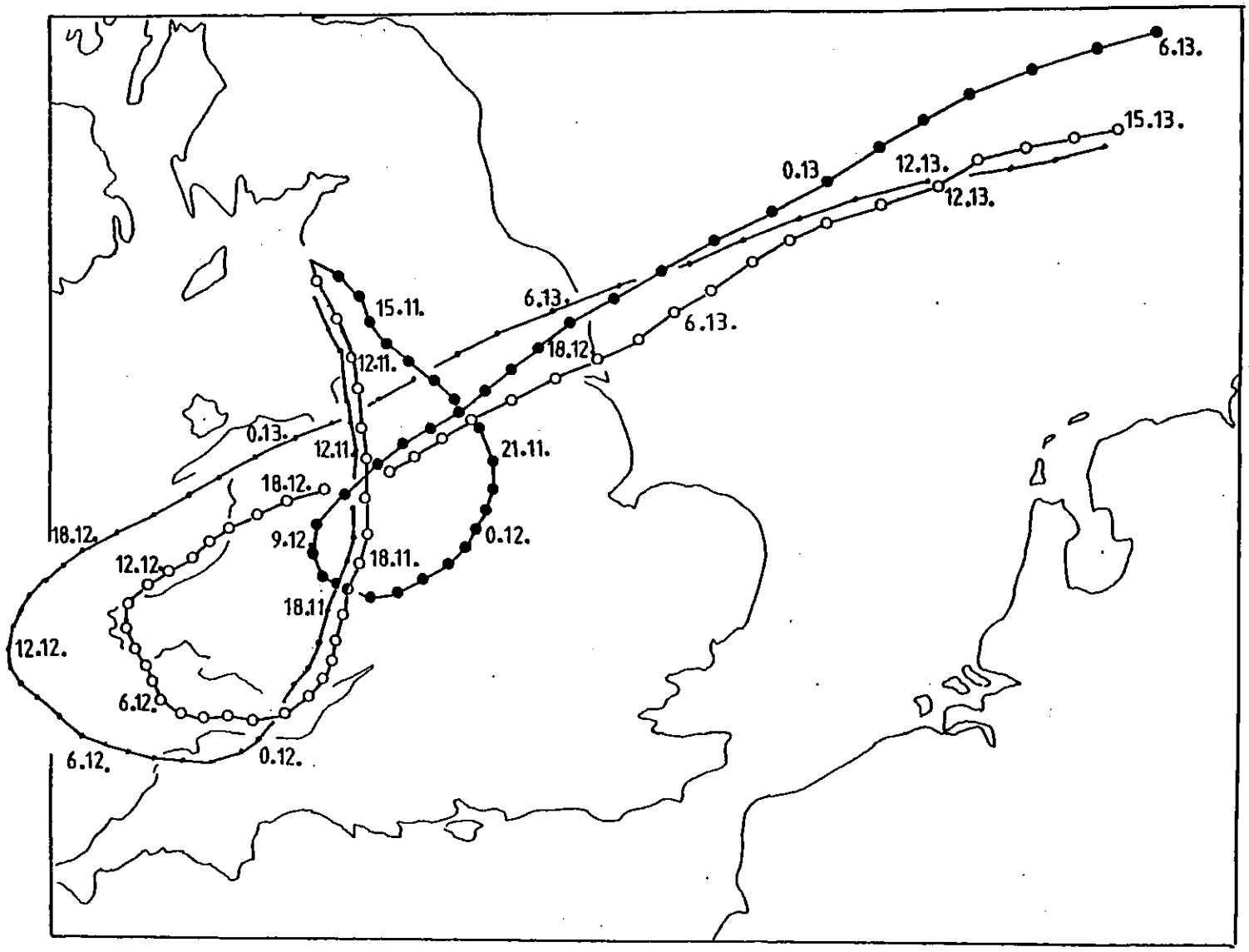
Trajectories for Puffs Released at 2100 and 2400 Hours on the 10th October, 1957




2100 hours

2400 hours

Figure (3.8)
Trajectories of Puffs
Released at 0600, 0900,
1200 Hours on the 11th
October, 1957




0600 hours

0900 hours

1200 hours

for this part of the release, but found that the best agreement with I131 measurements was produced by using the surface wind direction to define the trajectories. This additional backing in wind direction leads to a more south-easterly trend in the trajectories. It is therefore probable that activity released at this time subsequently reached further into Southern England than the geostrophic trajectories in Figure (3.8) suggest.

### 3.5.2 Regional Dispersion

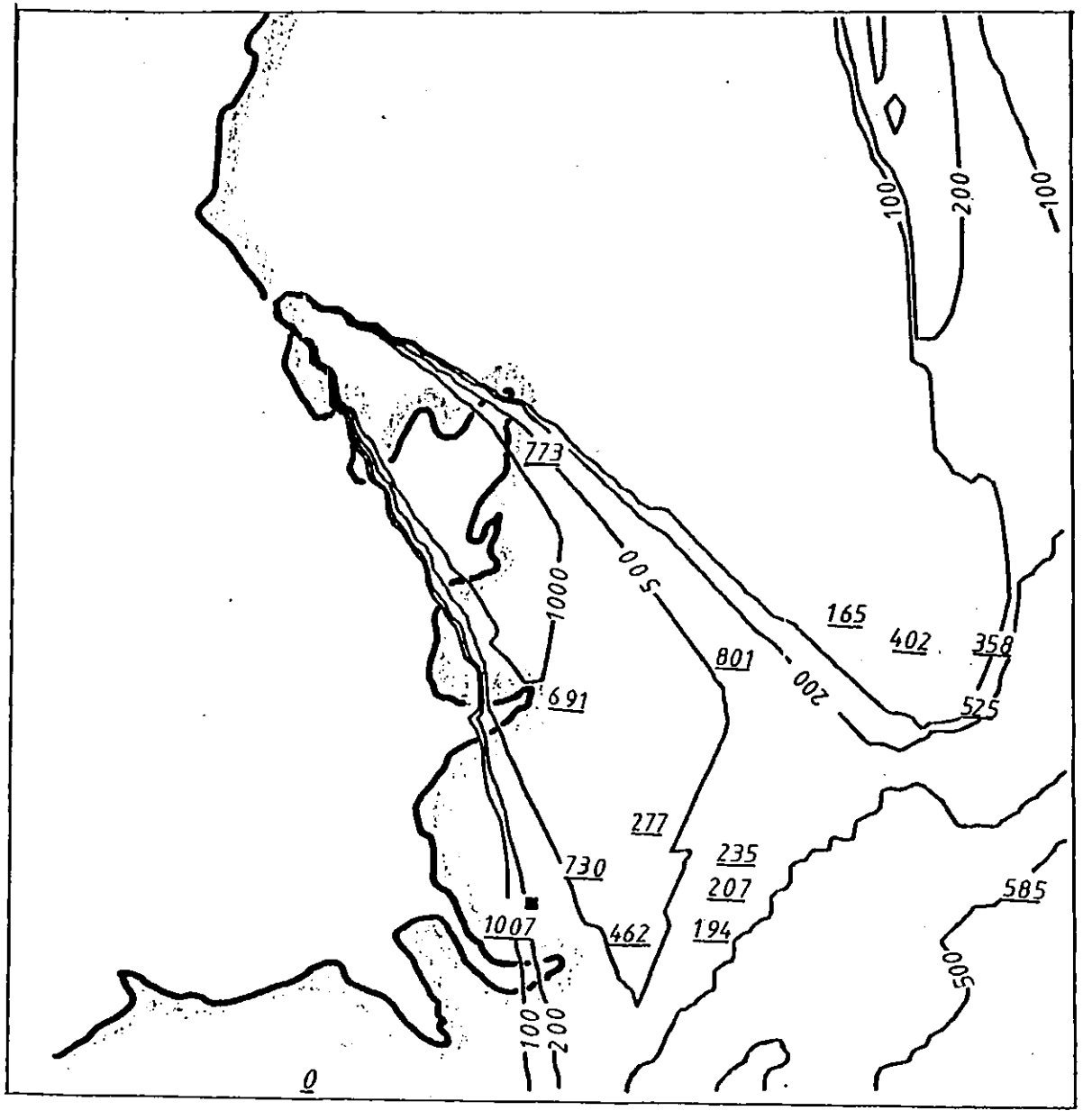
Predicted levels of I131 time integrated air concentrations over North West England are shown separately in Figures (3.9a) and (3.9b) for each source term at Windscale. The MESOS calculations are presented in the form of contours. Measurements, taken from Stewart and Crooks (1958), are indicated at different locations over the map.

The MESOS calculations show the dominance of the second peak in the I131 emissions which occurred after the front had passed over Windscale. This part of the release is dispersed in the form of a plume which travels along the Cumberland coast and spreads south-eastwards over Lancashire. Activity released at this time continues to move south, with increasing lateral dispersion, and subsequently returns in an anticyclonic motion to give a second pass exposure over South Lancashire. This recirculation leads to a region of fairly constant time integrated concentrations at the bottom of both regional maps.

Activity from the first peak in the release patterns is carried to the north-east of Windscale above the night inversion and only reaches ground level when fumigation occurs on the morning of the 11th October over North Yorkshire. The plume representing the first peak release therefore only appears on the regional map as it moves south over Yorkshire.

Early emissions from Windscale during the day of the 10th October are represented in the release pattern (b). The plume associated with these releases is seen along the coast to the north of Windscale. There is also some spread of activity over the Irish Sea due to the variability

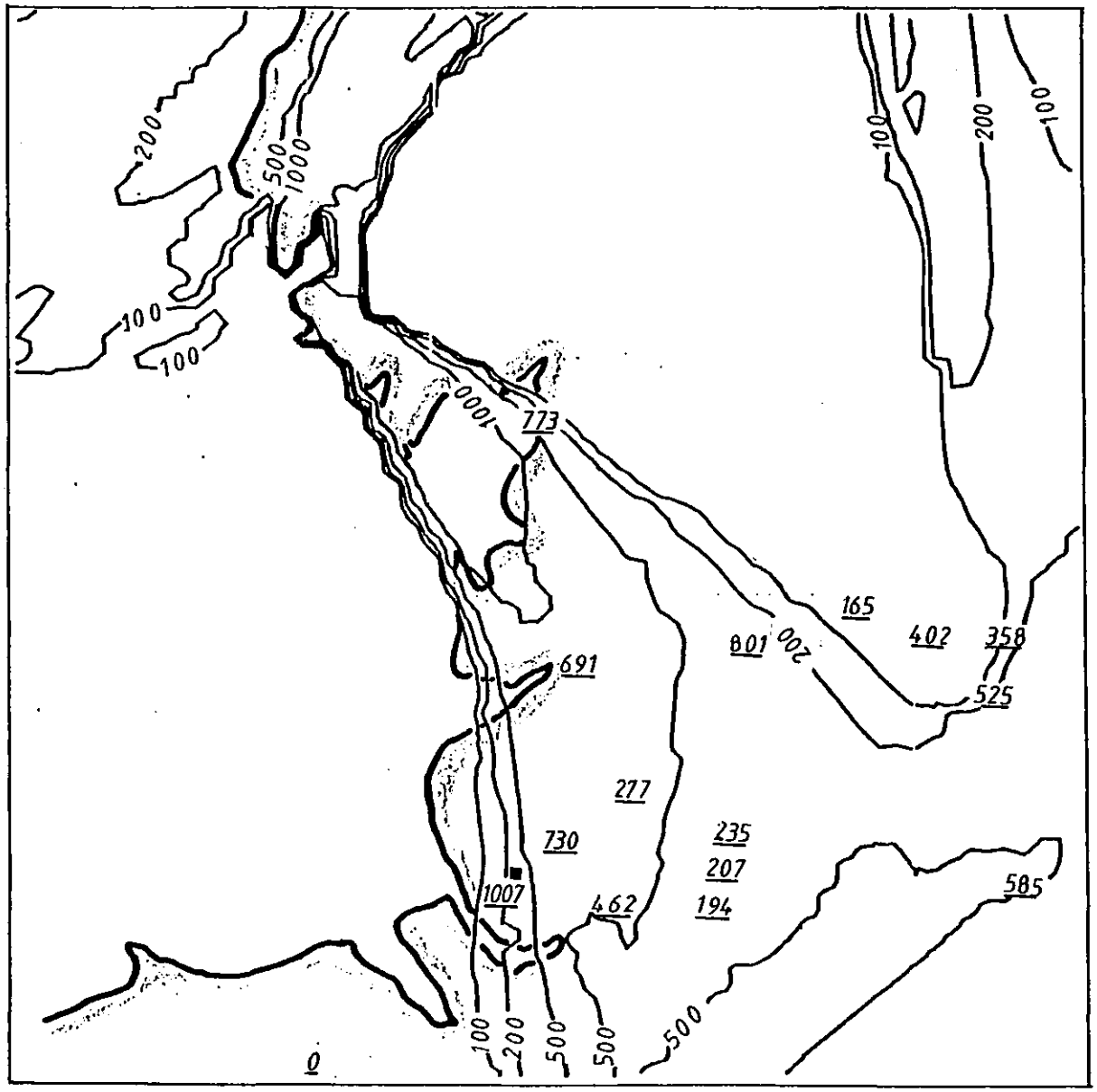
Figure (3.9a) Predicted and Measured Levels of I131 Time Integrated Air Concentrations over North-West England (Release Pattern (a))




— measurements ($pCi.days.m^{-3}$)

■ Liverpool measurement taken over a month

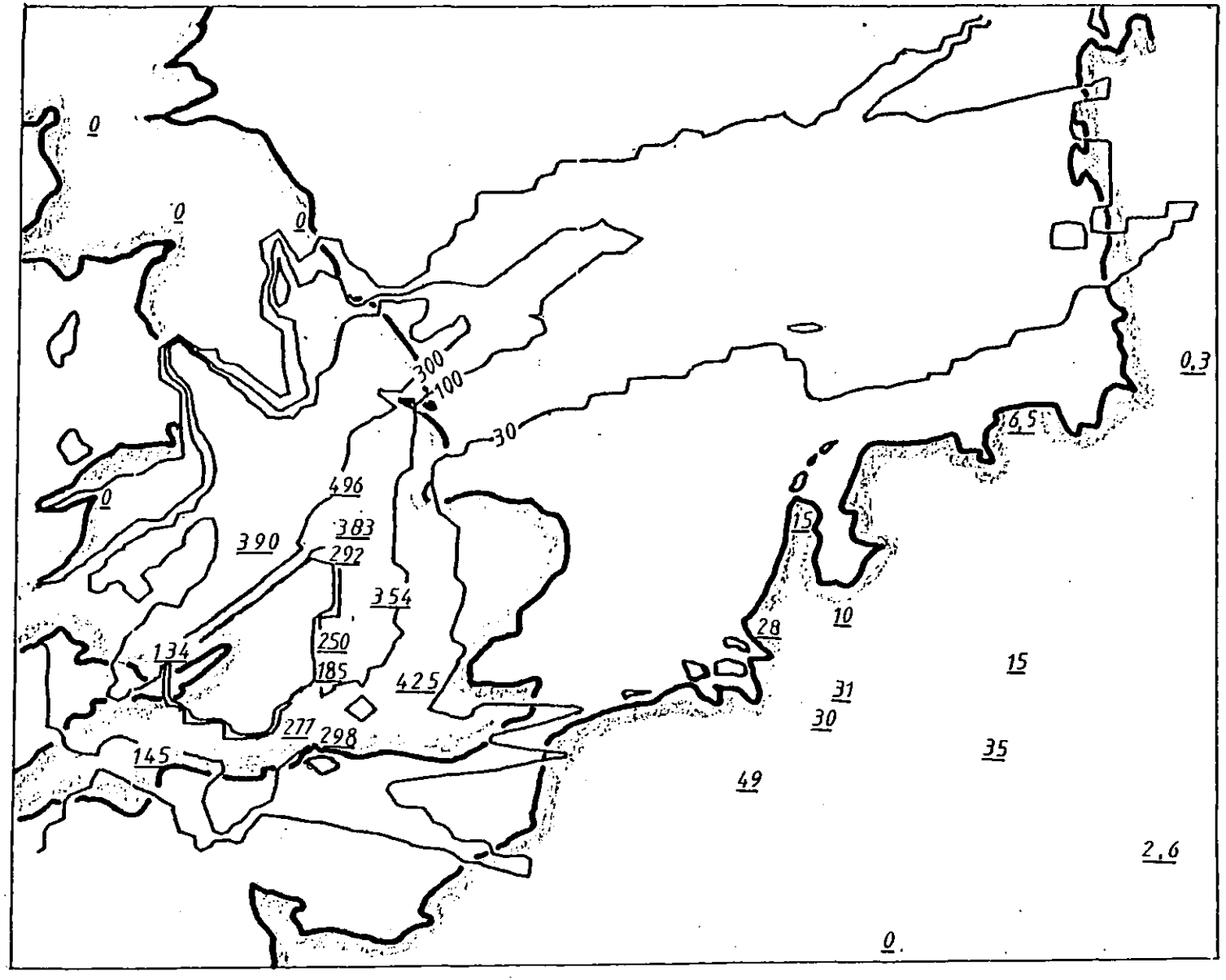
Figure (3.9b) Predicted and Measured Levels of I131 Time Integrated Air Concentrations over North-West England (Release Pattern (b))




— measurements ($pCi.days.m^{-3}$)

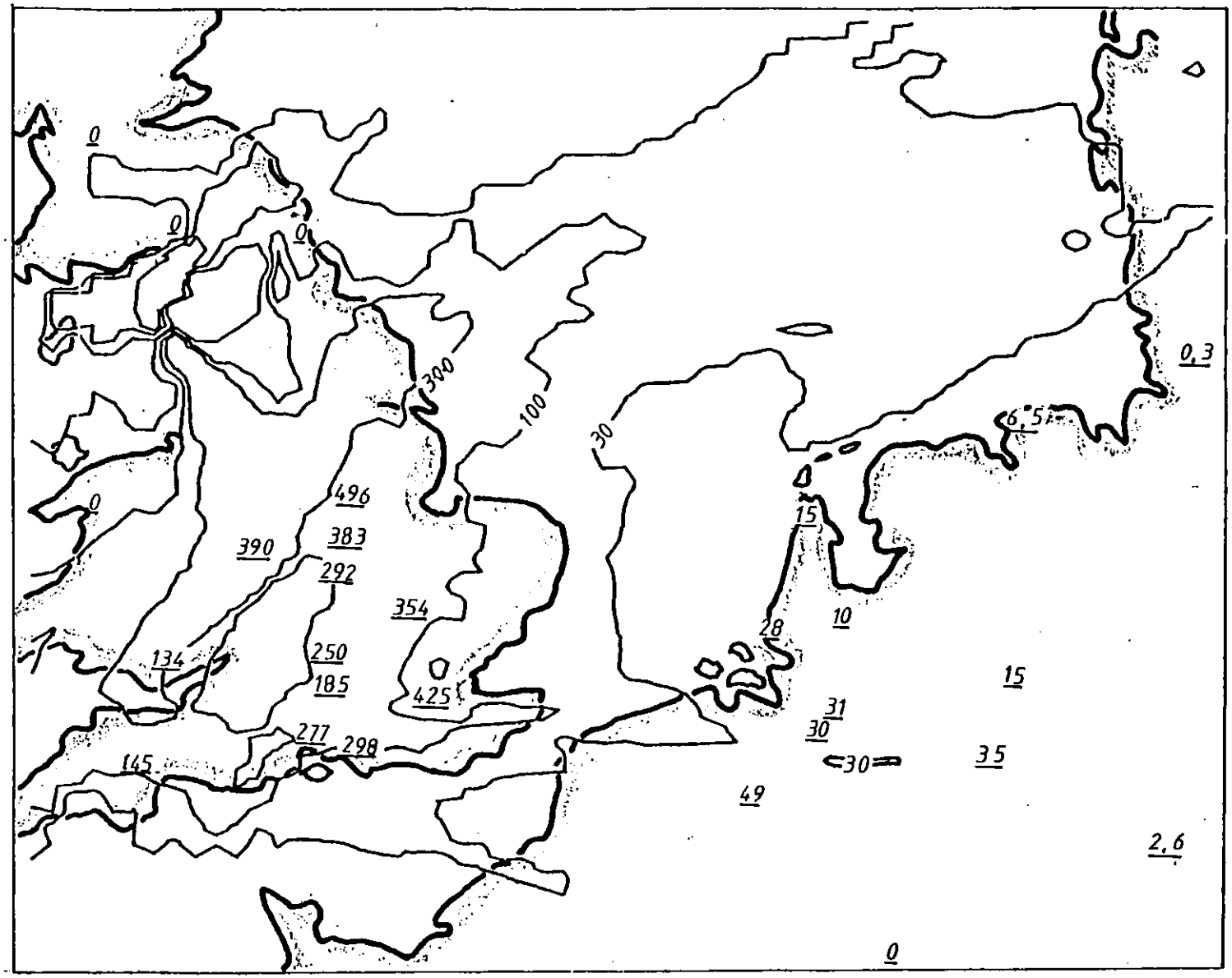
■ Liverpool measurement taken over a month

Figure (3.10a) Predicted and Measured Levels of I131 Time Integrated Air Concentrations over North-West Europe (Release Pattern (a))




— measurements
(pCi.days.m$^{-3}$)

Figure (3.10b) Predicted and Measured Levels of I131 Time Integrated Air Concentrations over North-West Europe (Release Pattern (b))




— measurements (pCi.days.m$^{-3}$)

in wind direction near Windscale during the day.

### 3.5.3 Long-Range Dispersion

The MESOS calculations for I131 time integrated air concentrations over Northern Europe are shown in Figures (3.10a) and (3.10b) for each release pattern.

The plumes from the two emission peaks are clearly seen over Northern England, but as activity spreads south, the contributions to time integrated concentrations from each plume become indistinct. However, the general dispersion behaviour can still be recognised. Activity from each plume spreads south into the high pressure system, slowly drifting around Central England, and finally disperses out over the North Sea.

Lateral dispersion spreads activity across the English Channel, but the peak release pattern (a) only gives low exposures on the French coast. Some additional contamination occurs over Belgium and Holland when early emissions are considered in release pattern (b), but this contribution is not sufficient to explain all the I131 measurements on the Continent.

### 3.5.4 Accuracy of the MESOS Calculations

A summary of calculated and measured I131 time integrated air concentrations is given in Figure (3.11). MESOS predictions are compared separately with regional measurements and measurements across Northern Europe for each I131 release pattern used in the study.

For regional dispersion, MESOS calculations are within a factor of three at all locations apart from two measurements made at Leeds and Batley. Air concentrations in West Yorkshire are underestimated because the plume representing the first peak in releases is too far over to the east. The deposition measurements, Figure (3.4), indicate that the blocking influence of the Pennines caused the relatively high

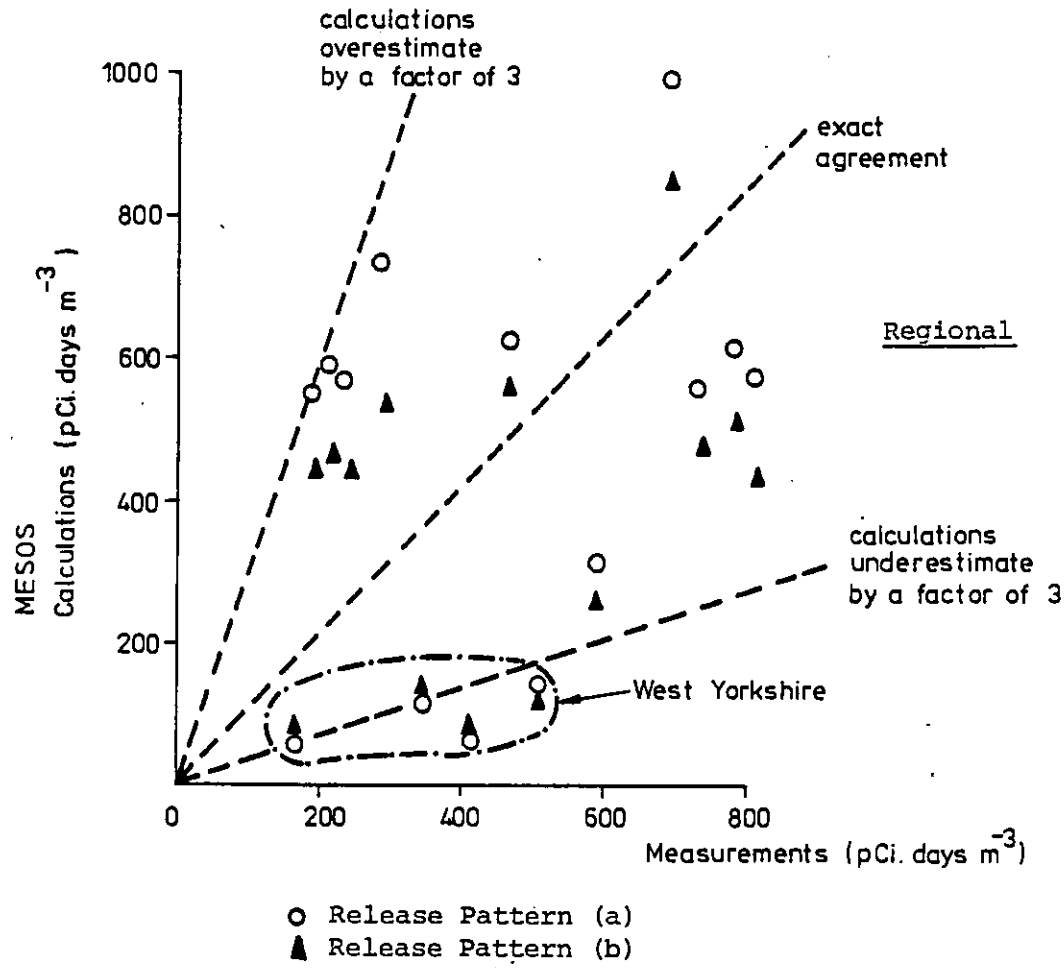
levels of contamination in West Yorkshire. A consideration of the effect of topography in the trajectory analysis would have substantially improved the MESOS calculations for this area. Calculated exposures over Lancashire due to the second release peak are in general agreement with the measurements.

The long-range dispersion calculations show a similar degree of accuracy. In assessing the dispersion calculations, it is reasonable to discount the predictions of exposure over North Wales and Newcastle, because these are due to errors in the trajectory analysis (Section 3.5.1). Similarly, the trajectory analysis cannot account for the transport of activity far into Europe. Measurements across Central and Southern England are, in general, underestimated by a factor of about two. This could either be caused by an overestimation of wind speeds or due to the fact that the second peak releases did not come far enough south in the anticyclonic trajectories. Uncertainties in the orientation of the second peak trajectories (Figure (3.8)) also contribute to the underestimation of air concentrations at Harrow and the overestimation of concentrations in Wales.

## 3.6 Summary

The application of the MESOS model to the dispersion of I131 releases during the Windscale accident has given reasonable agreement with measurements, in view of the uncertainties in the source term and the rather complicated meteorological conditions. MESOS calculations are generally within a factor of three of the measurements and this degree of accuracy is comparable with other long-range dispersion models (e.g. Maul, 1980).

The uncertainty in trajectories leads to the most significant errors in the dispersion calculations. Trajectories have been shown to be rather unstable because of the movement of the frontal system and the high pressure system during and after the period of I131 emissions at Windscale. Under such conditions, trajectories are sensitive to relatively small variations in the backing angle of the advecting boundary layer winds.



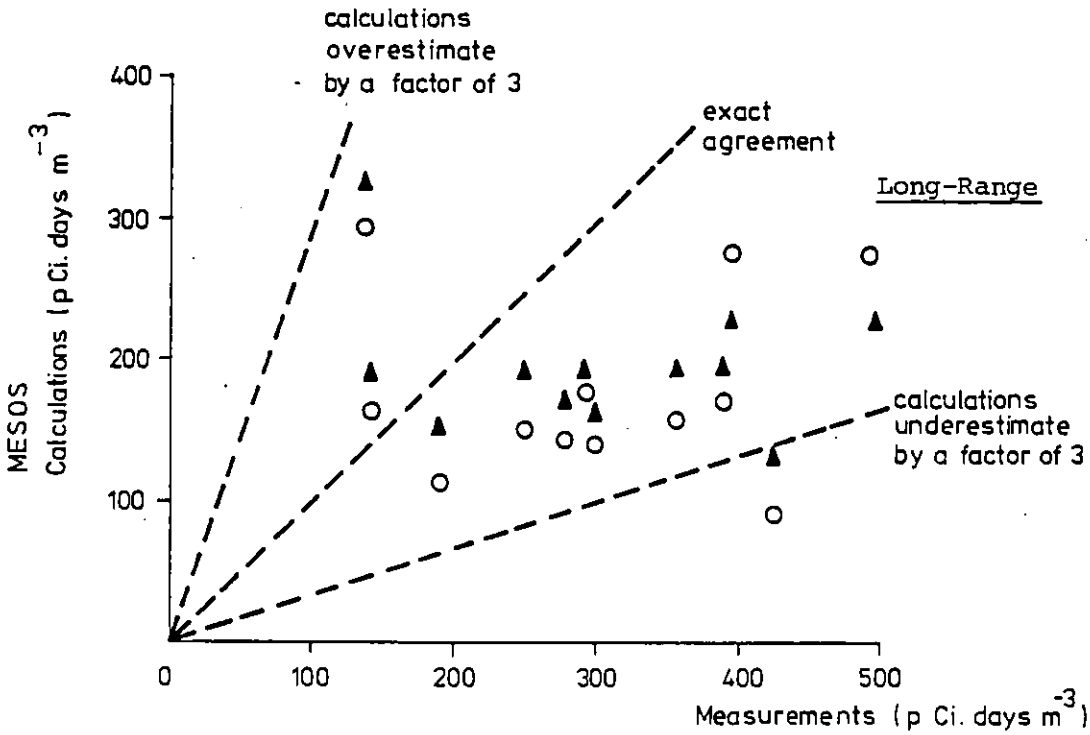




Figure (3.11) Comparison of MESOS Calculations with Measurements

The problems associated with predicting adequate boundary layer trajectories could limit the ability of dispersion models to forecast, with confidence, the consequences of an unplanned release incident. However, the specification of accurate trajectories is of lesser importance in the development of statistical forecasts for the impact of unplanned releases at remote receptors. In the statistical approach, predicting the frequency of exposure at remote receptors is the main interest, rather than giving accurate forecasts of individual trajectory paths. This statistical treatment of exposures from unplanned releases is described in Chapters 5 and 6.

# CHAPTER 4 DEVELOPMENT OF THE METEOROLOGICAL DATABASE

## 4.1 Introduction

The long-range atmospheric transport of a release of pollutant can be strongly influenced by the continuously changing meteorological conditions along the path of the release. It is therefore important to have information on the spatial and temporal variations in the conditions over the wide area in which the pollutants may disperse. The meteorological data required by the MESOS model for the parameterization of the boundary layer has been described in Chapter 2 and includes synoptic pressure fields, rainfall, cloud cover and temperature, at regular time intervals over the European map area.

This Chapter describes the methods used to process meteorological data, obtained from the reports of weather stations and ships, into a suitable form for use in the application of the MESOS model. The methods are generally applicable to any period of routine meteorological reporting and have been applied to the development of databases for 1973-74 and 1976. The emphasis of the work described in this thesis has been placed on the application of the 1973 database, rather than the more recently derived 1976 database, and this is reflected in the examples given in this Chapter.

## 4.2 Data Sources

The MESOS databases have been generated from raw data supplied by the Meteorological Office on a series of magnetic tapes. This meteorological data originates from surface weather observations which are reported, at three-hourly intervals, by a network of land stations and ships. The locations of land stations contributing weather observations for the 1973 database are shown in Figure (4.1). Land stations are unevenly distributed over the map. Although routine reports can be expected at three-hourly intervals, the number of reports collected from the network of stations at any given time can vary significantly. Typically, about 200 reports are available at any time during the night and this number increases to over 1,000 reports during the day. Weather reports from

ships give useful information over the North Sea and Atlantic Ocean; between 20 to 50 reporting ships may be in these areas at any given time.

The contents of weather reports from land stations, as they appear on magnetic tapes from the Meteorological Office, are shown in Figure (4.2). Each reporting land station has a unique code number which allows the position of the station to be identified (Section (4.4)). Ships report their position directly as they move across the map area. The synoptic data which are included in the MESOS database are the present weather code, cloud cover, temperature, height of low cloud and humidity. The present weather code is a weather classification scheme which is used in the database to identify the occurrence and intensity of precipitation (Section (4.4.2)). Temperature and cloud cover are used in MESOS to derive mixing layer development and stability conditions within the boundary layer. Relative humidity and cloud height are not currently used in MESOS, but may be of interest for future model development. The processing of these synoptic data is described in Section (4.4).

Wind direction and strength at 10m are also available in the station reports, but were not included in the database because it was felt that they may be subject to localised effects (e.g. topography) and could therefore be misleading when specifying the large-scale wind field. Instead, pressure data is used to calculate trajectories over large distances within the MESOS model. The treatment of pressure observations is described in the following section.

## 4.3 Pressure Data

The pressure fields are required at regular three-hourly intervals, on a fine grid mesh, so that puff trajectories can be calculated in MESOS. The derivation of satisfactory pressure fields from the scatter of observations is a non-trivial data fitting problem because account must be taken of the uneven spatial distribution and unreliable reporting of land stations and ships. Moreover, it is desirable that the computed pressure fields show good agreement with the Daily Weather Charts and

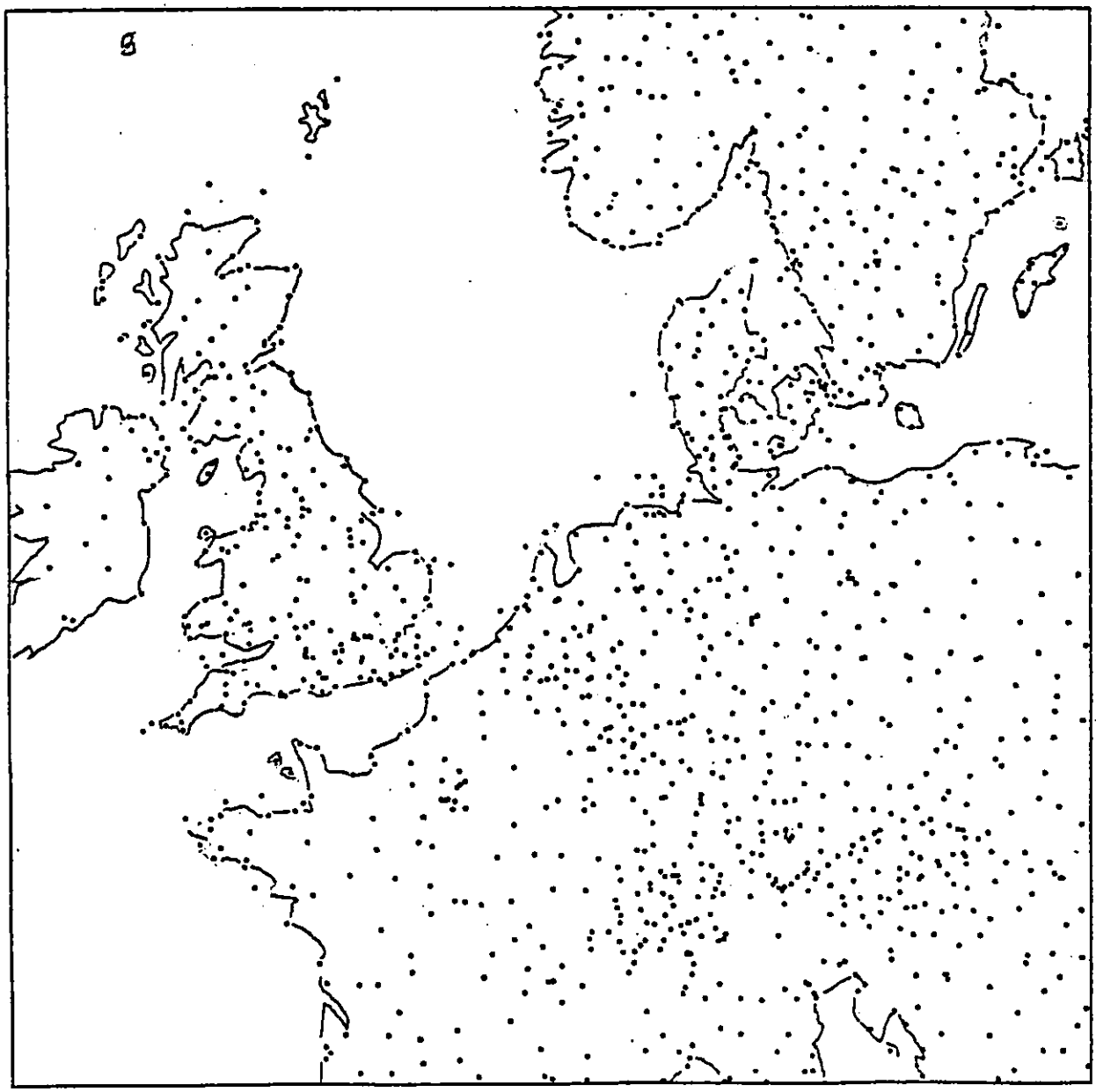


Figure (4.1) Distribution of Reporting Weather Stations

| Station Code No | Date | Time | | | Present Weather Code | | Total Cloud Cover | | | Height of low Cloud | | Temp °C | | | Relative Humidity | |
|---|---|---|---|---|---|---|---|---|---|---|---|---|---|---|---|---|
| 03002 | 16 673 | 0 | 170 | 20 | 45 | 5 | 9 | ****** | 9 | **** | 0 | 8.0 | 8.0 | 10.7 | 100 | 1023.6 |
| 03005 | 16 673 | 0 | 180 | 6 | 28 | 4 | 8 | 5**** | 8 | 0 | 320 | 9.0 | 9.0 | 11.5 | 100 | 1024.0 |
| 03010 | 16 673 | 0 | 0 | 0 | 1 | 2 | 5 | 5 7 0 | 3 | 60 | 5000 | 10.0 | 10.0 | 12.3 | 100 | 1020.1 |
| 03017 | 16 673 | 0 | 150 | 15 | 5 | 2 | 6 | 5 3** | 1 | 100 | 800 | 11.0 | 10.0 | 12.3 | 94 | 1020.7 |
| 03022 | 16 673 | 0 | 150 | 16 | 3 | 2 | 8 | 5 7** | 6 | 30 | 2500 | 13.0 | 11.0 | 13.1 | 88 | 1016.8 |
| 03026 | 16 673 | 0 | 150 | 11 | 3 | 1 | 8 | 5 7** | 3 | 60 | 1500 | 12.0 | 8.0 | 10.7 | 76 | 1018.3 |
| 03049 | 16 673 | 0 | 0 | 0 | 2 | 2 | 7 | 5**** | 5 | 60 | 5500 | 15.0 | 8.0 | 10.7 | 63 | 1019.0 |
| 03066 | 16 673 | 0 | 160 | 3 | 2 | 1 | 7 | 5 4 2 | 5 | 150 | 6000 | 15.0 | 10.0 | 12.3 | 72 | 1020.9 |
| 03075 | 16 673 | 0 | 180 | 9 | 5 | 6 | 6 | 5**** | 6 | 100 | 1500 | 11.0 | 9.0 | 11.5 | 87 | 1021.0 |
| 03091 | 16 673 | 0 | 150 | 6 | 3 | 8 | 7 | 0 3 2 | 5 | 250 | 2000 | 11.0 | 10.0 | 12.3 | 94 | 1022.9 |
| 03100 | 16 673 | 0 | 140 | 15 | 4 | 6 | 7 | 5 3 2 | 6 | 150 | 800 | 12.0 | 11.0 | 13.1 | 94 | 1018.0 |
| 03106 | 16 673 | 0 | 200 | 13 | 2 | 2 | 7 | 8**** | 7 | 60 | 2400 | 13.0 | 8.0 | 10.7 | 72 | 1019.9 |
| 03131 | 16 673 | 0 | 170 | 18 | 3 | 2 | 7 | 5 7** | 4 | 100 | 2400 | 13.0 | 11.0 | 13.1 | 88 | 1021.4 |
| 03135 | 16 673 | 0 | 110 | 6 | 2 | 1 | 7 | 5 7 8 | 1 | 150 | 2000 | 13.0 | 8.0 | 10.7 | 72 | 1022.0 |
| 03140 | 16 673 | 0 | 60 | 2 | 2 | 1 | 7 | 0 3 2 | 2 | 250 | 2000 | 13.0 | 8.0 | 10.7 | 72 | 1021.8 |
| 03160 | 16 673 | 0 | 0 | 0 | 2 | 1 | 7 | 5 3 2 | 2 | 150 | 1800 | 12.0 | 8.0 | 10.7 | 76 | 1022.8 |
| 03162 | 16 673 | 0 | 0 | 0 | 5 | 1 | 5 | 5 3 1 | 3 | 100 | 600 | 8.0 | 6.0 | 9.4 | 87 | 1024.3 |
| 03171 | 16 673 | 0 | 0 | 0 | 10 | 1 | 7 | 5 7 6 | 1 | 150 | 800 | 10.0 | 10.0 | 12.3 | 100 | 1022.7 |
| 03177 | 16 673 | 0 | 140 | 18 | 2 | 2 | 6 | 5 7** | 3 | 30 | 3000 | 12.0 | 10.0 | 12.3 | 88 | 1022.5 |
| 03185 | 16 673 | 0 | 200 | 11 | 3 | 2 | 7 | 8**** | 7 | 60 | 3500 | 15.0 | 13.0 | 15.0 | 88 | 1023.2 |
| 03190 | 16 673 | 0 | 200 | 10 | 3 | 2 | 6 | 0 7 6 | 3 | 250 | 1300 | 12.0 | 10.0 | 12.3 | 88 | 1023.5 |
| 03204 | 16 673 | 0 | 120 | 3 | 1 | 2 | 7 | 0 7 8 | 1 | 250 | 1200 | 12.0 | 8.0 | 10.7 | 76 | 1022.6 |
| 03208 | 16 673 | 0 | 140 | 8 | 2 | 0 | 4 | 5 3 1 | 2 | 100 | 2400 | 13.0 | 10.0 | 12.3 | 82 | 1022.9 |
| 03222 | 16 673 | 0 | 100 | 5 | 3 | 2 | 7 | 0 3 2 | 2 | 250 | 1000 | 12.0 | 10.0 | 12.3 | 88 | 1023.2 |

*denotes unreported item

Figure (4.2) Contents of Land Station Reports

it is particularly important that the differential pressure field is accurately represented since the geostrophic wind is derived from the pressure gradient.

The methods used to generate the database pressure fields are described by Sykes and Hatton (1976). The numerical scheme involves constructing interpolation polynomials which fit observations, in a least squares sense, both in space and time. The polynomials have to be of sufficiently high degree in order to represent adequately the small-scale features of the synoptic pressure field (e.g. centres of high and low pressure). The polynomials must also describe the pressure field over the complete map area. Piecewise fitting over sub-regions of the map is not used, because it is required that the pressure differential be continuous over the entire map area. Orthogonal polynomial techniques are used in the fitting procedure to allow polynomials of sufficiently high degree to be developed. This is a standard technique used for pressure field analysis at the Meteorological Office. The orthogonal polynomials which are fitted to the pressure observations are then evaluated at all grid points, on a mesh of $\frac{1}{2}^\circ$ latitude by $1^\circ$ longitude, to give database pressure fields at regular three-hourly intervals.

## 4.4 Synoptic Data

The processing of synoptic data differs from that of pressure data because representative data values are required over each database cell rather than at a mesh of grid points. The computer program SYNDA is used to process synoptic data and a flowchart is given in Figure (4.3). The objective is to group observations in the appropriate database cells ($1^\circ$ latitude by $2^\circ$ longitude) and then, within each cell, to assess the average precipitation, cloud cover, temperature, height of low cloud and humidity.

The location of each reporting land station is derived from its five digit code number (Figure (4.2)). The first two digits of the station code number refer to the country of origin (e.g. 03 indicates a U.K. station), and the remaining digits complete the station identification. These code numbers are catalogued with station position, enabling the

data of interest in the station report to be assigned to the appropriate database cell in the map area. Ship data can be allocated directly because each ship gives its position at the time of making the report.

The selected data is first checked to ensure that all data items are satisfactory. Inevitably, there are some errors in the data due to the large number of reports processed - over 1.2 million reports were processed in the production of the 1973 database. A station may not give a full report, or a data item may have an unreasonable value. Data is excluded if it is found to lie outside defined limits which are set to identify obvious errors, but are not too restrictive to exclude genuine but extreme meteorological conditions which may be of particular interest. The defined limits for most data items are fairly obvious; the present weather code should only take values between 0-99, cloud cover 0-9 oktas and relative humidity 0-100%. However, the quality control of temperature observations is difficult, because large temperature variations may naturally occur with time of day, season and geographical location. Consequently, only seasonal limits are imposed for temperature observations:

| | |
|---|---|
| Winter: | -16°C to 20°C |
| Spring/Autumn: | -16°C to 25°C |
| Summer: | - 8°C to 38°C |

If a station record contains an unreported or erroneous value for any one of the data items considered, the whole record is rejected. Typically, about 5% of reports are excluded in this way. This approach may reject genuine data, but it ensures that all reported data is reliable and considerably simplifies the data processing.

After checking and allocating all the available reports, representative values of data are required for each database cell. Therefore, if a cell has been assigned more than one report, the reported data items are averaged separately. However, it is likely that several cells contain no reported information due to the uneven distribution of reporting stations and ships. Database cells over land without reported data are usually surrounded by other cells in which reports are available and can be given meaningful data from the neighbouring cells. However, data-

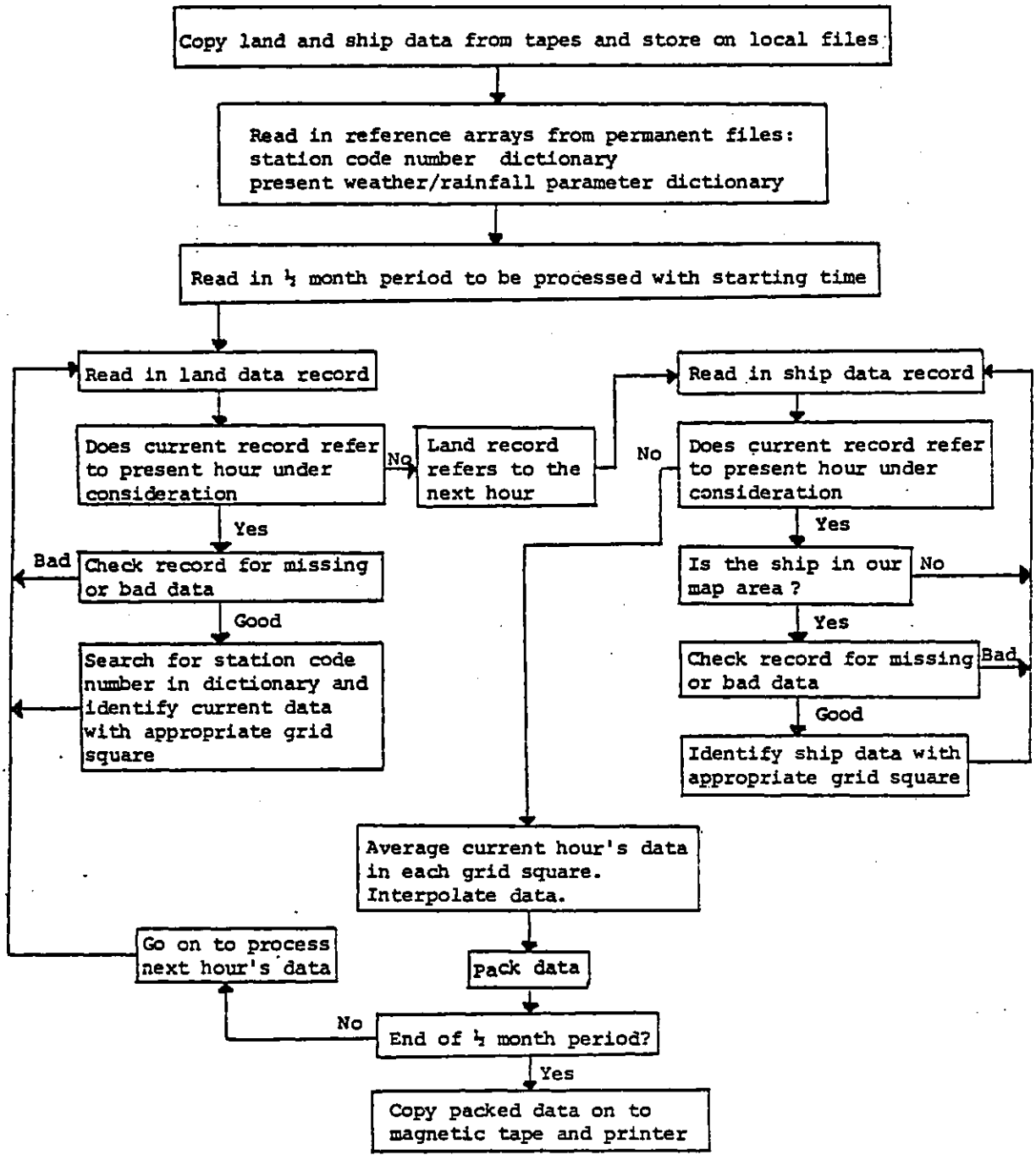



Figure (4.3) Flowchart for Synoptic Data Processing

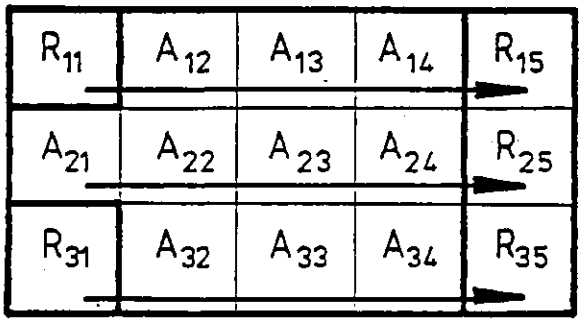
base cells over the sea without reported data are frequently surrounded by other cells without reported data, because of the limited number of reports in these areas. The problem of assigning reasonable data to cells without reported data is treated by a simple but effective numerical interpolation scheme. This scheme is described in the following section.

### 4.4.1 Interpolation Procedure for Synoptic Data

Several numerical schemes, of varying complexity, have been developed to attempt to solve the problem of defining synoptic data for database cells in which reported data is unavailable.

A simple method, based on adjacent cell averaging, was finally chosen for the production of the databases. Database cells are checked, in systematic order, for having reported data. If a cell has been assigned reported data, it is passed over and the next cell checked. However, any cell found to have no reported data is given data by taking the average of any data from adjacent cells. This data may be reported, or previously derived from the same averaging method. Previously averaged data has to be used to ensure that the numerical scheme continues over the entire map area, but care must be taken to avoid reported data being erroneously propagated across the map. It is particularly undesirable to spread extreme but localised data, for example, to extend orographic rain from Norway across the North Sea. The following example shows how erroneous data propagation can arise:

Example:



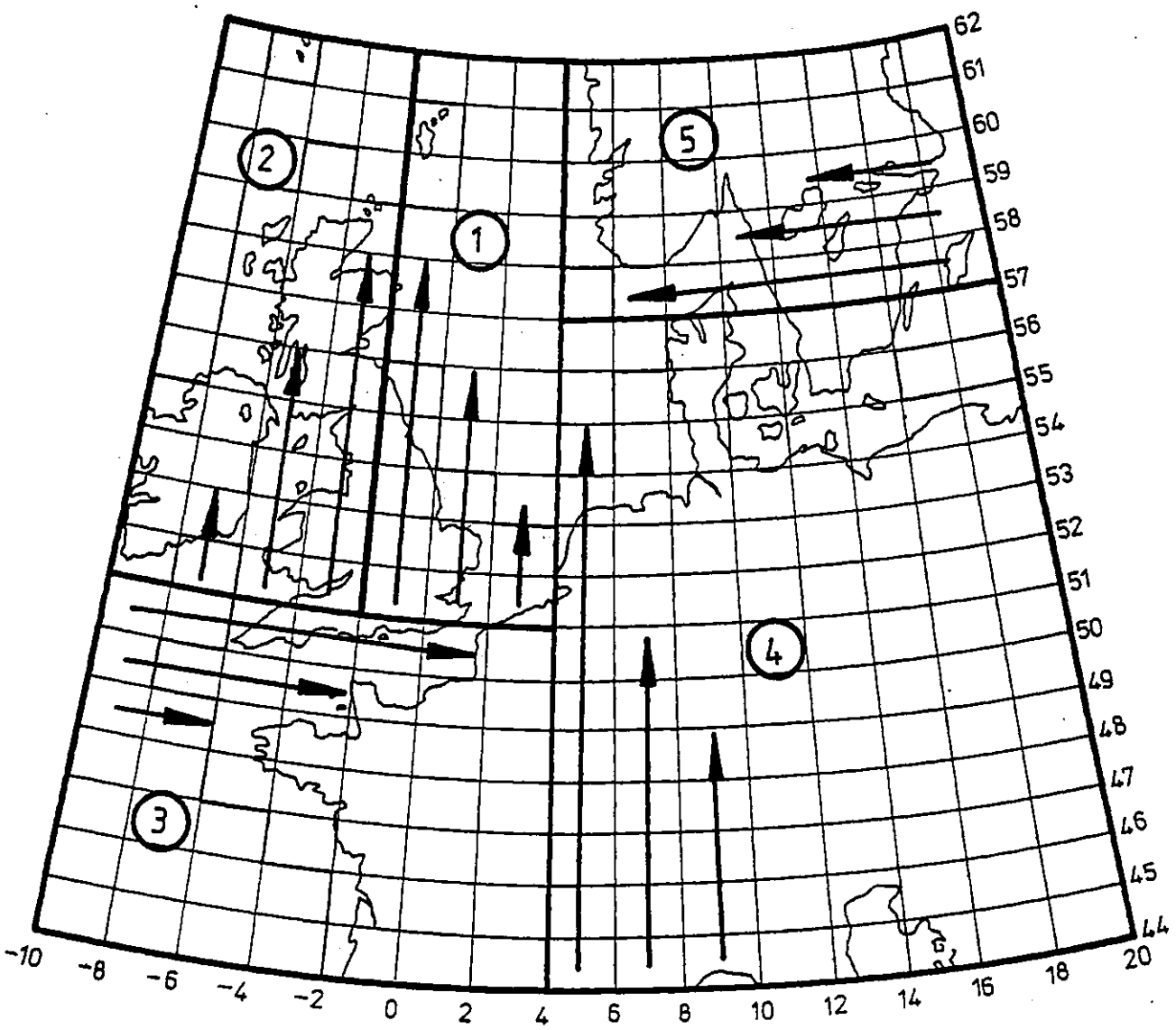

$R_{ij}$ = reported data
$A_{ij}$ = averaged data

The diagram above shows a subset of the map area in which there is reported data for only 5 of the 15 database cells. In an attempt to provide data for the remaining 10 cells, cell (1,1) may be chosen as the starting point of the interpolation scheme which has been described above. Cell (1,1) is checked and found to have reported data $R_{11}$. The scheme passes on to cell (1,2), for which there is no reported data. Averaged data $A_{12}$ must be given to this cell, and it is assigned data values, $A_{12} = R_{11}$, from cell (1,1) since this is the only adjacent cell containing data. Continuing the scheme, in the order shown, averaged data is assigned, in the following way, to each cell without reported data:

$$
\begin{aligned}
A_{13} &= A_{12} && = R_{11} \\
A_{14} &= \tfrac{1}{3}(A_{13} + R_{15} + R_{25}) && = \tfrac{1}{3}(R_{11} + R_{15} + R_{25}) \\
A_{21} &= \tfrac{1}{3}(R_{31} + R_{11} + A_{12}) && = \tfrac{1}{3}(2R_{11} + R_{31}) \\
A_{22} &= \tfrac{1}{5}(R_{31} + A_{21} + R_{11} + A_{12} + A_{13}) && = \tfrac{1}{15}(11R_{11} + 4R_{31}) \\
A_{23} &= \tfrac{1}{4}(A_{22} + A_{12} + A_{13} + A_{14}) && = \tfrac{1}{60}(46R_{11} + 5R_{15} + 5R_{25} + 4R_{31}) \\
&\ \ \vdots && \ \ \vdots
\end{aligned}
$$

The chosen ordering, in the above example, gives unsatisfactory results because each assigned value $A_{ij}$ is too heavily weighted on the reported data $R_{11}$ in the cell where the scheme commenced. The reported data is erroneously propagated, by this scheme, from left to right and from top to bottom across the map. Moreover, completely different estimates could be given to the cells if the scheme started from cell (1,5) and progressed from right to left across the map. The interpolations from both these orderings are obviously unacceptable, and careful consideration of the scheme's ordering is necessary. In fact, satisfactory interpolations could be obtained in the example if the scheme first progressed over columns 1 and 2, followed by columns 5 and 4, finally assigning data to the centre column 3.

The problem of erroneous data propagation was solved by dividing the database map area into subsections and operating on database cells in a carefully chosen order. Various divisions of the map were considered separately, and the resulting interpolations compared with more sophisticated interpolation schemes. The optimum division of the map and ordering of




The arrows indicate the order in which each database cell is tested for having reported data. The map area is divided into five regions which are treated in sequence.

Figure (4.4) Interpolation Scheme for Synoptic Data

the interpolations was found to be that shown in Figure (4.4). This scheme was used in the production of both the 1973 and 1976 databases, and gives particular consideration to the treatment of database cells over the sea, for which it is unlikely that reported data will be available. The numerical scheme has been found to give reliable interpolations and is computationally efficient.

### 4.4.2 Estimation of Rainfall from the Present Weather Code

Average rainfall rates in the database are derived from weather station reports on the present weather code. The code contains 100 different weather classifications, 60 of which are reserved for various forms of precipitation (Table (4.1)). The precipitation codes distinguish between precipitation type (e.g. rain, drizzle, snow), duration (continuous, intermittent, showery) and intensity (slight, moderate, heavy). Also, there are separate classifications for forthcoming precipitation, precipitation at the time of the report and precipitation occurring within the last hour. An appropriate precipitation code is selected by the reporting station on the basis of the observed rainfall, as specified by the Observers' Handbook (Met. Office (1969)). It is therefore possible to use the present weather report to give a quantitative estimate of the rainfall rate at the reporting station.

Rainfall rate is used in MESOS to predict the time dependent precipitation scavenging from a plume which may have dispersed over a large area. Consequently, it is desirable that the rainfall rate used in the MESOS calculations should be representative of precipitation conditions, not only at the reporting station, but also over the database cell and during the three-hour time interval. A rain index is used in the database in an attempt to give such information. Each present weather code is assigned an index value on the scale 0 to 9, to allow for the likely intensity, timescale and spread of the precipitation. Rainfall rates for common precipitation types and the associated rain index are shown in Table (4.2).

The consideration of precipitation timescale and spread is particularly important in the treatment of showers and intermittent precipitation. Showers, although often intense, tend to be localised ($\sim$ few $km^2$), and

brief (∿ few minutes). Hence, the value of the index given to showers is much lower than that given to continuous precipitation of the same intensity. Similarly, the index associated with intermittent precipitation is less than that of continuous precipitation.

The index reduction factors used in this treatment are shown in Table (4.2). As discussed below, these factors are necessarily tentative, but are shown to be consistent with other work in the field.

(i) Showers

Ritchie et al (1976) have proposed two models of typical rain systems based on meteorological radar data. The first model attempts to characterise a rainstorm in which four levels of rain activity are identified in the storm. Each region of activity has a different size, rainfall rate and duration (Figure (4.5)). The smallest regions give localised but intense showery precipitation and are contained within a rain system covering a considerable area ($>10^4$ km$^2$). Ritchie derives an average rainfall rate through the storm in terms of the rainfall rates expected in each region of activity. This average rainfall rate is about one-twelfth of the rainfall rate experienced within the showery regions.

The second model describes the typical structure of a frontal rain system. Rain activity is concentrated within a rainbelt about 30 km wide and of length scale 150-1500 km. Showery regions are again included in the model. The average rainfall rate across the frontal system is about one-quarter of the rainfall rate within the showery regions. However, the relatively narrow rainbelt would only cover a fraction of the area of a database cell, at any time, and a larger reduction factor may be appropriate in the context of the database.

Although the models of Ritchie et al (1976) are particular to two types of shower activity, it would seem that the reduction factor of one-tenth used for showers in the database treatment is quite reasonable. The main uncertainty in the treatment of showers is the lack of quantitative information on shower distribution and timescale over the database cell,

which cannot be adequately identified by the network of reporting stations.

(ii) Intermittent precipitation

The correlation between measured rainfall at a station and the reported present weather code has been studied by Sawyer (1952). Sawyer compared reports of intermittent and continuous rains from 47 British stations, with rainfall rates estimated from the measured amount of rainfall during the hour preceding the observation. This information can therefore be used to assess the relative rainfall rates of continuous and intermittent precipitation types of the same intensity. This comparison is given in Figure (4.6) and indicates that intermittent rains typically produce between one-third and two-thirds of the rainfall expected from similar continuous rains. In the database, it is assumed that intermittent rains produce half the rainfall of similar continuous rains.

(iii) Advantages and limitations of using the present weather code

The study of Sawyer (1952) has also shown that there can be considerable variation in the measured rainfall rate for a given present weather code. On some occasions the measured rainfall rates were not consistent with the classification scheme given in the Observers' Handbook. Other anomalies in present weather reporting have been discussed by Tucker (1961). In a survey of the frequency with which different stations report certain present weather codes, Tucker deduced that some stations tend to over and under-report certain precipitation codes. A survey of the frequencies of rainfall index for each cell in the 1973 database has also shown that some coastal stations tend to over-report heavy rainfall. Reporting the present weather code inevitably involves some degree of subjective judgement by the observer. These factors probably introduce the greatest uncertainties in the rainfall rates derived from present weather reports.

Despite these limitations, the method of using the present weather code

## Table Code for Present Weather (ww) (Code 4677)

**00–19 No precipitation at the station at the time of observation.**

| | | |
|---|---|---|
| 00 | Cloud development not observed. | Characteristic change of the state of the sky during the past hour. |
| 01 | Clouds generally dissolving or becoming less developed. | |
| 02 | State of sky on the whole unchanged. | |
| 03 | Clouds generally forming or developing. | |
| 04 | Visibility reduced by smoke, e.g., veldt or forest fire, industrial smoke or volcanic ashes. | |
| 05 | Haze | |
| 06 | Widespread dust in suspension in the air, not raised by wind at or near the station at the time of observation | |
| 07 | Dust or sand raised by wind at or near the station at the time of observation, but no well-developed dust whirl(s) or sand whirl(s), and no duststorm or sandstorm seen; or in the case of ships, blowing spray at the station. | |
| 08 | Well developed dust whirl(s) or sand whirl(s) seen at or near the station during the preceding hour, but no duststorm or sandstorm. | |
| (0) 09 | Duststorm or sandstorm within sight of the station or at the station during the preceding hour. | |
| 10 | Mist. | |
| 11 | Shallow fog or ice fog, in patches. | Fog not deeper than about 2 metres on land or 10 metres at sea. |
| 12 | Shallow fog or ice fog, more or less continuous. | |
| 13 | Lightning visible, no thunder heard. | |
| 14 | Precipitation within sight, not reaching the ground or the surface of the sea. | |
| 15 | Precipitation within sight, reaching the ground or the surface of the sea but distant (estimated to be more than 5 km) from the station. | |
| 16 | Precipitation within sight reaching the ground or the surface of the sea near to but not at the station. | |
| 17 | Thunderstorm, but no precipitation at time of observation. | |
| 18 | Squalls. | at or within sight of the station during the preceding hour or at the time of observation. |
| 19 | Funnel cloud(s)† | |

**20–29 Precipitation, fog or thunderstorm at station during the last hour but not at time of observation.**

| | | |
|---|---|---|
| (1) 20 | Drizzle (not freezing), or snow grains. | Not falling as shower(s). |
| (2) 21 | Rain (not freezing). | |
| (2) 22 | Snow. | |
| (2) 23 | Rain and snow or ice pellets type (a). | |
| (1) 24 | Freezing drizzle or freezing rain. | |
| (1) 25 | Shower(s) of rain. | |
| (1) 26 | Shower(s) of snow, or of rain and snow. | |
| (1) 27 | Shower(s) of hail*, or of hail and rain. | |
| (0) 28 | Fog or ice fog. | |
| (1) 29 | Thunderstorm (with or without precipitation). | |

**30–39 Duststorms, Sandstorms, drifting or blowing snow**

| | | |
|---|---|---|
| 30 | Slight or moderate duststorm or sandstorm. | has decreased during preceding hour. |
| 31 | | no appreciable change during preceding hour. |
| 32 | | has begun or has increased during preceding hour. |
| (0) 33 | Severe duststorm or sandstorm. | has decreased during preceding hour. |
| 34 | | no appreciable change during preceding hour. |
| 35 | | has begun or has increased during preceding hour. |
| 36 | Slight or moderate drifting snow. | generally low. |
| 37 | Heavy drifting snow. | |
| 38 | Slight or moderate blowing snow. | generally high. |
| 39 | Heavy blowing snow. | |

**40–49 Fog or ice fog at time of observation.**

| | | |
|---|---|---|
| 40 | Fog or ice fog at a distance at the time of observation, but not at the station during the last hour, the fog or ice fog extending to a level above that of the observer. | |
| 41 | Fog or ice fog in patches. | |
| 42 | Fog or ice fog, sky discernible. | has become thinner during the preceding hour. |
| 43 | Fog or ice fog, sky not discernible. | |
| (0) 44 | Fog or ice fog, sky discernible. | no appreciable change during the preceding hour. |
| 45 | Fog or ice fog, sky not discernible. | |
| 46 | Fog or ice fog, sky discernible. | has begun, or has become thicker during the preceding hour. |
| 47 | Fog or ice fog, sky not discernible. | |
| 48 | Fog, depositing rime, sky discernible. | |
| 49 | Fog, depositing rime, sky not discernible. | |

**50–59 Drizzle at time of observation.**

| | | |
|---|---|---|
| (1) 50 | Drizzle, not freezing, intermittent. | slight at time of observation. |
| (1) 51 | Drizzle, not freezing, continuous. | |
| (1) 52 | Drizzle, not freezing, intermittent. | moderate at time of observation. |
| (2) 53 | Drizzle, not freezing, continuous. | |
| (1) 54 | Drizzle, not freezing, intermittent. | heavy (dense) at time of observation. |
| (2) 55 | Drizzle, not freezing, continuous. | |
| (1) 56 | Drizzle, freezing, slight. | |
| (2) 57 | Drizzle, freezing, moderate or heavy (dense). | |
| (1) 58 | Drizzle and rain, slight. | |
| (4) 59 | Drizzle and rain, moderate or heavy. | |

**60–69 Rain at time of observation**

| | | |
|---|---|---|
| (1) 60 | Rain, not freezing, intermittent. | slight at time of observation. |
| (1) 61 | Rain, not freezing, continuous. | |
| (2) 62 | Rain, not freezing, intermittent. | moderate at time of observation. |
| (5) 63 | Rain, not freezing, continuous. | |
| (4) 64 | Rain, not freezing, intermittent. | heavy at time of observation. |
| (4) 65 | Rain, not freezing, continuous. | |
| (1) 66 | Rain, freezing, slight. | |
| (3) 67 | Rain, freezing, moderate or heavy. | |
| (1) 68 | Rain or drizzle, and snow, slight. | |
| (4) 69 | Rain or drizzle and snow, moderate or heavy. | |

**70–79 Solid precipitation not in showers.**

| | | |
|---|---|---|
| (1) 70 | Intermittent fall of snow flakes. | slight at time of observation. |
| (1) 71 | Continuous fall of snow flakes. | |
| (2) 72 | Intermittent fall of snow flakes. | moderate at time of observation. |
| (5) 73 | Continuous fall of snow flakes. | |
| (4) 74 | Intermittent fall of snow flakes. | heavy at time of observation. |
| (9) 75 | Continuous fall of snow flakes. | |
| (3) 76 | Ice prisms (with or without fog). | |
| (3) 77 | Snow grains (with or without fog). | |
| (3) 78 | Isolated starlike snow crystals (with or without fog). | |
| (3) 79 | Ice pellets type (a). | |

**80–90 Showery precipitation**

| | | |
|---|---|---|
| (1) 80 | Rain shower(s), slight. | |
| (4) 81 | Rain shower(s), moderate or heavy. | |
| (6) 82 | Rain shower(s), violent. | |
| (1) 83 | Shower(s) of rain and snow, slight. | |
| (4) 84 | Shower(s) of rain and snow, moderate or heavy. | |
| (1) 85 | Snow shower(s), slight. | |
| (4) 86 | Snow shower(s), moderate or heavy. | |
| (1) 87 | Shower(s), or snow pellets or ice pellets type (b) with or without rain or rain and snow mixed. | slight |
| (4) 88 | | moderate or heavy. |
| (1) 89 | Shower(s) of hail, with or without rain or rain and snow mixed, not associated with thunder. | slight. |
| (4) 90 | | moderate or heavy. |

**91–99 Precipitation with current or recent thunderstorm**

| | | |
|---|---|---|
| (1) 91 | Slight rain at time of observation. | thunderstorm during the preceding hour, but not at time of observation. |
| (6) 92 | Moderate or heavy rain at time of observation. | |
| (1) 93 | Slight snow, rain and snow mixed, or hail* at time of observation. | |
| (6) 94 | Moderate or heavy snow, rain and snow mixed or hail* at time of observation. | |
| (4) 95 | Thunderstorm, slight or moderate, without hail* but with rain and/or snow at time of observation. | |
| (4) 96 | Thunderstorm, slight or moderate, with hail* at time of observation. | |
| (5) 97 | Thunderstorm, heavy, without hail*, but with rain and/or snow at time of observation. | thunderstorm at time of observation. |
| (0) 98 | Thunderstorm combined with duststorm or sandstorm at time of observation. | |
| (5) 99 | Thunderstorm, heavy, with hail* at time of observation. | |

| Type of Precipitation | | Rainfall Rates (mm/h ) | Rainfall Parameter I |
|---|---|---|---|
| Rain | Slight | 0.0 - 0.5 | 1 |
| | Moderate | 0.5 - 4.0 | 5 |
| | Heavy | > 4.0 | 9 |
| *Showers | Slight | 0.0 - 2.0 | 1 |
| | Moderate | 2.0 - 10.0 | 2 |
| | Heavy | 10.0 - 50.0 | 6 |
| Drizzle | Slight | 0.2 | 1 |
| | Moderate | 0.5 | 2 |
| | Heavy | 0.75 | 2 |

* Rainfall parameter scaled down by factor of 10 to account for short duration and locality of showers.

Intermittent precipitation takes half parameter values.
Past and forthcoming precipitation dealt with similarly.
Snow, hail, ice pellets given same efficiency as rain.

Table (4.2) Rainfall Rates for Common Precipitation Types

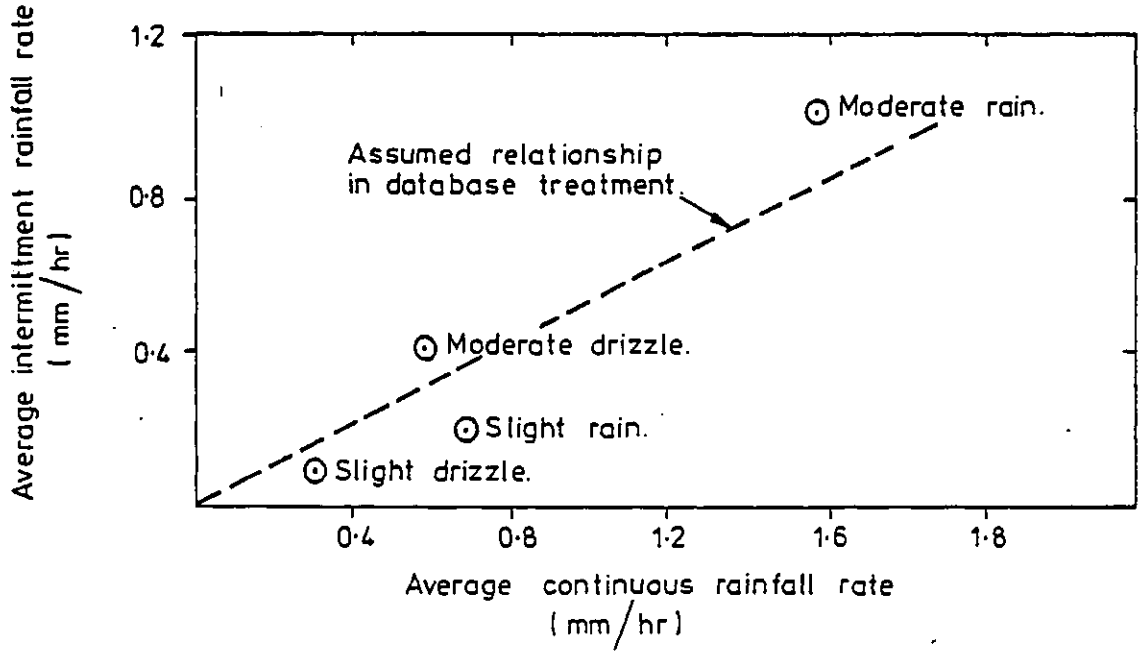
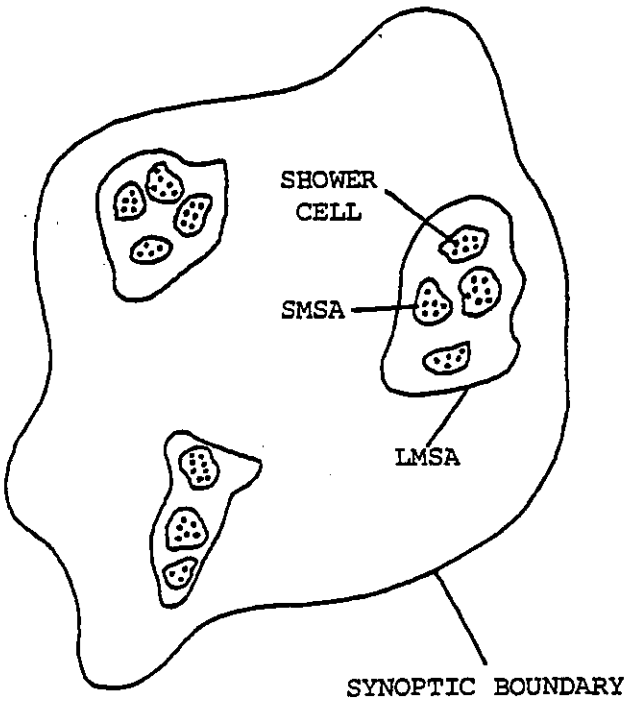



Figure (4.6) Comparison between Intermittent and Continuous Rainfall Rates




Spatial Schematic of Typical Rainstorm

| CHARACTERISTICS OF MODEL FOR GENERAL RAINSTORMS | | | | | |
|---|---|---|---|---|---|
| Level Designation | Size of Each Unit in Level | Average Rainfall Intensity in Level | Fraction of Storm Covered at Any One Time | Duration | Average Density of Units |
| Synoptic | $\geq 10^4$ km$^2$ | R | Entire storm | Few hours to few days | |
| Large Mesoscale Area (LMSA) | 4000 km$^2$ | 2R | 1/3 of storm | 1 to 12 hours | 1 LMSA per 12000 km$^2$ |
| Small Mesoscale Area (SMSA) | 250 km$^2$ | 4R | 1/9 of storm | 1 hour | 5.6 SMSA per LMSA |
| Shower Cell | 10 km$^2$ | 25R | 1/54 of storm | $t_c^* = \frac{1}{2} J_c$ | 4 cells per SMSA |

*$t_c$ = Duration of rain cell in minutes

$J_c$ = Rainfall rate in rain cell in mm/hr

Figure (4.5) Typical Structure of a Rainstorm

(taken from Ritchie et al (1976))

has considerable advantages over previous attempts to predict the occurrence of rainfall, usually involving measured rainfall totals over 12 or even 24 hour periods (e.g. OECD (1975, 1977)). Precipitation has considerable variability in time and the three-hourly present weather observations give an improved representation of this variability. Moreover, since the present weather code gives a detailed descriptive account of the form of precipitation, it is possible to allow for both the timescale and spread of precipitation which is not known from measurements of total rainfall at a fixed station. The latter information is particularly useful in the context of the modelling of the precipitation scavenging from a widely dispersed plume, since it allows for a better description of the pollutant washout throughout the plume.

## 4.5 Database Production

The methods described in the previous sections have been used to establish two databases for the years 1973 and 1976. For each year, the three-hourly pressure and synoptic data fields were processed separately and then finally merged, in chronological order, onto a single magnetic tape. This format means that the databases can be easily accessed by MESOS and allows for repeated dispersion calculations over a long database time period.

The amount of meteorological data contained in the 1973 database is shown in Table (4.3). Although there are periods when either raw pressure or synoptic data were unavailable from the Meteorological Office, the 1973 database contains 272 days of complete data and each season is well represented. The 1976 database is more complete and gives 355 days of data. The 1976 database also contains data for a greater area which extends south over the Mediterranean Sea down to latitude 36°N. The production of the 1976 database is described by ApSimon et al (1981).

## 4.6 Quality of the Database Information

Samples of database grids have been compared with the corresponding Daily Weather Reports at the Meteorological Office. This check on

| | JAN | FEB | MARCH | APRIL | MAY | JUNE | JULY | AUG | SEPT | OCT | NOV | DEC | JAN 74 | FEB 74 |
|---|---|---|---|---|---|---|---|---|---|---|---|---|---|---|
| 1 | | PS | PS | PS | | PS | S | PS | PS | PS | PS | PS | PS | PS |
| 2 | | S | S | PS | | PS | S | PS | PS | PS | PS | PS | PS | PS |
| 3 | | S | S | PS | P | PS | PS | PS | PS | PS | PS | PS | PS | PS |
| 4 | | S | S | PS | P | PS | PS | PS | PS | PS | PS | PS | PS | PS |
| 5 | | S | S | PS | P | PS | PS | PS | PS | PS | PS | PS | PS | PS |
| 6 | | S | S | PS | P | PS | PS | PS | PS | PS | PS | PS | PS | PS |
| 7 | | S | S | PS | P | PS | PS | PS | PS | PS | PS | PS | PS | PS |
| 8 | | S | S | PS | P | PS | PS | PS | PS | PS | PS | PS | PS | PS |
| 9 | | S | PS | PS | P | PS | PS | PS | PS | PS | PS | PS | PS | PS |
| 10 | | S | S | PS | P | PS | PS | PS | PS | PS | PS | PS | PS | PS |
| 11 | | S | S | PS | P | S | PS | PS | PS | PS | PS | PS | PS | PS |
| 12 | | S | S | PS | P | PS | PS | PS | PS | PS | PS | S | PS | PS |
| 13 | | S | PS | PS | P | P | PS | PS | PS | PS | PS | S‡ | PS | PS |
| 14 | | S | PS | PS | P | P | PS | PS | PS | PS | PS | S‡ | PS | PS |
| 15 | | S | PS | PS | P | P | PS | PS | PS | P | PS | PS | PS | PS |
| 16 | | S | P | PS | P | PS | PS | PS | PS | PS | PS | P | PS | PS |
| 17 | | S | P | PS | P | PS | PS | PS | PS | PS | PS | P | PS | PS |
| 18 | | S | P | PS | P | PS | PS | PS | PS | PS | PS | P | PS | PS |
| 19 | | S | P | PS | P | PS | PS | PS | PS | PS | PS | | PS | PS |
| 20 | | S | P | PS | P | PS | PS | PS | PS | PS | PS | | PS | PS |
| 21 | | S | P | PS | P | PS | PS | PS | PS | PS | PS | | PS | PS |
| 22 | | S | P | PS | P | PS | PS | PS | PS | PS | PS | P | PS | PS |
| 23 | P | S | P | PS | P | PS | PS | PS | PS | PS | PS | P | PS | PS |
| 24 | P | S | P | PS | P | PS | PS | PS | PS | PS | PS | P | PS | PS |
| 25 | | S | | PS | P | PS | PS | PS | PS | PS | PS | P | PS | PS |
| 26 | | S | | PS | P | PS | PS | PS | PS | PS | PS | P | PS | PS |
| 27 | | S | | PS | P | PS | PS | PS | PS | PS | PS | P | PS | PS |
| 28 | | S | | PS | P | PS | PS | PS | PS | PS | PS | P | P | PS |
| 29 | P | | | PS | P | PS | PS | PS | PS | PS | PS | P | P | |
| 30 | P | | | | P | PS | PS | PS | PS | PS | PS | | P | |
| 31 | P | | P | | P | | PS | PS | | PS | S | | P | |

P = PRESSURE DATA

S = SYNOPTIC DATA

‡ DATA FOR 1500 and 1800 hours MISSING

Table (4.3) Availability of Synoptic and Pressure Data in the 1973 Database

database reliability has shown that there is generally good agreement for all data items. Temperature distributions are particularly well represented in the database. Occasional differences have been noticed in data items which are expected to vary over an area less than that of a database cell. For example, cloud cover and rainfall rate can vary over relatively small distances and these variations sometimes cannot be resolved by the network of reporting weather stations. Although the detailed structure of some rain systems (e.g. Figure (4.5)) cannot be represented in the database, the comparison with the Daily Weather Charts has shown that the major rain systems are adequately resolved in space and time.

Database samples have been made available to Maul (1980) for a study of episodes of long-range transport of $SO_2$ to Norway. Maul was interested in wet deposition, and gives comparison of database rainfall estimates with measurement at OECD monitoring sites in Norway. These comparisons, for five episodes during 1973 and 1974, are given in Figure (4.7). Although the patterns of measured rainfall and rainfall deduced from the database are in general agreement, heavy rainfall in these episodes appears to be underestimated in the database. This may be due to the averaging procedure over a database cell in the treatment of intense but localised rains, as described in Section (4.4.2). It is difficult to improve on this treatment of localised rainfall with the present network of reporting stations.

The database rain index has also been used to estimate the total rainfall in each database cell during 1973. These database rainfall totals are compared with measured rainfall, taken from the relevant monthly climatic records (WMO (1973-74)), in Fig. (4.8). There is general agreement between the database rainfall totals and the measurements over the map area. A notable feature in the database rainfall is the representation of orographic rains giving high rainfall over the Alps and the Norwegian mountains. The relatively low rainfall totals over the sea are also consistent with the fact that orographic and convective processes are limited in areas of open sea. The realistic representation of rainfall over the sea therefore gives confidence in the reliability of the interpolation procedure which is used for completing synoptic data fields over the full European map area.

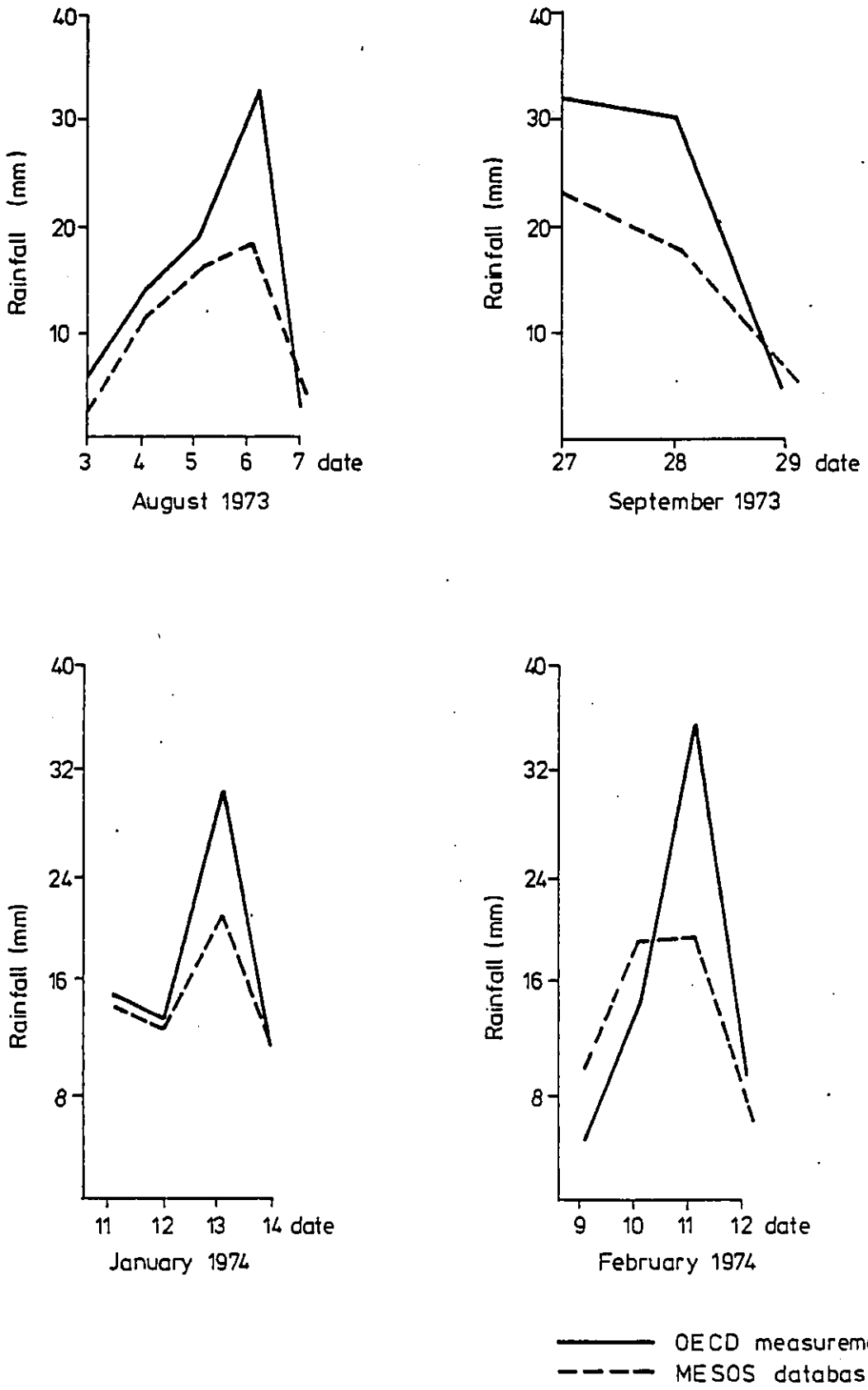
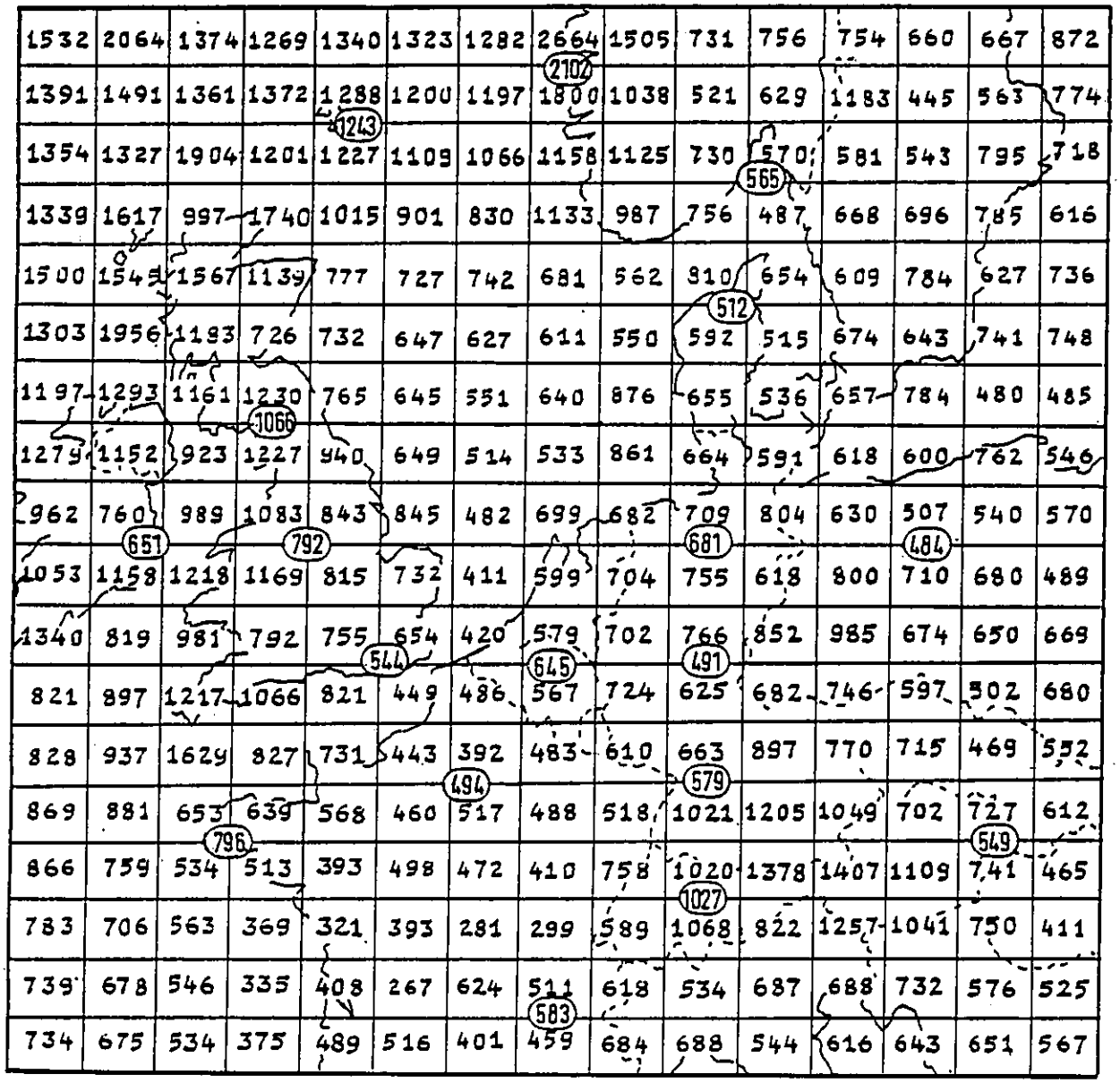



Figure (4.7) Comparison of Rainfall Episodes from the 1973 Database with Measurements at OECD Sites in Norway (taken from Maul (1980))




Total rainfall from weather stations (WMO (1973-74))

Figure (4.8) Comparison of Total Rainfall from the 1973 Database with Corresponding Totals Measured at European Weather Stations

## 4.7 Summary

Methods have been developed to process routine meteorological data, reported from land stations and ships, into a form which is suitable for use in long-range dispersion models such as MESOS. A large database of relevant meteorological data has been established for the European map area. The information includes synoptic pressure fields, rainfall, cloud cover and temperature; these data are available at three-hour intervals for most of 1973 and, more recently, throughout 1976.

It is believed that the databases contain a comprehensive selection of meteorological conditions, thus providing a suitable basis for the statistical study of unplanned and planned releases from European sites.

# CHAPTER 5 ASSESSMENT OF THE DISPERSION CHARACTERISTICS OF PLANNED AND UNPLANNED NOTIONAL RELEASES FROM MOL DURING 1973

## 5.1 Introduction

The aim of this Chapter is to illustrate the application of the MESOS model and meteorological database in the assessment of the long-range dispersion of planned and unplanned releases from nuclear installations. Dispersion calculations are presented and discussed for notional releases of a selection of nuclides from Mol, a site located in Belgium.

The derivation of the dispersion and exposure calculations using MESOS and the database is described in Section (5.2). The methods are generally applicable and are used in all the MESOS site investigations.

The sequence of trajectories, initiated at three-hourly intervals throughout the 1973 database period, is used to identify the most frequently exposed regions remote from Mol (Section (5.3)). Frequency distributions are developed to show the chances of different levels of nuclide exposure at remote receptors due to unplanned releases from Mol. The frequency distributions of exposure are discussed in relation to release duration, dispersion characteristics and receptor location. Episodes which lead to relatively high levels of contamination are analysed in an attempt to determine the most unfavourable dispersion conditions (Section (5.4)).

Annual average patterns of air and ground contamination, resulting from continuous nuclide releases, are finally presented in Section (5.5). These are discussed in relation to recurring synoptic features in the pressure field and nuclide depletion characteristics during atmospheric transport.

## 5.2 Operational Methods

The MESOS model and meteorological databases have been described in

Chapters 2 and 4 respectively. This section outlines the way in which MESOS and the database are interfaced to generate a series of dispersion calculations relating to nuclide releases from a given site. The derivation of the associated patterns of exposure and statistical information on levels of exposure is also described.

The basic dispersion and exposure calculations are generated in two separate stages. In the first stage, MESOS is used with the database to generate a sequence of puff histories throughout the period under consideration. These puff histories describe the atmospheric transport of material released into the boundary layer, and are used in the second stage calculations to derive patterns of exposure over the area of interest. The two stage calculation procedure reduces the main MESOS computer runs to reasonable proportions, and also allows useful information on source meteorology and puff histories to be archived, in an easily accessible form, onto magnetic tape. The organisation of the MESOS computer runs is shown in Table (5.1).

### 5.2.1 Derivation of Puff Histories

Time dependent meteorology is used from the database to calculate the dispersion histories of puffs released at three-hourly intervals from the source. The puff histories describe the trajectories, vertical and lateral spread, and removal by dry and wet deposition of material released into the boundary layer.

Puff development is followed in a Lagrangian manner for four days or until trajectories leave the map. Therefore, it may be necessary to have five consecutive days of meteorological data to be able to process each three-hourly release fully on any particular day. Gaps in the sequence of meteorological data mean that releases during certain days cannot be considered. Releases on a given day are only processed when there is a complete sequence of meteorological data for at least four consecutive days. Experience has shown that this is the period in which the vast majority of trajectories leave the European map. Hence, 253 days of releases from Mol were processed from a total of 272 days of meteorological data in the 1973 database. The sequence of data in

| Stage 1: Puff histories at regular three-hourly intervals | | | Stage 2: Nuclide exposure calculations | |
|---|---|---|---|---|
| Pollutant | Deposition velocity ($cms^{-1}$) | Washout coefficient ($s^{-1}$) | Application | Nuclide half life |
| A | 0.3 | $5\ 10^{-5}\ J^{0.8}$ | I131(P) | 8.1 days |
| B | 0.3 | $1.5\ 10^{-5}\ J^{0.8}$ | I131(G) | 8.1 days |
| C | 0.1 | $1.5\ 10^{-5}\ J^{0.8}$ | Cs137 | 28 years |
| D | 0 | 0 | Kr85 | 10 years |
| | | | Xe133 | 5.3 days |
| | | | Xe135 | 9.1 hours |

**Input data:** meteorological database
source location

**Output data:**

(1) Source meteorology: windspeed and direction
Pasquill category
mixing layer height

(2) Trajectories and development of mixing layer

(3) At each time step along trajectory:
Airborne fluxes (pollutants A, B, C, D)
Dry depositions (pollutants A, B, C)
Wet depositions (pollutants A, B, C)

**Archiving:** All puff histories and source meteorology

**Input data:** puff histories from Stage 1
radial grid system

**Output data:**

(1) Time integrated air concentrations for all nuclides

(2) Dry and wet depositions for I131(P), I131(G), Cs137

**Archiving:** Exposures over complete grid system for daily releases
Exposures at 16 receptors for three-hourly releases

Table (5.1) Organisation of the MESOS Dispersion Calculations

the 1976 database is more complete and this allows 360 days to be treated in the dispersion calculations.

Source meteorology is archived during the puff history calculations to give the initial windspeed and direction, Pasquill category and depth of mixing layer for each three-hourly release. This data is useful for checking the reliability of the meteorological database, since it can be compared with any available site observations. Winds and Pasquill categories derived from the database have been compared with observations from Mol and other sites (ApSimon et al (1980)). A typical comparison of wind direction frequencies for Mol during 1973 is shown in Figure (5.1). In this particular comparison, the MESOS 10m wind directions have an additional backing relative to the 69m winds measured at Mol. In general, there is reasonable agreement between the frequency of observed winds and winds derived from the MESOS database, allowing for topographical effects which are not modelled.

The selection of nuclides considered in the MESOS calculations is shown in Table (5.1). Radioactive decay is not included in the puff history calculations because it can be easily incorporated into the second stage exposure computations. This is because the puff histories specify airborne fluxes and ground depositions explicitly in terms of travel time from source. The puff history calculations relate to four pollutant species (A-D), each with different deposition characteristics. The deposition velocity and washout coefficient for each of these pollutants are chosen so that each pollutant can be associated with a nuclide, or set of nuclides, when radioactive decay is introduced into the exposure calculations. For example, puff histories calculated for pollutant (D), which has zero deposition velocity and washout coefficient, are subsequently used in the second stage calculations to derive exposures for the three inert nuclides Kr85, Xe133 and Xe135, each with a different half life. This method of calculating exposures considerably reduces the computer time and storage requirements.

The depositing nuclides I131 and Cs137 are also considered in the MESOS calculations. Two separate forms of I131 are treated: gaseous I131(G) and particulate I131(P), each of which has the same dry deposition

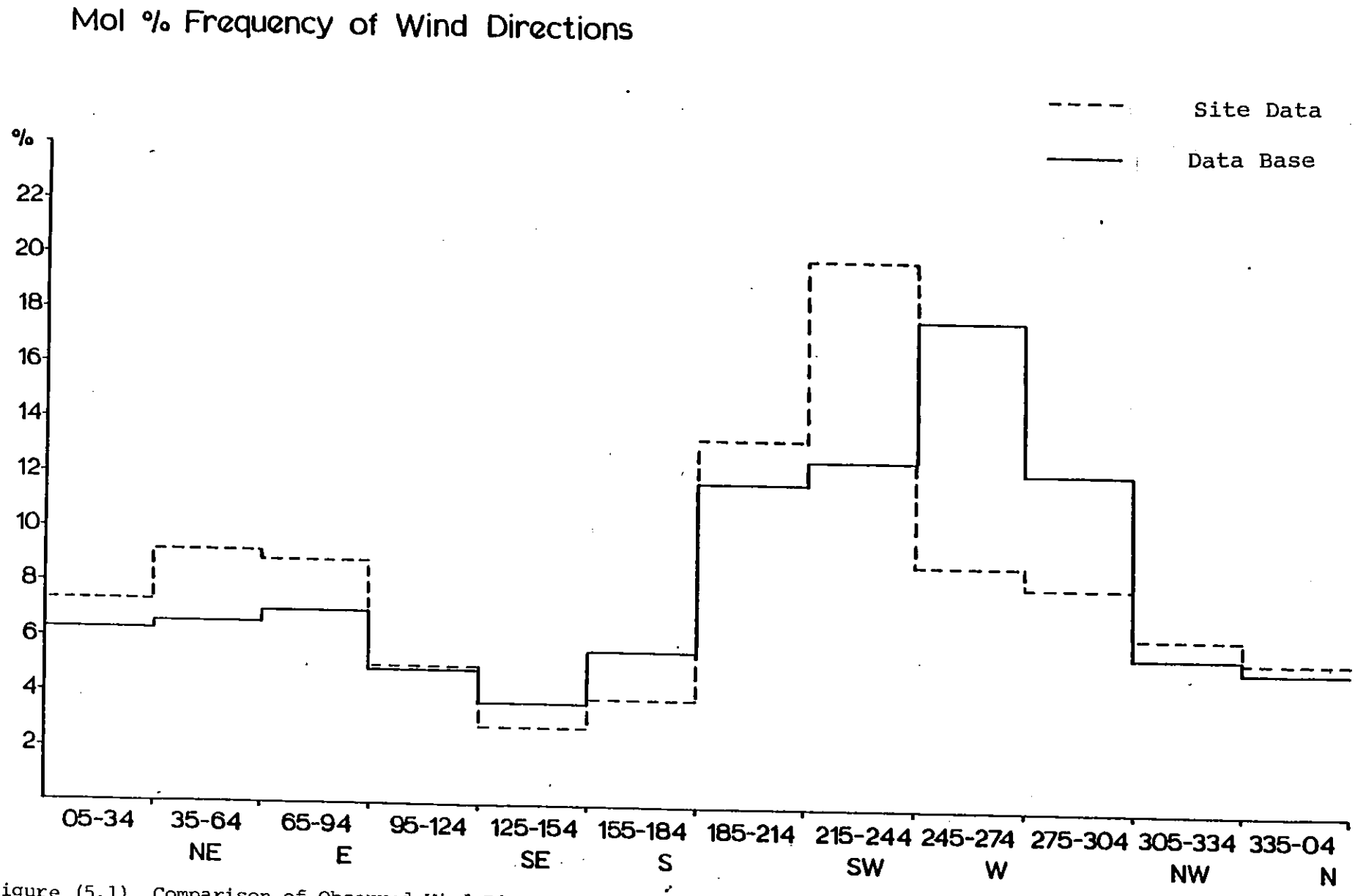



Figure (5.1) Comparison of Observed Wind Direction Frequencies at Mol (1973) with Winds Derived from the MESOS Database

velocity and half life. However, particulate 1131 is believed to be more easily removed by precipitation scavenging and is therefore given a higher washout coefficient (Chamberlain (1980)).

### 5.2.2 Treatment of Exposures

Time integrated air concentrations are generated in the second stage calculations for each of the nuclides shown in Table (5.1). Dry and wet depositions are also considered for the nuclides I131(P), I131(G) and Cs137. These exposures are calculated at each point in a suitable grid system. A site-orientated radial grid system is used so that the distance and directional variations in exposure can be more easily assessed and compared between different sites. The Mol radial grid system is shown in Figure (5.2).

Radial grid construction is the same for each site. The grid system is defined by the spacing of grid points along 64 directions of constant bearing from the site. The distance between grid points gradually increases along the 16 principal directions (N, NNE, NE, ENE, E... etc.). In the first 100 km from the site, grid points are spaced at 10 km intervals; 25 km intervals are used between 100 km and 200 km, and grid points are spaced at 100 km intervals beyond 200 km. Extra grid points, with 100 km spacing, are introduced along 48 intermediate directions to increase the density of grid points in the outer regions of the map area.

Puff histories are used to derive exposures resulting from a three-hourly unit release (1 Curie) of each nuclide. The exposures are calculated at every radial grid point for each three-hourly release during the period under consideration. This processing can produce a substantial amount of information. For example, there are 2,024 three-hourly release periods in the 1973 database, 667 grid points in the Mol radial grid system and 12 different modes of nuclide exposure. This represents over 16 million numbers which have to be processed just for one site. In order to reduce the storage requirement, three-hourly exposure maps are summed to give daily exposure maps. These are then archived, in chronological order, onto magnetic tape.

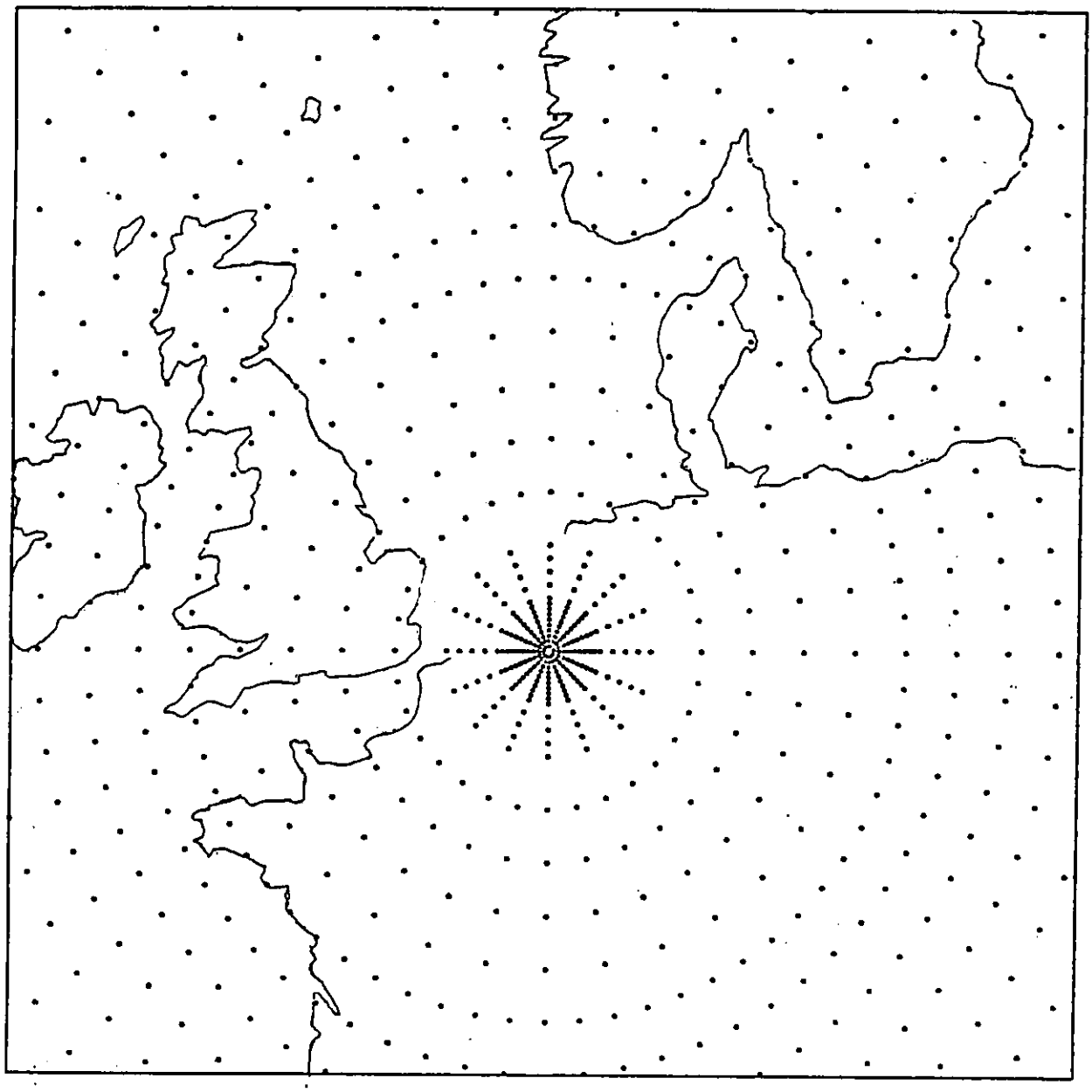


Figure (5.2) Radial Grid System for Mol

However, three-hourly releases are of particular interest for the development of statistics on the exposures resulting from unplanned releases. Consequently, three-hourly exposures at a chosen subset of grid points (usually 16 grid points) are also archived, in chronological order, onto the same magnetic tape. This archiving means that the following statistics on unplanned releases can be considered:

(i) Release durations which are multiples of three hours: all modes of exposure at 16 chosen grid points.

(ii) Release durations which are multiples of 24 hours: all modes of exposure at all grid points (complete exposure maps).

Patterns of exposures for long-term continuous releases are easily simulated by considering the cumulative effect of exposures from daily releases. Individual nuclide exposure maps are summed over the chosen period and then renormalised to represent exposures per Curie of nuclide released. Annual average exposures are developed in this manner (Section 5.5). This treatment of sequential exposures also means that an arbitrary time dependent release rate can be considered over the release period without any increase in the computational requirement (e.g. the release patterns used in the Windscale study, Chapter 3). However, since the site investigations in this and the following Chapter relate to notional releases, all the results are normalised to represent a total of 1 Curie released over the appropriate release period. This also allows direct comparison between results for different sites and different release durations.

## 5.3 Long-Range Transport

The regions most frequently affected by the long-range transport of notional releases from Mol during 1973 are identified in this section. The frequency or probability of exposure of a particular receptor depends on the number of trajectories which pass nearby the receptor. The movement of successive trajectories, initiated at regular three-hourly intervals from Mol, is described with reference to typical

features which occur in the synoptic pressure field. The trajectory analysis is then used to discuss the spatial variations in the probability of exposure over the European map area.

### 5.3.1 Trajectory Analysis

The methods used in the trajectory analysis are the same for each MESOS site investigation. The bearings where trajectories cross circles of given radii (usually 100, 300, 500 and 750 km), centred on the site, are extracted from the three-hourly puff history records. The number of trajectories crossing 10° sectors of each circle are then counted and are used to produce a trajectory rose for the site. Trajectories are only counted once as they first cross each circle; returning trajectories are considered in Section (5.3.2).

The Mol trajectory rose for 1973 is shown in Figure (5.3), and includes 2,024 trajectories, initiated at three-hourly intervals throughout the period covered by the 1973 database. The distribution of trajectories crossing the inner circle (100 km) is similar to the wind rose at Mol which is shown in Figure (5.1). However, the initial site wind rose becomes less relevant as trajectories move further away from Mol. The trajectory distributions at 300, 500 and 750 km show increasing distortion and reflect the meandering of trajectories under the influence of synoptic pressure systems. This trajectory meandering demonstrates certain systematic characteristics which are represented by the trajectory clustering and divergence in the directional distributions.

#### (i) Influence of the Alpine barrier

The most noticeable divergence in the trajectory distributions occurs to the south-east of Mol over a region which corresponds to the location of the Alps. Although the effects of topography are not explicitly modelled in MESOS, it seems that the influence of the Alps is

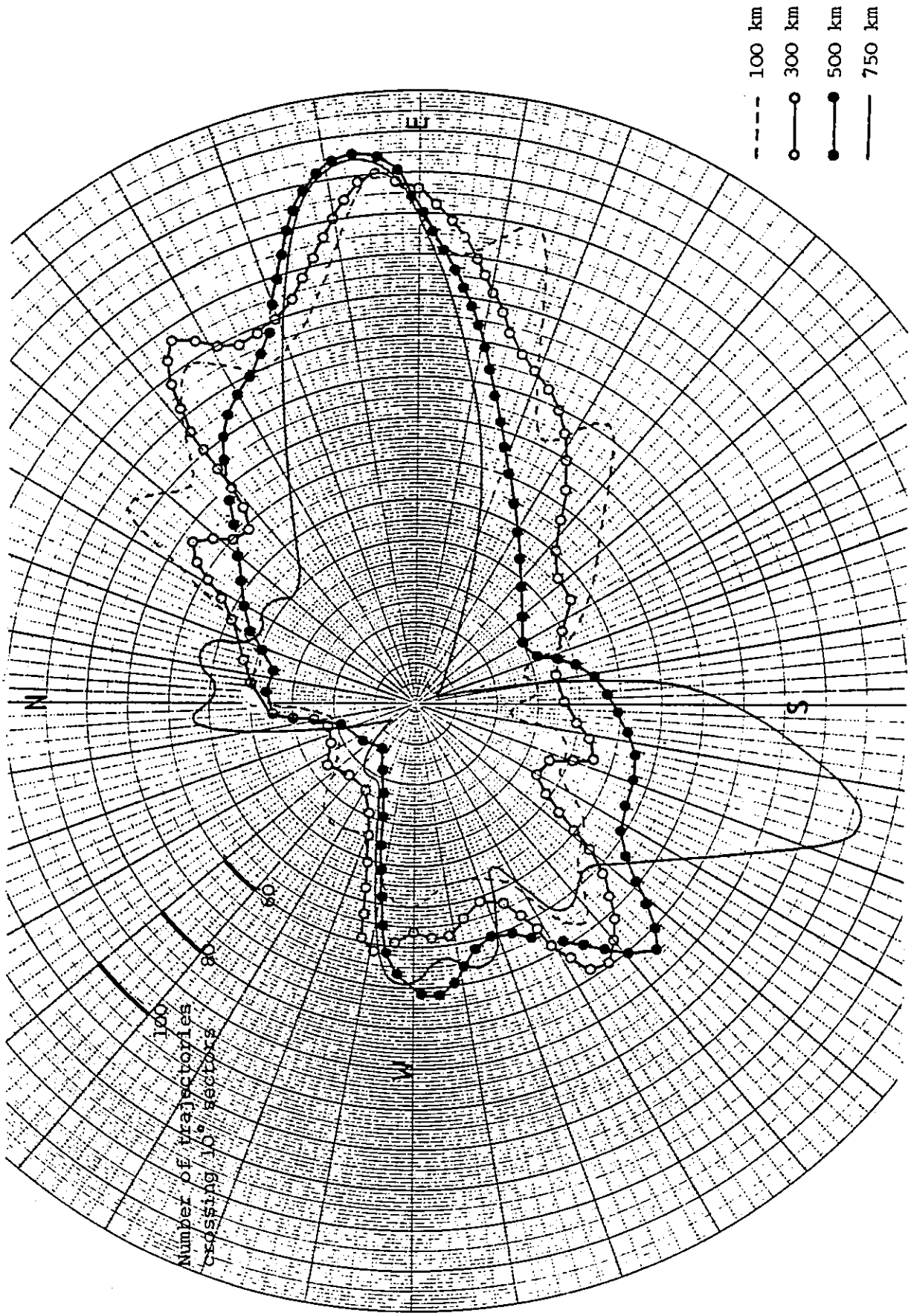



Figure (5.3) Trajectory Rose for Mol (1973)

shown through the use of real synoptic pressure data from the meteorological database.

The influence of the Alpine barrier on the synoptic pressure field is known to cause the formation of deep depressions over Northern Italy and the Mediterranean Sea. Localised depressions are also often established in the lee of the Alps, particularly in the Genoa region. Available knowledge on the formation and frequency of depressions near the Alps has been reviewed by Speranza (1975). The most favourable conditions for the formation of such depressions is a north-westerly frontal flow in which the Alps act as a barrier to the motion of cold air masses from the north. Consequently, the conditions in which pollution is advected towards the Alps, from North European sources, are likely to coincide with the presence of depressions near the Alps. Trajectories heading towards the Alps are frequently deflected over Southern France under the geostrophic control of the depressions near the Alps. This effect is clearly shown in the trajectory analysis for Mol and other European sites which are considered in Chapter 6.

(ii) Other influences

A divergence in the trajectories also occurs in a direction to the north-west of Mol. Trajectories leaving Mol in this direction are either deflected over the North Sea towards Norway or are forced over Central and Southern England. It is difficult to give completely rigorous explanations of this effect, but it is possible that the frequent location of high pressure systems over Scandanavia, and the typical eastwards movement of depressions across the British Isles are the primary cause. In the former case, trajectories would have an anticyclonic curvature over the North Sea. In the latter situation, it is likely that the direction of the trajectory path would change significantly as the depression progressed eastwards.

In an independent long-range trajectory analysis, Smith (1980) has proposed that trajectories are subject to a gradual rotational motion due to the eastward movement of depressions. Smith showed that trajec-

tories tend to converge in an easterly direction relative to the point of release. The trajectory analysis for Mol only gives a slight suggestion of this effect, and it is likely that trajectory analysis over greater distances (∿2,000 km) is necessary before this small but systematic motion can be clearly recognised.

### 5.3.2 Probability of Exposure

The number of trajectories which pass over a region is relevant to the frequency with which the region is exposed from continuous releases at a remote site. Lateral dispersion of material between successive trajectories during transit is also important and both these aspects are discussed in relation to the spatial variations in the probability of exposure.

The probability of air contamination due to successive continuous releases over 24-hourly periods is shown in Figure (5.4a). This is the shortest release duration for which exposures are known over the complete map area; the effect of release duration on probability of exposure will be discussed in Section (5.4.5).

#### (i) Pathways to exposures

Although all exposure incidents, however small, are included in Figure (5.4a), it is interesting to note the relatively high probability with which exposure can occur. For example, there is approximately a 50% chance of some air contamination at receptors 100 km to the east of Mol and, on average, there is about 33% probability for all directions 100 km away from Mol. If it is assumed that trajectories leave the map directly, this would imply that material would have an average angular spread of 120° at 100 km.

However, an angular spread of between 30°-60° is typical at 100 km for 24-hourly releases (Smith (1980)). The reason for the relatively high probabilities of exposure in the MESOS calculations is that trajectories seldom leave the map directly and are often found to travel

large distances over the map area before returning to give indirect exposure at receptor points.

To demonstrate this fact, trajectory characteristics are shown in Figure (5.5) at the time of exposure of two different receptors 100 km away from Mol. Frequency distributions are given for the following parameters:

(a) travel time, t, between source (Mol) and the receptor.

(b) lateral spread of material at the receptor, as represented by the separation S , between the two trajectories spanning the release, at the time of peak exposure:

$$S = |\underline{x}(T_1,t) - \underline{x}(T_2,t)|$$

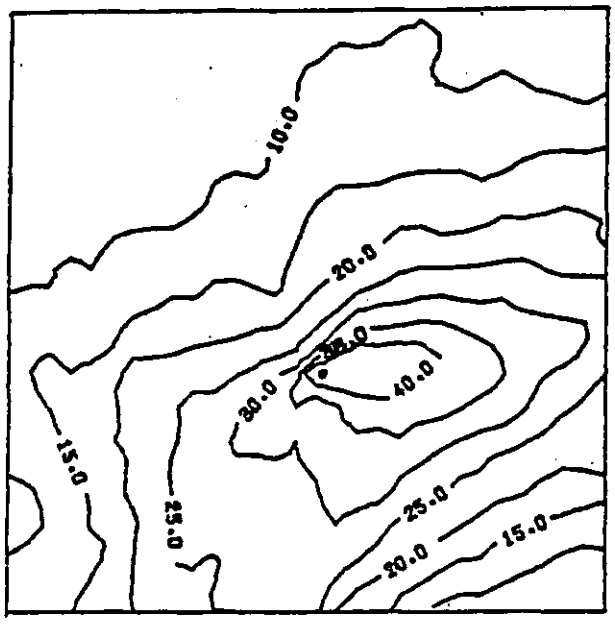
(c) the curvature or "tortuosity" factor $\kappa$ of the first trajectory, defined by:

$$\kappa = \frac{\ell}{r} = \frac{\overline{u}t}{r}$$

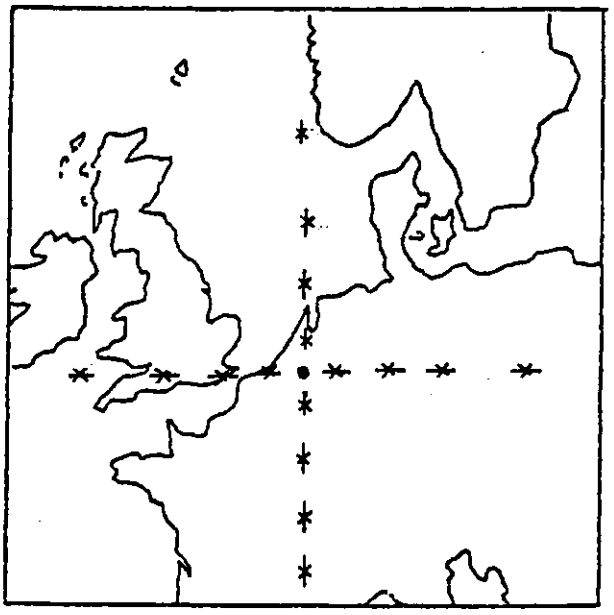
where $\ell$ is the trajectory length and r is the distance of the receptor from source.

The frequency distributions are shown for trajectory pairs initiated at three-hourly intervals because this gives the largest sample size for exposures. The frequencies of fairly direct trajectory paths ($\kappa \sim 1$) between source and receptor is closely related to the wind direction frequencies at Mol. This is also reflected in the relative frequencies of short travel times to each point. However, there is a relatively slow tail-off in each frequency distribution which indicates that long trajectories and travel times between source and receptor occur quite often. Lateral dispersion is likely to be considerable in such circumstances and this will substantially increase the chances of a receptor point being exposed via an indirect pathway from the source.

In general, up to 50% of exposure incidents at receptors in the MESOS calculations can be attributed to indirect trajectory paths between source and receptor. In Section (5.4) it will be shown that the majority




(a) Probability (%) of air contamination



(c) Database map area and Mol receptors




(b) Probability (%) of wet deposition

Figure (5.4) Probability of Air Contamination and Wet Deposition due to Daily Releases from Mol during 1973

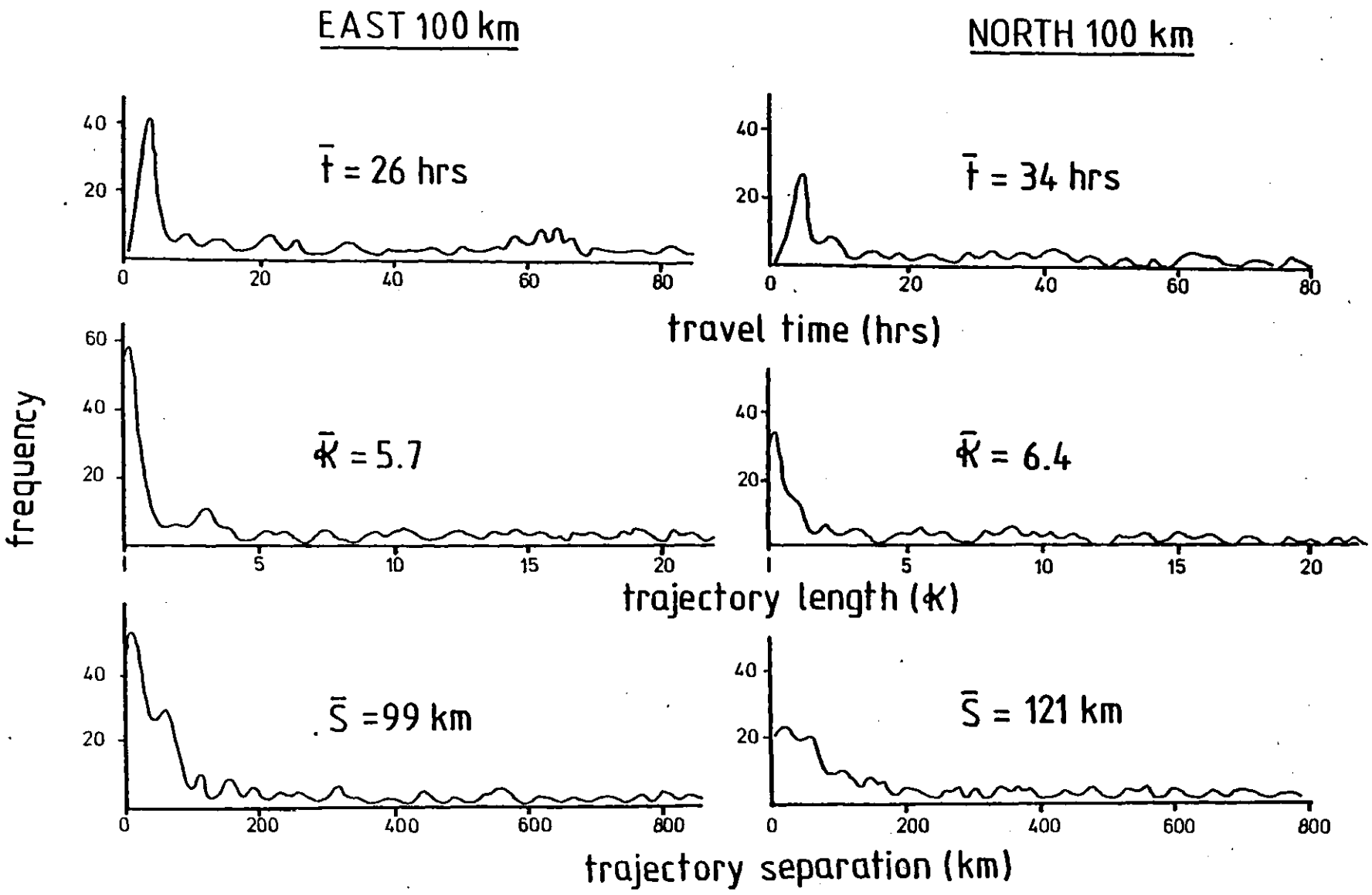



Figure (5.5) Trajectory Characteristics at the Time of Receptor Exposure

of these exposure incidents give relatively low levels of exposure, particularly for rapidly decaying nuclides such as Xe135.

(ii) Variation of probability of exposure with distance from source

The probability of exposure generally decreases with increasing distance from source. This is because the separation and lateral dispersion between successive trajectories tends to increase at a slower rate than the distance travelled. Correlations relating the separation S, between successive trajectories, to the distance travelled can be developed by considering the statistical properties of a large number of trajectories (e.g. Durst et al (1959), Smith (1980)). In principle, these correlations may then be combined with frequency distributions of wind direction at source, to estimate the probability of exposure at remote receptors. However, this approach was found to be of limited use in the present study because of the following complications associated with curved trajectories:

(a) The contribution of second pass exposures at receptors after material has circulated around the map area.

(b) The systematic influences of the synoptic pressure field, causing areas of trajectory divergence and convergence.

The latter effect is illustrated by the influence of depressions on trajectories heading towards the Alps. Probability of exposure drops rapidly across the Alps, but trajectories moving around the Alps lead to a considerable area with relatively constant probability of exposure over Central and Southern France. Similarly, the probability of air contamination decreases rapidly with distance to the north-west of Mol, due to trajectory divergence in this direction. The wide spectrum of pathways to exposure and systematic trajectory meandering combine to produce a rather complex pattern of air contamination probabilities which is difficult to simulate from simple considerations of wind direction frequencies at Mol and averaged characteristics of lateral dispersion.

(iii) Probability of wet deposition

The probability of wet deposition [1] over the map area is shown in Figure (5.4b) for daily continuous releases from Mol.

Wet deposition occurs less often than air contamination because it is necessary that precipitation occurs during the period in which the region is exposed. Consequently, the frequency of wet deposition is strongly dependent on the wetness characteristics of the transporting air masses. Westerlies are not only the most frequent winds at Mol, but are also the wettest. Easterlies, on the other hand, are relatively dry because they are often associated with anticyclonic conditions. The occurrence of wet deposition is thus strongly biased towards the east of Mol, and this is reflected in the patterns of annual average wet deposition presented in Section (5.5).

## 5.4 Exposure from Unplanned Releases

The long-range dispersion of an unplanned release of nuclides may lead to the exposure of a considerable area away from the site. The level of exposure received at a receptor will depend on the prevailing meteorological conditions at the time of the release. By simulating the dispersion of notional releases over a long period, it is possible to develop useful statistical information on the probability that a given level of exposure will not be exceeded at a fixed receptor away from the site.

Frequency distributions which show the chances of different levels of exposure due to notional releases from Mol during 1973 have been derived from the MESOS dispersion calculations (Section (5.2)). In this section, frequency distributions of exposure are presented and discussed in relation to the following:

---

[1] The probability of wet deposition should be interpreted as an upper limit because of the treatment of rainfall as an average over a region in the database.

- receptor location
- nuclide deposition and natural decay rates
- mode of exposure (i.e. time integrated air concentrations, dry and wet depositions)
- release duration

The levels of exposure at remote receptors due to three-hourly releases from Mol are considered first.

### 5.4.1 Exposure Frequency Distributions for Three-Hourly Releases

Frequency distributions of different levels of contamination resulting from three-hourly, 1 Curie releases of a selection of nuclides, are shown in Figures (5.6) to (5.9). The number of releases which subsequently lead to given levels of exposure at the 16 chosen receptors, shown in Figure (5.4), are given in the form of histograms. Logarithmic intervals of exposure are used and are such that exposures may vary by a factor of about three in each exposure interval. The exposures relate to time integrated air concentrations of I131(P), Kr85 and Xe135. Levels of wet deposition are also shown for I131(P) in Figure (5.9).

The natural decay and deposition rates of each of these nuclides are summarised in Table (5.2). An indication of effective nuclide half lives during atmospheric transport is also given in Table (5.2). The effective half life for the depositing nuclide I131(P) is of order two days in dry trajectories (for an average mixing depth of 1,000 m), but can be as short as 4 hours when heavy rainfall ($\sim$5 mm/hr) occurs continuously during transit.

The probability of exposure determines the sample size in each histogram; 2,024 possible exposures can occur at each receptor for three-hourly releases using the 1973 database. Spatial variations in the probability of exposure have been discussed in Section (5.3.2), and these are reflected in the histograms. For example, the greatest probability of air contamination occurs to the east of Mol because of the prevailing Westerlies and this leads to a sample size of about 350 exposure incidents at 100 km to the east of Mol. The sample size for

the wet deposition histograms is considerably smaller because rain only occurs for a fraction (≈10%) of the time.

| Nuclide | Deposition Velocity $cm\,s^{-1}$ | Washout Coefficient $s^{-1}$ | Half life due to natural decay | Effective half life during transport |
|---|---|---|---|---|
| I131(P) | 0.3 | $5\,10^{-5}J^{0.8}$ | 8.1 days | ≈4 hours* / ≈2 days† |
| Kr85 | 0 | 0 | 10 years | 10 years |
| Xe135 | 0 | 0 | 9.1 hours | 9.1 hours |

* Heavy rainfall

† no rainfall

Table (5.2) Depletion Rates for Nuclides

## 5.4.2 Consideration of the Exposure Frequency Distributions

The histograms presented in Figures (5.6) to (5.9) show that exposures can range over several orders of magnitude at a given receptor, due to the large variety of dispersion conditions which can occur between the source and receptor. Certain notable features appear in the histograms. For example, many of the histograms are skew with the most probable exposure being within one or two orders of magnitude of the maximum exposure. The histograms for Kr85 exposures are contained within a smaller range than the histograms for I131(P) and Xe135 at corresponding receptors. The Xe135 histograms have the greatest spread and also show that bimodalities can occur in the histograms for rapidly depleting nuclides. This section attempts to explain why such features exist in the histograms and how these are related to the dispersion conditions and nuclide depletion rates between source and receptor.

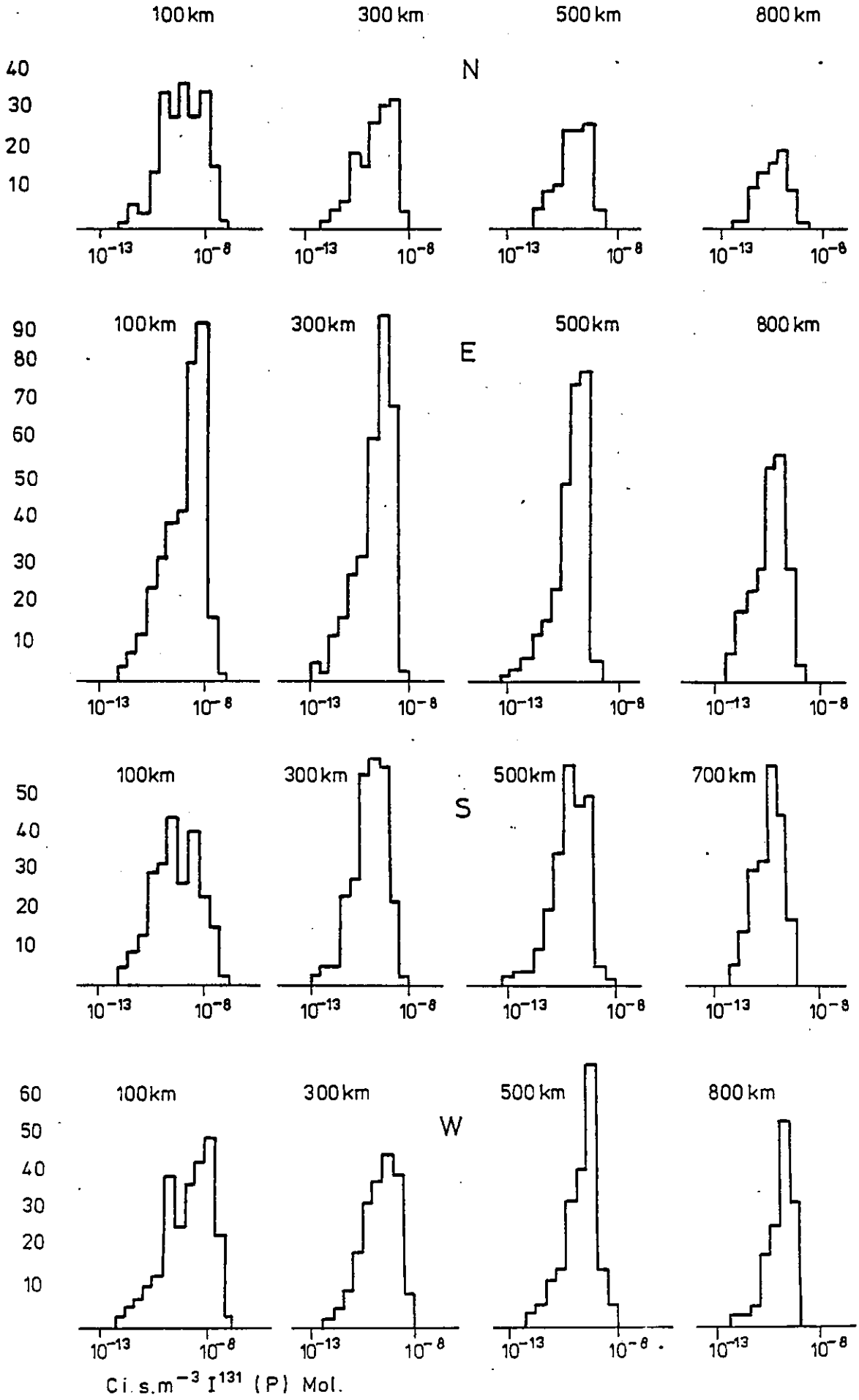



Figure (5.6) Histograms for Time Integrated Air Concentrations due to Three-Hourly Releases of I131(P) from Mol during 1973

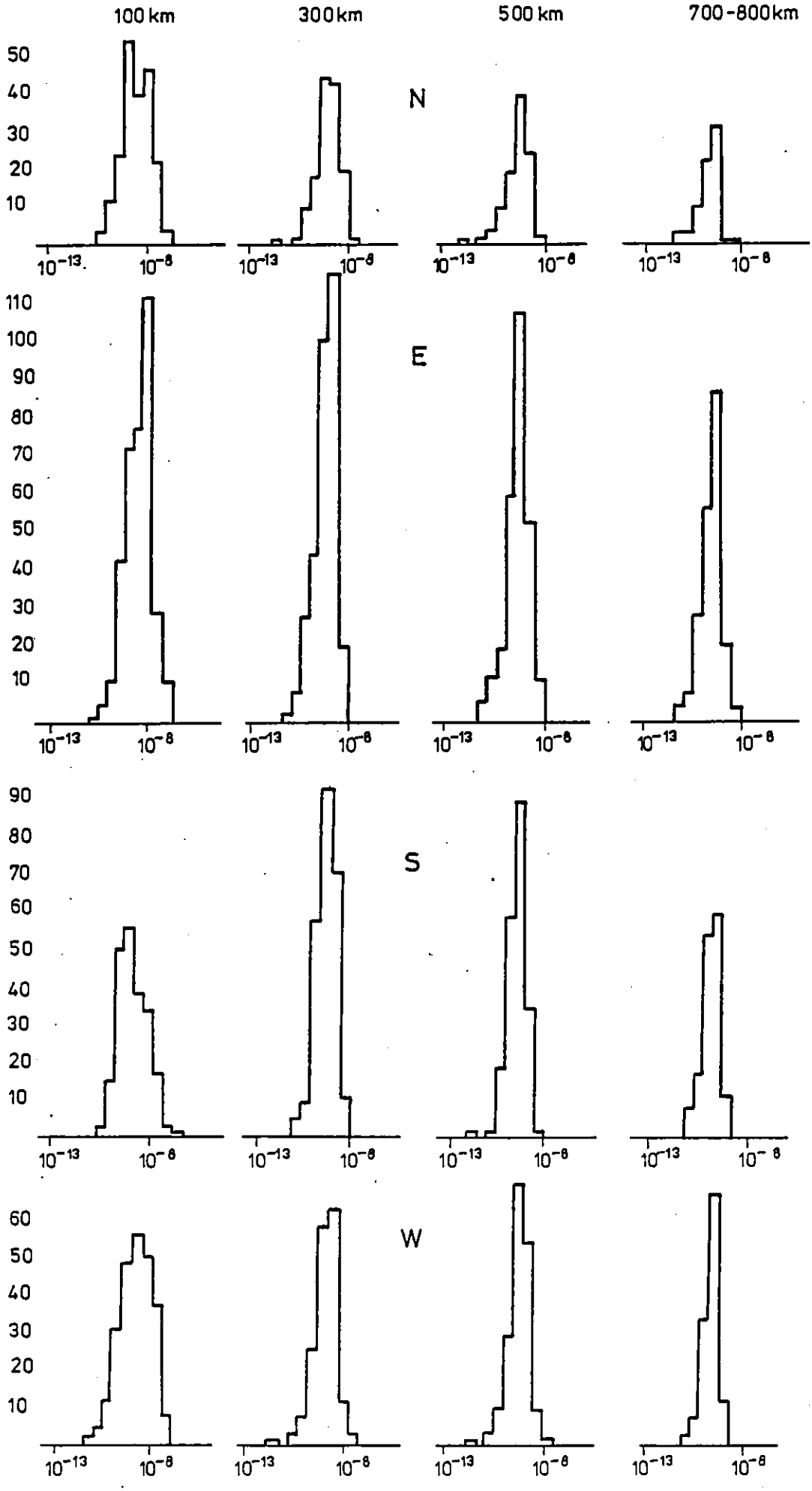



Figure (5.7) Histograms for Time Integrated Air Concentrations due to Three-Hourly Releases of Kr85 from Mol during 1973

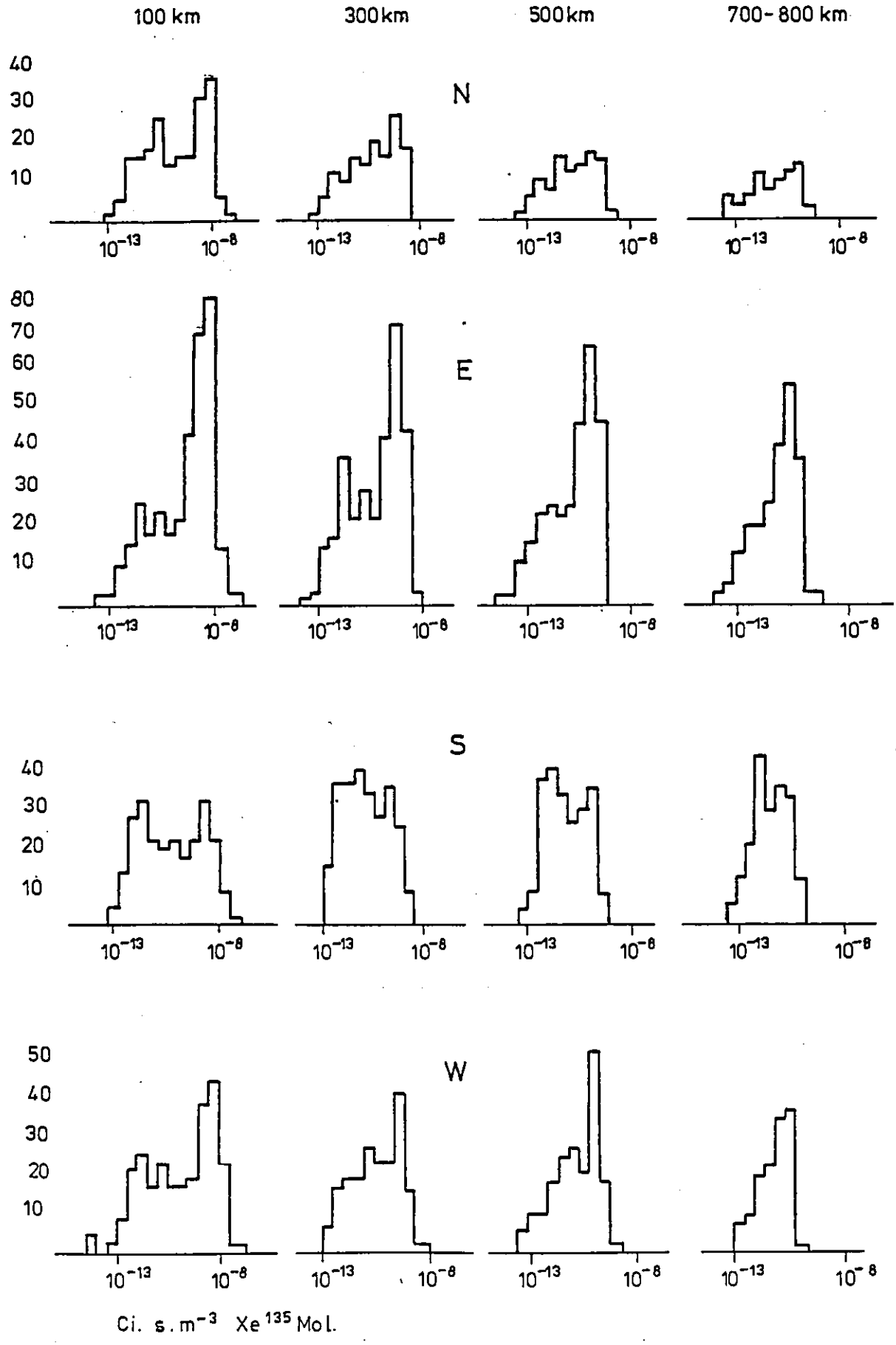



Figure (5.8) Histograms for Time Integrated Air Concentrations due to Three-Hourly Releases of Xe135 from Mol during 1973

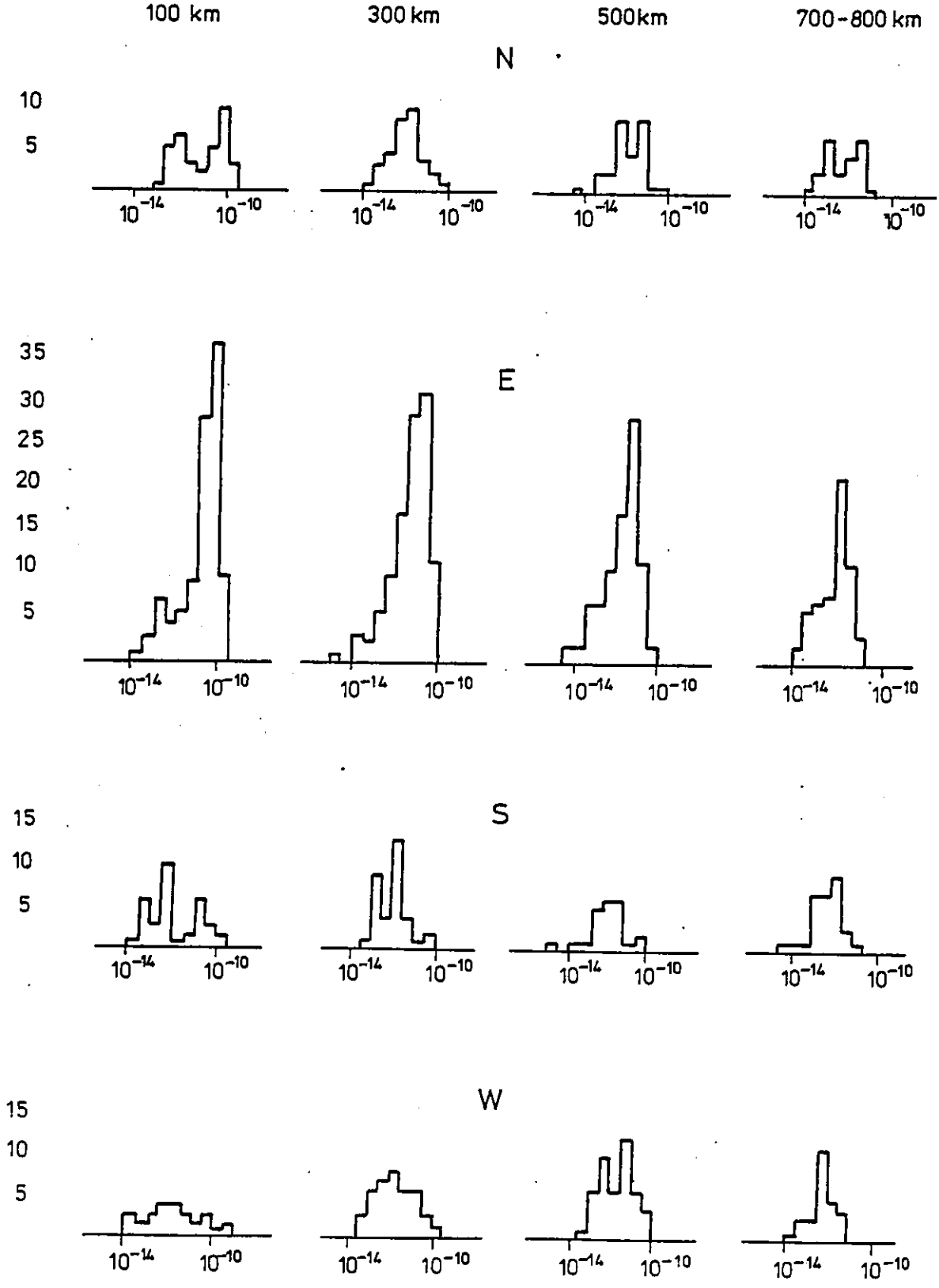



Figure (5.9) Histograms for Wet Depositions due to Three-Hourly Releases of I131(P) from Mol during 1973

(i) Correlation of exposures with nuclide depletion rate and time of travel between source and receptor

The time integrated air concentration $(TINC)_N$ resulting from the passage of a nuclide N over a given receptor after travel time t from the site of release can by approximated by:

$$(TINC)_N \simeq (S\bar{u}h_{max})_t^{-1} \exp - \bar{\lambda}_N^* t \qquad \text{where:}$$

$$\bar{\lambda}_N^* = \frac{1}{t} \int_0^t \left(\frac{V_N}{h} + \Lambda_N^* J^{0.8}\right) d\tau + \lambda_N \,, \qquad \ldots (5.1)$$

is the average depletion rate due to natural decay, dry deposition and possible washout during transit.

Dry and wet deposition per unit area at the receptor can be obtained by multiplying $(TINC)_N$ by the appropriate nuclide deposition velocity and washout coefficient respectively.

Individual exposure incidents at two different receptors, 100 km from Mol, are plotted with time of travel in the form of scatter diagrams (Figure (5.10)). Time integrated air concentrations are shown for the nuclides I131(P), Kr85 and Xe135. Time of travel is chosen as the independent variable because it enters directly into the depletion process and also, to a lesser extent, into the dispersion parameters S, $h_{max}$ and $\bar{u}$.

The correlation of $(TINC)_N$ with depletion rate is clearly shown in the scatter diagrams. For the inert nuclide Kr85, with half life of ten years, there is effectively no depletion mechanism for the range of travel times which are considered. Levels of TINC for Kr85 are effectively determined by the lateral and vertical spread and the windspeed at the time of exposure. Although lateral and vertical spread generally increase with travel time between source and receptor, Kr85 TINCs are only weakly correlated with time of travel. The Kr85 scatter diagrams indicate that the parameter $(S\bar{u}h_{max})_t$ can vary over about two orders of magnitude for any given travel time. Natural decay is the only depletion process for Xe135, but this nuclide has a very short half life of

nine hours. Since all nuclides experience the same dispersion history between source and receptor, the distributions of Xe135 and Kr85 TINCs are the same apart from a factor of exp - $(\lambda_{Xe135} - \lambda_{Kr85})t$ for each exposure incident in the scatter diagrams. Although this connection does not necessarily hold for I131(P), due to variable depletion from dry and wet deposition during transit, the average depletion rate of I131(P) is generally intermediate between that of Kr85 and Xe135.

(ii) Direct and indirect exposures

The scatter diagrams in Figure (5.10) show that all travel times, ranging from a few hours to a few days, are possible before the receptors are exposed. Travel time distributions relating to these two receptors were discussed in Section (5.3.2). Trajectory length distributions were also presented to show that many of the exposure incidents occur after several hundred kilometres of travel before trajectories return to expose the receptors only 100 km away from source. Lateral dispersion will probably be considerable in such circumstances and all points near the source are likely to be exposed by the same release. However, it was shown that the frequency of short travel times to a receptor was sensitive to the location of the receptor and reflected the wind direction frequencies at the source.

Consequently, exposure incidents in the scatter diagrams can be broadly classified with either direct ($\kappa \sim 1$) or indirect ($\kappa >> 1$) pathways to the receptors. Direct exposure incidents, with relatively short travel times, tend to give the highest levels of exposure and the frequency of such incidents is strongly related to the receptor position. For example, there are about twice as many direct exposures at 100 km to the east of Mol than there are to the north of Mol, due to the prevailing Westerlies. However, the frequency of the indirect exposure episodes associated with long travel times is comparable for both receptors. The levels of exposure associated with long travel times are sensitive to the nuclide depletion rate, but are less sensitive for shorter travel times. Similar features are apparent in the scatter diagrams for receptors at 800 km from Mol (Figure (5.11)), but transport over the longer distances means that direct travel takes longer

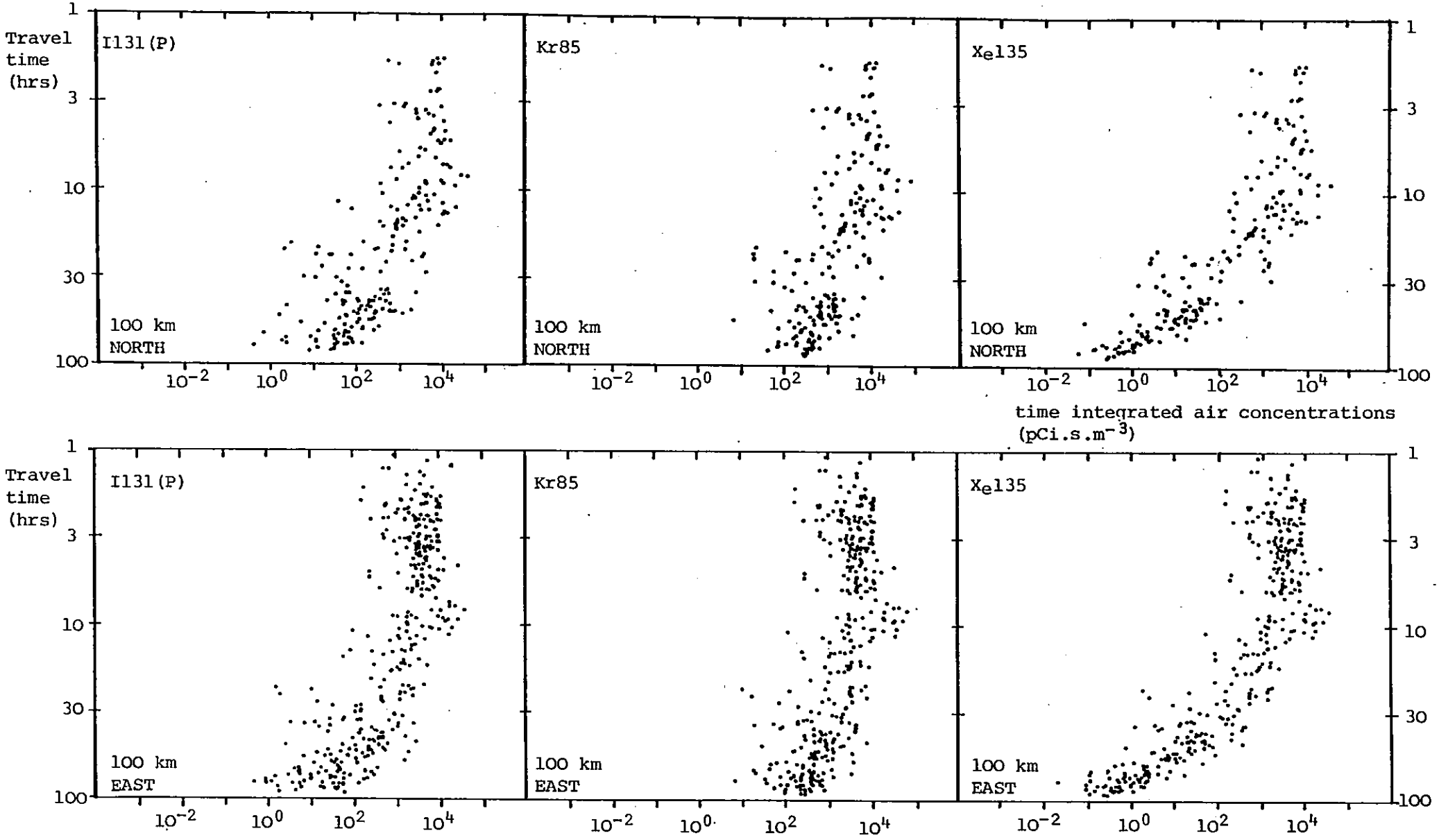



Figure (5.10) Scatter Diagrams for Nuclide Exposures at 100 km Receptors

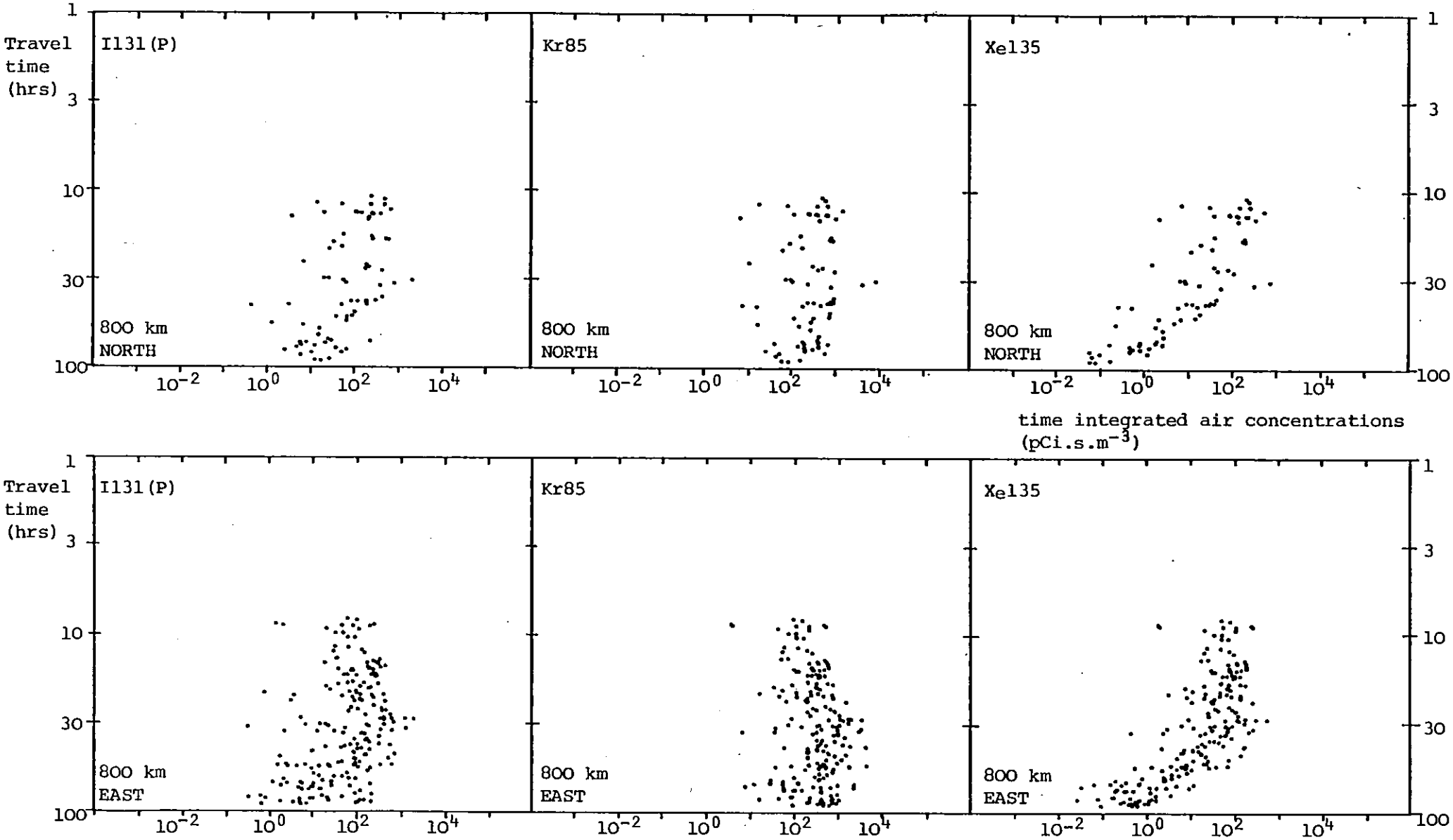



Figure (5.11) Scatter Diagrams for Nuclide Exposures at 800 km Receptors

(∿1 day) and the associated exposures are correspondingly lower.

The scatter diagrams in Figures (5.10) and (5.11) are useful for understanding why the different forms of histograms arise. In a simple manner, it is convenient to interpret the histograms as being a composite of two different exposure distributions; one relating to direct transport regimes and the other corresponding to indirect transport regimes.

(a) The direct exposure distribution is relatively insensitive to the nuclide depletion rate because the exposures are associated with relatively short travel times between source and receptor. However, the level of exposure and the number of exposure incidents in this distribution are sensitive to receptor location.

(b) The lower indirect exposure distribution is sensitive to the nuclide depletion rate because the exposures are associated with long travel times between source and receptor. However, the number of exposure incidents in this distribution is relatively insensitive to receptor location.

For histograms at a given receptor, increasing the nuclide depletion rate effectively separates the indirect exposure distribution from the direct exposure distribution. This is the reason why bimodalities occur in the Xe135 histograms but exposures in the Kr85 histograms are contained within a relatively small range. Conversely, for a given nuclide, increasing the receptor distance from source produces lower levels of exposure in the direct exposure distribution and the two distributions merge to give a typically skew frequency distribution. For example, bimodalities in the Xe135 histograms tend to disappear with increasing receptor distance from source. Since the depletion rate of I131(P) is usually less than that of Xe135 but greater than that of Kr85, the histograms for I131(P) are of intermediate form. These aspects of the frequency distributions are also seen in the following section when the distributions are represented in cumulative form.

### 5.4.3 Representation of the Exposure Frequency Distributions

The representation of exposure frequency distributions in terms of concise mathematical expressions is of considerable interest. This allows the distributions to be easily derived and the sensitivity of the distributions to the controlling parameters can be more readily assessed. There are two main approaches to this treatment and these are discussed separately in relation to the present work.

(i) Mathematical formulation from first principles

Time integrated air concentrations and ground depositions can be expressed in terms of dispersion parameters and nuclide depletion rates (e.g. Equation (5.1)). In principle, it is then possible to combine the frequency distributions of each parameter in the expression to derive the required exposure frequency distribution. The main difficulty is specifying the frequency distribution of the dispersion parameters and in general these parameters are not independent. For example, lateral spread S, vertical spread $h_{max}$ windspeed $\bar{u}$ and travel time t, are probably related to some extent for each exposure incident.

An alternative approach is to attempt to represent all the dispersion parameters in terms of one variable (e.g. $\bar{u}$ or t) for which the frequency distribution is known with reasonable confidence. Attempts to formulate a simple model have been described by Scriven (1980) and ApSimon et al (1980a). Unfortunately, the problem is complicated even when the simplest assumptions are used to specify lateral and vertical spread. Moreover, the scatter diagrams shown in Figures (5.10) and (5.11) suggest that representation of exposure in terms of a single parameter cannot adequately describe all exposure incidents. Atmospheric dispersion has an important stochastic component which is difficult to treat in a simple mathematical model of the exposure frequency distributions. For example, the windspeed at the time of exposure may in general be comparable to the average windspeed during transit, but this may not always be the case. These aspects of dispersion are clearly illustrated in the study of episodes which lead to relatively high contamination (Section (5.4.4)).

(ii) Empirical representations of exposure frequency distributions

Standard probability distributions may be fitted to either measured or calculated concentration data to give an empirical representation. The mostcommonly used distribution for fitting air concentration data is the Lognormal distribution, originally proposed by Larsen (1969). Several other probability distributions have been proposed in the literature and Pollack (1975) has assessed the applications of the Normal, Gamma, Pearsonand Weibull distributions.

The Weibull distribution (Weibull (1951)) has been found to be the most useful distribution for representing the MESOS exposure frequency distributions. The Weibull distribution takes a particularly simple form:

$$pr(D>d) = \exp - \left(\frac{d}{d_o}\right)^{\beta} \qquad \ldots (5.2)$$

The main advantage of this distribution is that it is flexible and can approximate other standard distributions by varying the shape parameter $\beta$ and the location parameter $d_o$ (Steiger (1971)). Weibull distributions have been fitted to all the exposure frequency distributions for Mol and examples are shown in Figures (5.12) and (5.13). In these examples, I131(P), Kr85 and Xe135 time integrated concentrations are plotted individually on a Weibull cumulative probability scale to examine the goodness of fit and, if appropriate, determine the parameters $\beta$ and $d_o$ (Gumbel (1958)).

The Weibull distribution has been found to be appropriate for slowly depleting nuclides (e.g. Kr85) and the fit generally improves for all nuclide exposures at increasing distances from source. The shape parameter $\beta$ is of order 0.8 for the Kr85 distributions and the location parameter $d_o$ is closely related to the average exposure at the receptor (Section (5.4.5)). Time integrated Xe135 air concentrations are the least amenable to a single fit with a simple distribution and the bimodal nature of the Xe135 distribution is clearly evident on the Weibull probability scale. The Weibull plots are therefore consistent with the discussion on the composite nature of the exposure frequency distributions (Section (5.4.2)).

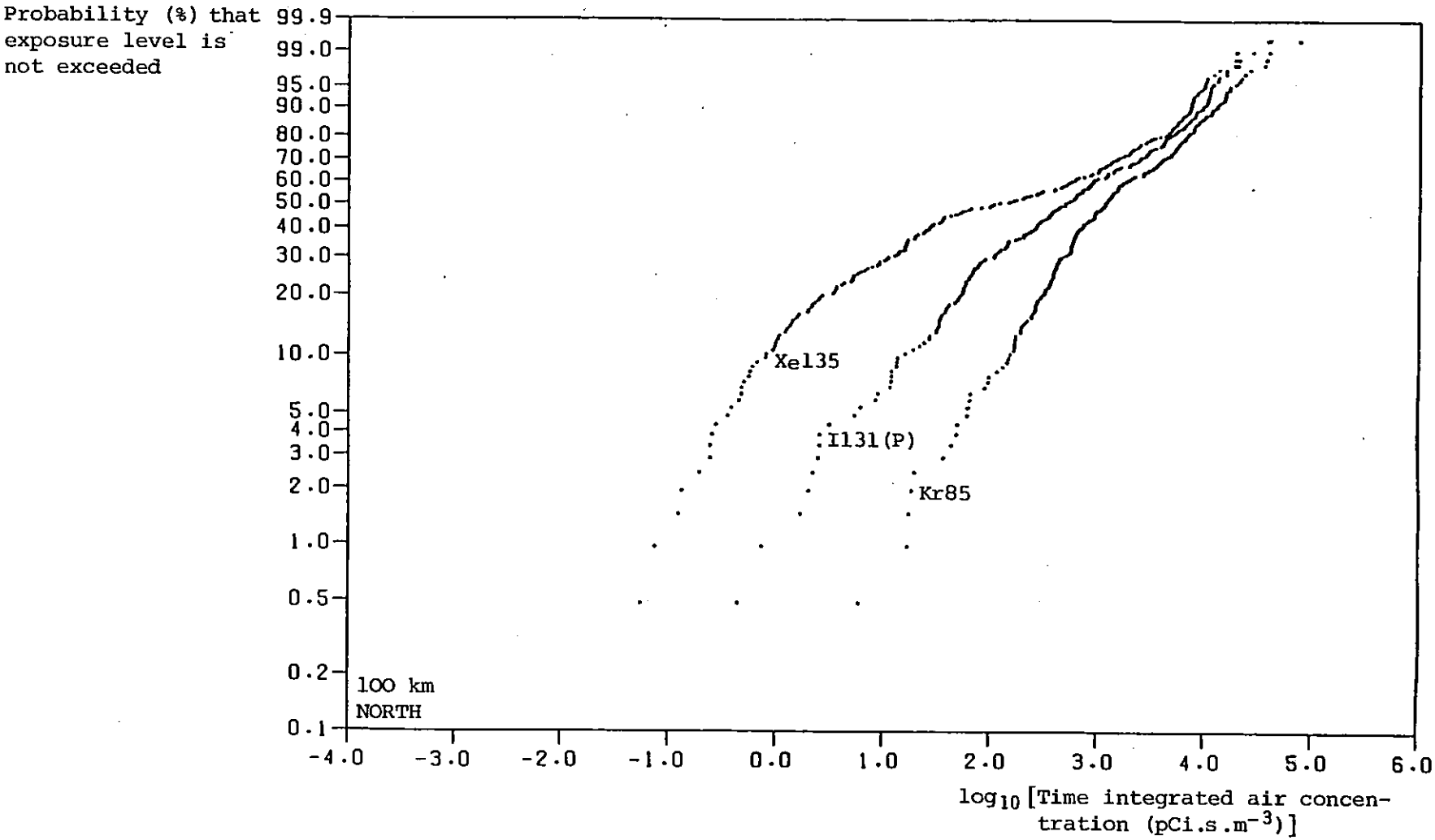



Figure (5.12) Cumulative Frequency Distributions of Nuclide Exposures at the 100 km North Receptor due to Three-Hourly Releases

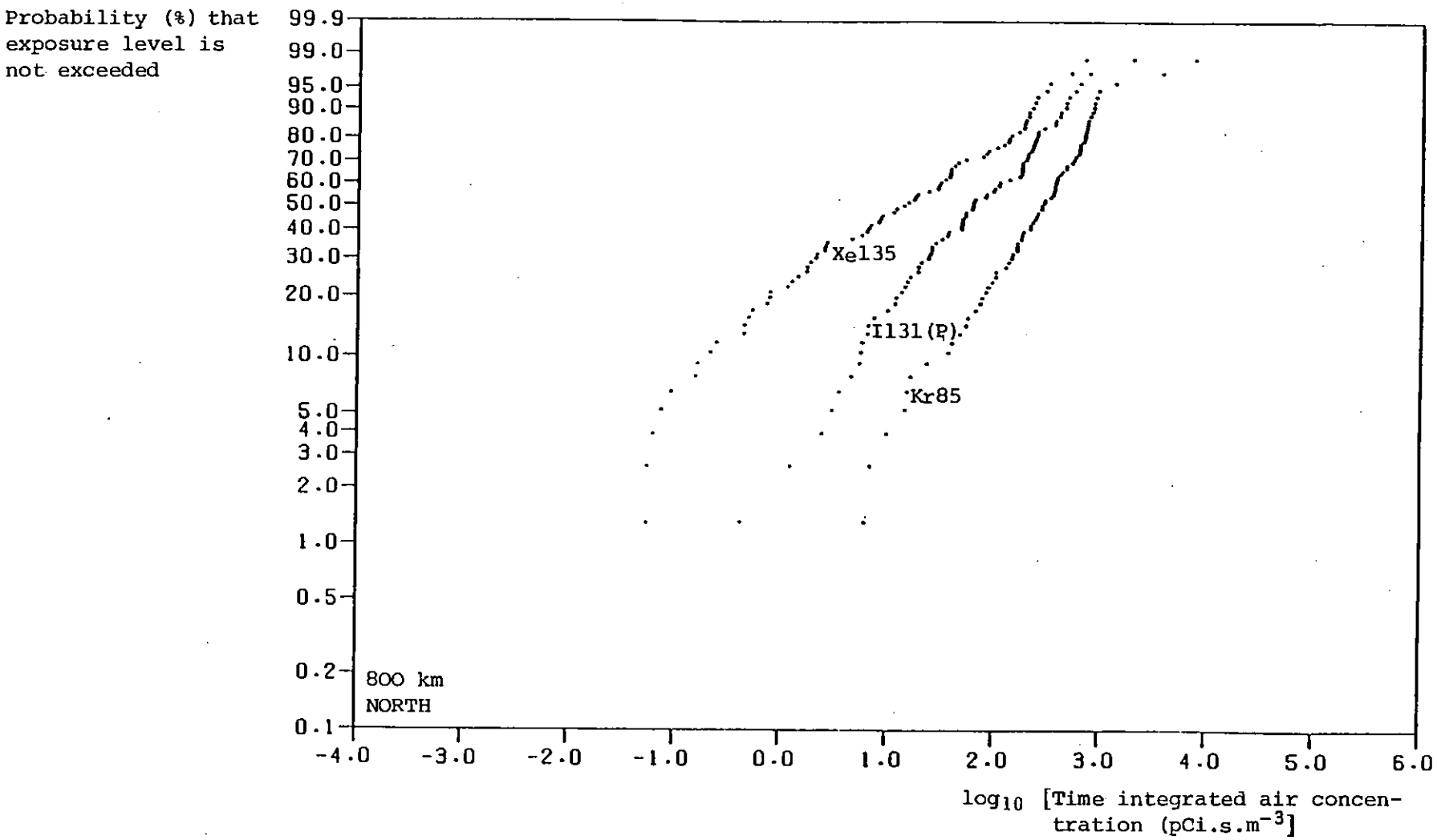



Figure (5.13) Cumulative Frequency Distributions of Nuclide Exposures at the 800 km North Receptor due to Three-Hourly Releases

Fitting a probability distribution to MESOS exposure calculations is also useful for assessing the overall consistency of the calculations since statistical outliers may be identified. For example, it can be seen that the Weibull fit is excellent for the Kr85 exposures at 800 km north of Mol, apart from two very high exposures (Figure (5.13)). These exposures have been identified to originate from the same dispersion episode on the 26th October 1973. This episode will be considered in detail in Section (5.4.4) and it is shown that these exposures coincided with high $SO_2$ air concentrations monitored at OECD sites near the 800 km North receptor.

### 5.4.4 Episodes Leading to Relatively High Exposures

The meteorological conditions and dispersion characteristics which lead to relatively high exposures at remote receptors are discussed in this section. A summary of the dispersion characteristics of three-hourly releases from Mol which subsequently lead to the eight highest I131(P), Kr85 and Xe135 time integrated concentrations at the 100 km and 800 km receptors during 1973, is given in Tables (5.3) and (5.4) respectively. These episodes relate to exposures in the upper percentiles of the frequency distributions and have a corresponding low probability (0.4%) of occurrence.

For receptors relatively close to source (e.g. 100 km), the same dispersion episodes tend to produce high levels of exposure from all nuclides. However, this is not necessarily the case for receptors at 800 km, and nuclide depletion rates are more important for defining the worst episodes. In general, the episodes with relatively short travel times are more likely to produce the highest levels of exposure at 800 km for rapidly depleting nuclides such as Xe135.

Many of the episodes giving high exposures close to source are associated with slow transport in anticyclonic conditions during the late Summer and Autumn of 1973. Average windspeeds during transit are of order $3 m.s^{-1}$ and in several episodes the windspeed drops at the time of passage over the receptor, thus giving relatively long exposure times at the receptor. Relatively slow transport episodes are also

prominent in the Kr85 exposures futher away from source, but less so for the depleting nuclides I131(P) and Xe135.

The time of release is important for episodes giving high exposure at receptors close to source. Evening and night-time releases are a notable feature of the episodes in Table (5.3). Material released after dusk can travel slowly in stable night-time conditions with limited vertical dispersion, and easily reach 100 km before dawn. In several episodes, the time of release and subsequent travel time are such that material reaches the receptor just before dawn. Windspeeds and vertical dispersion are both minimal in such conditions, and this results in large exposures at the receptor.

Time of release is not very important for exposures at 800 km, because stable conditions are likely to break up during transit. Vertical dispersion is generally 1,000 m or more by the time material reaches the 800 km receptors since travel times involve at least one diurnal cycle of convective mixing. However, from Table (5.4) it can be seen that vertical dispersion can be as low as 400 m for transport over the North Sea to the 800 km North receptor. Lower mixing depths generally occur over the sea because convective and mechanical mixing processes are limited.

An interesting feature of many of the episodes, both at 100 km and 800 km, is that the lateral spread S, between trajectories spanning the release, is much less than the small-scale diffusive spread B of individual puffs. In some cases the lateral spread S is less than 10 km even at the 800 km receptors. In many of the episodes, trajectories follow very similar paths because the synoptic pressure field remains virtually stationary during the release duration. Moreover, in some cases, episodes occur in succession over periods in which stationary anticyclones persist in the synoptic pressure field. Unfavourable dispersion conditions in stationary synoptic fields are illustrated by the following episodes.

(i) Releases from Mol during the period 4th - 11th September 1973

Releases during the period 4th September (day 247) to the 11th September (day 254) resulted in the highest exposures at the 100 km receptors to

| Receptor | Largest TICs at receptor ($10^4$ pCi s $m^{-3}$) $Kr^{85}$ | $I^{131}$ | $Xe^{135}$ | Episode Release Time Day | Time | Travel time to receptor t (hrs) | Puff Width B (km) | Puff Separation S (km) | Windspeed ($m\ s^{-1}$) $\bar{U}_t$ | $\bar{U}$ | Vertical Dispersion $h_{max}$ (m) |
|---|---|---|---|---|---|---|---|---|---|---|---|
| N100 | 7.5 | 3.9 | 3.8 | 247 | 15-18 | 9.0 | 40 | 7 | 5.7 | 4.6 | 300 |
| | 3.9 | 2.1 | 2.0 | 228 | 18-21 | 13.6 | 61 | 43 | 4.6 | 3.7 | 500 |
| | 3.7 | 2.8 | 1.9 | 178 | 0-3 | 8.9 | 40 | 32 | 0.9 | 3.3 | 900 |
| | 3.6 | 2.0 | 1.9 | 247 | 18-21 | 10.2 | 46 | 57 | 4.4 | 4.1 | 100 |
| | 2.6 | 1.4 | - | 266 | 0-3 | 14.7 | 66 | 79 | 1.1 | 3.1 | 600 |
| | 2.3 | - | - | 278 | 12-15 | 14.5 | 65 | 13 | 3.7 | 3.6 | 200 |
| | 2.2 | 1.3 | 1.2 | 178 | 18-21 | 7.8 | 35 | 35 | 3.2 | 3.6 | 300 |
| | 2.1 | 1.6 | 1.4 | 305 | 21-24 | 5.7 | 25 | 30 | 5.2 | 5.2 | 300 |
| | - | 1.6 | 1.1 | 306 | 3-6 | 8.1 | 36 | 8 | 3.7 | 5.0 | 600 |
| | - | - | 1.0 | 167 | 21-24 | 5.0 | 22 | 54 | 2.7 | 3.0 | 300 |
| E100 | 6.9 | 3.9 | 3.7 | 248 | 21-24 | 8.2 | 37 | 7 | 2.4 | 3.0 | 300 |
| | 5.5 | 2.8 | 2.7 | 248 | 15-18 | 9.3 | 42 | 25 | 2.7 | 1.9 | 200 |
| | 4.4 | 2.4 | 2.5 | 268 | 21-24 | 7.8 | 35 | 29 | 3.2 | 3.7 | 100 |
| | 3.9 | 2.0 | 1.8 | 214 | 18-21 | 10.4 | 47 | 26 | 4.2 | 3.7 | 300 |
| | 3.6 | 1.7 | - | 248 | 18-21 | 11.4 | 51 | 9 | 3.0 | 2.8 | 300 |
| | 3.6 | - | 1.8 | 34 | 15-18 | 9.3 | 42 | 54 | 2.8 | 3.1 | 100 |
| | 3.4 | 2.8 | 2.4 | 215 | 0-3 | 4.6 | 21 | 14 | 4.1 | 4.4 | 100 |
| | 3.3 | 1.8 | 1.9 | 268 | 18-21 | 7.8 | 35 | 31 | 4.0 | 4.5 | 100 |
| | - | 1.7 | - | 279 | 21-24 | 7.4 | 33 | 9 | 5.5 | 5.1 | 600 |
| | - | - | 1.6 | 34 | 18-21 | 9.5 | 43 | 67 | 3.2 | 3.3 | 100 |
| S100 | 10.0 | 7.6 | 7.2 | 254 | 0-3 | 4.5 | 20 | 5 | 4.1 | 4.4 | 100 |
| | 4.2 | 2.4 | 1.3 | 229 | 12-15 | 19.3 | 87 | 34 | 1.0 | 1.4 | 1300 |
| | 3.9 | 3.3 | 2.8 | 252 | 18-21 | 4.5 | 20 | 7 | 5.1 | 5.2 | 500 |
| | 3.2 | 2.2 | 1.8 | 240 | 21-24 | 7.4 | 33 | 15 | 3.5 | 4.0 | 300 |
| | 2.8 | 2.0 | 1.6 | 240 | 18-21 | 7.4 | 33 | 11 | 5.2 | 4.3 | 600 |
| | 2.6 | 1.7 | 1.2 | 302 | 9-12 | 11.9 | 54 | 6 | 3.2 | 3.8 | 600 |
| | 2.1 | - | - | 261 | 0-3 | 12.9 | 58 | 24 | 3.2 | 2.9 | 500 |
| | 2.1 | 1.8 | 1.4 | 209 | 18-21 | 5.4 | 24 | 5 | 7.5 | 6.7 | 600 |
| | - | 1.5 | 1.3 | 209 | 21-24 | 3.3 | 15 | 2 | 6.7 | 7.2 | 700 |
| W100 | 7.3 | 4.2 | 4.1 | 251 | 18-21 | 7.7 | 34 | 39 | 3.7 | 4.8 | 300 |
| | 5.6 | 2.0 | 2.7 | 171 | 15-18 | 9.7 | 43 | 19 | 2.6 | 1.7 | 200 |
| | 5.2 | 4.0 | 3.0 | 212 | 15-18 | 7.4 | 33 | 22 | 5.9 | 6.2 | 600 |
| | 4.8 | 2.5 | 2.7 | 238 | 18-21 | 8.4 | 38 | 44 | 3.0 | 4.7 | 100 |
| | 4.4 | 2.2 | 2.3 | 251 | 21-24 | 8.8 | 50 | 25 | 2.1 | 3.2 | 200 |
| | 4.3 | 2.4 | 2.2 | 222 | 18-21 | 10.4 | 47 | 7 | 3.6 | 3.1 | 200 |
| | 4.0 | 2.4 | 1.9 | 222 | 21-24 | 8.1 | 36 | 8 | 3.2 | 3.3 | 400 |
| | 3.4 | 2.7 | 2.1 | 277 | 12-15 | 6.3 | 28 | 32 | 8.4 | 8.3 | 400 |

Table (5.3) Episodes Leading to Relatively High Nuclide Exposures at the 100 km Receptors

| Receptor | Largest TICs at receptor ($10^2$ pCi s $m^{-3}$) $Kr^{85}$ | $I^{131}$ | $Xe^{135}$ | Episode Release Time Day | Time | Travel time to receptor $t$ (hrs) | Puff Width B (km) | Puff Separation S (km) | Windspeed (m $s^{-1}$) $\tilde{U}_t$ | $\bar{U}$ | Vertical Dispersion $h_{max}$ (m) |
|---|---|---|---|---|---|---|---|---|---|---|---|
| | 76.0 | 20.0 | 7.0 | 299 | 21-24 | 32.1 | 145 | 44 | 3.3 | 7.5 | 400 |
| | 38.0 | 7.7 | 3.0 | 299 | 18-21 | 33.5 | 151 | 135 | 8.3 | 8.5 | 800 |
| | 14.0 | 6.3 | 5.2 | 7 | 9-12 | 12.8 | 58 | 217 | 26.6 | 21.7 | 1900 |
| | 9.5 | - | 3.3 | 16 | 6-9 | 14.2 | 64 | 272 | 19.1 | 16.8 | 1700 |
| | 8.9 | - | - | 43 | 21-24 | 28.3 | 127 | 138 | 9.1 | 8.3 | 1000 |
| | 8.5 | 4.6 | - | 299 | 3-6 | 39.9 | 179 | 156 | 13.5 | 5.9 | 1000 |
| N800 | 8.4 | - | - | 298 | 21-24 | 42.0 | 189 | 122 | 11.3 | 4.7 | 400 |
| | 8.1 | 5.7 | - | 3 | 15-18 | 18.9 | 85 | 98 | 15.9 | 13.1 | 800 |
| | - | 4.9 | - | 3 | 18-21 | 18.8 | 84 | 67 | 15.7 | 12.0 | 1100 |
| | - | 4.6 | 2.4 | 5 | 9-12 | 11.2 | 50 | 105 | 21.6 | 22.6 | 2100 |
| | - | 4.6 | 2.5 | 46 | 3-6 | 12.0 | 54 | 53 | 21.0 | 20.0 | 1800 |
| | - | - | 2.2 | 6 | 0-3 | 13.6 | 61 | 86 | 25.0 | 18.1 | 1600 |
| | - | - | 2.0 | 7 | 6-9 | 10.8 | 49 | 17 | 17.9 | 20.7 | 1800 |
| | 43.0 | 6.3 | - | 266 | 21-24 | 53.9 | 243 | 14 | 1.0 | 4.1 | 900 |
| | 33.0 | 20.0 | 5.6 | 219 | 18-21 | 29.6 | 133 | 41 | 7.0 | 9.3 | 1600 |
| | 33.0 | 13.0 | 2.7 | 199 | 3-6 | 33.6 | 151 | 36 | 6.9 | 8.5 | 1300 |
| | 29.0 | 6.3 | 2.2 | 245 | 12-15 | 34.5 | 155 | 13 | 5.6 | 6.6 | 1100 |
| | 23.0 | - | - | 191 | 21-24 | 68.9 | 310 | 59 | 1.2 | 3.4 | 1100 |
| | 22.0 | - | - | 191 | 18-21 | 71.7 | 322 | 20 | 1.2 | 3.3 | 1100 |
| | 18.0 | - | - | 268 | 0-3 | 41.9 | 188 | 170 | 4.3 | 7.0 | 1300 |
| E800 | 17.0 | - | - | 267 | 3-6 | 54.2 | 244 | 25 | 1.7 | 4.8 | 1100 |
| | - | 13.0 | 3.1 | 219 | 15-18 | 29.5 | 133 | 69 | 4.0 | 8.4 | 1500 |
| | - | 7.3 | - | 219 | 6-9 | 46.9 | 211 | 120 | 7.7 | 6.4 | 1500 |
| | - | 6.9 | - | 199 | 6-9 | 31.0 | 139 | 61 | 6.8 | 8.2 | 1300 |
| | - | 6.3 | - | 24 | 21-24 | 29.5 | 133 | 103 | 6.2 | 8.0 | 1100 |
| | - | - | 2.8 | 96 | 9-12 | 23.6 | 106 | 21 | 9.1 | 10.4 | 1400 |
| | - | - | 2.7 | 237 | 12-15 | 8.9 | 40 | 22 | 33.9 | 25.8 | 2900 |
| | - | - | 2.4 | 316 | 21-24 | 8.7 | 39 | 60 | 26.9 | 26.3 | 2700 |
| | - | - | 1.9 | 313 | 9-12 | 14.9 | 67 | 68 | 16.9 | 15.7 | 1700 |

Table (5.4) Episodes Leading to Relatively High Nuclide Exposures at the 800 km Receptors

/Continued ...

| Receptor | Largest TICs at receptor ($10^2$ pCi s $m^{-3}$) $Kr^{85}$ | $I^{131}$ | $Xe^{135}$ | Episode Release Time Day | Time | Travel to Receptor t (hrs) | Puff Width B (km) | Puff Separation S (km) | Windspeed (m $s^{-1}$) $\bar{U}_t$ | $\bar{U}$ | Vertical Dispersion $h_{max}$ (m) |
|---|---|---|---|---|---|---|---|---|---|---|---|
| S700 | 20 | 8.5 | - | 240 | 15-18 | 42.2 | 190 | 114 | 8.0 | 5.5 | 1000 |
| | 15 | - | - | 229 | 18-21 | 62.7 | 282 | 161 | 3.0 | 2.6 | 1200 |
| | 14 | - | - | 152 | 6-9 | 27.8 | 170 | 55 | 6.1 | 6.2 | 1100 |
| | 14 | - | - | 228 | 9-12 | 19.7 | 359 | 33 | 1.5 | 3.2 | 1300 |
| | 14 | - | 2.2 | 108 | 0-3 | 24.6 | 111 | 22 | 9.4 | 9.2 | 1300 |
| | 14 | 4.8 | 2.7 | 108 | 3-6 | 21.9 | 99 | 21 | 8.6 | 8.8 | 1300 |
| | 12 | 6.5 | - | 230 | 9-12 | 50.2 | 255 | 33 | 2.7 | 2.9 | 1300 |
| | 12 | 6.6 | - | 230 | 6-9 | 52.0 | 234 | 5 | 3.1 | 2.9 | 1300 |
| | - | 6.1 | 1.8 | 100 | 12-15 | 20.0 | 90 | 311 | 12.3 | 11.7 | 1900 |
| | - | 5.1 | - | 208 | 9-12 | 34.3 | 154 | 23 | 9.0 | 6.4 | 1500 |
| | - | 4.7 | - | 229 | 18-21 | 62.7 | 282 | 164 | 3.0 | 2.6 | 1200 |
| | - | 4.4 | - | 229 | 3-6 | 79.3 | 357 | 41 | 3.2 | 2.7 | 1400 |
| | - | - | 1.7 | 110 | 0-3 | 21.0 | 95 | 42 | 10.2 | 9.3 | 1200 |
| | - | - | 1.6 | 289 | 21-24 | 25.3 | 114 | 4 | 8.9 | 7.5 | 1100 |
| | - | - | 1.4 | 152 | 15-18 | 26.7 | 120 | 38 | 6.4 | 6.6 | 1200 |
| | - | - | 1.2 | 93 | 6-9 | 10.7 | 48 | 68 | 26.0 | 22.0 | 2700 |
| | - | - | 1.1 | 207 | 15-18 | 23.3 | 105 | 116 | 10.5 | 10.1 | 1300 |
| W800 | 22 | 9.5 | - | 225 | 6-9 | 46.4 | 209 | 3 | 5.1 | 6.4 | 1000 |
| | 22 | - | - | 232 | 18-21 | 67.1 | 302 | 6 | 0.6 | 6.0 | 1300 |
| | 22 | 7.5 | 0.88 | 225 | 3-6 | 42.1 | 189 | 15 | 3.7 | 6.8 | 1300 |
| | 20 | 6.1 | - | 302 | 9-12 | 62.1 | 280 | 7 | 5.5 | 5.7 | 900 |
| | 19 | 3.4 | - | 235 | 9-12 | 44.3 | 200 | 3 | 6.4 | 5.5 | 700 |
| | 17 | - | - | 47 | 15-18 | 80.7 | 363 | 39 | 4.2 | 5.2 | 800 |
| | 14 | 9.1 | 1.1 | 250 | 9-12 | 34.1 | 153 | 12 | 7.9 | 6.7 | 1300 |
| | 13 | - | - | 232 | 3-6 | 72.4 | 317 | 29 | 1.6 | 5.0 | 1500 |
| | - | 5.9 | 0.89 | 224 | 18-21 | 22.9 | 153 | 11 | 6.4 | 7.4 | 1400 |
| | - | 5.3 | - | 250 | 12-15 | 37.5 | 169 | 12 | 6.6 | 6.6 | 1300 |
| | - | 5.3 | - | 226 | 6-9 | 49.0 | 220 | 136 | 2.3 | 5.7 | 1500 |
| | - | - | 1.3 | 276 | 0-3 | 20.2 | 91 | 71 | 15.1 | 11.8 | 1300 |
| | - | - | 0.98 | 113 | 21-24 | 21.0 | 94 | 123 | 13.1 | 11.2 | 1500 |
| | - | - | 0.97 | 223 | 18-21 | 31.9 | 140 | 20 | 6.8 | 7.6 | 700 |
| | - | - | 0.92 | 223 | 15-18 | 24.9 | 112 | 13 | 9.2 | 7.5 | 500 |
| | - | - | 0.84 | 223 | 21-24 | 31.1 | 140 | 62 | 6.8 | 7.5 | 1000 |

Table (5.4) continued

the north, east, south and west of Mol (Table (5.3)). Other large exposures occurred during this period at receptors close to source.

The development of the synoptic pressure field during this period is shown in Figure (5.14). The sequence of 0000 hr. pressure charts is given because the highest levels of exposure resulted from atmospheric transport in night-time conditions.

The slack pressure field over the Continent on the evening of 4th September gave very light southerly boundary layer winds in the Mol region, and the 100 km North receptor experienced two large exposures from successive releases in the evening. Although the pressure field remained slack during the 5th September, small high pressure cells developed over Northern France and three successive evening releases gave high exposures at the receptor 100 km to the east of Mol. Windspeeds during this period were only about 2 $m.s^{-1}$.

During the 6th, 7th and 8th September, an anticyclone persisted over Southern England and slow transport episodes gave high exposures at the receptors 100 km and 800 km to the west of Mol. The stationary anticyclone was temporarily disturbed by a cold front which moved south over the British Isles during the 9th September. Just before the front reached the Continent, a release from Mol lead to high levels of exposure at the 100 km South receptor. An anticyclone developed behind the front and remained stationary over Northern England for five successive days. During this period the highest levels of exposure occurred again at the 100 km South receptor.

The meteorological conditions and dispersion characteristics which occurred during this period are typical of episodes which lead to high exposures close to source in the MESOS calculations. The pressure field was stationary for long periods and the windspeeds in the anticyclonic conditions were very low. Stable conditions at night meant that vertical dispersion during transport was also minimal.

Although the importance of these meteorological conditions can be identified by an analysis of the MESOS dispersion calculations, it is recognised that there is some uncertainty in the predicted levels of time integrated

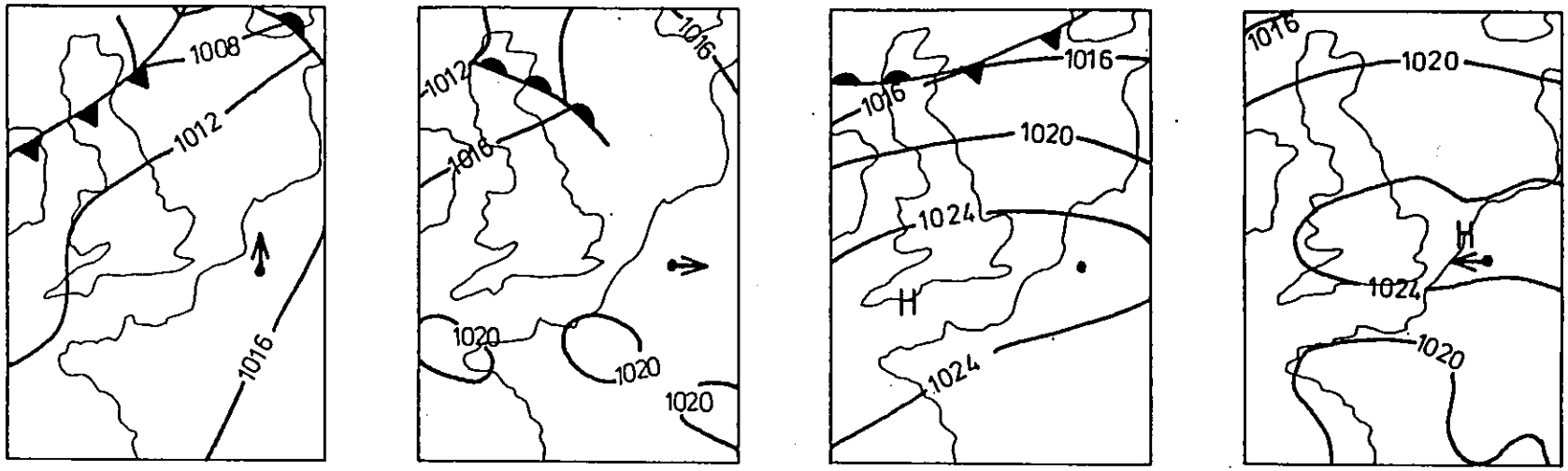



Figure (5.14) Development of the Synoptic Pressure Field during 4th-11th September 1973

concentrations. For example, a small error in estimating the windspeed (say 1 $m.s^{-1}$) is significant when windspeeds are low ($\sim$2 $m.s^{-1}$) and can produce a factor of two in the time integrated concentrations. Moreover, small-scale turbulent diffusion is important when trajectories follow similar paths. A limitation of the Lagrangian puff method, as used in MESOS, is that turbulent diffusion can only be allowed for in a simple manner, and more sophisticated modelling techniques may be necessary to give a better representation of turbulent diffusion in very light wind conditions.

(ii) Releases from Mol on the 26th October 1973

Four of the eight highest Kr85 time integrated concentrations at the 800 km North receptor originated from releases in the early hours and late evening of the 26th October (day 299). These four releases contributed to approximately 20% of the total Kr85 contamination during 1973 at this receptor. This episode is also of particular interest since the two evening releases gave unusually high exposures in relation to other exposures at 800 km North (Figure (5.13)).

The synoptic pressure charts and trajectories for this episode are shown in Figure (5.15). Trajectories moved slowly to the north under the influence of a high pressure system centred over Eastern Europe. Vertical dispersion was low since trajectories left the Belgian coast before dawn and then travelled over the North Sea towards the 800 km North receptor. Just before the last trajectories passed over the receptor, the wind direction veered and the windspeed dropped as a weak cold front approached from the north. Material from the evening release stagnated in the frontal region, giving a long exposure time at the receptor. The highest exposure occurred early on the 28th October, just before trajectories returned south under the influence of winds behind the front. Trajectories for the earlier releases were not affected by the front, and material reached the 800 km receptor around noon on the 27th October.

It is interesting that high levels of $SO_2$ were recorded at OECD monitoring sites in Southern Norway from the 26th to the 28th October 1973

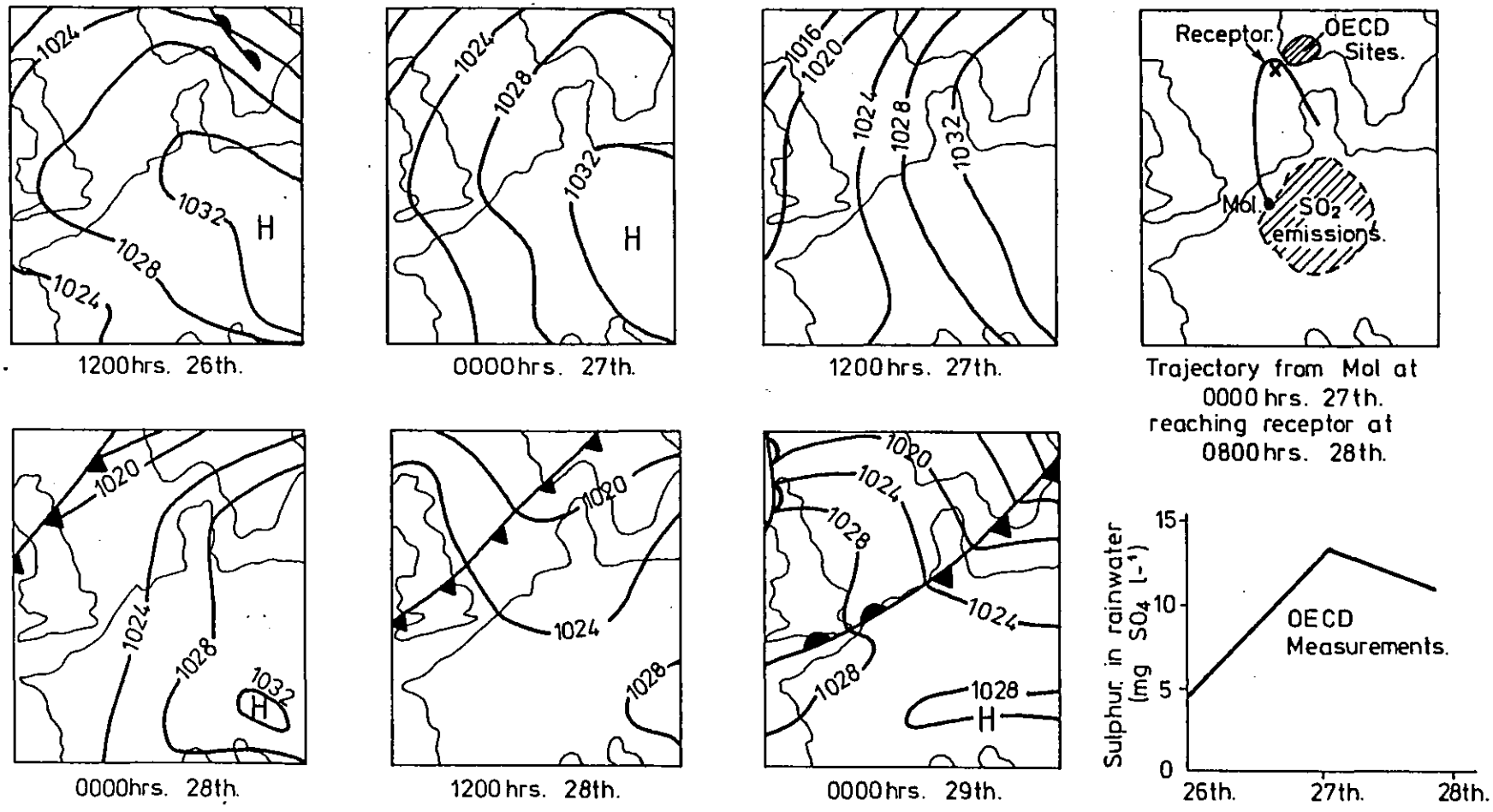



Figure (5.15) Development of the Synoptic Pressure Field during 26th-29th October 1973

(OECD (1977)). The measurements of sulphur in rainwater were particularly high as is shown in Figure (5.15). In an independent study of $SO_2$ transport to Norway during this period, Maul (1980) has identified that the most significant contribution to the sulphur measurements in Norway came from Continental $SO_2$ emissions. Consequently, the very high levels of Kr85 exposure during this episode are credible since Mol and the 800 km North receptor are close to the major $SO_2$ emission area and OECD monitoring sites respectively (Figure (5.15)).

### 5.4.5 Consideration of Release Duration

Exposure frequency distributions relating to three-hourly continuous releases have been discussed in the previous sections. In this section, the dependence of the exposure frequency distributions on release duration at source is considered.

The duration of unplanned releases in a real accident is likely to range from a few hours to a few days. Illustrative results are therefore given for six different release durations; 3, 6, 12 hours and 1, 3, 7 days. The results are normalised to represent an emission of 1 Curie spread over each release period.

#### (i) Frequency distributions

A typical set of exposure frequency distributions relating to each of these release durations is shown in Figure (5.16). In this example, the frequency distributions are represented in cumulative form, on a Weibull probability scale (Section (5.4.3)), and show the probabilities that different levels of Kr85 time integrated concentrations are not exceeded when the receptor 800 km East of Mol is exposed.

The most important feature of the frequency distributions is that exposures tend to decrease as the release duration increases. In general, the lateral dispersion of a plume will increase as the wind direction changes, either randomly or systematically, with time during the release period. Consequently, one expects that the probability of exposure will increase and the average exposure will decrease when a fixed amount of

material is released over a longer release period.

(ii) Dependence of probability of exposure and average exposure on release duration

The variation of lateral dispersion with release duration, or sampling duration, has received considerable interest in the literature. For relatively short-range transport, the lateral spread of a plume has been shown to be related to the square root of the release duration (e.g. Moore (1976), Inoue (1952)). For long-range transport, the lateral dispersion is progressively dominated by the separation S between the two trajectories spanning the release. Durst et al (1959) have analysed the distribution of trajectories initiated successively over different periods $\Delta T$, and have found that the mean trajectory separation $\overline{S}$ increases with $\Delta T^{0.5}$. Other long-range trajectory analyses have confirmed that a power law relationship exists between $\overline{S}$ and $\Delta T$ (e.g. Smith (1980)).

The MESOS results also reflect a simple power law relationship for lateral spread and release duration. The probability of exposure $P_r(\underline{x},\Delta T)$ and average exposure $\hat{E}_N(\underline{x},\Delta T)$ when a receptor $\underline{x}$ is exposed, are plotted in Figure (5.17) against release duration $\Delta T$. Time integrated Kr85 air concentrations at receptors to the east and west of Mol are used to illustrate the power law relationships. In general, it is found that a reasonable fit is given by:

$$\frac{P_r(\underline{x},\Delta T_1)}{P_r(\underline{x},\Delta T_2)}=\left(\frac{\Delta T_1}{\Delta T_2}\right)^{\beta} \quad \text{and} \quad \frac{\hat{E}_N(\underline{x},\Delta T_1)}{\hat{E}_N(\underline{x},\Delta T_2)}=\left(\frac{\Delta T_1}{\Delta T_2}\right)^{-\beta} \qquad \ldots (5.3)$$

where $\beta$ varies slightly with receptor location, but usually lies in the range 0.5 - 0.6 for air and dry deposition exposure.

The probabilities of air and wet deposition exposure for all Mol receptors are tabulated in Table (5.5). The probability of wet deposition generally increases more rapidly with release duration because exposure times at the receptor are likely to be longer and so there is also an increased chance of rain. In general, the probability of wet deposition

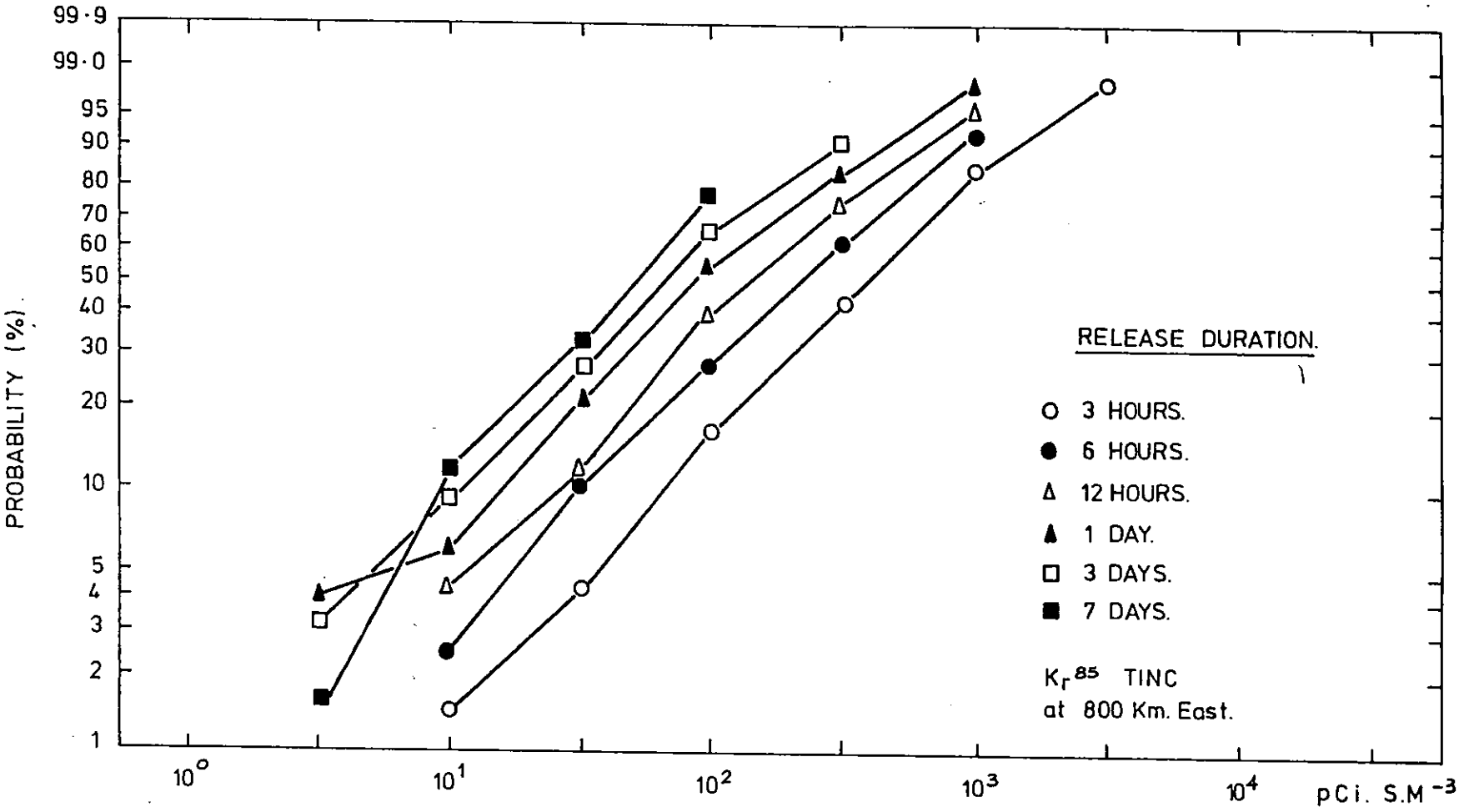
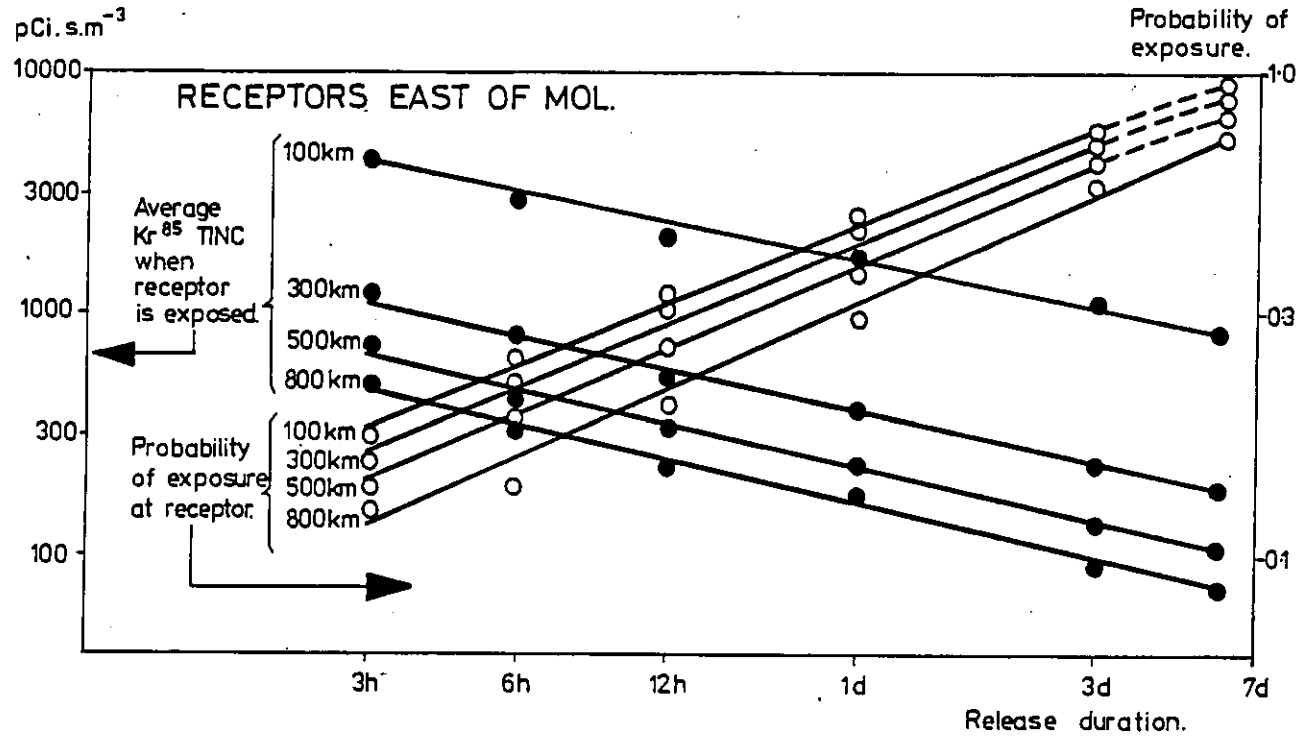



Figure (5.16) Cumulative Frequency Distributions of Kr85 Time Integrated Air Concentrations at the 800 km East Receptor for Different Release Durations



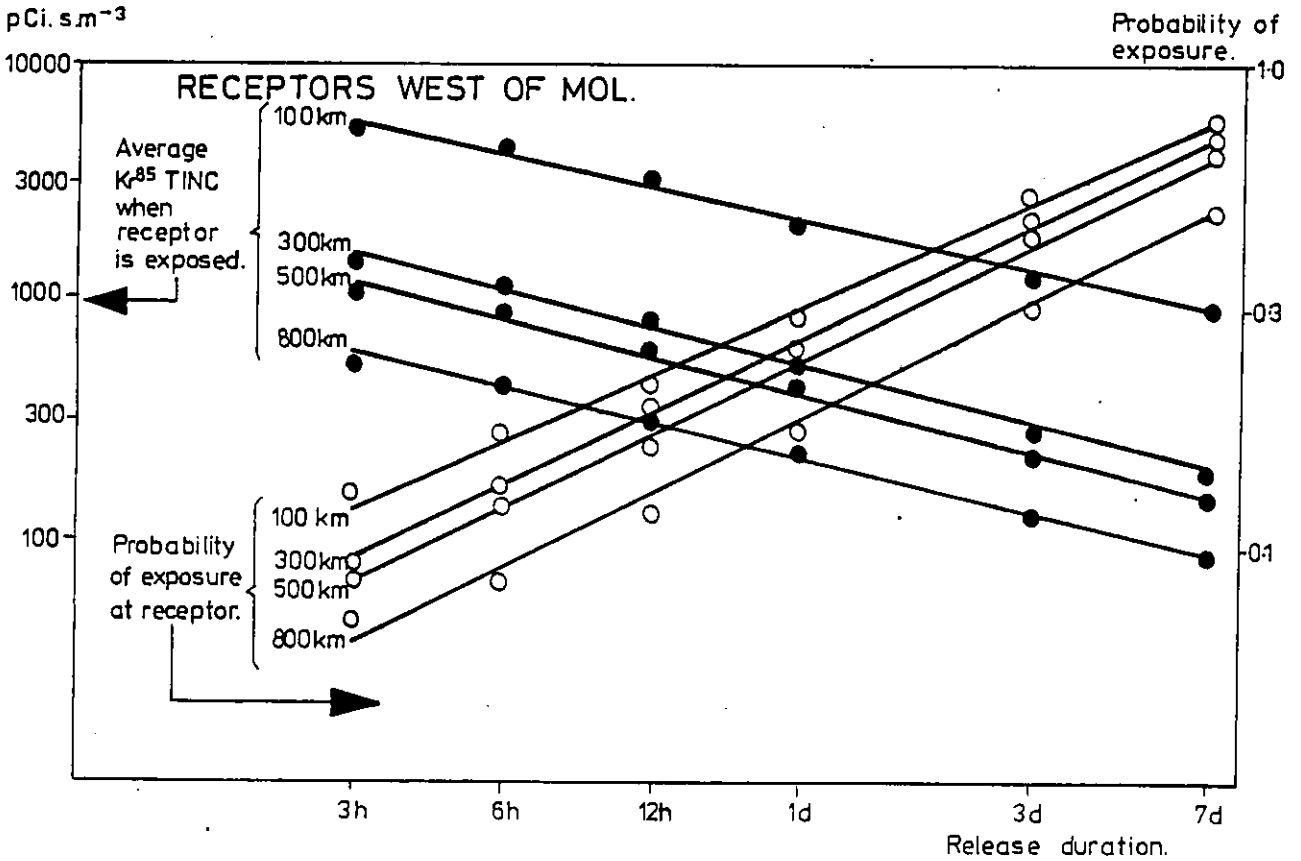




Figure (5.17) Variation of Time Integrated Air Concentrations and Probability of Exposure with Release Duration

| Receptors | Probability (%) of exposure | | | | | | Probability (%) of wet deposition | | | | | |
|---|---|---|---|---|---|---|---|---|---|---|---|---|
| | 3hrs | 6hrs | 12hrs | 1day | 3days | 7days | 3hrs | 6hrs | 12hrs | 1day | 3days | 7days |
| N100 | 11 | 14 | 20 | 26 | 50 | 75 | 2 | 4 | 6 | 10 | 25 | 43 |
| 300 | 9 | 10 | 14 | 19 | 39 | 59 | 2 | 3 | 5 | 8 | 19 | 34 |
| 500 | 5 | 8 | 11 | 16 | 33 | 53 | 2 | 3 | 6 | 9 | 20 | 39 |
| 800 | 4 | 5 | 9 | 13 | 26 | 41 | 2 | 2 | 4 | 7 | 14 | 24 |
| E100 | 18 | 25 | 35 | 48 | 75 | 95 | 6 | 9 | 16 | 25 | 51 | 76 |
| 300 | 16 | 21 | 33 | 47 | 73 | 93 | 6 | 10 | 15 | 25 | 51 | 69 |
| 500 | 14 | 20 | 27 | 40 | 69 | 90 | 5 | 8 | 13 | 20 | 43 | 60 |
| 800 | 10 | 14 | 21 | 31 | 58 | 81 | 3 | 5 | 8 | 15 | 32 | 50 |
| S100 | 11 | 16 | 23 | 34 | 58 | 81 | 2 | 3 | 6 | 8 | 22 | 42 |
| 300 | 12 | 17 | 23 | 30 | 50 | 75 | 2 | 3 | 6 | 10 | 22 | 42 |
| 500 | 11 | 16 | 22 | 30 | 51 | 74 | 1 | 2 | 4 | 7 | 18 | 34 |
| 700 | 19 | 14 | 20 | 29 | 52 | 74 | 2 | 3 | 6 | 10 | 24 | 43 |
| W100 | 13 | 16 | 21 | 30 | 53 | 75 | 2 | 3 | 5 | 7 | 19 | 35 |
| 300 | 9 | 13 | 18 | 25 | 48 | 72 | 2 | 4 | 7 | 10 | 23 | 39 |
| 500 | 9 | 13 | 16 | 24 | 43 | 68 | 2 | 4 | 5 | 10 | 20 | 39 |
| 800 | 5 | 8 | 11 | 15 | 31 | 50 | 2 | 2 | 3 | 5 | 13 | 27 |

Table (5.5) Probability of Air Contamination and Wet Deposition for Different Release Durations

| Receptor Point | Average time integrated atmospheric concs. when exposed. ($pCi.s.m^{-3}$) | | | | | | Maximum time integrated atmospheric concs. ($pCi.s.m^{-3}$) | | | | | |
|---|---|---|---|---|---|---|---|---|---|---|---|---|
| | 3hrs | 6hrs | 12hrs | 1day | 3days | 7days | 3hrs | 6hrs | 12hrs | 1day | 3days | 7days |
| N100 | 2792 | 2069 | 1467 | 1106 | 577 | 378 | 39450 | 19730 | 15160 | 8115 | 4795 | 2200 |
| 300 | 685 | 494 | 347 | 250 | 119 | 78 | 6436 | 4496 | 3011 | 1898 | 1302 | 585 |
| 500 | 295 | 192 | 134 | 95 | 46 | 30 | 3115 | 1558 | 1017 | 801 | 399 | 171 |
| 800 | 163 | 115 | 73 | 49 | 24 | 15 | 1987 | 1581 | 690 | 432 | 160 | 72 |
| E100 | 2961 | 2097 | 1493 | 1110 | 721 | 577 | 39310 | 28160 | 21320 | 11020 | 4411 | 3099 |
| 300 | 598 | 411 | 284 | 205 | 129 | 101 | 5270 | 2943 | 2311 | 1407 | 718 | 362 |
| 500 | 249 | 170 | 122 | 85 | 49 | 38 | 1416 | 1082 | 851 | 456 | 264 | 133 |
| 800 | 148 | 106 | 72 | 49 | 26 | 20 | 2001 | 1261 | 948 | 591 | 97 | 102 |
| S100 | 2358 | 1680 | 1159 | 790 | 457 | 357 | 75780 | 37890 | 18950 | 9473 | 5386 | 2688 |
| 300 | 330 | 241 | 181 | 138 | 81 | 57 | 3655 | 2623 | 1768 | 1217 | 554 | 255 |
| 500 | 199 | 138 | 99 | 72 | 41 | 30 | 1599 | 1048 | 635 | 527 | 309 | 166 |
| 700 | 100 | 69 | 48 | 32 | 18 | 13 | 847 | 658 | 379 | 322 | 171 | 78 |
| W100 | 3608 | 2790 | 2119 | 1420 | 849 | 622 | 42510 | 32170 | 22120 | 12830 | 4550 | 3423 |
| 300 | 743 | 537 | 388 | 256 | 138 | 92 | 9862 | 5876 | 3151 | 1794 | 809 | 520 |
| 500 | 485 | 357 | 278 | 187 | 107 | 71 | 7812 | 6521 | 4266 | 2133 | 750 | 427 |
| 800 | 195 | 156 | 115 | 84 | 45 | 31 | 954 | 646 | 464 | 385 | 266 | 155 |

Table (5.6) Maximum and Average Time Integrated I131(P) Air Concentrations from Mol Releases during 1973

| Receptor Point | Average deposition when exposed (pCi . $m^{-2}$) | | | | | | Maximum deposition (pCi . $m^{-2}$) | | | | | |
|---|---|---|---|---|---|---|---|---|---|---|---|---|
| | 3 hrs | 6 hrs | 12 hrs | 1 day | 3 days | 7 days | 3 hrs | 6 hrs | 12 hrs | 1 day | 3 days | 7 days |
| N100 | 27 | 17 | 10 | 5.9 | 2.4 | 1.4 | 110 | 100 | 50 | 37 | 12 | 5.5 |
| 300 | 4.3 | 2.7 | 1.6 | 1.1 | .50 | .27 | 46 | 23 | 1.5 | 8.4 | 3.7 | 1.8 |
| 500 | 3.5 | 2.0 | 1.1 | .77 | .31 | .16 | 38 | 20 | 9.4 | 4.7 | 1.6 | .67 |
| 800 | 2.5 | 1.6 | 1.1 | .66 | .28 | .18 | 22 | 11 | 5.7 | 2.8 | .95 | .46 |
| E100 | 37 | 23 | 13 | 8.1 | 4.0 | 2.8 | 290 | 170 | 83 | 45 | 18 | 9.4 |
| 300 | 13 | 7.7 | 4.8 | 2.9 | 1.4 | .96 | 95 | 56 | 36 | 27 | 10 | 6.7 |
| 500 | 5.1 | 3.1 | 1.9 | 1.2 | .57 | .40 | 4.9 | 25 | 12 | 6.2 | 2.3 | 1.4 |
| 800 | 2.4 | 1.5 | .90 | .52 | .22 | .15 | 14 | 10 | 5.0 | 2.5 | 1.5 | .72 |
| S100 | 14 | 8.5 | 5.0 | 3.4 | 1.1 | .61 | 180 | 100 | 50 | 25 | 8.4 | 3.9 |
| 300 | 5.5 | 3.4 | 1.8 | 1.1 | .48 | .28 | 70 | 65 | 32 | 16 | 6.5 | 2.8 |
| 500 | 1.4 | .80 | .46 | .26 | .11 | .064 | 14 | 7.2 | 3.6 | 1.8 | .85 | .37 |
| 700 | 1.6 | .90 | .51 | .30 | .12 | .066 | 19 | 9.6 | 4.8 | 2.4 | .80 | .34 |
| W100 | 33 | 19 | 11 | 7.4 | 2.8 | 1.0 | 360 | 350 | 180 | 97 | 32 | 15 |
| 300 | 11 | 6.6 | 3.7 | 2.4 | 1.0 | .52 | 101 | 50 | 25 | 13 | 5.2 | 2.2 |
| 500 | 7.5 | 4.5 | 3.0 | 1.7 | .79 | .35 | 71 | 35 | 18 | 11 | 4.3 | 2.5 |
| 800 | 1.4 | 1.0 | .77 | .41 | .18 | .087 | 6.5 | 6.3 | 3.2 | 1.6 | 1.0 | .44 |

Table (5.7) Maximum and Average I131(P) Wet Depositions from Mol Releases during 1973

is found to increase with release duration to the power $\beta \simeq 0.75$.

Although these power law fits cannot be extrapolated over very long release durations (as $P_T(\underline{x},\Delta T) \leqslant 1$), for practical purposes, they give reasonable estimates.

(iii) Dependence of maximum exposures on release duration

Average and maximum time integrated I131(P) air concentrations and wet depositions for all Mol receptors are given in Tables (5.6) and (5.7) respectively. Although maximum exposures decrease with increasing release duration, the dependence is not well-defined. The maximum exposure for a given release duration comes from one particular dispersion episode and average relationships between lateral spread and release duration may not be appropriate in such circumstances. The maximum exposure in a given sample can also be considered as a statistical variable which increases with sample size (Gumbel (1958)). In the statistical treatment of the MESOS results, the sample size for three-hourly release durations is greater than that for seven-day releases, and so the variation of maximum exposures with release duration must be interpreted accordingly.

## 5.5 Annual Average Exposures

Patterns of annual average exposure are presented in this section, and discussed in relation to the mode of exposure and nuclide characteristics.

Contours of time integrated air concentrations ($Ci.s.m^{-3}$), dry and wet ground depositions ($Ci.m^{-2}$), resulting from I131(P) continuous releases at Mol throughout the 1973 database period, are shown in Figure (5.18). Patterns of exposure are also given for Cs137 (Figure (5.19)) and the inert nuclides Kr85, Xe133, Xe135 (Figure (5.20)). The exposures are normalised to represent a uniform release of 1 Curie for each nuclide over the 1973 database period. The dry deposition velocities, washout coefficients and natural decay constants of the nuclides are shown in

Table (5.1). Exposures decrease by factors of $10^{0.5} \simeq 3$ along successive contours away from source; a uniform spacing of contours would therefore indicate an exponential decrease in levels of exposure with distance. A diagram of the European map is scaled to the same size as the exposure maps, and included in each Figure for reference.

Annual average exposures are best discussed in relation to the probability of exposure and the average level of exposure when a receptor is exposed. Suppose there are $n(\Delta T)$ successive unit releases of duration $\Delta T$ over a given period, and $m(\underline{x},\Delta T)$ of these releases subsequently result in a non-zero exposure $E_N^i(\underline{x},\Delta T)$, $i = 1$ to $m$, at the receptor location $\underline{x}$. Then the average exposure, $\bar{E}_N(\underline{x})$ over the period from all releases is given by:

$$\bar{E}_N(\underline{x}) = \sum_{i=1}^{i=m} \frac{E_N^i(\underline{x},\Delta T)}{n(\Delta T)} = \frac{m(\underline{x},\Delta T)}{n(\Delta T)} \sum_{i=1}^{i=m} \frac{E_N^i(\underline{x},\Delta T)}{m(\underline{x},\Delta T)}$$

$$= P_r(\underline{x},\Delta T) \cdot \hat{E}_N(\underline{x},\Delta T) \qquad \ldots (5.4)$$

where $P_r(\underline{x},\Delta T)$ is the probability of exposure, and $\hat{E}_N(\underline{x},\Delta T)$ is the average exposure when the receptor is exposed. Spatial variations in the probability of exposure and average levels of exposure have been considered in Sections (5.3.2) and (5.4.5) respectively.

### 5.5.1 Time Integrated Air Concentrations

Air concentrations drop rapidly within the first 100 km of travel as material diffuses vertically to fill the mixing layer. Annual average time integrated air concentrations are of order 300 $pCi.s.m^{-3}$ at 100 km from Mol for all nuclides except Xe135, which tend to be a factor of two lower, due to the short Xe135 half life of nine hours. Further away from Mol, the nuclide depletion rates become more important in determining the annual average levels of air concentration. The annual average concentrations for Xe135 are generally a factor of 30 lower than the corresponding levels of Kr85 towards the boundaries of the map area (Figure (5.20)). The inert nuclide Kr85 has a very long half life

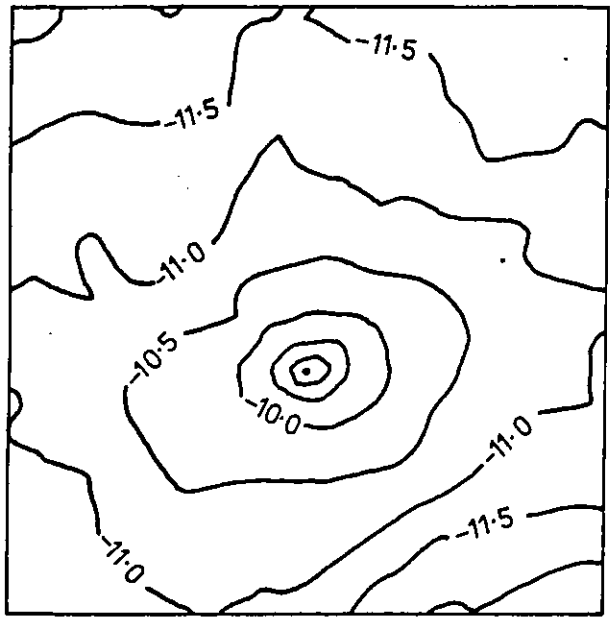
and Kr85 air contamination only decreases by a factor of 30 between 100 and 1,000 km from source. This indicates that very long-range transport up to the scale of global recirculation may be important for planned releases of Kr85.

The influence of the synoptic pressure field on the patterns of annual average air contamination become apparent with increasing distance from Mol. In Section (5.3) it was shown that certain recurring features in the synoptic pressure field affect the movement of trajectories, and consequently produce significant spatial variations in the probability of air contamination over the map area. The main features of the trajectory distributions (Figure (5.3)) and the probability of air contamination (Figure (5.4)) can be seen in the patterns of annual average air contamination for all nuclides. For example, trajectories moving to the south-east of Mol are frequently channelled over the South of France under the geostrophic control of depressions near the Alps. This leads to a rapid decrease in air contamination across the Alpine barrier, but also gives a relatively slow decrease in air contamination over Central and Southern France. Trajectories moving to the north-west of Mol tend to be caught in depressions over England or diverted over the North Sea. This effect leads to a rapid decrease in annual average air contamination over Northern England and relatively high contamination over the North Sea.

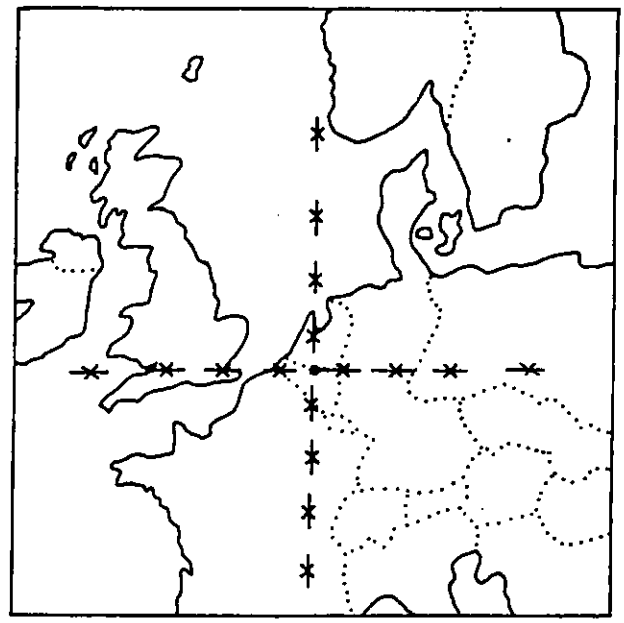
Spatial variations in the level of air contamination when the receptors are exposed are also important in determining the patterns of annual average contamination. For example, relatively high levels of annual average contamination occur to the west of Mol, although receptors in this direction only have a moderate chance of exposure (Tables (5.5) and (5.6)). Receptors to the west of Mol receive the highest levels of air contamination when exposed, probably due to unfavourable dispersion conditions which often occur when transport is associated with anticyclonic pressure systems over the British Isles.

### 5.5.2 Dry and Wet Deposition

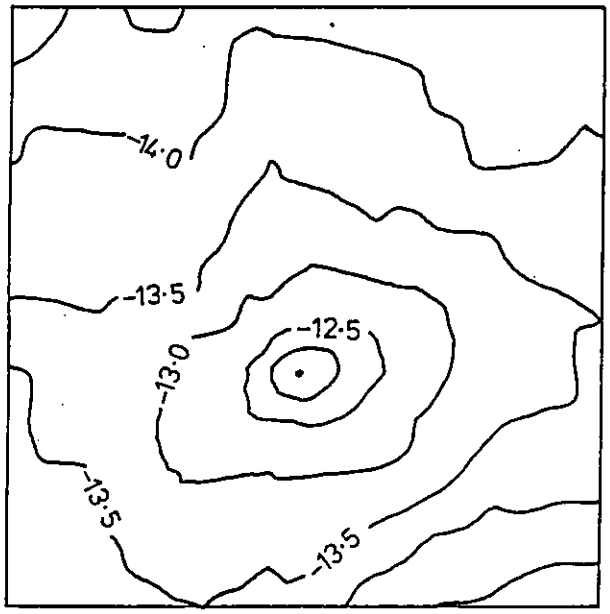
The patterns of nuclide dry deposition and air contamination are similar



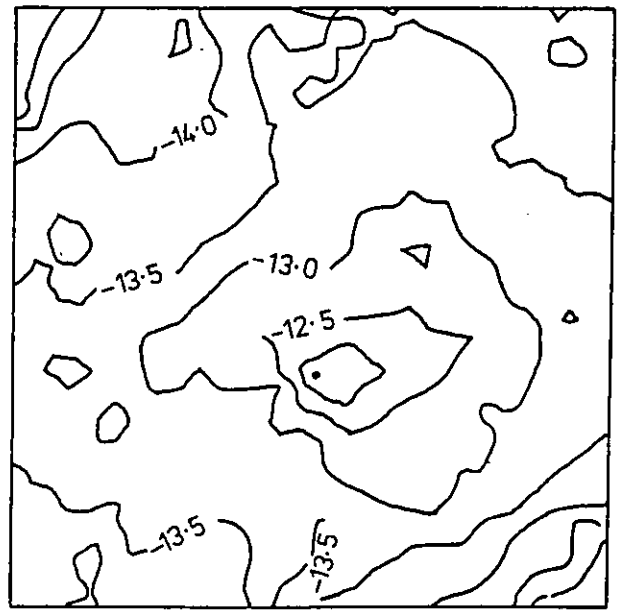

I131(P) time integrated air concentrations $\log_{10}$ (Ci.s.m$^{-3}$)



Mol receptors

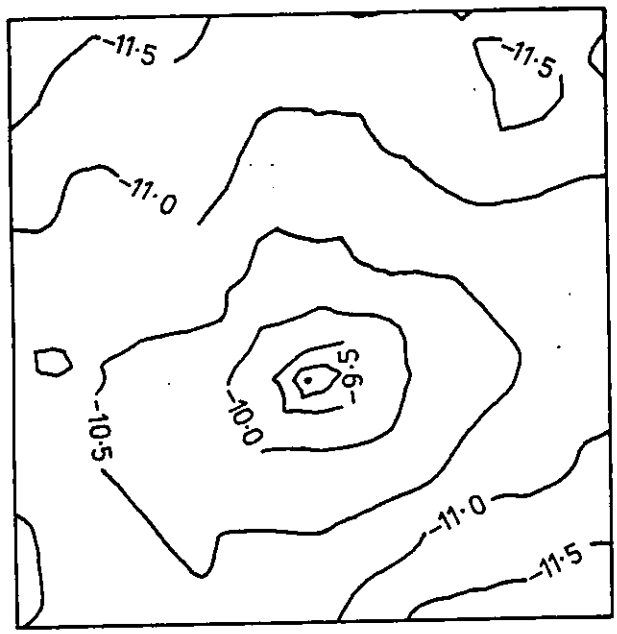



I131(P) dry deposition $\log_{10}$(Ci.m$^{-2}$)

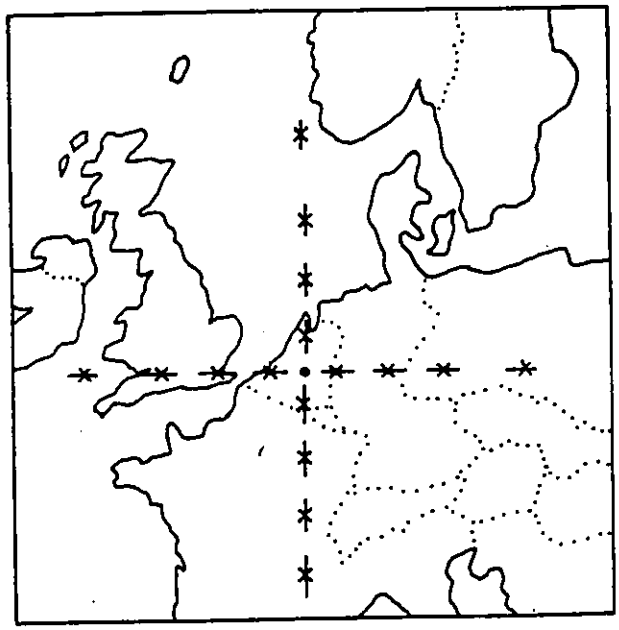



I131(P) wet deposition $\log_{10}$(Ci.m$^{-2}$)

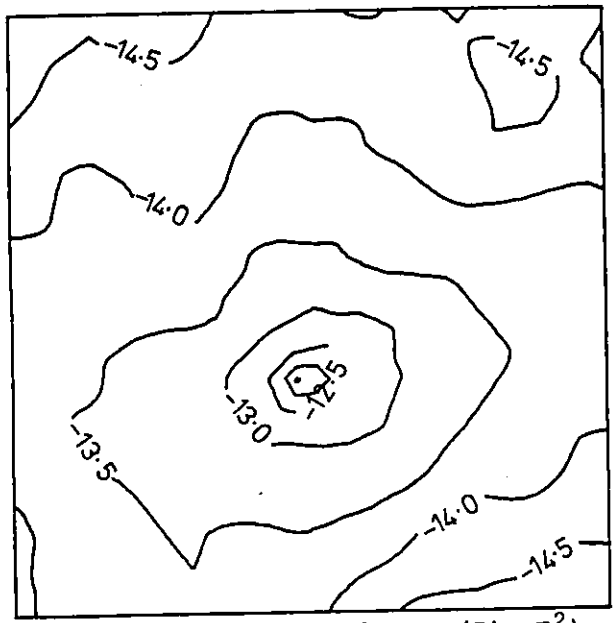
Figure (5.18) Annual Average I131(P) Exposures from Mol Releases during 1973



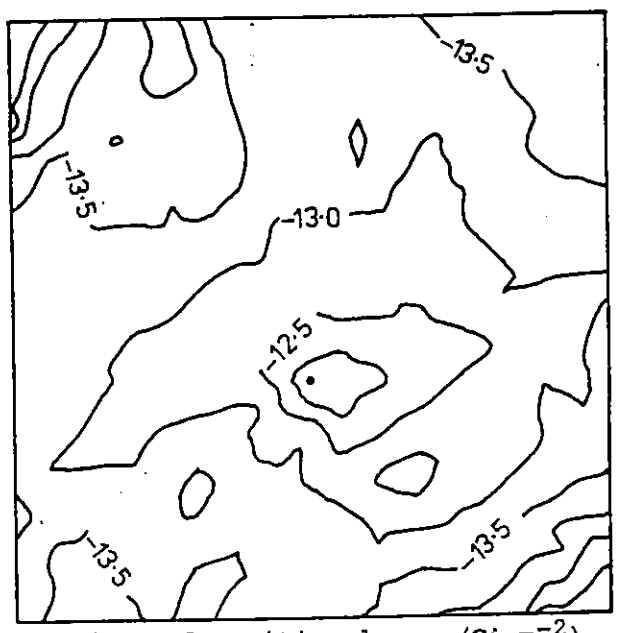

Cs137 time integrated air concentrations $\log_{10}$ (Ci.s.m$^{-3}$)



Mol receptors

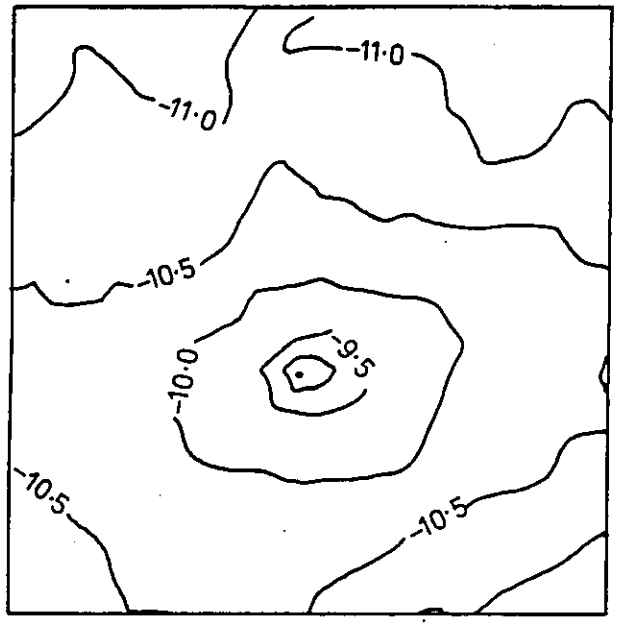



Cs137 dry deposition $\log_{10}$ (Ci.m$^{-2}$)

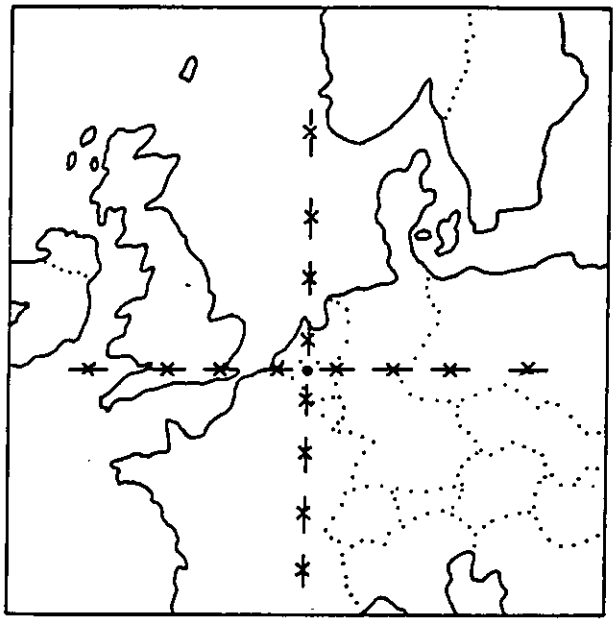



Cs137 wet deposition $\log_{10}$ (Ci.m$^{-2}$)

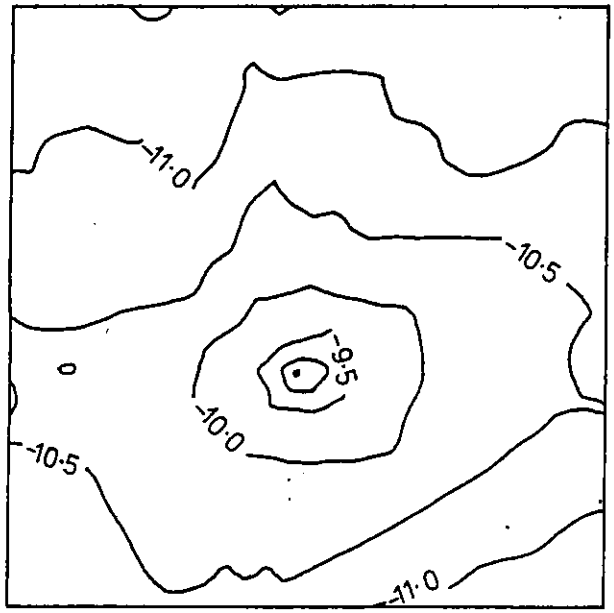
Figure (5.19) Annual Average Cs137 Exposures from Mol Releases during 1973



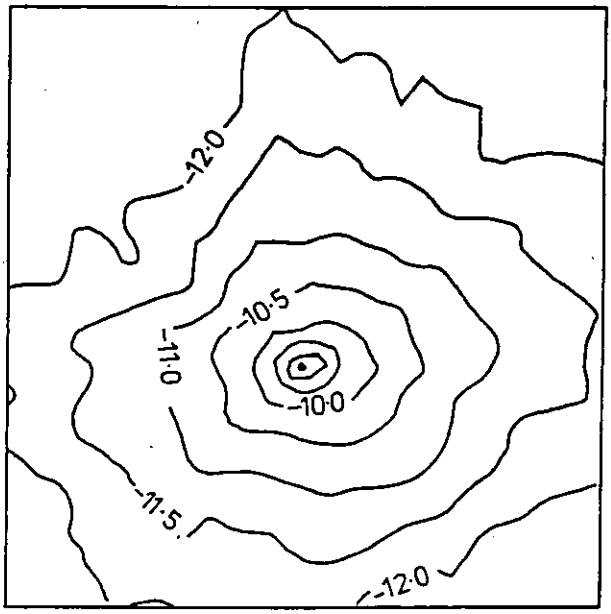

Kr85 time integrated air concentrations $\log_{10}$ (Ci.s.m$^{-3}$)



Mol receptors




Xe133 time integrated air concentrations $\log_{10}$(Ci.s.m$^{-3}$)




Xe135 time integrated air concentrations $\log_{10}$(Ci.s.m$^{-3}$)

Figure (5.20) Annual Average Kr85, Xe133 and Xe135 Exposures from Mol Releases during 1973

because dry deposition is directly related to air concentrations through the nuclide deposition velocity. In the MESOS dispersion calculations, the deposition velocity of a nuclide is adjusted to account for the effects of boundary layer stability (Section (2.4.1)). However, this adjustment is generally small due to the relatively low nuclide deposition velocities and no important systematic effect can be detected in the patterns of annual average dry deposition. Consequently, the average level of dry deposition for I131(P) and Cs137 can be estimated by multiplying the average air contamination by the nuclide deposition velocity ($3.10^{-3}ms^{-1}$ for I131, and $10^{-3}ms^{-1}$ for Cs137).

The contours of I131(P) and Cs137 wet deposition have irregular features which reflect the spasmodic nature of rainfall along trajectories and the different wetness characteristics of transporting air masses. Patterns of annual rainfall measured at stations do not always give a correct indication of the levels of wet deposition. Regions to the east of Mol (e.g. the Netherlands) only have moderate annual rainfall ($\sim$500 mm), but incur the heaviest wet deposition from Mol due to the high probability of rain in the prevailing Westerlies. However, the effects of very high annual rainfall over the Norwegian mountains ($\sim$2,000 mm) and over the Alps ($\sim$1,300 mm) are represented in the patterns of annual average wet deposition. It is also interesting to note that relatively high wet deposition occurs over England, and this is consistent with trajectories moving towards depressions which pass over the British Isles from the Atlantic.

## 5.6 Summary

The long-range dispersion of notional releases of a selection of nuclides from Mol has been studied using the MESOS model and the 1973 database. The simulation of dispersion over this period has been used to develop frequency distributions of exposure for different release durations and patterns of annual average exposure. Additional analyses have also been presented to illustrate the factors which affect the frequency distributions and patterns of exposure.

Exposures at a remote receptor resulting from short unplanned releases

can vary over several orders of magnitude, due to the wide spectrum of dispersion conditions and trajectory pathways between source and receptor. The form of the frequency distribution of exposure is complicated by the possibility of indirect pathways between source and receptor. Long trajectories substantially increase the probability of exposure, but generally lead to small exposures at the receptor, particularly for rapidly depleting nuclides such as Xe135.

Episodes which lead to relatively high levels of exposure are often associated with unexpected dispersion conditions. Windspeeds may drop significantly just before activity arrives at the receptor, giving long exposure times. Lateral dispersion may be minimal when stationary anticyclones persist in the synoptic pressure field. Vertical dispersion can be limited in stable night-time transport over land or when the route between source and receptor is primarily over the sea. One or more of these conditions may occur, in an essentially random manner, to give high levels of exposure at remote receptors. However, the likelihood of such unfavourable chance events is correspondingly small.

Probability of exposure, maximum and average levels of exposure have been shown to depend on the duration of the unplanned release, due to the synoptic swinging of trajectories over the release period. Probability of exposure and average exposure are inversely proportional and vary approximately with the square root of the release duration. However, maximum levels of exposure cannot be expressed simply in terms of the release duration.

Long-term patterns of exposure have been discussed with reference to the distributions of trajectories initiated at three-hourly intervals from Mol. The trajectory analysis has shown that the movement of trajectories through the synoptic pressure fields can have systematic characteristics which are associated with certain recurring synoptic features (e.g. anticyclones and depressions). These effects may produce important features in the patterns of annual average contamination, and can also be identified in the site assessments presented in the following Chapter.

# CHAPTER 6 COMPARISON OF THE DISPERSION OF PLANNED AND UNPLANNED NOTIONAL RELEASES FROM SELECTED SITES DURING 1973 AND 1976

## 6.1 Introduction

The long-range dispersion of notional nuclide releases from Mol during 1973 has been considered in Chapter 5. Annual average patterns of exposure and frequency distributions of exposure at remote receptors were discussed in relation to dispersion characteristics from Mol during this period.

The dispersion of notional releases from other European sites may be expected to depend on the site location and the period under consideration. The aim of this Chapter is to assess the sensitivity of long-term patterns of exposure and exposure frequency distributions to these factors.

Selective results, using the 1973 meteorological database, are presented for Heysham, a coastal site in North-West England, and Karlsruhe in Southern Germany. This allows comparison between levels of exposure from three different sites: Mol, Heysham and Karlsruhe, during the same 1973 database period.

The weather during 1973 was representative of an "average" year in terms of seasonal variations and general European climate. However, unusually persistent anticyclonic conditions occurred during 1976, giving a long hot Summer in the British Isles. Dispersion calculations have been repeated for Mol using the 1976 meteorological database to show how changes in the climate may affect the annual average levels of exposure. Patterns of exposures due to Summer and Winter releases from Mol during 1976 are also considered.

## 6.2 The 1973 Studies for Karlsruhe and Heysham

The methods used in the MESOS site assessments have been described in Section (5.2). The long-range dispersion of successive three-hourly releases from the site are derived using MESOS and the appropriate database. Exposures are then calculated at all grid points within a radial grid system centred on the site. This allows long-term patterns of exposure to be developed, and also gives useful information on the frequency of different levels of exposure at remote receptors. Exposure frequency distributions relating to notional unplanned releases of duration ranging from three hours to seven days are considered in detail at 16 chosen receptors remote from the site.

The location of the selected receptors for the Karlsruhe and Heysham studies are shown in Figure (6.1). The position of these sites within the European database map area for 1973 allows the detailed study of exposures at receptors up to 1,300 km from site. Receptors located at 100, 300, 500 and 800 km are also considered so that meaningful comparisons can be made between unplanned notional releases from Mol, Karlsruhe and Heysham during 1973.

The long-range dispersion of nuclide releases from Karlsruhe and Heysham is discussed in relation to a trajectory analysis for each site. The patterns of air and ground contamination resulting from nuclide releases during 1973 are then selectively presented. This is followed by a consideration of the frequency distributions of exposure at the Karlsruhe and Heysham receptors.

### 6.2.1 Trajectory Analysis

Trajectory roses showing the movement and directional distributions of trajectories initiated at Karlsruhe and Heysham are shown in Figures (6.2) and (6.3) respectively. Each trajectory rose includes 2,024 trajectories representing successive three-hourly releases throughout

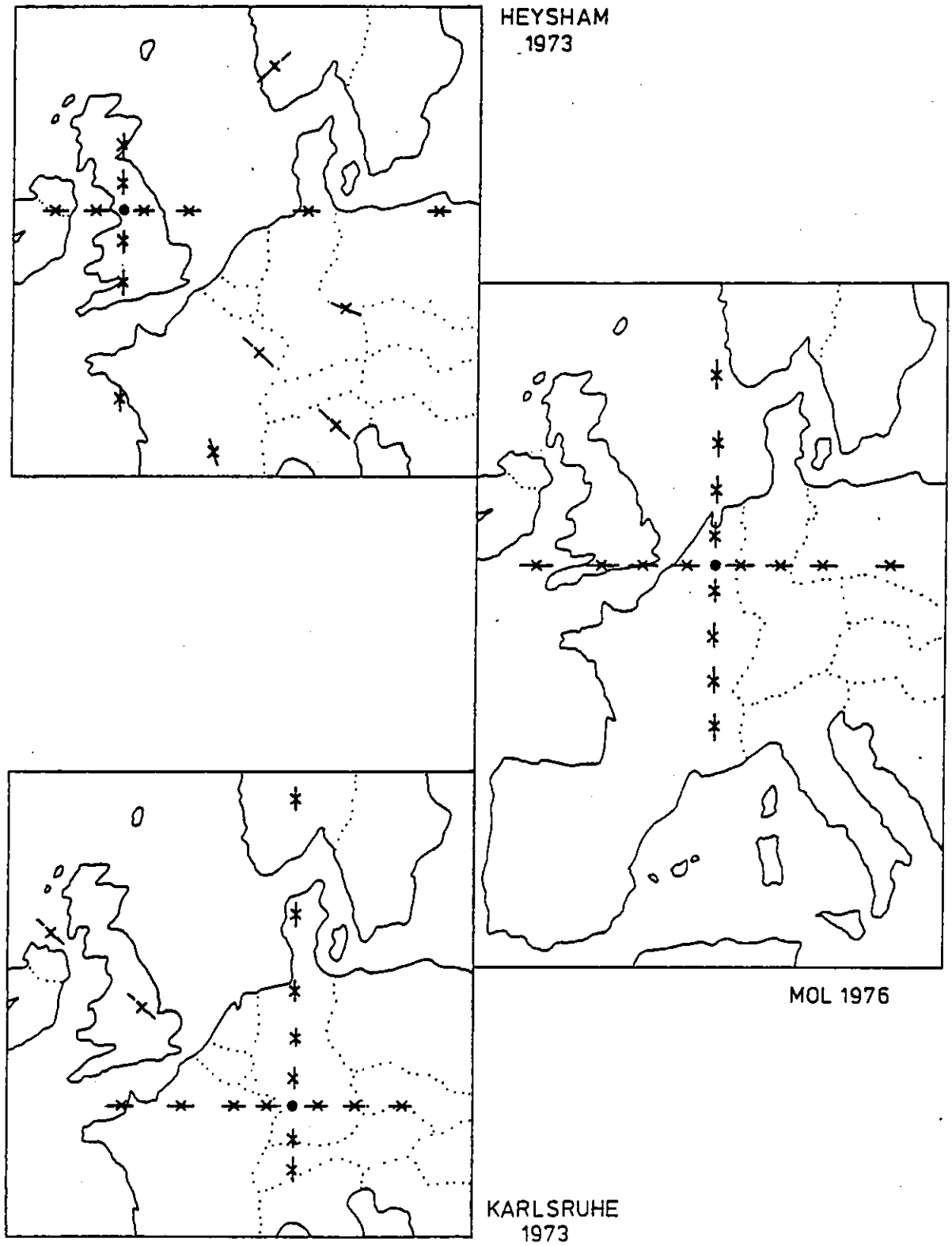



Figure (6.1) Location of Receptors for Karlsruhe, Heysham and Mol

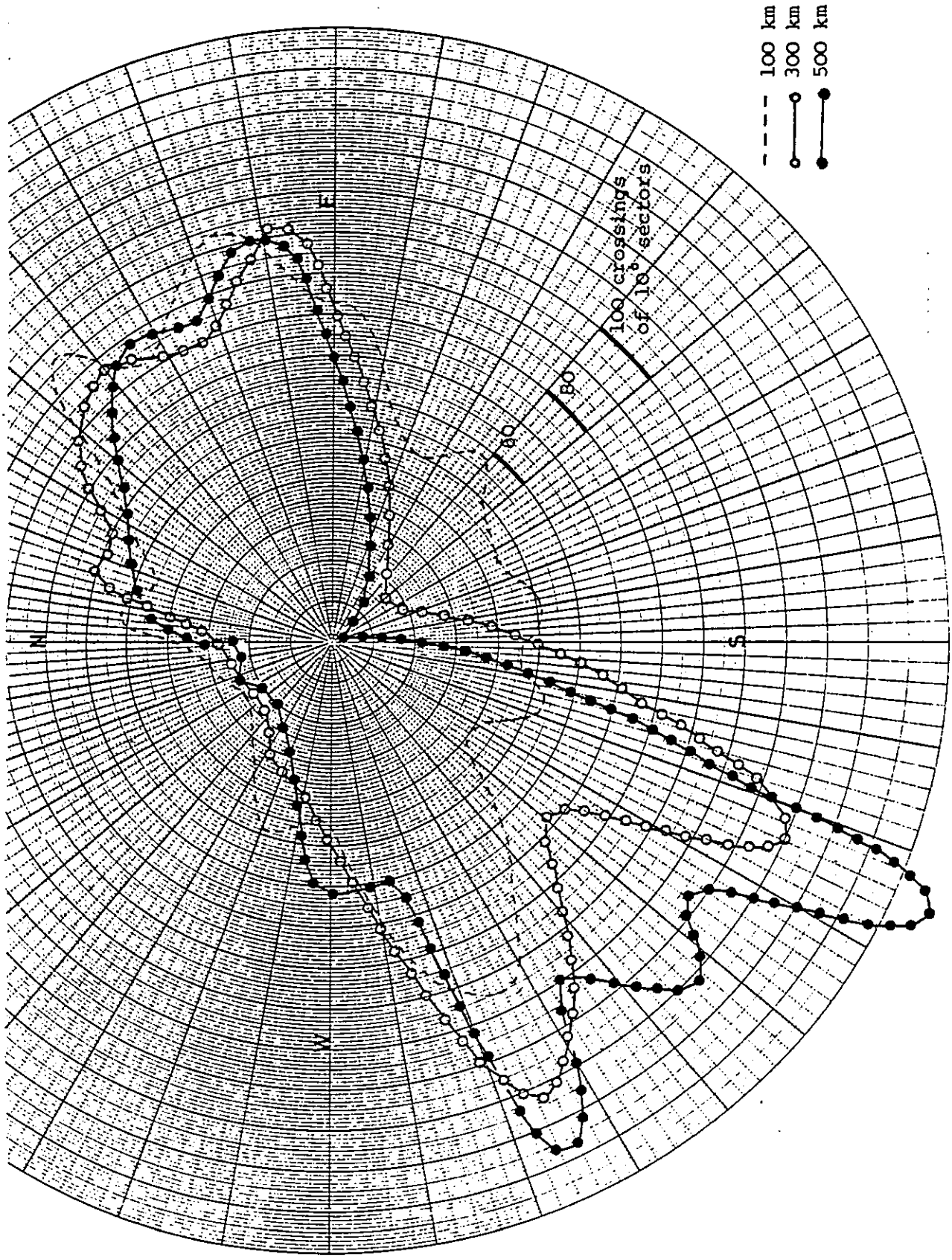



Figure (6.2) Trajectory Rose for Karlsruhe (1973)

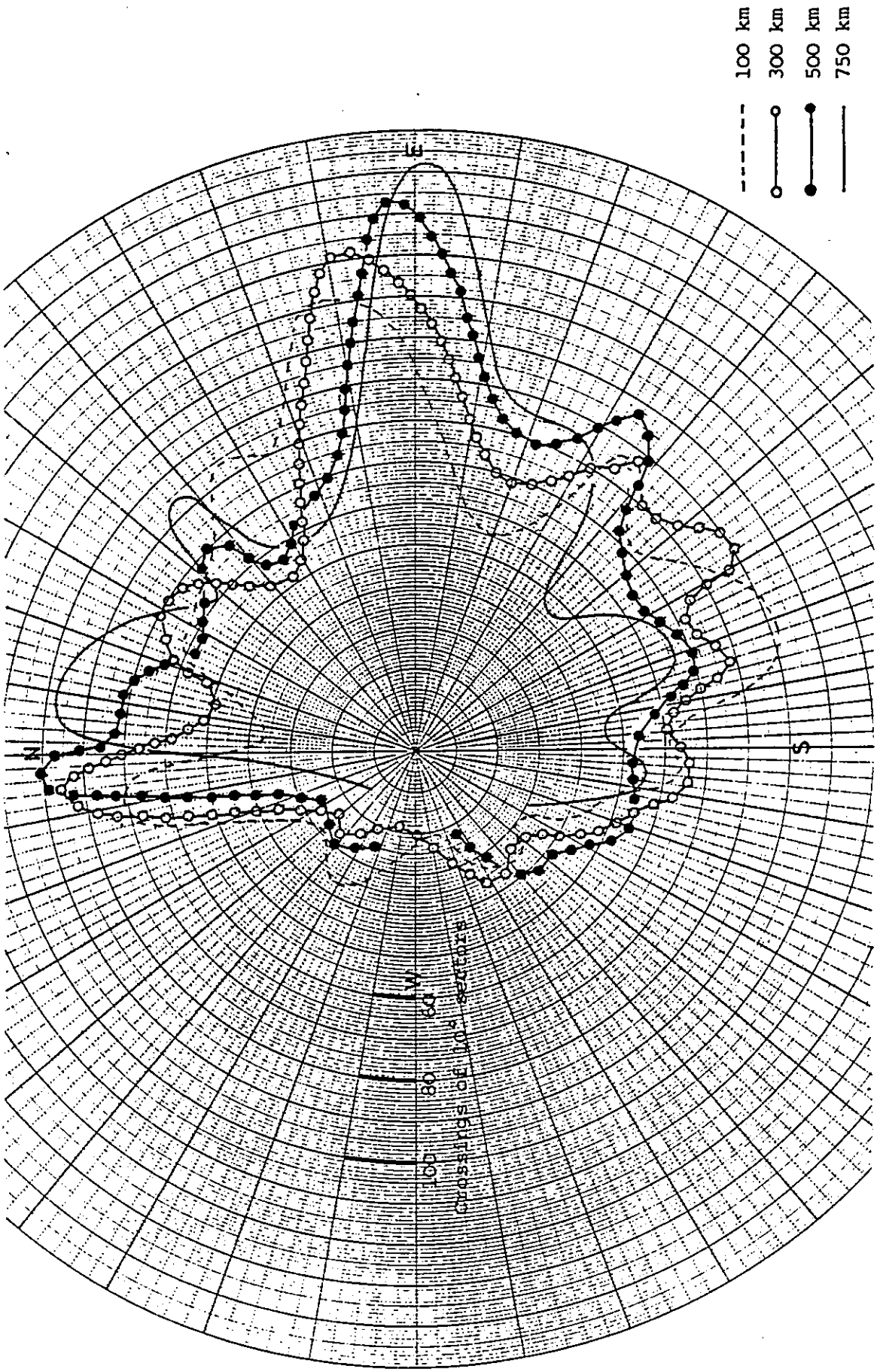



Figure (6.3) Trajectory Rose for Heysham (1973)

the 1973 database period. The trajectory roses for Karlsruhe, Heysham and Mol (Figure (5.3)) can be directly compared since they relate to the same time sequence of releases.

(i) Karlsruhe

The distribution of trajectories crossing the 100 km circle suggests that there is a strong directional bias to the north-east and south-west in the frequency of predicted boundary layer winds at Karlsruhe. Predicted frequencies of the 10m wind direction have been compared with observations at Karlsruhe (ApSimon et al (1980)). The site observations show an even greater frequency of winds from the north-east (∿25%) and south-west (∿50%). Karlsruhe is situated in the Rhine Valley and the higher frequencies of winds in these directions are probably due to topographical effects which are not represented in the MESOS model.

The initial north-east and south-west bias in the distribution of trajectories is emphasised at large distances from Karlsruhe. The location of Karlsruhe relative to the Alps leads to a strong divergence in the trajectory distributions to the south-east of Karlsruhe. The effect of the Alpine barrier has been discussed in Section (5.3.1). Trajectories from Karlsruhe move systematically to the west of the Alps under the geostrophic control of depressions; less than 10% of trajectories moving towards the Alps from Karlsruhe continue across the Alps into Northern Italy.

(ii) Heysham

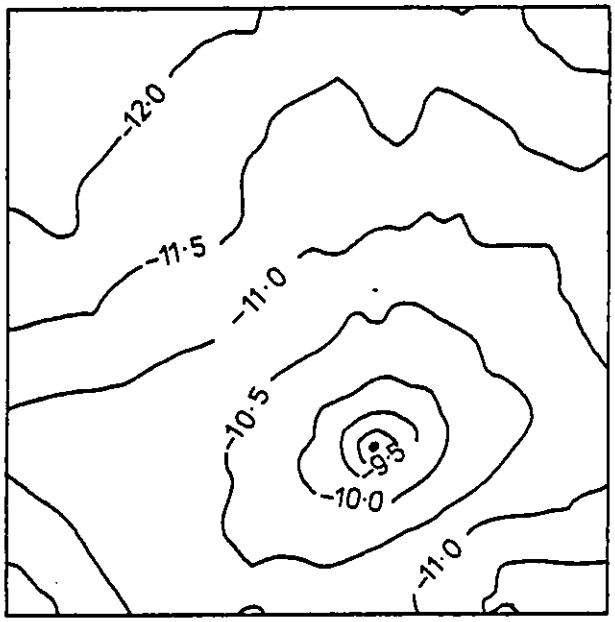
The trajectory rose for Heysham (Figure (6.3)) is substantially different from the Mol and Karlsruhe trajectory roses. Boundary layer winds at Heysham, derived from the database, show a high frequency of Westerlies and South-Westerlies. This is representative of wind direction frequencies in Northern England due to the general movement of depressions across the British Isles.

A notable feature of the trajectory rose for Heysham is the very low frequency of Easterlies. In a pollution monitoring study on the Heysham Peninsula during 1973, Harrison and Holman (1979) have shown that a high proportion of Easterlies are associated with night-time land breezes from the coast. This is supported by a study of wind observations further down the coast at Blackpool (ApSimon et al (1980)). Localised land-sea breezes are not modelled in MESOS and this means that the frequency of Easterlies and Westerlies is likely to be underestimated at Heysham. However, this is not expected to affect substantially the long-range transport from Heysham.

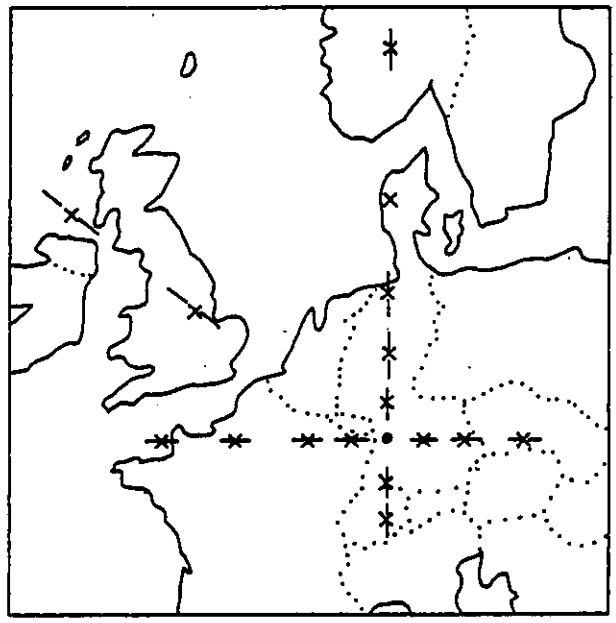
The distribution of trajectories further away from Heysham suggests that trajectories are gradually swept towards the east. This effect is particularly noticeable for trajectories initially moving to the north and to the north-east of Heysham. The trajectory distributions in these directions indicate an eastward rotation of about 15° over 750 km of travel. This small but systematic average bending of trajectories to the east has also been identified by Smith (1980). Smith suggests that this effect is consistent with the tendancy of synoptic features, particularly depressions, to move eastwards across the British Isles.

### 6.2.2 Annual Average Patterns of Exposure

Patterns of annual average time integrated I131(P) and Kr85 air concentrations for releases from Karlsruhe and Heysham are shown in Figures (6.4) and (6.5) respectively. Annual average levels of I131(P) wet deposition are also shown. The spatial variation of I131(P) dry deposition is very similar to that of I131(P) air contamination and can be obtained by factoring the air contamination by the deposition velocity of $3.10^{-3}m.s^{-1}$ (Section (5.5.2)). Annual average exposures from the other nuclides considered in the MESOS calculations are given by ApSimon et al (1981).



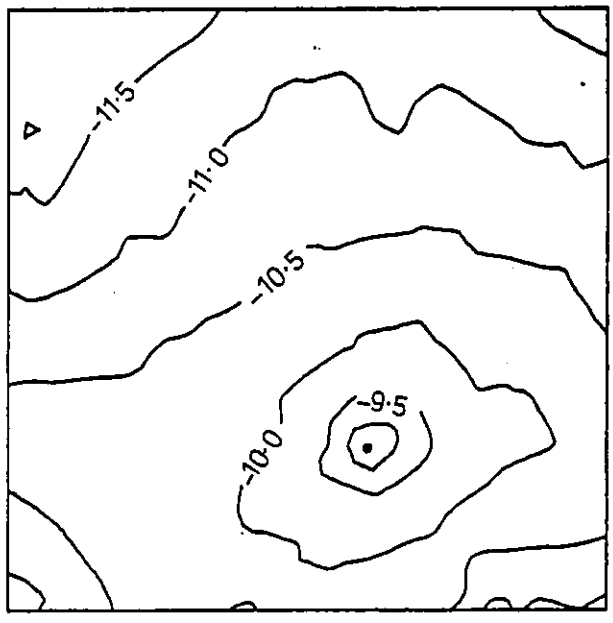

I131(P) time integrated air concentrations $\log_{10}$ (Ci.s.m$^{-3}$)




Karlsruhe receptors

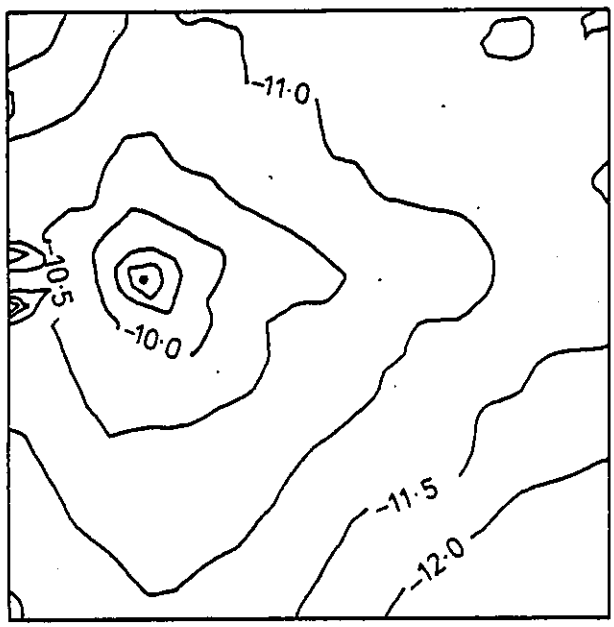



I131(P) wet deposition $\log_{10}$ (Ci.m$^{-2}$)

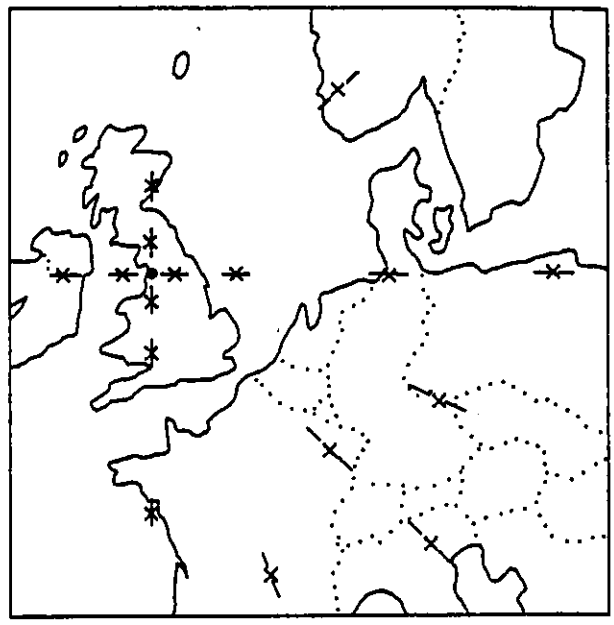



Kr85 time integrated air concentrations $\log_{10}$ (Ci.s.m$^{-2}$)

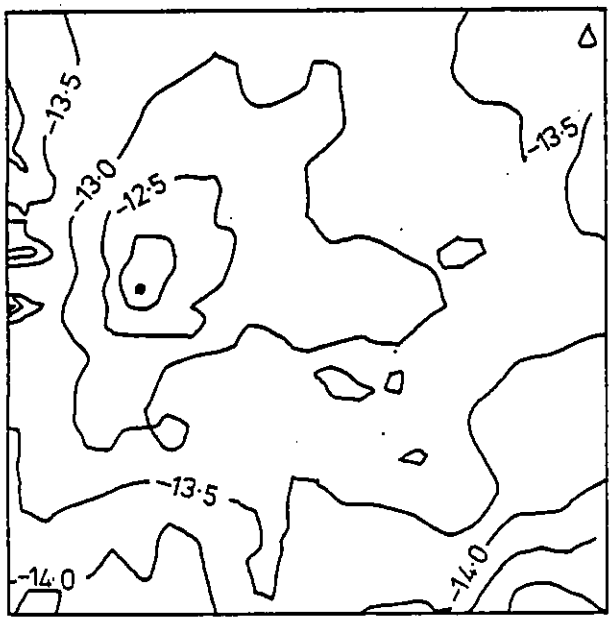
Figure (6.4) Annual Average I131(P) and Kr85 Exposures from Karlsruhe Releases during 1973



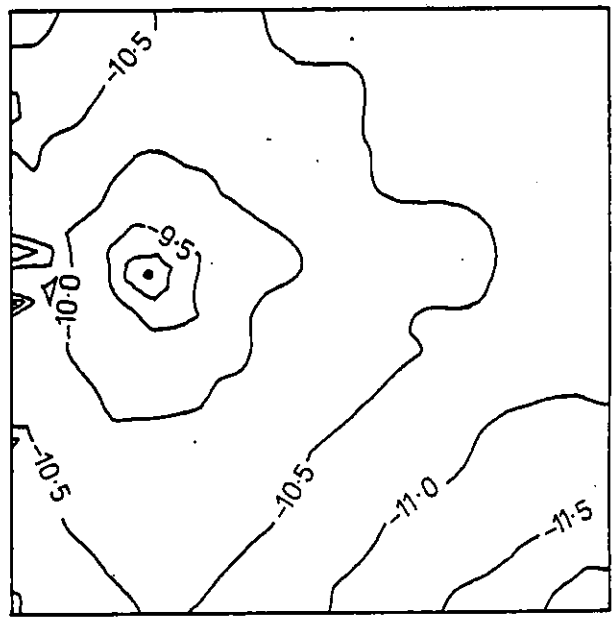

I131(P) time integrated air concentrations $\log_{10}$ (Ci.s.m$^{-3}$)



Heysham receptors




I131(P) wet deposition $\log_{10}$ (Ci.m$^{-2}$)




Kr85 time integrated air concentrations $\log_{10}$ (Ci.s.m$^{-3}$)

Figure (6.5) Annual Average I131(P) and Kr85 Exposures from Heysham Releases during 1973

(i) Karlsruhe

The trajectory analysis for Karlsruhe shows that long-range transport occurs most frequently to the north-east and south-west. Consequently, the probability of exposure and annual average air contamination is greatest in these directions. Air contamination drops most rapidly to the south-east of Karlsruhe, since the region to the south of the Alps is very rarely exposed. Relatively high contamination occurs over the North Sea and to the west of Karlsruhe. The patterns of annual average air contamination for Karlsruhe and Mol are broadly similar in these respects.

The patterns of wet deposition are very irregular, but certain features can be identified. Relatively high wet deposition occurs over Scandinavia, reflecting the very high rainfall in this area. There is also a ridge of high wet deposition immediately to the west of the Alps, since trajectories moving in this direction are generally associated with depressions and frontal flow from the north. The south-westerly winds also give relatively high levels of I131(P) wet deposition to the north-east of Karlsruhe.

(ii) Heysham

The patterns of annual average air contamination from Heysham releases are quite distinctive and are substantially different from those relating to releases from Mol and Karlsruhe. The levels of air contamination show a strong directional bias, particularly at larger distances, as expected from the Heysham trajectory rose (Figure (6.3)). Peak levels of air contamination occur in directions to the north, east and south at distances greater than 300 km from Heysham. Air contamination at corresponding distances but in intermediate directions, can be lower by a factor of three or more. For example, there are two relatively small regions over Northern and Central Ireland, in which annual average air contamination is lower, by a factor of ten, than in the surrounding areas. This is mainly due to the low probability

of exposure in these areas.

The contours of annual average air contamination are more symmetric relatively close to Heysham. An interesting feature is that levels of air contamination immediately to the west of Heysham are not substantially different from contamination in other directions. Direct transport to the west of Heysham is infrequent, but exposures over the Irish Sea, when they occur, tend to give relatively high contamination due to the limited mixing depths and vertical dispersion. The contribution of second pass exposures, which are not represented in the trajectory rose, also tend to smooth out the directional differences in annual average air contamination close to Heysham.

Directional variations in the probability of exposure are also reflected in the pattern of I131(P) wet deposition. A comparison of the air contamination and wet deposition contours shows that rain is more likely to occur in westerly and south-westerly air flows from the Atlantic. Annual average wet deposition is generally higher for Heysham than for Mol and Karlsruhe during the same period. These aspects are typical of the British climate.

### 6.2.3 Exposure from Notional Unplanned Releases

Exposure from notional unplanned releases at Mol, Karlsruhe and Heysham during 1973 are compared in this section. Frequency distributions of exposure at each chosen set of site receptors (Figure (6.1)) are considered for a fixed release duration. Average and maximum levels of exposure are then discussed for release durations ranging from three hours to seven days. Time integrated I131(P) air concentrations are used to illustrate the results for each site.

#### (i) Exposure frequency distributions

The frequency of different levels of I131(P) air contamination at each

of the Mol, Karlsruhe and Heysham receptors are shown in the form of histograms in Figures (6.6), (6.7) and (6.8) respectively. The histograms relate to 1 Curie releases spread uniformly over each day in the 1973 database period.

The general form of the exposure histograms has been discussed in connection with three-hourly releases from Mol, in Section (5.4.2). The qualitative description of the histograms appears to be applicable to all the sites considered. The histograms are typically skew with the most probable level of contamination a factor of 10 to 30 less than the maximum contamination. The most distinctive feature of each histogram is the frequency of the higher levels of exposure, as represented by the probability of exposure from relatively direct transport between source and receptor.

The probability of exposure from direct transport can vary considerably for receptors in different directions relative to a site. This is particularly evident in the Heysham histograms (Figure (6.8)). For example, there is a higher chance of exposure at 1,300 km to the east than at the receptor only 300 km to the west of Heysham, due to the very low frequency of Easterlies at this site. Easterly winds are also relatively infrequent at Mol and Karlsruhe.

Although the frequency of direct transport to receptors tends to dominate the shape of individual histograms, the associated levels of exposure are generally comparable for receptors at similar distances and directions from each site. This aspect is shown more clearly when average levels of exposure are compared.

(ii) Maximum and average levels of exposure

The maximum and average levels of I131(P) air contamination at the Karlsruhe and Heysham receptors are shown in Tables (6.1) and (6.2) respectively. These relate to six different release durations,

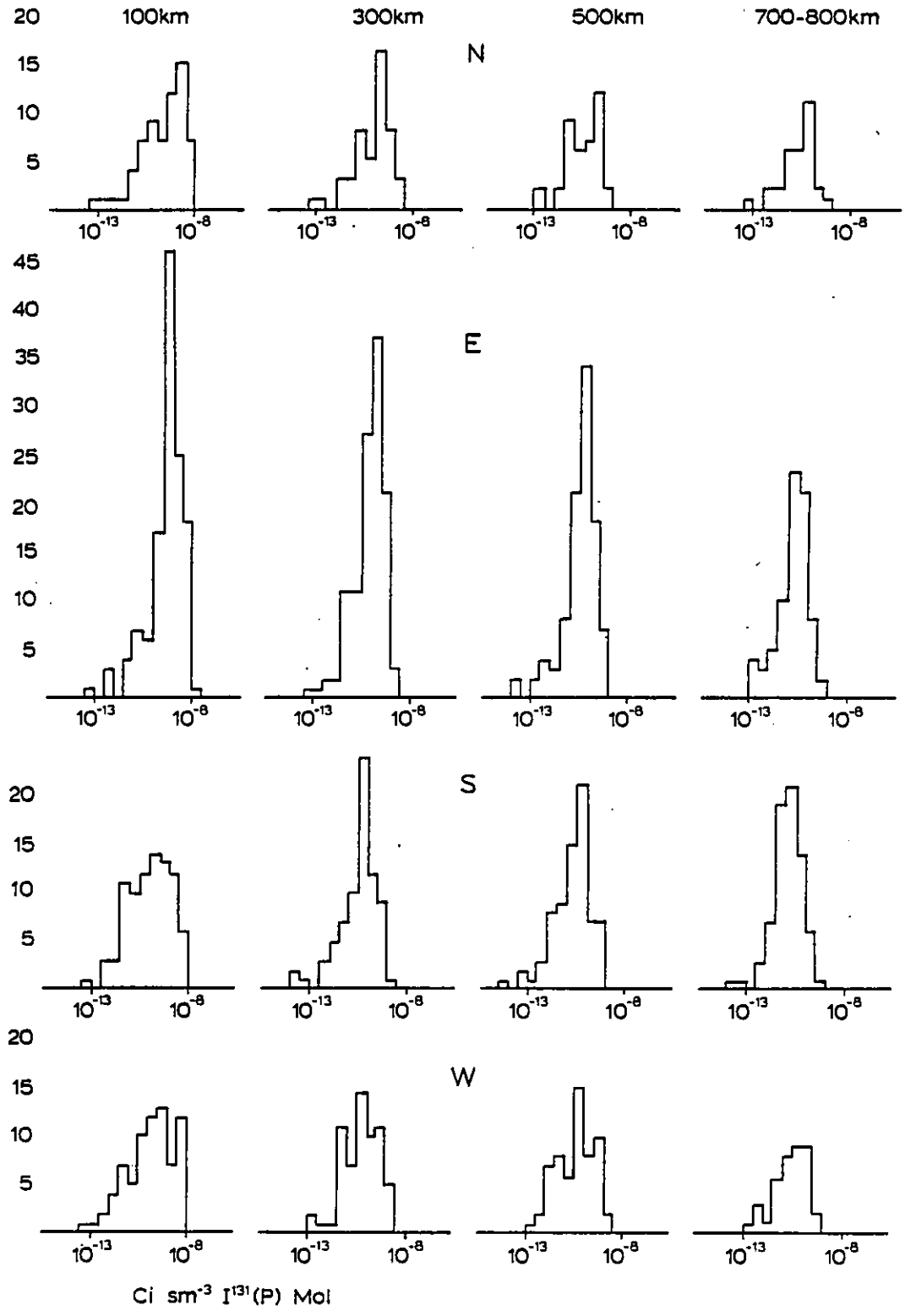



Figure (6.6) Histograms for Time Integrated Air Concentrations due to Unit Releases of I131(P) over 24 Hours from Mol during 1973

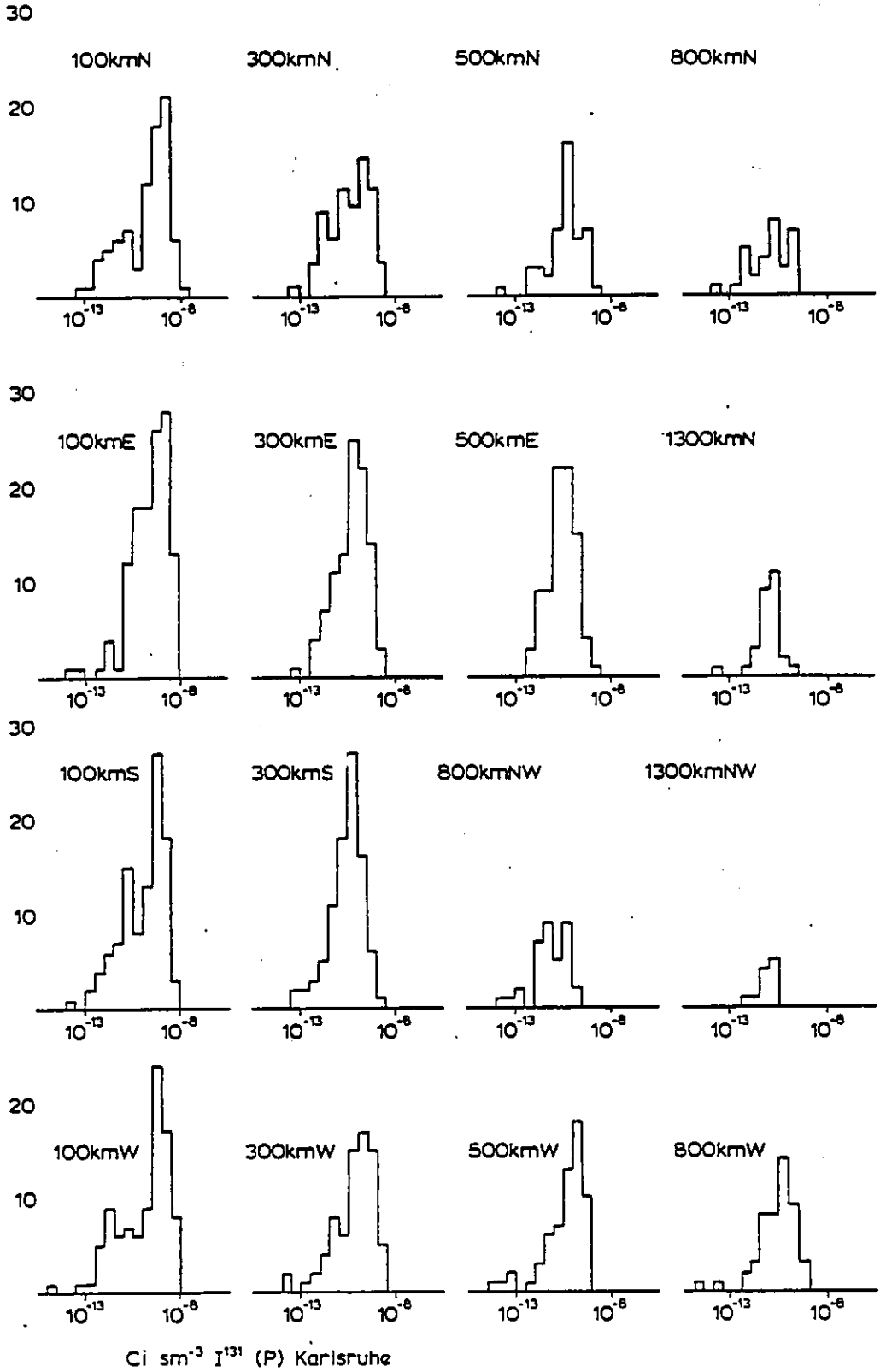



Figure (6.7) Histograms for Time Integrated Air Concentrations due to Unit Releases of I131(P) over 24 Hours from Karlsruhe during 1973

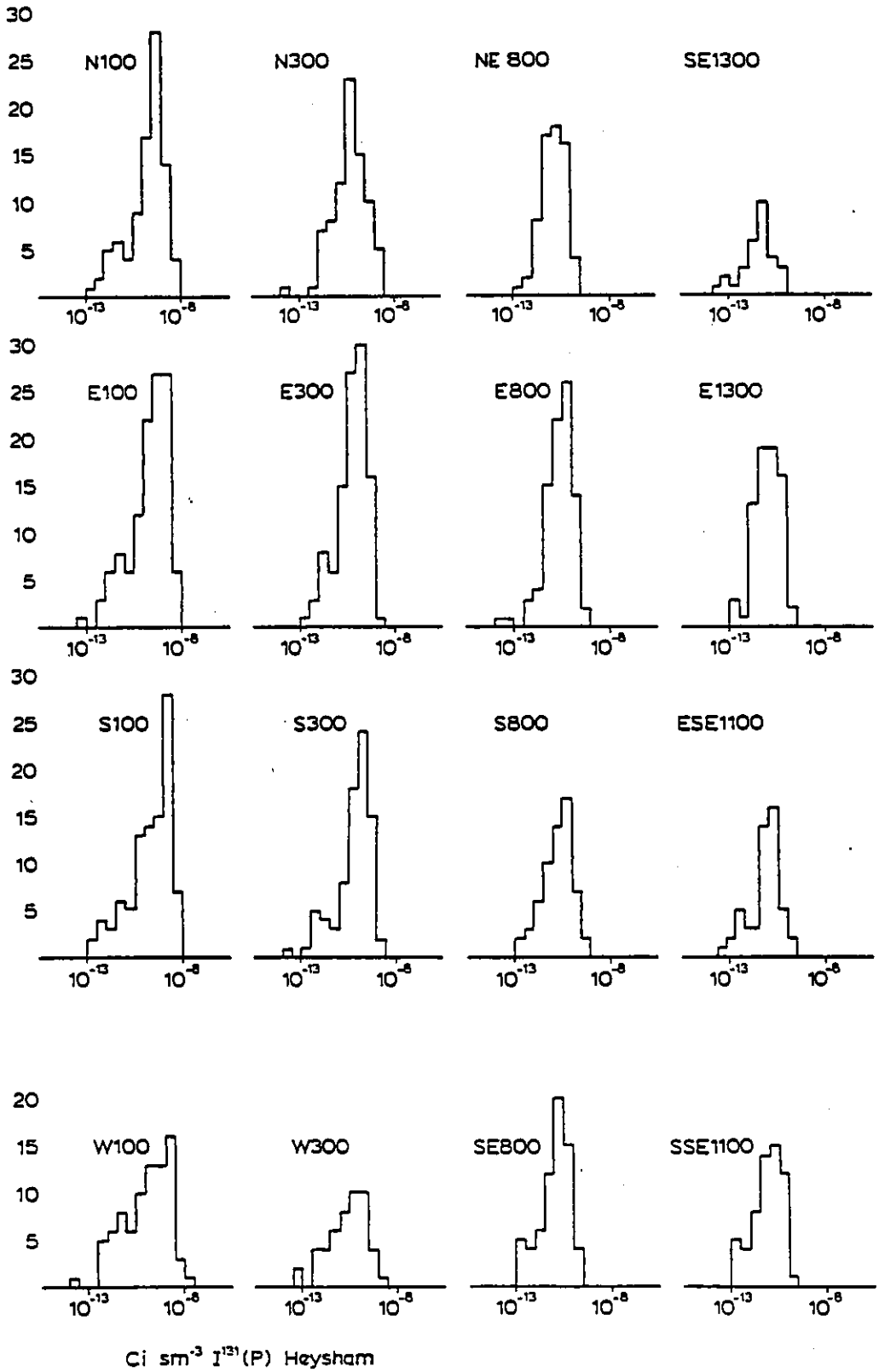



Figure (6.8) Histograms for Time Integrated Air Concentrations due to Unit Releases of I131(P) over 24 Hours from Heysham during 1973

ranging from three hours to seven days. The corresponding levels of I131(P) air contamination at the Mol receptors are shown in Table (5.6).

Levels of air contamination decrease with increasing receptor distance and release duration at each site. For a given release duration, average levels of I131(P) air contamination tend to decrease by a factor of 15 to 20 over distances between 100 km and 800 km from each site. At a fixed receptor, an increase in the release duration from three hours to seven days reduces the average air contamination by a factor of about seven. The dependence of average levels of exposure and probability of exposure on release duration has been discussed in Section (5.4.5). A simple square-root power law representation of this dependence appears to give an adequate approximation for most of the receptors considered in the 1973 studies.

When average air contamination is compared for receptors at corresponding distances and directions from each site, the variation is generally less than 50%. However, there is greater variability in the maximum levels of air contamination at corresponding receptors for each site. The maximum levels of air contamination appear to be lower for the Heysham releases, and this could be due to less frequent anticyclonic conditions over Northern England. The notable exception in the Heysham results is the maximum I131(P) air contamination at the 100 km West receptor, which is located over the Irish Sea. The time integrated I131(P) air concentration of 109,600 $pCi.s.m^{-3}$ is the largest I131(P) air contamination at all the receptors considered in the 1973 studies.

## 6.3 Comparison between the 1973 and 1976 Studies for Mol

The MESOS results for Mol, using the 1973 and 1976 meteorological databases, are compared in this section. The 1976 database extends further south (Figure (6.1)) than that for 1973, thus allowing dispersion over a larger area, including Southern Italy and part of

| Receptor Points | Average time integrated atmospheric concs. when exposed ($pCi\ s\ m^{-3}$) | | | | | | Maximum time integrated atmospheric concs. ($pCi\ s\ m^{-3}$) | | | | | |
|---|---|---|---|---|---|---|---|---|---|---|---|---|
| | 3hrs | 6hrs | 12hrs | 1day | 3days | 7days | 3hrs | 6hrs | 12hrs | 1day | 3days | 7days |
| N100 | 2936 | 2168 | 1528 | 1097 | 641 | 404 | 28560 | 25800 | 19470 | 13570 | 4630 | 2012 |
| N300 | 621 | 461 | 325 | 229 | 126 | 80 | 6563 | 3647 | 3238 | 2111 | 1001 | 434 |
| N500 | 395 | 282 | 206 | 144 | 74 | 39 | 3822 | 2686 | 1946 | 1041 | 431 | 185 |
| N800 | 159 | 108 | 66 | 46 | 27 | 15 | 928 | 632 | 556 | 278 | 157 | 72 |
| N1300 | 57 | 41 | 29 | 20 | 13 | 7 | 321 | 307 | 216 | 108 | 56 | 24 |
| E100 | 2947 | 2142 | 1512 | 1075 | 682 | 551 | 46880 | 28610 | 15340 | 8495 | 3946 | 2109 |
| E300 | 545 | 384 | 266 | 178 | 111 | 85 | 6179 | 4365 | 2182 | 1335 | 760 | 458 |
| E500 | 310 | 216 | 141 | 93 | 57 | 45 | 3560 | 2565 | 1674 | 1039 | 509 | 304 |
| S100 | 1817 | 1285 | 902 | 655 | 395 | 322 | 25040 | 15540 | 10920 | 7712 | 3362 | 1903 |
| S300 | 271 | 195 | 135 | 98 | 58 | 38 | 5768 | 2927 | 2556 | 1305 | 435 | 187 |
| W100 | 2682 | 1963 | 1433 | 945 | 582 | 423 | 29630 | 17040 | 12060 | 8471 | 3339 | 2706 |
| W300 | 662 | 461 | 331 | 227 | 135 | 97 | 6092 | 3789 | 1991 | 1277 | 659 | 387 |
| W500 | 383 | 283 | 207 | 143 | 82 | 57 | 2757 | 1871 | 988 | 711 | 430 | 323 |
| W800 | 214 | 168 | 122 | 88 | 49 | 35 | 2079 | 1198 | 782 | 560 | 384 | 209 |
| NW800 | 107 | 78 | 51 | 32 | 12 | 7 | 786 | 576 | 460 | 305 | 65 | 29 |
| NW1300 | 61 | 38 | 24 | 13 | 6 | 3 | 181 | 111 | 56 | 28 | 17 | 7 |

Table (6.1) Maximum and Average Time Integrated I131(P) Air Concentrations from Karlsruhe Releases during 1973

| Receptor Points | Average time integrated atmospheric conc. when exposed. ($pCi\ s\ m^{-3}$) | | | | | | Maximum time integrated atmospheric concs. ($pCi\ s\ m^{-3}$) | | | | | |
|---|---|---|---|---|---|---|---|---|---|---|---|---|
| | 3hrs | 6hrs | 12hrs | 1day | 3days | 7days | 3hrs | 6hrs | 12hrs | 1day | 3days | 7days |
| N100 | 2138 | 1489 | 1001 | 694 | 409 | 307 | 19300 | 12380 | 8303 | 5603 | 3271 | 1539 |
| N300 | 654 | 440 | 294 | 197 | 121 | 91 | 5299 | 3664 | 2502 | 1913 | 1321 | 828 |
| NE800 | 101 | 69 | 45 | 31 | 17 | 10 | 1117 | 721 | 371 | 197 | 106 | 61 |
| E100 | 2851 | 1960 | 1333 | 863 | 517 | 401 | 28670 | 15840 | 13540 | 7593 | 5280 | 2442 |
| E300 | 568 | 378 | 239 | 180 | 102 | 78 | 5268 | 3166 | 1885 | 1675 | 639 | 370 |
| E800 | 196 | 132 | 89 | 61 | 38 | 29 | 1902 | 1450 | 971 | 489 | 252 | 135 |
| E1300 | 67 | 46 | 30 | 21 | 12 | 8 | 776 | 338 | 212 | 141 | 83 | 49 |
| ESE1100 | 85 | 52 | 24 | 21 | 11 | 7 | 1008 | 738 | 467 | 240 | 89 | 50 |
| SE800 | 108 | 71 | 44 | 26 | 14 | 9 | 1747 | 904 | 425 | 226 | 75 | 37 |
| SE1300 | 44 | 27 | 17 | 10 | 4 | 2 | 353 | 176 | 94 | 69 | 23 | 11 |
| SSE1100 | 68 | 40 | 30 | 20 | 11 | 7 | 354 | 290 | 287 | 211 | 84 | 36 |
| S100 | 2653 | 1919 | 1400 | 974 | 611 | 462 | 29520 | 15330 | 10800 | 8461 | 4844 | 2646 |
| S300 | 520 | 379 | 270 | 192 | 113 | 75 | 3886 | 3573 | 2213 | 1107 | 500 | 282 |
| S800 | 183 | 127 | 85 | 56 | 36 | 22 | 1709 | 1188 | 932 | 465 | 167 | 88 |
| W100 | 2420 | 1714 | 1210 | 878 | 518 | 382 | 109600 | 54970 | 29000 | 14780 | 5552 | 4484 |
| W300 | 329 | 214 | 154 | 107 | 73 | 65 | 4857 | 2824 | 1412 | 1305 | 555 | 260 |

Table (6.2) Maximum and Average Time Integrated I131(P) Air Concentrations from Heysham Releases during 1973

the Mediterranean, to be assessed. In addition, the 1976 database contains a nearly complete sequence of meteorological data with only one day of data missing. Consequently, more releases can be treated in the 1976 calculations and, in particular, it allows separate studies of Summer and Winter patterns of exposure.

The method of analysis is identical to that used for the 1973 studies. The trajectory rose for Mol during 1976 is presented and briefly discussed in relation to the prevailing synoptic pressure features during this period. The trajectory analysis is then used to interpret the patterns of annual average exposure for 1976. Levels of exposure from unplanned releases are directly compared for the two years at the set of receptors shown in Figure (6.1).

### 6.3.1 Trajectory Analysis

The directional distribution of the 2,880 trajectories initiated from Mol at three-hourly intervals during 1976, is shown in Figure (6.9). This trajectory rose can be compared with the Mol 1973 trajectory rose which is given in Figure (5.3).

The notable differences in the 1973 and 1976 trajectory roses for Mol can be reasonably explained in terms of the persistent anticyclonic conditions which occurred during the Summer of 1976. During this period the synoptic pressure field often featured a high pressure system centred over Southern Ireland (Green (1977)). The location of this high pressure system leads to a series of trajectories moving to the south-west of Mol. Trajectories to the east of Mol occur less frequently during 1976, and this may also be due to the prevailing anticyclonic features.

Although the directional distribution of trajectories is rather different for the two years, the systematic divergence of trajectories

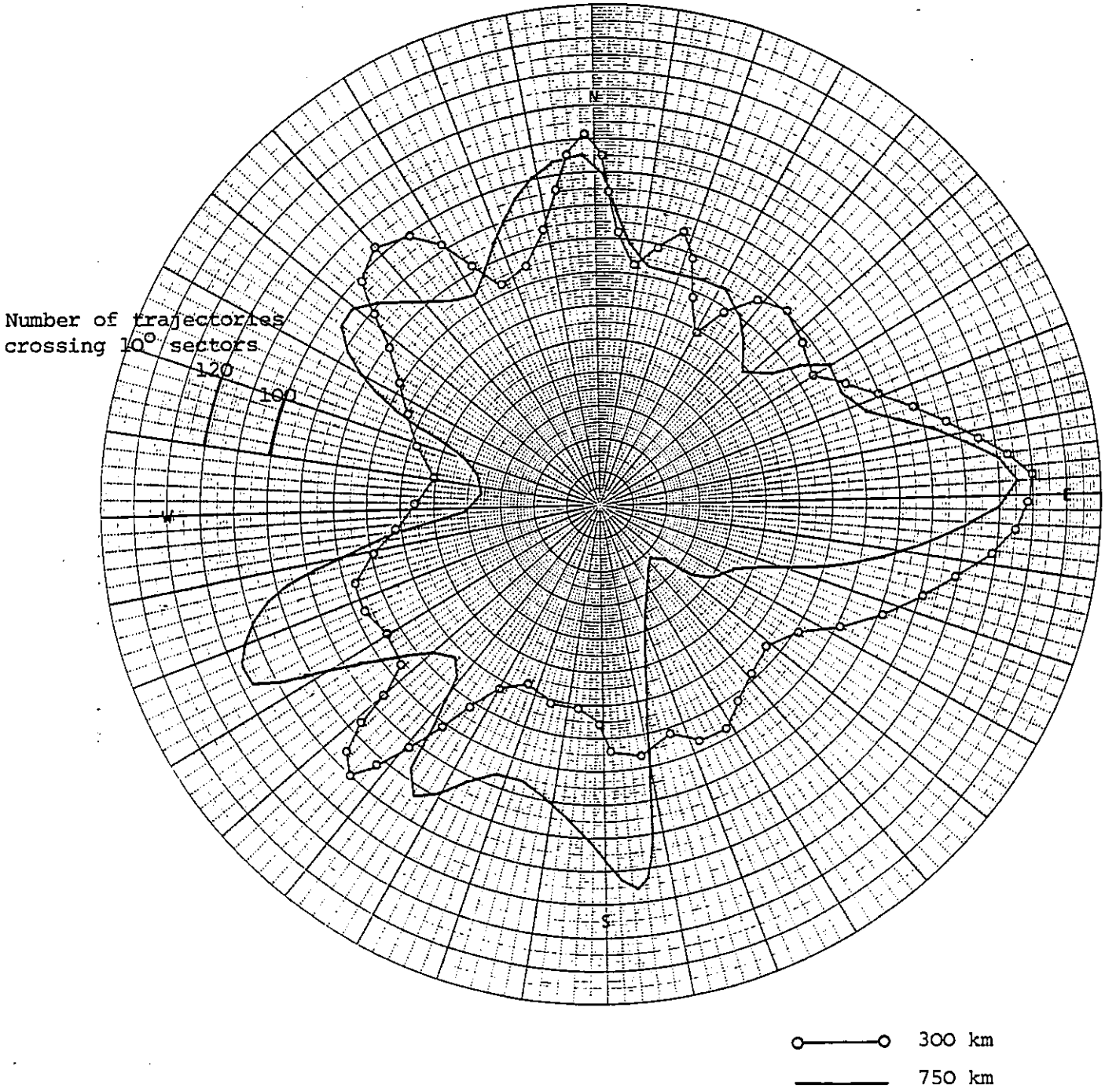



Figure (6.9) Trajectory Rose for Mol (1976)

to the south-east of Mol is still prominent in the 1976 trajectory rose. This effect is due to the geostrophic control of depressions near the Alps, and is represented in the Summer and Winter patterns of exposure which are discussed in the following section.

### 6.3.2 Long-Term Patterns of Exposure

#### (i) Summer and Winter releases from Mol during 1976

It is interesting to consider the separate contributions of Summer and Winter releases to the patterns of annual average exposure for 1976. These seasonal average exposures are compared in Figure (6.10) and relate to I131(P), Kr85 and Xe135 exposures from releases during the following six-monthly periods:

Summer period: April to September 1976
Winter period: January to March and October to December 1976

Releases from Mol during these two periods result in substantially different patterns of exposure, due to the characteristics of the synoptic pressure field controlling the long-range transport.

The persistent anticyclonic conditions during the Summer lead to relatively high Kr85 and 1131(P) air contamination, particularly to the south-west of Mol. Dispersion in stationary anticyclonic conditions is likely to lead to episodes of high contamination for these nuclides (Section (5.4.4)), and this can be seen by comparing the areas within corresponding contours for Summer and Winter exposures. For example, average Kr85 air contamination to the south-west of Mol is a factor of three higher during the Summer in comparison to the average contamination during the Winter months.

However, Xe135 air contamination tends to be lower during the Summer months due to the significant natural decay during the relatively slow transport in anticyclonic conditions. This feature of the

seasonal average Xe135 air contamination is more apparent for long-range transport from Mol.

Transport during the Winter months is primarily to the north and east of Mol. This indicates the more usual features of the synoptic pressure field with depressions moving across the British Isles to the north of Mol. The pattern of I131(P) wet deposition during the Winter also shows that rain is more likely in these trajectories which are associated with depressions. Wet deposition is considerably higher during the Winter, particularly to the north-west of Mol over the British Isles. Britain experienced a drought during the Summer, and this is reflected in very low levels of I131(P) wet deposition.

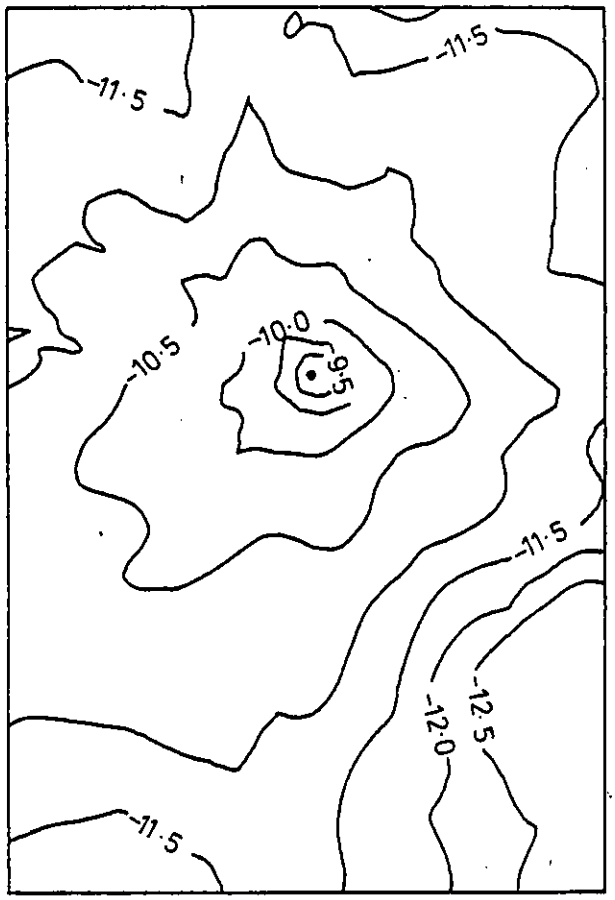
The extension of the map area to the south for the 1976 calculations gives a clear picture of the long-range transport around the Alpine barrier. Levels of contamination drop rapidly across the Alps and Northern Italy as trajectories are diverted over the South of France under the influence of depressions.

Most of Italy is protected from exposure, due to this blocking of trajectories by the depressions. However, further south, trajectories begin to recirculate eastwards and this effect is sufficient to increase levels of contamination with increasing distance from Mol, in the south-east corner of the map.

(ii) Comparison of annual average exposures for 1973 and 1976

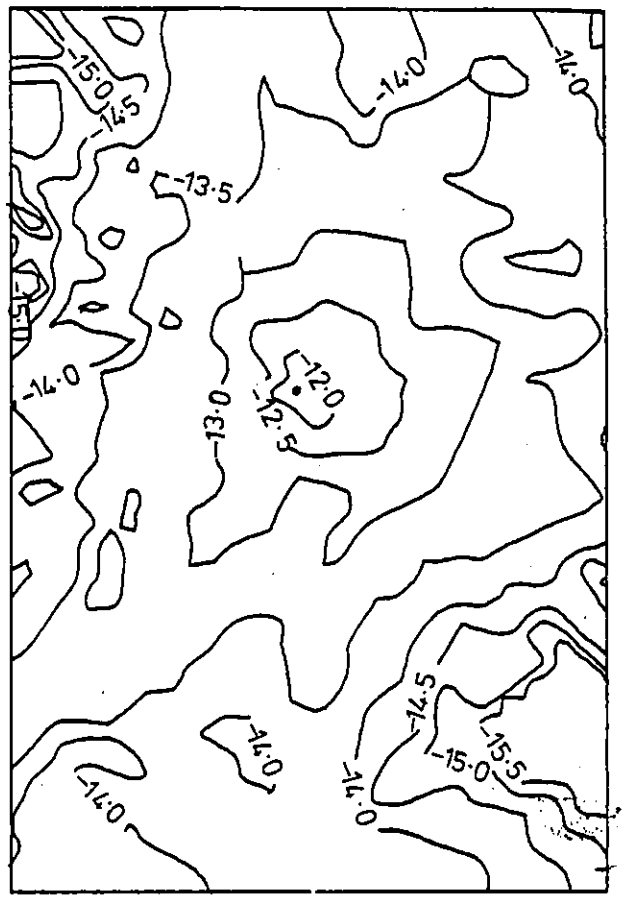
Annual average exposures for 1973 and 1976 are compared in Figure (6.11). These patterns of exposure relate to 1 Curie releases of I131(P), Kr85 and Xe135 through each year.

The contributions of Summer and Winter releases are clearly illustrated in the patterns of annual average exposure for 1976. The highest levels of I131(P) and Kr85 air contamination during 1976 occur to the




SUMMER

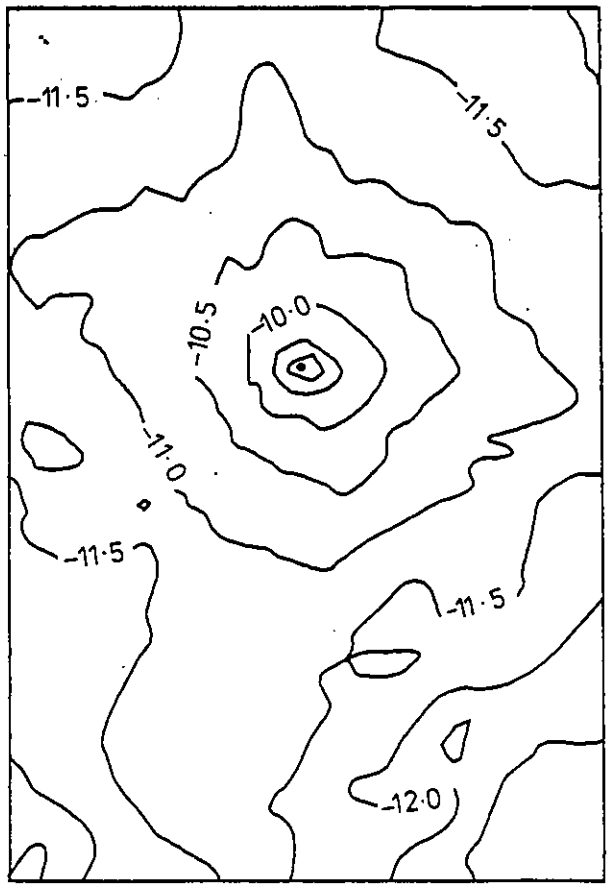
I131(P) time integrated air concentrations $\log_{10}$ (Ci.s.m$^{-3}$)




SUMMER

I131(P) wet deposition $\log_{10}$ (Ci.m$^{-2}$)

WINTER




WINTER

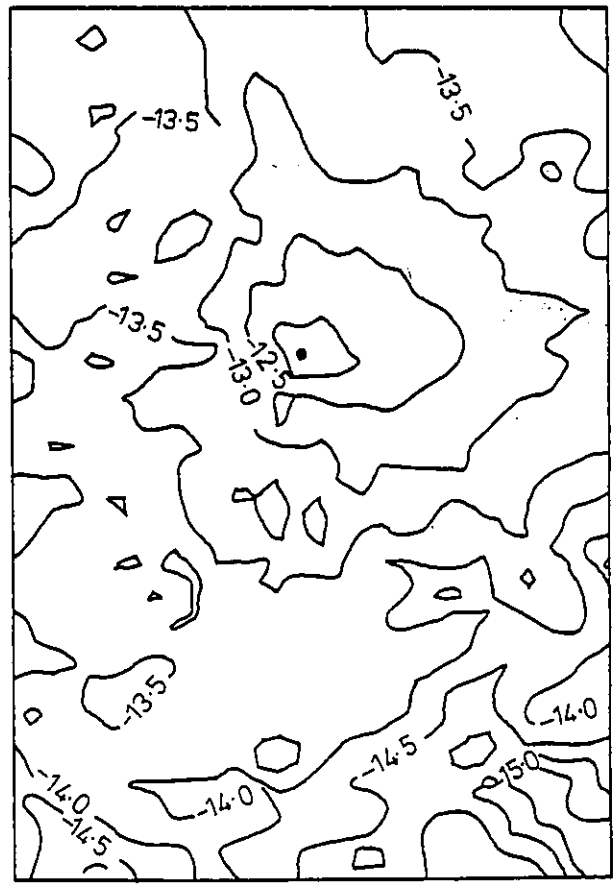
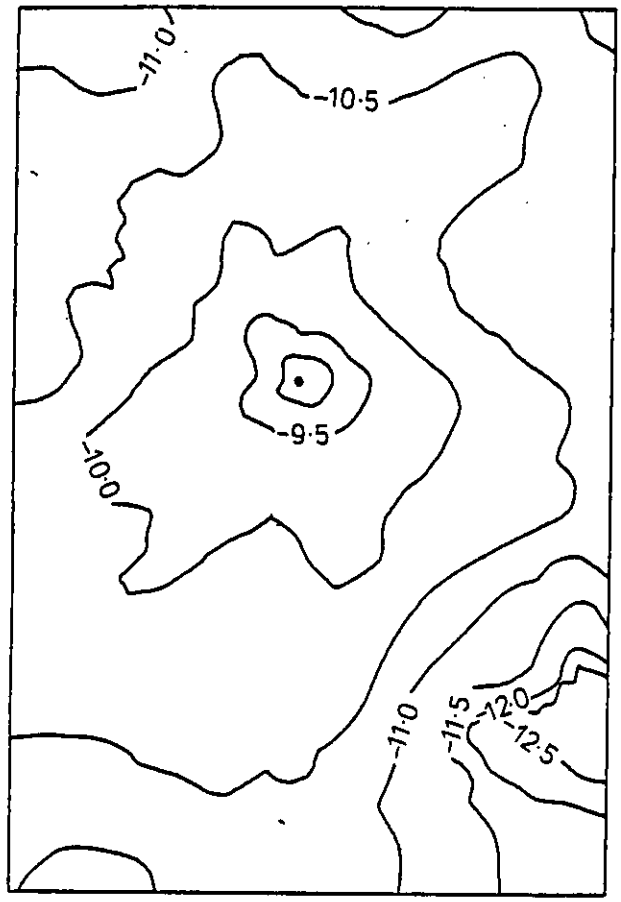
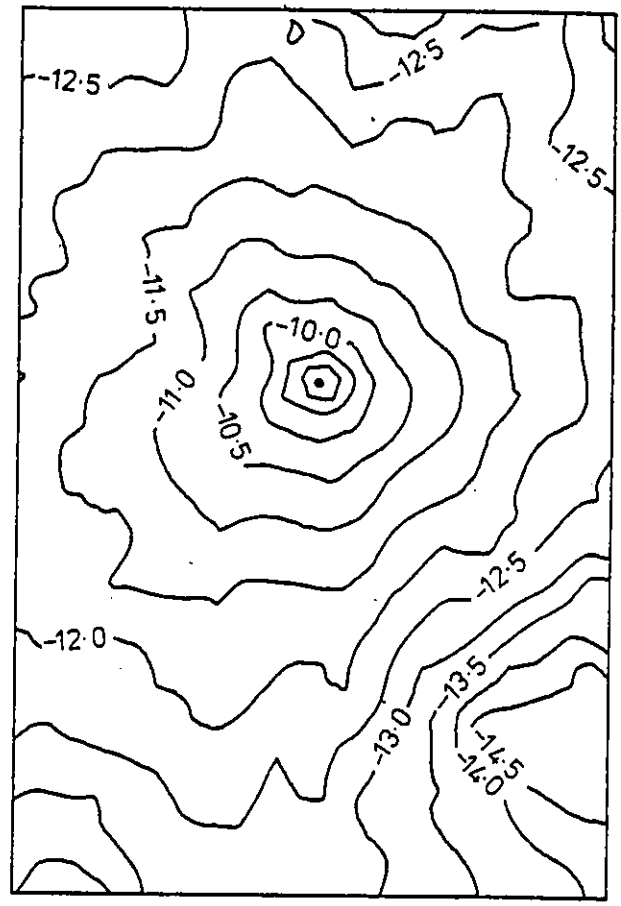


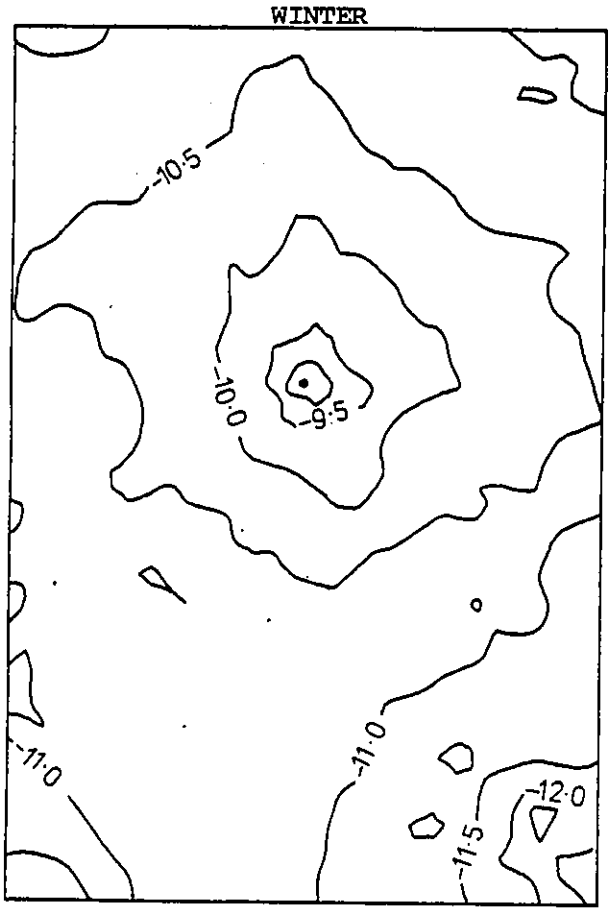

Figure (6.10a) Seasonal Average I131(P) Exposures from Mol Releases during 1976




Kr85 time integrated air concentrations $\log_{10}$ (Ci.s.m$^{-3}$)




Xe135 time integrated air concentrations $\log_{10}$ (Ci.s.m$^{-3}$)



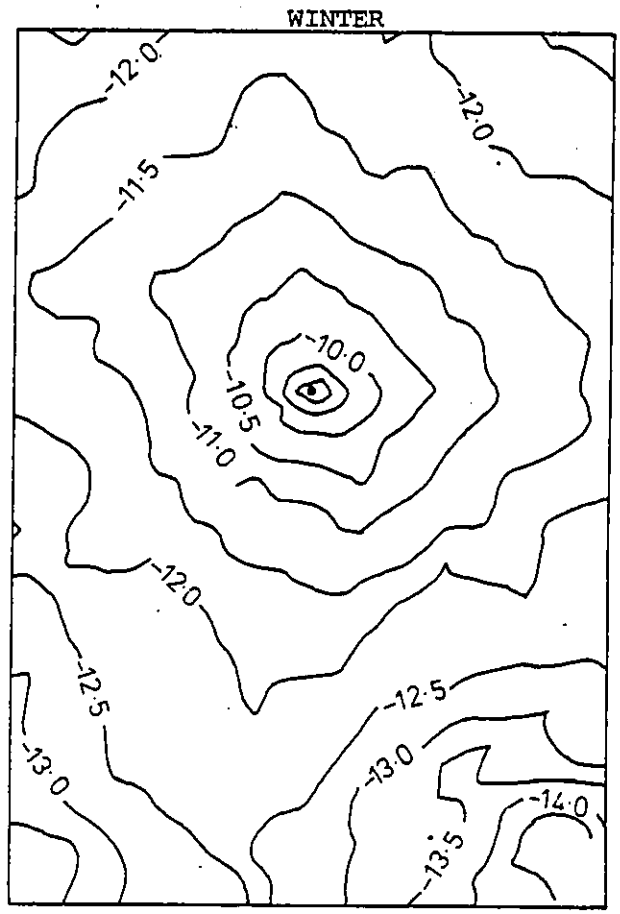
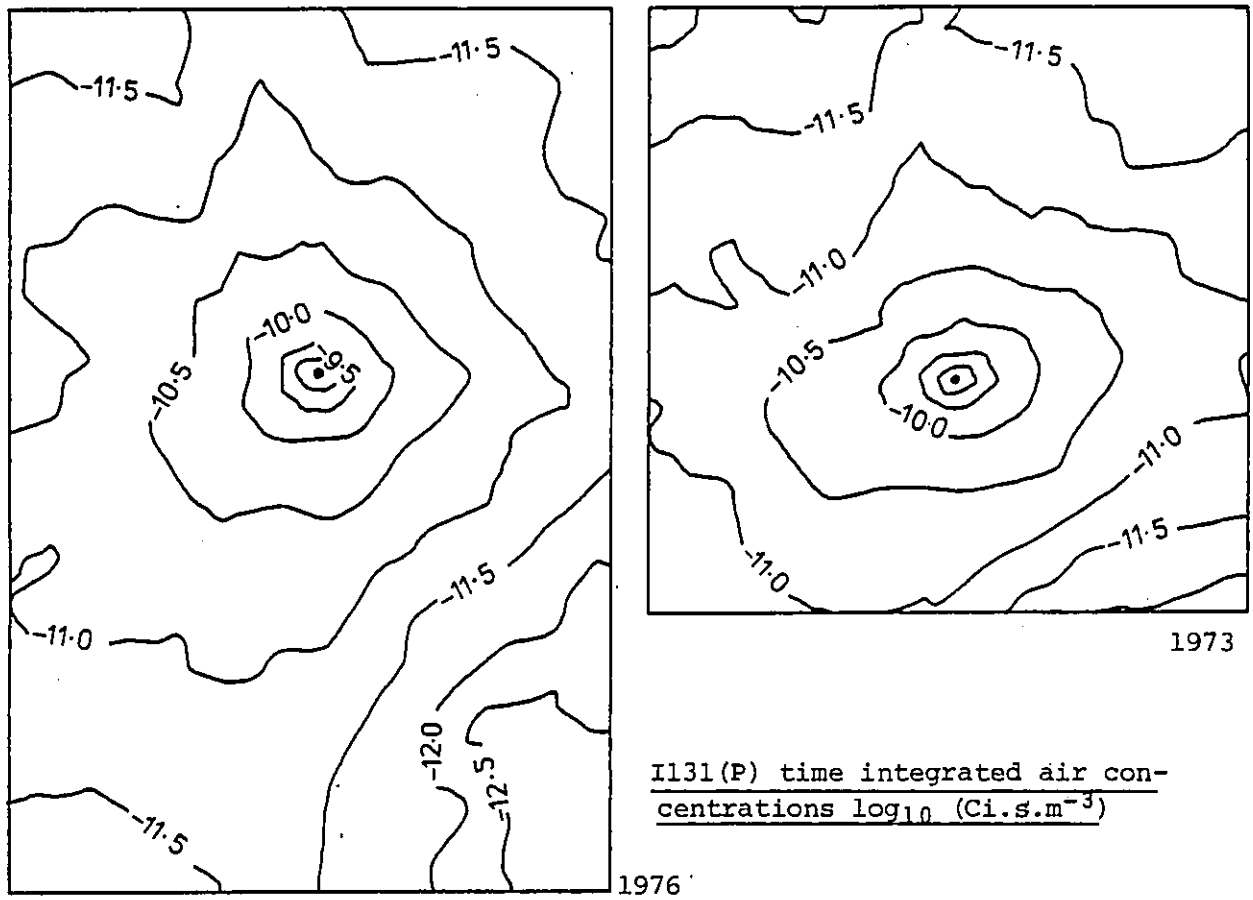
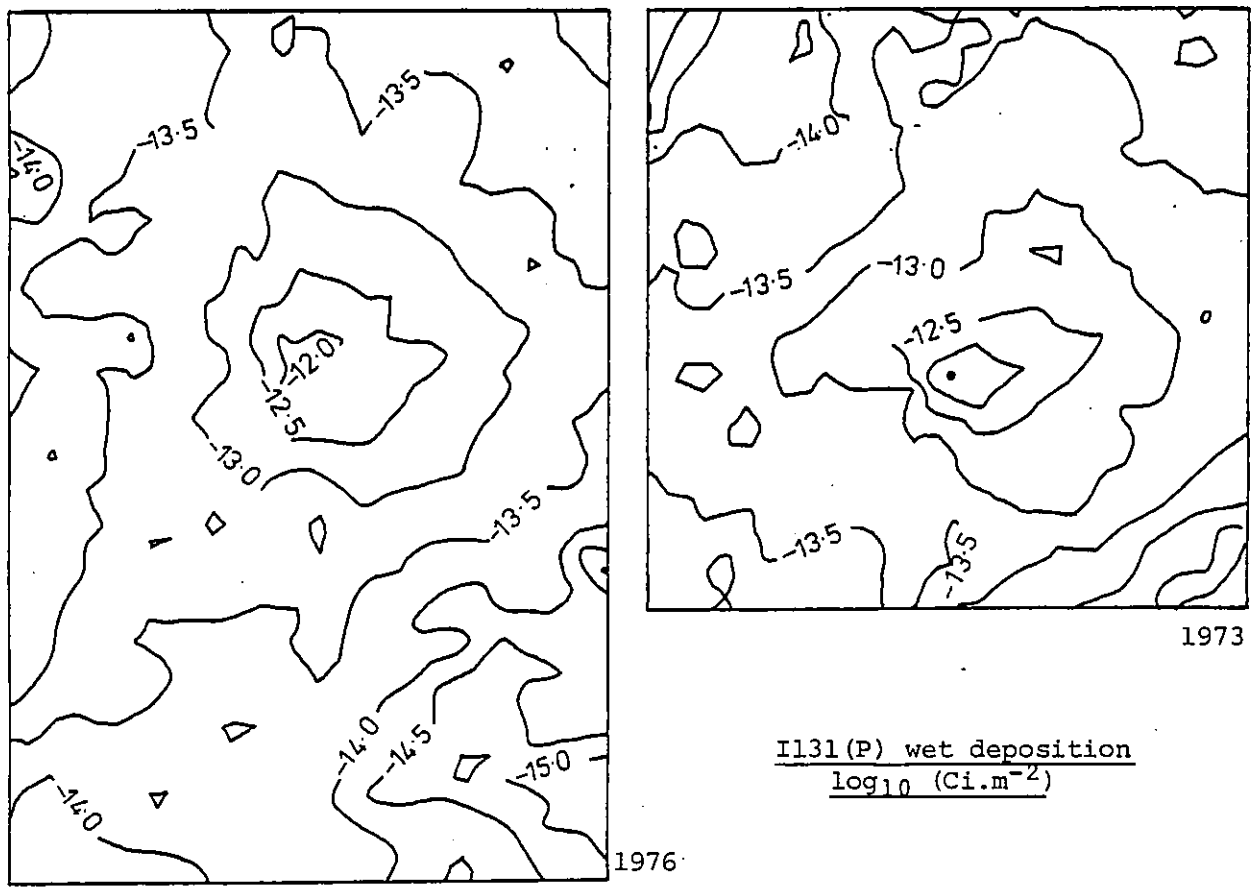




Figure (6.10b) Seasonal Average Kr85 and Xe135 Time Integrated Air Concentrations from Mol Releases during 1976

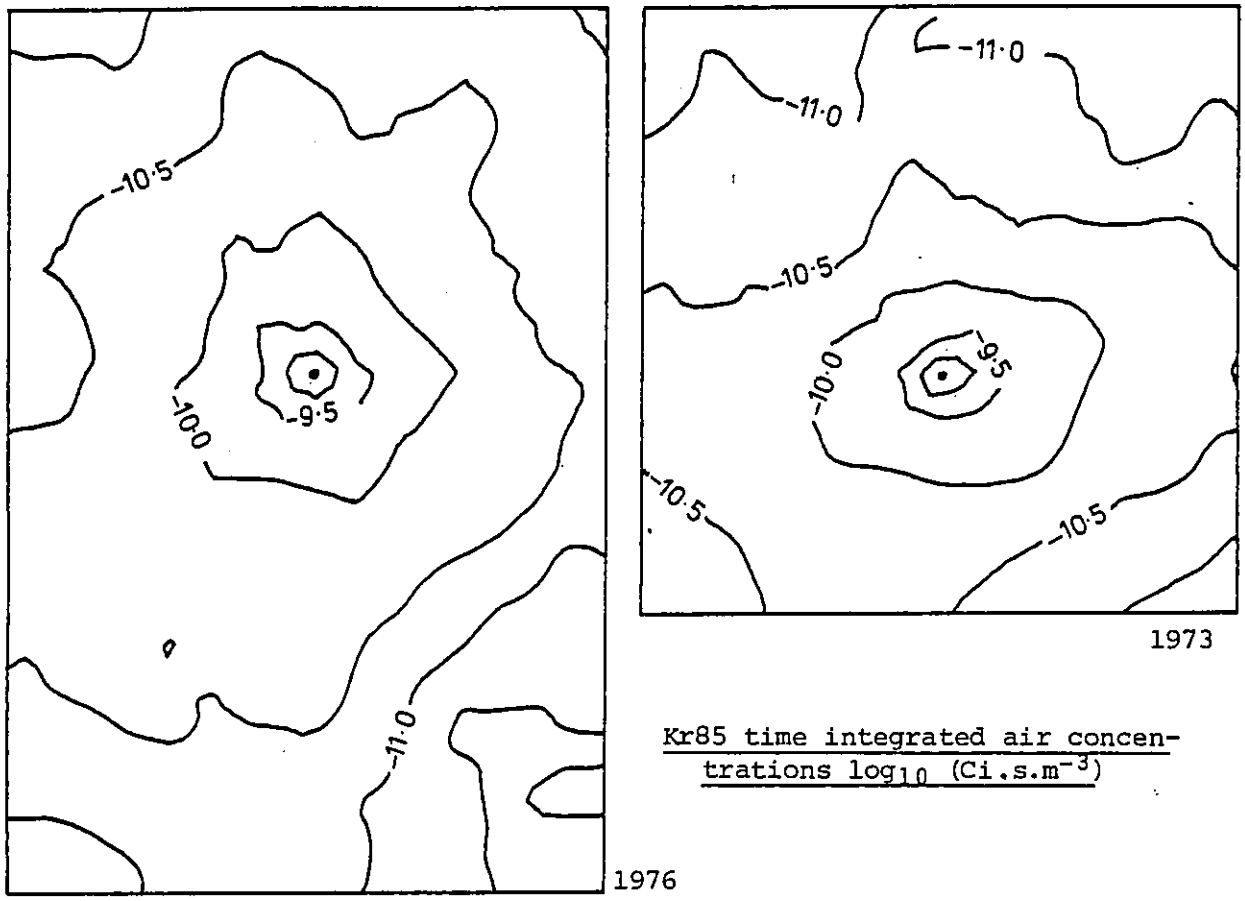



I131(P) time integrated air concentrations $\log_{10}$ (Ci.s.m$^{-3}$)

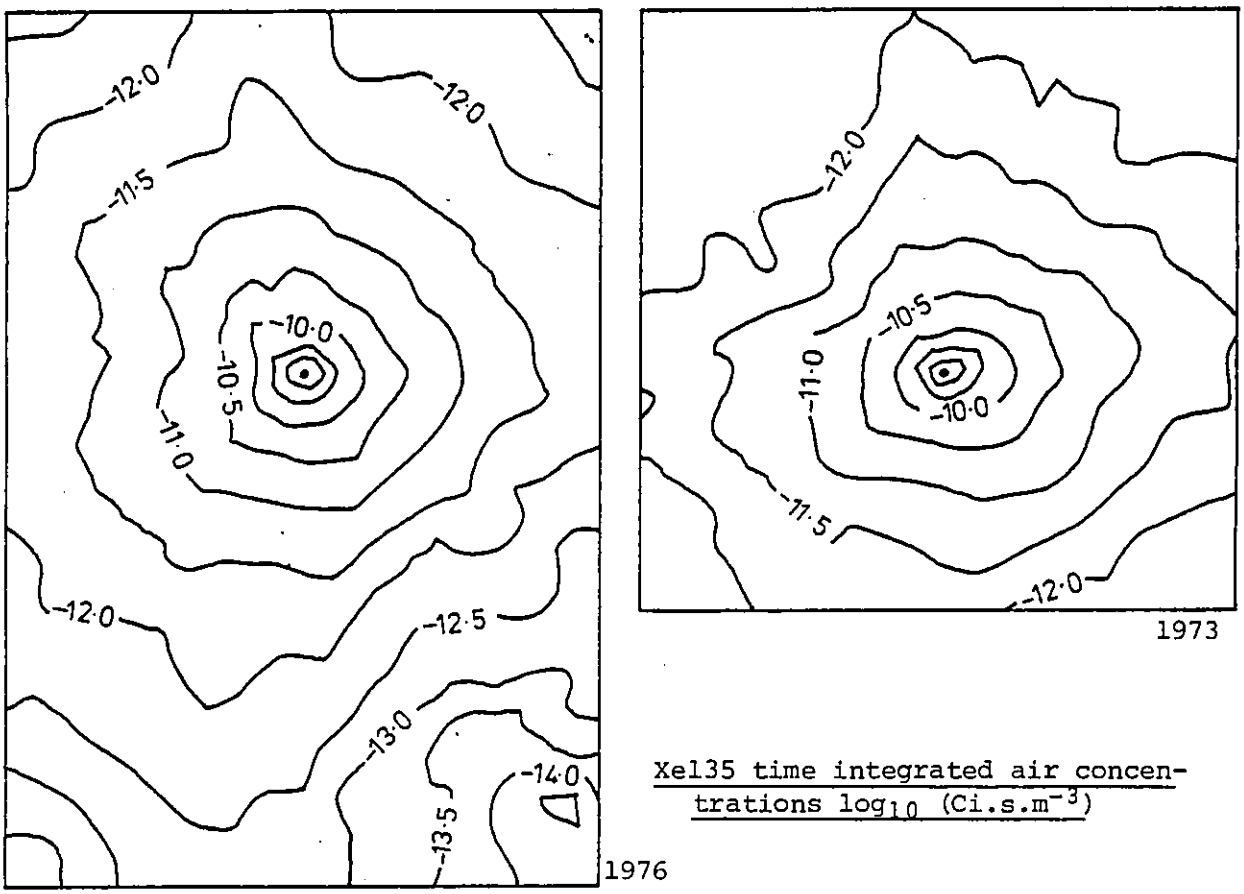



I131(P) wet deposition $\log_{10}$ (Ci.m$^{-2}$)

Figure (6.11a) Comparison of Annual Average I131(P) Exposures from Mol Releases during 1973 and 1976




Kr85 time integrated air concentrations $\log_{10}$ (Ci.s.m$^{-3}$)




Xe135 time integrated air concentrations $\log_{10}$ (Ci.s.m$^{-3}$)

Figure 6.11(b) Comparison of Annual Average Kr85 and Xe135 Time Integrated Air Concentrations from Mol Releases during 1973 and 1976

south-west and north of Mol, since these regions are most frequently exposed during the Summer and Winter months respectively. Annual average contamination in these directions are consequently greater for 1976. However, Westerlies were less frequent during 1976 and so the average air contamination to the east of Mol is lower. These differences in the patterns of air contamination for the two years can therefore be associated with the different trajectory distributions as represented in the 1973 and 1976 trajectory roses for Mol. Allowing for this, the patterns of air contamination are broadly similar and annual averages generally differ by less than a factor of two over the map area.

Annual average I131(P) wet deposition to the north of Mol is greater during 1976 due to the relatively high frequency of wet trajectories moving in this direction during the Winter months. In particular, annual average wet deposition over the British Isles is greater for 1976 despite the very dry Summer. However, the broad-scale features of wet deposition are comparable for the two years and reflect the wetness characteristics of westerly and south-westerly winds over North-West Europe.

### 6.3.3 Exposure from Notional Unplanned Releases

Levels of exposure due to notional unplanned releases from Mol during 1973 and 1976 are discussed in this section. The probabilities of exposure at each of the Mol receptors are compared for 1973 and 1976 in Figure (6.12). Maximum and average exposures are also compared for three-hourly releases of I131(P) and Kr85 throughout each year.

Average time integrated concentrations when receptors are exposed are generally higher for releases during 1976, but are mainly within a factor of two of the 1973 averages. The higher air contamination at receptors to the east and south of Mol is partially offset by the lower probabilities of exposure so that annual averages are more comparable for the two years. In fact, there is a general tendency for average

air contamination and probability of exposure to be inversely correlated. This effect can be considered in terms of the separation between successive trajectories describing the lateral dispersion of a release; small lateral dispersion will give relatively high contamination at a receptor, but the probability of exposure will be correspondingly low. Relatively small lateral dispersion and trajectory separation are likely to occur in stationary anticyclonic conditions (Section (5.4.4)) and such conditions prevailed during the Summer of 1976.

However, the probability of exposure also depends on the frequency of trajectories which travel towards the receptor. For example, both the probability of exposure and Kr85 average air contamination are higher for receptors to the north of Mol during 1976. Average I131(P) air contamination tends to be slightly lower in this direction during 1976 due to the higher probability of wet deposition during transport to the north. This is particularly noticeable at increasing distances to the north where I131(P) wet deposition is systematically higher during 1976.

The probabilities and average levels of wet deposition at receptors show a greater variability over the two years than the corresponding air exposures. For example, during 1976 the I131(P) wet deposition is a factor of four lower at the 300 and 500 km West receptors, but wet deposition is a factor of two higher at the 800 km West receptor. Maximum levels of wet deposition and air contamination can also vary by factors of four or more at corresponding receptors for each year. These variations indicate that the exposure frequency distributions at receptors can be non-stationary with respect to the period under consideration. This possible non-stationarity is likely to complicate the modelling of the exposure frequency distributions and the forecasting of maximum levels of exposure for different years.

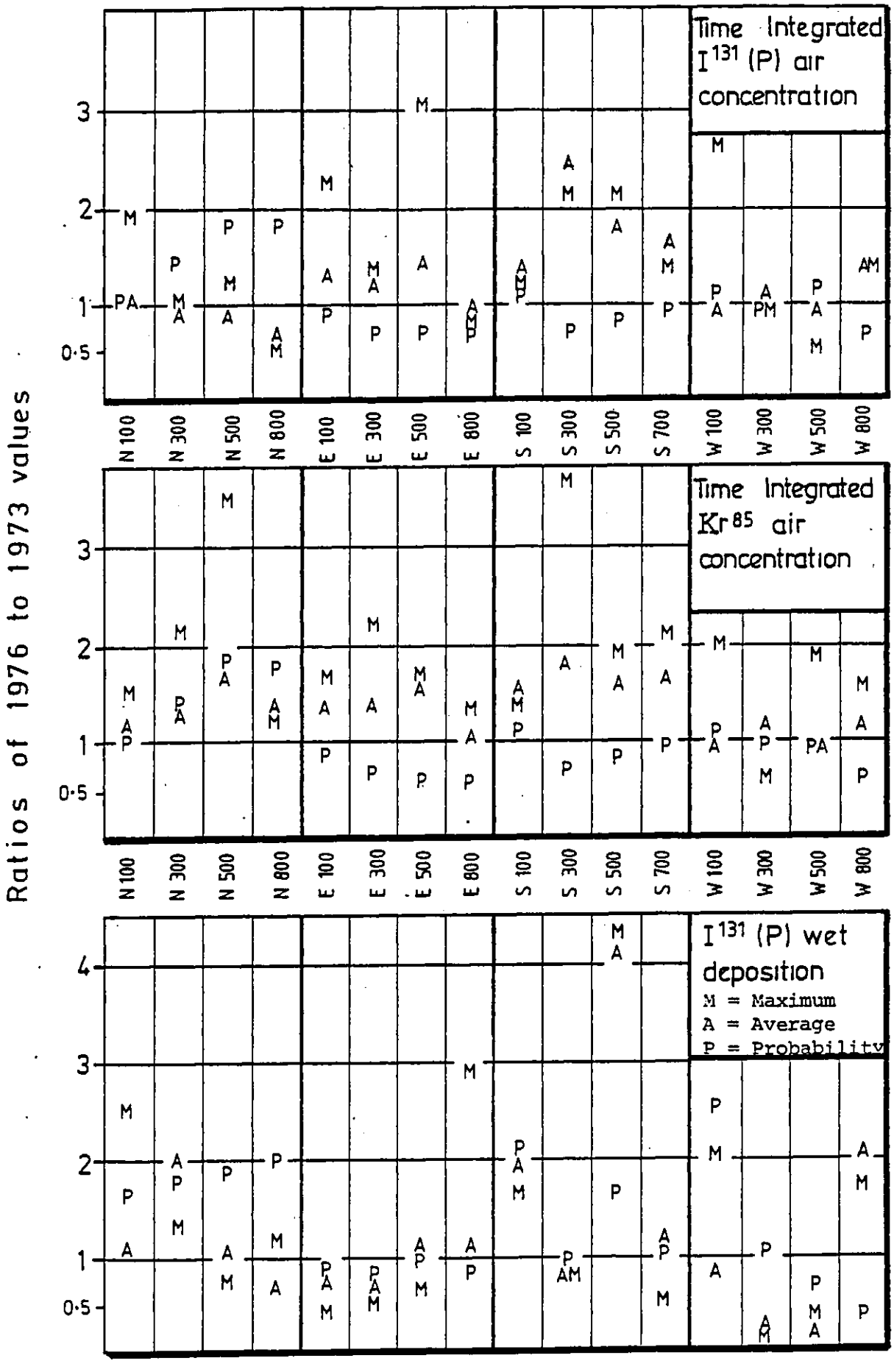



Figure (6.12) Comparison of Receptor Exposure Characteristics for Three-Hourly Releases from Mol during 1973 and 1976

## 6.4 Summary

The MESOS model and meteorological databases have been used to study the long-range dispersion of notional nuclide releases from Mol, Karlsruhe and Heysham. Annual average patterns of exposure and frequency distributions of exposure have been selectively presented and compared for releases from each of these sites during 1973. The sensitivity of long-term patterns of exposure to the release period has also been considered in connection with nuclide releases from Mol during 1973 and 1976.

Trajectory analyses have been used to interpret the annual average patterns of exposure from each site. Since the long-range transport is controlled by the sequence of changing pressure fields, the patterns of exposure may vary considerably with site location and the release period. Consequently, there are substantial differences in the patterns of exposure from Heysham releases in comparison to releases from Mol and Karlsruhe during the same period. This can be reasonably explained by the location of Heysham with respect to the typical movement of depressions across the British Isles. The seasonal average exposures from Mol releases during 1976 also differ significantly, due to the persistent anticyclonic features during the Summer. However, the annual average patterns of exposure for 1973 and 1976 are broadly similar over most of the European map area.

The frequency distributions of exposure at remote receptors are particularly sensitive to the frequency of relatively direct transport between source and receptor, and can be described qualitatively in these terms. Consequently, is it not generally possible to assume that the frequency distributions of exposure at a given receptor remain stationary over different time periods. For example, the probability of exposure, maximum and average levels of exposure at a receptor can vary by a factor of four or more when releases from Mol during 1973 and 1976 are compared. The magnitude of this variation, even in long-term statistics, emphasises the need to give careful consideration to the prevailing meteorological conditions during the period of interest.

# CHAPTER 7 CONCLUSIONS

## 7.1 Contributions of the Work

The long-range dispersion of an atmospheric release of pollutant has been shown to be strongly influenced by the continuously changing meteorological conditions along the path of the release. Consequently, for realistic modelling, it is important to know the spatial and temporal changes in meteorological conditions over a wide area. Methods have been developed to process routine reports of meteorological data from the European network of weather stations and ships into a form suitable for use in long-range dispersion models. A large meteorological database has been established for Europe. This information includes synoptic pressure fields, temperature, cloud-cover and rainfall which are available at three-hourly intervals for most of 1973 and throughout 1976. The methods of data processing can also be applied to any other period of routine meteorological reporting.

The MESOS model has been developed into a form which allows reported meteorological data to be incorporated into the description of long-range dispersion. The variable state of the boundary layer and time dependent depletion processes (dry and wet deposition) are assessed from the local meteorological conditions along the trajectories of specimen puffs. These puff trajectories are derived from the synoptic pressure data so that the lateral dispersion of a plume is modelled explicitly. Reported meteorological data is used in specifying the vertical structure of the boundary layer in terms of stability conditions and the mixing layer depth. Variations in the mixing depth effectively control the vertical development of material during long-range transport. An efficient numerical scheme has been incorporated into the MESOS program in order to improve the treatment of mixing layer development.

Attempts to determine rainfall location and intensity from reports on the present weather code have also given a better representation of

precipitation scavenging within the model.

The application of the MESOS model in the study of accidental releases from Windscale during October 1957 has enabled model calculations to be compared with measurements. Although the MESOS predictions are in broad agreement with measurements, the uncertainties in the exact release pattern and the boundary layer trajectories tend to make an accurate analysis of the accident rather difficult. The study has indicated some of the inherent uncertainties associated with modelling short-term accidental releases in a real situation. A detailed knowledge of nuclide emissions and atmospheric conditions, as well as the use of more sophisticated modelling techniques, are probably necessary for determining the dispersion of accidental releases with confidence.

Although the MESOS model may presently lack the sophistication for use in a predictive mode in real accidental conditions, a useful methodology has been developed in which the consequences of accidental releases can be quantified using a statistical treatment. This methodology has been demonstrated in the dispersion studies of notional unplanned releases from selected European sites. The probability of different levels of time integrated air concentrations, dry and wet depositions resulting from notional releases (ranging from three hours to seven days) have been derived for a selection of important nuclides including I131, Cs137 and Kr85. The consequences of routine releases from nuclear installations have also been assessed by considering the cumulative effect of short-term releases to give annual average patterns of nuclide exposure. In addition, analyses of the dispersion calculations have produced several interesting results relating to the nature of long-range dispersion in real meteorological conditions.

## 7.2 Future Work

The extensive dispersion calculations using MESOS and the meteorological databases have yielded a large body of useful information

which may be used for further studies. This information includes time series of boundary layer trajectories, airborne pollutant fluxes, ground depositions and exposure patterns over a wide area. Only a partial examination of this information has been possible during the present work, and further analyses may lead to a better understanding of many important topics. Moreover, there is scope for incorporating the MESOS results into simpler methods to simulate patterns of long-term exposure and frequency distributions of exposure from short releases.

The existing MESOS results may also be used to assess European population doses resulting from routine nuclide releases. External irradiation and inhalation collective dose distributions can be derived directly from the patterns of annual average air contamination by combining with population distributions and applying appropriate dose factors. Similarly, the patterns of annual average dry and wet depositions may be combined with agricultural production data to determine the contamination of foodstuffs which are available for consumption. This work has already been undertaken for notional nuclide releases during 1973 (ApSimon et al (1981)).

The MESOS model, meteorological databases and the general methodologies described in this thesis can be used to study the atmospheric dispersion of other pollutants such as $SO_2$.

The MESOS model also has potential for further development. The following additional features could be introduced and quantified from the existing meteorological data:

- Plume rise
- Ageostrophic effects in the windfield
- The effects of large-scale vertical motions in the atmosphere
- Improved treatment of small-scale lateral dispersion

Although such refinements may cause excessive computer costs for routine use of the program, they could be usefully included to study, in greater detail, a few episodes which have already been identified as showing interesting dispersion characteristics.

REFERENCES

ApSIMON, H.M., CROMPTON, S., GODDARD, A.J.H. and WRIGLEY, J. (1981, 1980)
"Atmospheric transport of radioisotopes and the assessment of population doses on a European scale"
Environmental Safety Group, Mech.Eng. Dept., Imperial College, London.
Internal reports: SAF 034, January 1981; SAF 025, July 1980.

ApSIMON, H.M., GODDARD, A.J.H. and WRIGLEY, J. (1980a)
"Estimating the transfrontier consequences of accidental releases: the MESOS model for long-range atmospheric dispersal"
Proc. CEC Seminar, 22-25 April 1980, Risø, Denmark, Vol II, pp 819-842.

ApSIMON, H.M., EARNSHAW, D., GODDARD, A.J.H. and WRIGLEY, J. (1978)
"Modelling of meso-scale atmospheric dispersion and the application of the MESOS model to the 1957 Windscale release"
Environmental Safety Group, Mech.Eng. Dept., Imperial College, London.
Final Report Contract 1113-77-10 L/V, SAF 013, October 1978.

ApSIMON, H.M., EARNSHAW, D., GODDARD, A.J.H. and WRIGLEY, J. (1978a)
"On the importance of the vertical structure of the boundary layer in modelling the long-range transport following an accidental release of pollutant"
WMO Symposium on Boundary Layer Physics applied to Specific Problems of Air Pollution, Norrköping, Sweden, June 1978.

ARIS, R. (1956)
"On the dispersion of a solute in a fluid flowing through a tube"
Proc. Roy. Soc. A235, pp 67-77.

ATOMIC ENERGY OFFICE (1957)
"The accident at the Windscale No. 1 pile on 10th October 1957"
HMSO, London, Cmnd. 302.

BETTS, A. K. (1973)
"Non-precipitating cumulus convection and its parameterization"
Quart. J.R. Met. Soc. 99, pp 178-196.

/Continued ...

References (continued)

CARSON, D.J. and SMITH, F.B. (1977)
"Some thoughts on the specification of the boundary layer relevant to numerical modelling"
Boundary Layer Met. 12, pp 307-330.

CARSON, D.J. and SMITH, F.B. (1974)
"Thermodynamic model for the development of a convectively unstable boundary layer"
Advances in Geophysics 18A, pp 111-124.

CARSON, D.J. (1973)
"The development of a dry inversion-capped convectively unstable boundary layer"
Quart. J.R. Met. Soc. 99, pp 450-467.

CHAMBERLAIN, A.C. (1980)
Private communication on the choice of nuclide deposition rates

CHAMBERLAIN, A.C. (1959)
"Deposition of I131 in Northern England in October 1957"
Quart. J.R. Met. Soc. 85, pp 350-361

CLARKE, R.H. (1979)
"A model for the short and medium range dispersion of radionuclides released to the atmosphere"
Working Group on Atmospheric Dispersion, NRPB-R91, HMSO, London.

CLARKE, R.H. (1974)
"An analysis of the 1957 Windscale accident using the WEERIE code"
Annals of Nucl. Sci. and Eng. 1, pp 73-82.

CRABTREE, J. (1959)
"The travel and diffusion of the radioactive material emitted during the Windscale accident"
Quart. J.R. Met. Soc. 85, pp 363-371.

/Continued ...

References (continued)

CSANADY, G.T. (1973)
"Turbulent Diffusion in the Environment"
Reidel Publishing Co., Dordrecht.

DEARDORFF, J.W. (1972)
"Parameterization of the planetry boundary layer for use in general circulation models"
Monthly Weather Review 100, No. 2, pp 93-106

DRAXLER, R.R. and ELLIOT, W.P. (1977)
"Long-range travel of airborne material subjected to dry deposition"
Atmos. Env. 11, pp 35-40

DURST, C.S., CROSSLEY, A.F. and DAVIS, N.E. (1959)
"Horizontal diffusion in the atmosphere as determined by geostrophic trajectories"
Journ. Fluid Mech. 6, pp 401-422

DUTTON, (1977)
Private communication on temperature profiles

ENGELMANN, R.J. (1971)
"Scavenging prediction using ratios of concentrations in air pollution and precipitation"
Journ. App. Met. 10, pp 493-497

ENGELMANN, R.J. (1965)
"Calculation of precipitation scavenging"
USAEC Report BNWL77, Battelle Northwest Lab., July 1965.

FRYER, L.S. and KAISER, G.D. (1978)
"TIRION4 - A computer program for use in nuclear safety studies"
Safety and Reliability Directorate, Report SRD R134, U.K.A.E.A., Culcheth, Warrington.

/Continued ...

References (continued)

GIFFORD, F.A. (1976)
"A review of turbulent diffusion typing schemes"
Nucl. Safety 17, pp 68-86

GREEN, J.A. (1977)
"The weather during July 1976; some dynamical considerations of the drought"
Weather 32, no. 4, pp 121-126

GUMBEL, E.J. (1958)
"Statistics of Extremes"
Columbia University Press, New York

HARDY, R.N. (1975)
"Statistics of inversions at Cardington in Bedfordshire"
Met. Office Note 108, Bracknell, Berks.

HARRISON, R.M. and HOLMAN, C.D. (1979)
"The contribution of middle and long-range transport of tropospheric photochemical ozone to pollution at a rural site in N.W. England"
Atmos. Env. 13, pp 1535-1545.

HEFFTER, J.L. (1964)
"The variation of horizontal diffusion parameters with time for periods of one hour or longer"
Journ. App. Met. 4, pp 153-156

HORST, T.W. (1977)
"A surface depletion model for deposition from a Gaussian Plume"
Atmos. Env. 11, pp 41-46.

INOUE, E. (1952)
"On the Lagrangian correlation coefficient for turbulent diffusion"
Air Force Cambridge Research Center, Geo. Res. Papers, No. 19, p. 397.

/Continued ...

References (continued)

INTERNATIONAL COMMISSION ON RADIOLOGICAL PROTECTION (1977)
"Recommendations of the ICRP"
ICRP Publication 26, Annals of the ICRP, 1, 3, Pergamon Press, Oxford.

LARSEN, R.I. (1969)
"A new mathematical model of air pollutant concentration averaging time and frequency"
Journ. Air Pollut. Control Assess., 19, pp 24-30

LE GRAND, J. DEPRÈS, A. and DOURY, A. (1980)
"Le programme de calcul TALD pour l'évaluation des transferts atmosphériques à longue distance dans les basses couches de l'atmosphère.
Proc. CEC Seminar, April 1980, Risø, Denmark, Vol. II, pp 743-776

MAUL, P.R. (1980)
"Atmospheric transport of sulphur compound pollutants"
Ph.D thesis, London University.

MAUL, P.R. (1977)
"The mathematical modelling of the mesos-scale transport of gaseous pollutants"
Atmos. Env. 11, pp 1191-1195.

METEOROLOGICAL OFFICE (1975)
"Handbook of Weather Forecasting"
Chapter 17, Met. 0875, Met. Office, Bracknell, Berks.

METEOROLOGICAL OFFICE (1969)
"Observer's Handbook"
1st Edition, Met. 0805, HMSO, London.

MOORE, D.J. (1976)
"Calculation of ground level concentrations for different sampling periods and source location"
Atmospheric Pollution, Elsevier Publishing Co., pp 51-60.

/Continued ...

References (continued)

O.E.C.D. (1977)
"The long-range transport of air pollutants"
Final Report.

O.E.C.D. (1975)
"LRTAP ground sampling stations site descriptions"
LRTAP 2/75

PARKER, HON. JUSTICE (1978)
"The Windscale Inquiry"
Report by HMSO, London.

PASQUILL, F. (1974)
"Atmospheric Diffusion"
Ellis Horwood, London.

PASQUILL, F. (1961)
"The estimation of the dispersion of windborne material"
Met. Mag. 90, pp 33-49.

POLLACK, R.I. (1975)
"Studies of pollutant concentration frequency distributions"
U.S. Environmental Protection Agency, Triangle Park, North Carolina.
Report No. EPA-650/4-75-004

PRAHM, L.P. and BERKOWICZ, R. (1978)
"Predicting concentrations in plumes subject to dry deposition"
Nature 271, pp 232-234.

PRAHM, L.P. and CRISTENSEN, O. (1977)
"Long-range transmission of pollutants simulated by a two-dimensional pseudospectral dispersion model"
Journ. App. Met. 16, no. 9, pp 896-910

/Continued ...

References (continued)

RASMUSSEN, N.C. (1975)
"Reactor safety study; an assessment of accident risks in U.S. commercial nuclear power plants"
U.S. Nuclear Regulatory Commission, WASH-1400 (NUREG-75/014)

RITCHIE, L.T., BROWN, W.D. and WAYLAND, J.R., (1976)
"Effects of rainstorms and runoff on consequences of nuclear reactor accidents"
Sandia Laboratories Report SAND76-0429.

SAFFMAN, P.G. (1962)
"The effect of windshear on horizontal spread from an instantaneous ground source"
Quart. J.R. Met. Soc. 88, pp 382-393.

SAWYER, J.S. (1952)
"The estimation of rainfall amount from observations of present weather"
Met. Office Orders C5/1952, Bracknell, Berks.

SCRIVEN, R.A. (1980)
"Sensitivity analysis for average and maximum dose at large distances"
CEC METEO Group of Experts (unpublished note)

SCRIVEN, R.A. and FISHER, B.E.A. (1975)
"The long-range transport of airborne material and its removal by deposition and washout - II. The effect of turbulent diffusion"
Atmos. Env. 9, pp 59-68.

SEHMEL, G.A. (1980)
"Particle and gas dry deposition; a review"
Atmos. Env. 14, pp 983-1012

SLADE, D.H. (Editor) (1968)
"Meteorology and Atomic Energy"
USAEC/Division of Technical Information, Report TID-24190

/Continued ...

References (continued)

SLINN, W.G.N. (1978)
"Parameterizations for resuspension and for wet and dry deposition of particles and gases for use in radiation dose calculations"
Nucl. Safety 19, pp 205-219.

SMITH, F.B. (1980)
"The influence of meteorological factors on radioactive dosages and depositions following an accidental release"
Proc. CEC Seminar, 22-25 April, 1980, Risø, Denmark, Vol. I, pp 223-245.

SMITH, F.B. (1975)
"Turbulence in the atmospheric boundary layer"
Science Progress, Oxford, pp 127-151; also Met. Office Note TDN No. 63, Bracknell, Berks.

SMITH, F.B. (1972)
"A scheme for estimating the vertical dispersion of a plume from a source near ground level"
Proc. of the Third Meeting of the Expert Panel on Air Pollution Modelling, NATO/CCMS, Report No. 14, Brussels (1972).

SPERANZA, A. (1975)
"The formation of baric depressions near the Alps"
Rome Inst. Naz. Geof, Ann. Geof. 28, pp 177-217.

STEIGER, F.H. (1971)
"Practical applications of the Weibull distribution function"
Chem. Technol. 1, pp 225-231.

STEWART, N.G. and CROOKS, R.H. (1958)
"Long-range travel of the radioactive cloud from the accident at Windscale"
Nature 182, pp 627-628.

/Continued ...

References (continued)

STRACHAN, S.J., (1979)
"Modelling the nature and consequences of accidental radioactive releases to the atmosphere"
Ph.D thesis, London University.

SYKES, R.I. and HATTON, L. (1976)
"Computation of horizontal trajectories based on the surface geostrophic wind"
Atmos. Env. 10, pp 925-934.

SYKES, R.I. (1974)
"Comparisons and verification of models for the evolution of the convective boundary layer"
Met. Office Note TDN, No. 57, Bracknell, Berks.

TUCKER, G.B. (1961)
"Precipitation over the North Atlantic Ocean"
Quart. J.R. Met. Soc. 87, pp 147-158.

TURNER, D.B. (1970)
"Workbook of Atmospheric Dispersion Estimates"
Environmental Health Series, Report No. 999-AP-26.
U.S. Environmental Protection Agency, North Carolina

VAN DER HOVEN, I. (1968)
"Deposition of particles and gases"
Meteorology and Atomic Energy (Slade, D.H., Ed.) USAEC, Report TID - 24190, pp 202-208.

WEIBULL, W. (1951)
"A statistical distribution function of wide applicability"
Journ. App. Mech. 18, pp 293-297.

WEST GERMAN MINISTRY FOR SCIENCE AND TECHNOLOGY (1979)
"Deutsche Risikostudie, Kernkraftwerke"
Published by Verlag TÜV, Rheinland GmbH, Köln.

/Continued...

References (continued)

WORLD METEOROLOGICAL ORGANISATION (1973-74)
"Monthly climatic data for the world"
U.S. Dept. of Commerce, Environmental Data Service, Asheville, North Carolina.

WRIGLEY, J., ApSIMON, H.M. and GODDARD, A.J.H. (1979)
"Meteorological data and the MESOS model for the long-range transport of pollutants"
Proc. WMO Symposium, Bulgaria, October 1979.

# APPENDIX A THE DEPTH OF THE DAYTIME MIXING LAYER

## A.1 Introduction

This Appendix describes a model (HTBL2) which is used to predict the evolution of the daytime mixing layer in the MESOS code.

A new solution method has been applied to the representation of the convective boundary layer proposed by Carson and Smith (1974). This method now allows for the treatment of a general temperature stratification within the boundary layer. Wind induced turbulent mixing is also included in a computationally efficient manner.

The mixing layer model and solution method are described in detail. Mixing layer calculations, using HTBL2, are compared with measurements in the atmosphere and other model predictions. The sensitivity of mixing layer development to the boundary layer temperature stratification is considered and discussed in relation to the use of an average temperature profile in dispersion calculations.

## A.2 Model for the Convective Growth of the Mixing Layer

The thermal structure of the boundary layer, adopted in the model, is shown in Figure (A.1). Convective mixing in the boundary layer is assumed to produce a constant potential temperature[1] profile $\theta_c(t)$ up to a height $h(t)$ which defines the depth of the mixing layer.

An inversion is typically found above the mixing layer. The upper inversion is modelled by a temperature change $\Delta\theta(t)$, across an entrainment layer, and by a stable temperature profile $\theta_s(z)$ above the mixing layer. The stable temperature profile can be represented by a series of stratified air layers with constant potential temperature gradient.

---

[1] Potential temperature is defined as the temperature which would occur when an air parcel is brought adiabatically to 1000 mb. Air is classified as stable, neutral or unstable, according to whether the potential temperature gradient is positive, zero or negative, respectively.

The potential temperature profile through the boundary layer is therefore taken as:

$$\theta(z,t) = \begin{cases} \theta_c(t) & \text{for } z < h(t) \\ \Delta\theta(t) = \theta_s(h(t)) - \theta_c(t) & \text{at } z = h(t) \\ \theta_s(z) = \theta_i + \gamma_i z & \text{for } z > h(t) \end{cases} \quad \ldots \text{(A1)}$$

Throughout the day, the ground is heated by solar insolation, and gives a sensible heat flux $H(o,t)$ into the mixing layer. The warmed air near the ground rises by convection to the top of the mixing layer, and can penetrate the stable layers above the mixing layer. Thermals, which reach the top of the mixing layer, entrain warmer stable air into the mixing layer, and this effect produces an additional sensible heat flux into the growing mixing layer.

These processes, which determine the convective growth of the mixing layer, can be summarised in the following set of equations (Carson and Smith (1974)):

$$H(o,t) - H(h(t),t) = \rho c_p h \frac{d\theta_c}{dt} \quad \ldots \text{(A2a)}$$

$$H(h(t),t) = -\rho c_p \left(\frac{dh}{dt}\right) \Delta\theta \quad \ldots \text{(A2b)}$$

$$H(h(t),t) = -AH(o,t) \quad \ldots \text{(A2c)}$$

Equation (A2a) relates the increase in mixing layer temperature to the total sensible heat flux into the mixing layer. Evaporation processes are not considered in the model, although they may be important in certain circumstances. The entrained heat flux at the top of the mixing layer is expressed in terms of the rate of growth of the mixing and the temperature increase across the entrainment layer (A2b). The heat flux at the top of the mixing layer is also assumed to be proportional to the surface heat flux. The entrainment parameter A is introduced to characterise the degree of entrainment. Although there is some degree of uncertainty in the choice of the entrainment parameter, a value of about 0.2 is typical (e.g. Betts (1973), Carson (1973))

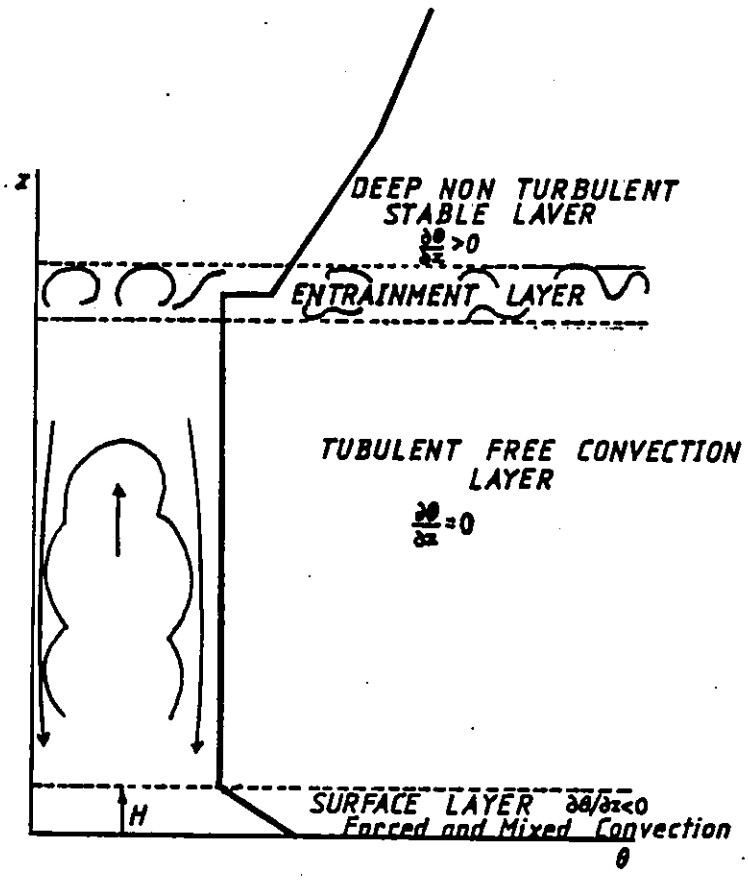



Figure (A1) Model of the Convective Mixing Layer
[taken from Carson (1973)]

## A.3 Specification of the Surface Heat Flux

The sensible heat flux from the ground can be derived from a consideration of the incoming solar radiation R. In rural areas the surface heat flux is typically one-third of the incoming solar radiation with an adjustment for the amount of cloud cover (Smith (1975)).

$$H(o,t) = \frac{r(c)R}{3} \qquad \ldots \text{(A4a)}$$

The reduction factors r(c) for cloud cover, are taken from Smith (1975) and are given in Table (A1). The surface heat flux can differ by a factor of 4, according to whether the sky is clear (0 oktas) or overcast (8 oktas). Cloud cover is therefore an important parameter and is taken directly from themeteorological database (Chapter 4).

| Cloud Cover (oktas) | Reduction factor | Cloud Cover (oktas) | Reduction factor |
|---|---|---|---|
| 0 | 1.0 | 5 | .67 |
| 1 | .89 | 6 | .59 |
| 2 | .81 | 7 | .45 |
| 3 | .76 | 8 | .23 |
| 4 | .72 | | |

Table A1: Reduction factors for cloud cover

The incoming solar insolation, in the absence of cloud cover, is estimated on the basis of elevation of the sun (ApSimon et al (1978)). Solar insolation depends on time of day t, day of year d, latitude $\phi$, and time of local noon $t_n$.

$$R = 950\ (\cos\zeta \cos\eta \cos\phi + \sin\zeta \sin\phi)\ W/m^2, \quad \text{where:}$$

$$\eta = \tan^{-1}\ [0.4348 \sin\ (\pi(d - 79)/180)] \qquad \ldots \text{(A4b)}$$

$$\zeta = \pi(t - t_n)/12$$

## A.4 Solution Method

The numerical scheme used in the program HTBL2 is described in this section. The solution method is based on a consideration of the transient heat content of the mixing layer and is represented schematically in Figure (A2). The formulation of the problem in terms of mixing layer heat content leads to a rapid calculation scheme for a more general treatment of the boundary layer. Convective and mechanical turbulence are both included in the model and are described separately.

### A.4.1 Convective Mixing

The heat flux Equations (A2) can be developed into a form which describes the heat energy transfer into the mixing layer over a time step $(t,t+\delta t)$.

$$\delta E = \int_{t}^{t+\delta t} H(o,\tau)d\tau \qquad \ldots \text{(A5a)}$$

$$\frac{(1+A)\delta E}{\rho c_p} = \int_{t}^{t+\delta t} (h.\frac{d\theta_c}{d\tau})d\tau = h(t)\cdot\delta\theta_c + O(\delta h.\delta\theta_c) \qquad \ldots \text{(A5b)}$$

$$\frac{A\delta E}{\rho c_p} = \int_{t}^{t+\delta t} (\Delta\theta.\frac{dh}{d\tau})d\tau = \frac{\delta h}{2}\,[\theta_s(h(t+\delta t)) + \theta_s(h(t)) - 2\theta_c(t+\delta t)] + O(\delta h.\delta\theta_c) \qquad \ldots \text{(A5c)}$$

The terms on the right hand side of Equations (A5b) and (A5c) represent the increase in mixing layer heat content and the heat content of entrained air, as indicated in Figure (A2).

The program requires the boundary layer temperature profile to be specified at dawn. The mixing depth and temperature profile are then updated for each time step between dawn and dusk in accordance with Equations (A5).

The calculation procedure for each time is as follows:

(i) The heat input $\delta E$ into the boundary layer due to the surface sensible heat flux is found by integration over the time step (A5a).

(ii) The increase in mixing layer temperature $\delta\theta_c$ caused by the surface heat flux and entrained heat flux is calculated (A5b).

(iii) The new temperature profile and mixing depth at time $(t+\delta t)$ are derived from a consideration of heat exchange from the eroded stable layers into the mixing layer (A5c).

The terms of order $(\delta h.\delta\theta_c)$ are relatively small and can be neglected if a sufficiently small time step $\delta t$ is used in the computations. Numerical studies with HTBL2 have shown that the value of the entrainment parameter A controls the size of time step required for convergence; smaller time steps are required as A increases. Satisfactory solutions are obtained (Section A.5) using a time step of one hour if the entrainment parameter is taken to be 0.15. This choice of entrainment parameter is slightly less than the value of 0.2 used by Carson and Smith (1974), but is considered acceptable due to the uncertainties in specifying the entrainment process. Optimisation justifies the use of a relatively large time step. This is important in the context of the work described in this thesis, as calculations for mixing layer development have been repeated several thousand times in the MESOS dispersion calculations.

### A.4.2 Wind Induced Mixing

Turbulent mixing due to the motion of an air mass over the ground, is incorporated into HTBL2 by using a simple but adequate method. The wind speed 10m above ground is first used to give an estimate of the depth of mechanical mixing which would occur, over typical rural terrain, without ground heating (Smith (1975)).

$$h_m(t) = 140\ u_{10}(t) \qquad \ldots (A6)$$

The depth of mechanical mixing is then compared to the existing mixing layer depth at each time step in the calculation procedure. If the

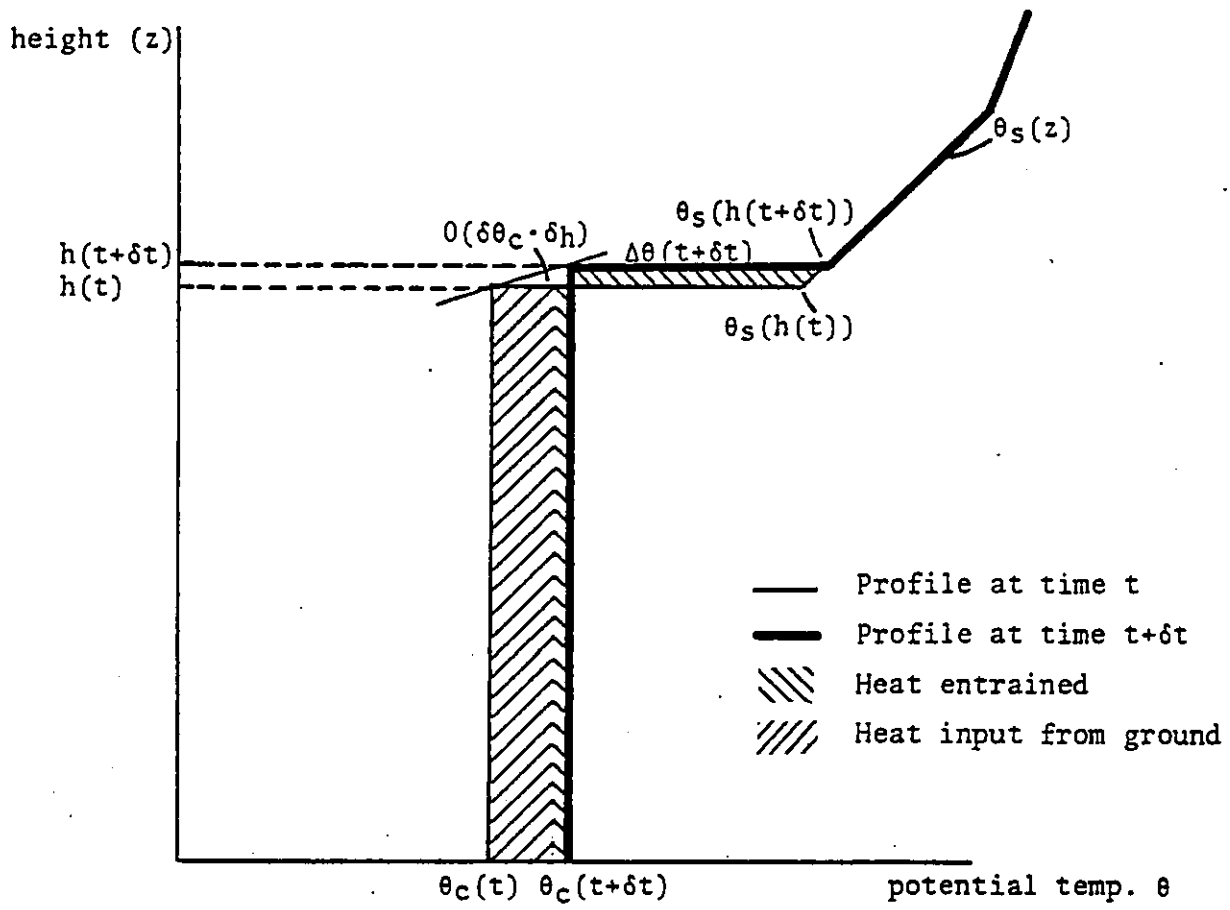



Figure.(A2a) Mixing Layer Development over a Timestep

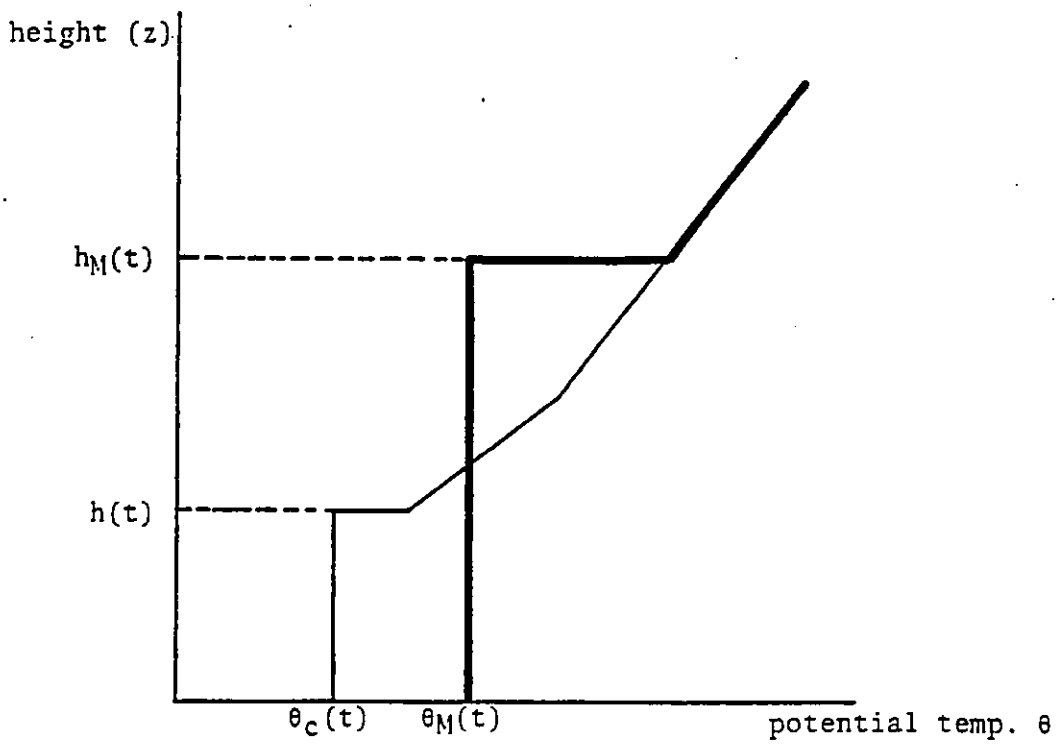



Figure (A2b) Adaption for Mechanical Mixing

depth of mechanical mixing is less than the existing mixing depth, then convective mixing is dominant and convective growth over the time step is not directly affected by mechanical mixing.

However, if the mechanical mixing depth is found to be greater than the existing mixing layer depth, the temperature profile is matched to the depth of the mechanical layer. The potential temperature $\theta_m(t)$ of the mechanically mixed layer is again assumed to be constant, and is calculated from a consideration of energy redistribution (Figure (A2b)). The energy content of the upper stable layers is considered to be absorbed into the mixing layer, so that:

$$\theta_m(t)\ h_m(t) = \theta_c(t)\ h(t) + \int_{h(t)}^{h_m(t)} \theta_s(z)dz \qquad \ldots(A7a)$$

The existing temperature profile is updated at the beginning of the time step to account for the dominance of mechanical mixing.

$$\theta(z,t) = \begin{cases} \theta_m(t) & \text{for } z < h_m(t) \\ \theta_s(z) = \theta_i + \gamma_i z & \text{for } z > h_m(t) \end{cases} \qquad \ldots (A7b)$$

The updated temperature profile is then used to predict convective development of the mixing layer over the following time step, as described in Section (A.4.1).

Although the numerical method distinguishes between mechanical and convective mixing, the two mixing processes are inseparable in the atmosphere. However, realistic mixing layer development is simulated by the numerical scheme because the two mixing processes are closely linked together over each time step. In general, either mechanical or convective mixing dominates the overall mixing layer development in the atmosphere.

## A.5 Validation of the Model

The model has been compared with mixing depth measurements in the atmosphere and with results from other models.

### A.5.1 Comparison with Measurements

Sykes (1974) discusses the predictive capability of mixing layer models by comparison with boundary layer measurements made on Day 33 of the Wangara Study. Numerical simulation of mixing layer development is difficult for the type of temperature stratification which occurred at dawn on that day. The temperature stratification consisted of a neutral layer, approximately 400m deep, existing above a surface inversion up to a height of about 150m. Calm conditions prevailed throughout the day.

The evolution of the convective mixing layer, as predicted by each model, is compared with measurements in Figure (A.3). The observed rapid increase in the mixing depth is successfully reproduced by both models. The HTBL2 model is in good agreement with measurements throughout the day.

### A.5.2 Comparison with Smith's Nomogram

The HTBL2 model has been compared to mixing layer depths given by the nomogram of Smith (1975), as recommended by the Working Group on Atmospheric Dispersion (Clarke, 1979). This nomogram is based on results from the model of Carson and Smith (1974) and gives mixing depths for general conditions of insolation and windspeed.

A comparison of results from HTBL2 and the nomogram for mixing layer development in Spring, Summer and Winter is given in Figure (A4). Insolation with clear skies is considered for calm and moderately strong wind conditions. In calm conditions, the HTBL2 calculations indicate a more rapid mixing layer development, but by dusk, both models are in reasonable agreement. In stronger winds, the mixing layer is already considerable at dawn and convective growth during the day is less significant. Table (A2) shows that the depths of the fully developed mixing layers, predicted by each model, are in reasonable agreement for a wide range of windspeeds in each season.

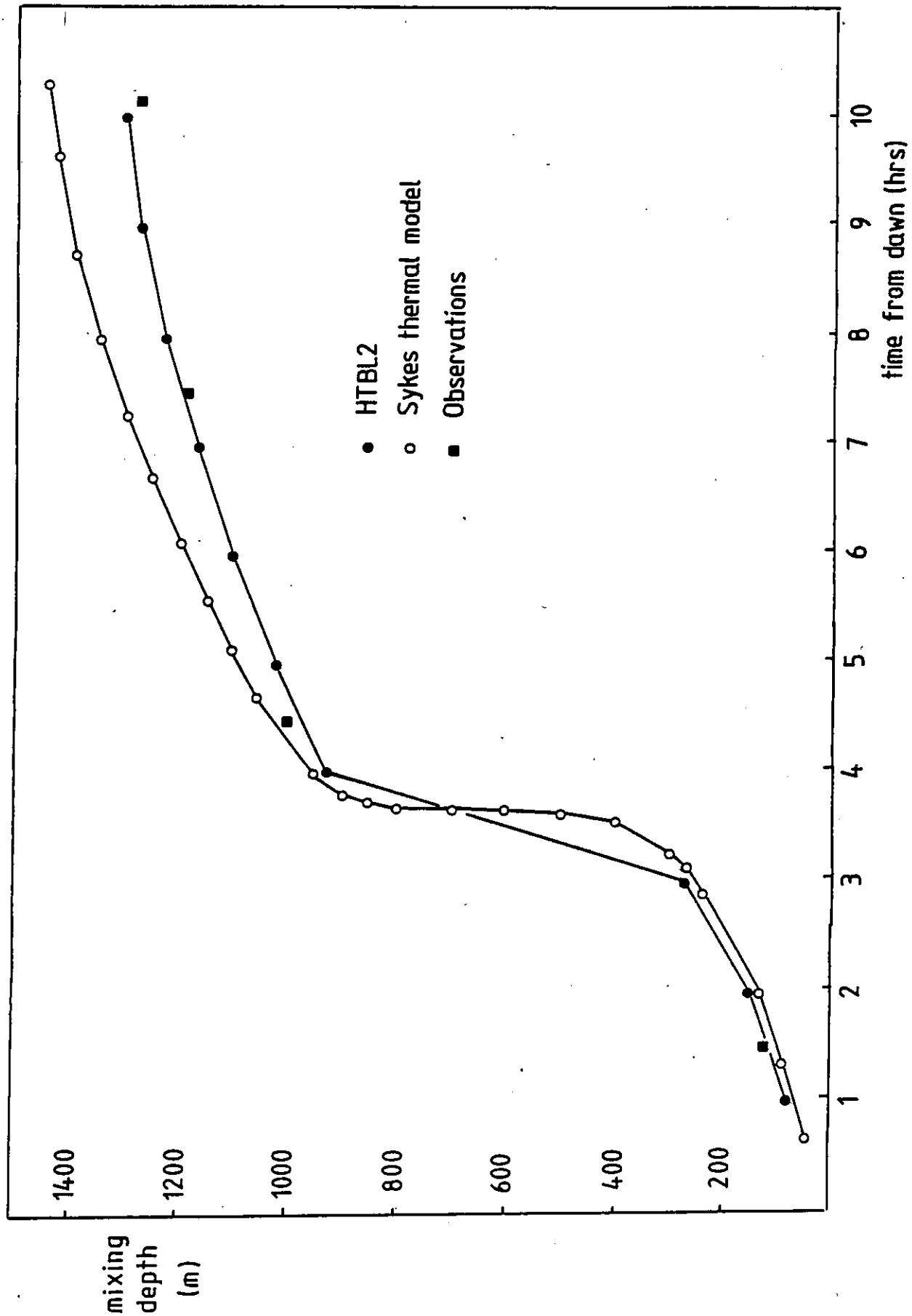



Figure (A3) Measurements and Model Calculations on Day 33 of the Wangara Study

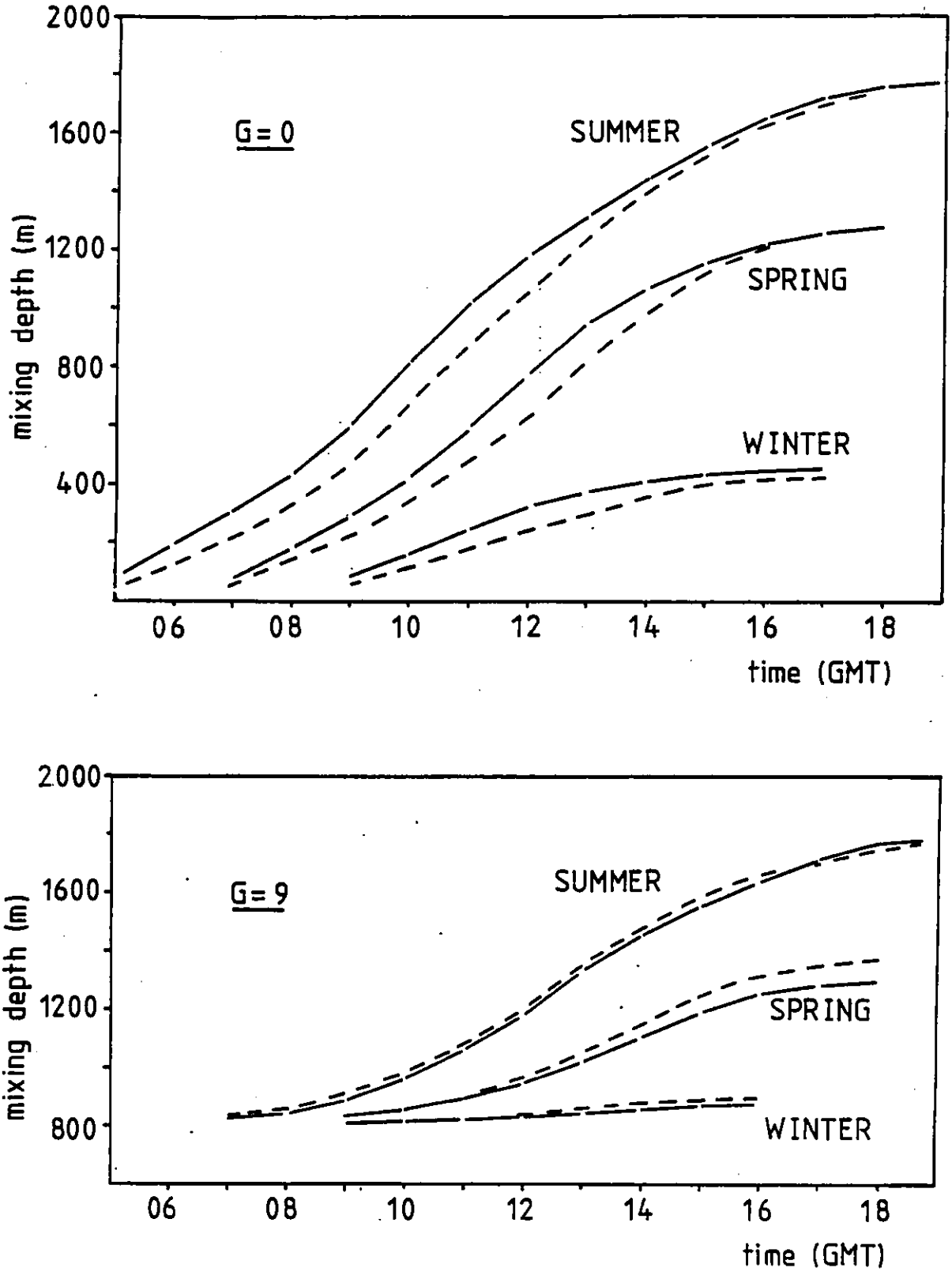



Figure (A4) Comparison of Model Calculations

| | | Geostrophic wind (m/s) | | | | | | |
|---|---|---|---|---|---|---|---|---|
| | | 0 | 3 | 6 | 9 | 12 | 15 | 18 |
| Day 80 | HTBL2 | 1275 | 1275 | 1275 | 1290 | 1381 | 1560 | 1782 |
| | Smith | 1290 | 1300 | 1330 | 1370 | 1500 | 1640 | 1870 |
| Day 170 | HTBL2 | 1789 | 1789 | 1789 | 1790 | 1801 | 1856 | 1986 |
| | Smith | 1780 | 1780 | 1780 | 1780 | 1800 | 1900 | 2000+ |
| Day 350 | HTBL2 | 461 | 463 | 633 | 878 | 1133 | 1393 | 1657 |
| | Smith | 420 | 510 | 690 | 890 | 1160 | 1410 | 1650 |

Table (A2) Comparison of mixing layer maximum depths predicted by HTBL2 and Carson and Smith's nomogram

| Day of year | Potential temp. gradient above 300m | Dutton lapse classes below 300m | | | |
|---|---|---|---|---|---|
| | | 5 | 6 | 7 | 8 |
| Day 80 | 6°C/km | 1431 | 1404 | 1383 | 1366 |
| | 12°C/km | 1035 | 1022 | 1007 | 966 |
| Day 170 | 6°C/km | 1903 | 1883 | 1867 | 1854 |
| | 12°C/km | 1363 | 1353 | 1342 | 1333 |
| Day 350 | 6°C/km | 767 | 717 | 673 | 637 |
| | 12°C/km | 588 | 562 | 535 | 512 |

Table (A3) Effect of stability on maximum mixing layer depths

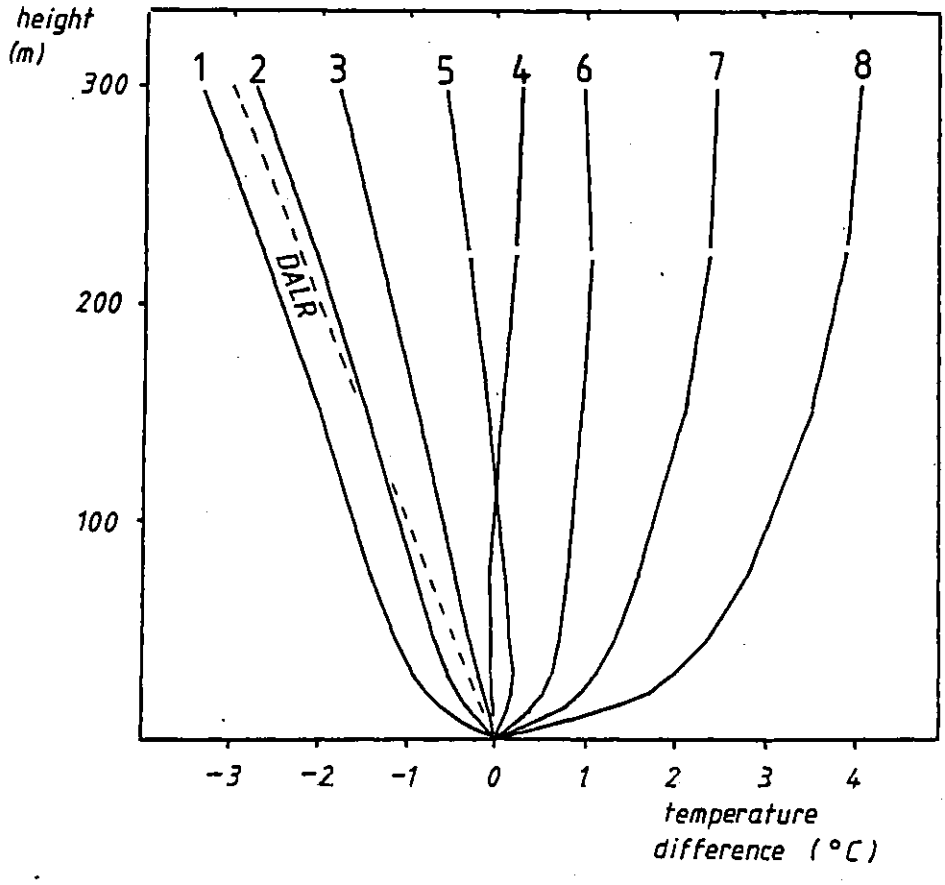
## A.6 Sensitivity of Mixing Layer Development to Temperature Stratification in the Boundary Layer

The program HTBL2 requires a temperature profile to be specified at dawn in order to predict the mixing layer development during the following day. Only a limited number of meteorological stations give frequent reports on the temperature stratification and such information is not included in the MESOS database. This section explains the choice of a suitable temperature profile at dawn for the HTBL2 calculations and examines the sensitivity of mixing layer growth to typical variations from this temperature profile.

Dutton(1977) has analysed the boundary layer temperature stratification below 300m, using upper air records from Cardington over a ten year period. The results are presented as a set of temperature profiles which are representative of different meteorological conditions. The Dutton temperature profiles are shown in Figure (A5) with an assessment of the most likely temperature profile at any given time. The probable range of temperature stratifications at dawn in moderate or low winds is given by profiles 5 to 8. In strong winds, turbulent mixing extends above 300m and dominates the temperature stratification in the lower region of the boundary layer. The HTBL2 model reflects this situation and subsequent mixing layer calculations are not affected by the details of the low level temperature profile.

The Cardington data also shows that the average temperature lapse rate between 300m and 1200m is usually about 6°C/km. Statistics on upper inversions at Cardington (Hardy, 1975) indicate that the lapse rate is very unlikely to exceed 12°C/km; only one lapse rate greater than 12°C/km was observed over ten years at Cardington.

The sensitivity of mixing layer development was therefore considered by defining a set of initial conditions using each of the Dutton profiles 5 to 8 below 300m, matched with lapse rates of 6°C/km and 12°C/km above 300m. The convective growth of the mixing layer was computed using HTBL2 for typical insolation conditions in Spring, Summer and Winter. A comparison of mixing layer depths obtained from each dawn temperature profile is given in Table (A3).




Temperature Profiles

| wind (m.s⁻¹) \ cloud (oktas) | 0 – 1 | 2 – 4 | 5 – 7 | 8 |
|---|---|---|---|---|
| 0 - 1 | 8 | 8 | 7 | 5 |
| 2 - 4 | 8 | 7 | 6 | 5 |
| 5 - 9 | 7 | 7 | 6 | 5 |
| 10 - 14 | 6 | 6 | 5 | 5 |
| ≥ 15 | 5 | 5 | 5 | 3 |

Probable Temperature Profile

Figure (A5) Temperature Profiles at Dawn

(Dutton (1977))

Mixing depths are found to be relatively insensitive to the initial temperature stratification below 300m. This is because the heat flux into the boundary layer during the morning is usually sufficient to erode the surface inversion. The heat energy needed to raise the temperature of a column of air increases with the depth of the air column. Convective penetration of an upper inversion requires significantly more energy than the erosion of a surface inversion. Mixing layer depths are therefore more sensitive to the upper air stabilities.

In view of the insensitivity of convective growth to the lower temperature stratification and the lack of meteorological reports on upper air stabilities, it is reasonable to use an average temperature profile within the MESOS dispersion calculations. An average temperature profile lying between the Dutton 6 and 7 profiles is used below 300m and this is matched to a constant lapse rate of 6°C/Km above 300m. The use of an average temperature profile is considered adequate for an estimate of mixing layer depth, since mixing layer development is dominated by the wind conditions and the time integrated heat input from the ground during the day.